AD/A-002 672

OH-58A PROPULSION SYSTEM VIRBRATION INVESTIGATION

James A. White

Bell Helicopter Company

Prepared for:

Army Air Mobility Research and Development Laboratory

August 1974

EUSTIS DIRECTORATE POSITION STATEMENT

This program was one of three contractual efforts in an initial attempt to define a better engine-airframe-propulsion installation interface. The long-range goal is to provide adequate design and test methods to insure compatibility of the engine and airframe.

Analytical and experimental work was conducted relative to a comparison of engine/airframe vibratory interface design techniques. Correlation was satisfactory to a frequency of approximately 40 Hz.

The technical monitor for this contract was Mr. James Gomez, Technology Applications Division.

Unclassified

SECURITY CLASSIFICATION OF THIS PAGE (*When Data Entered*)

AD/A002 672

REPORT DOCUMENTATION PAGE

READ INSTRUCTIONS
BEFORE COMPLETING FORM

1. REPORT NUMBER USAAMRDL-TR-74-47	2. GOVT ACCESSION NO.	3. RECIPIENT'S CATALOG NUMBER
4. TITLE (*and Subtitle*) OH-58A PROPULSION SYSTEM VIBRATION INVESTIGATION		5. TYPE OF REPORT & PERIOD COVERED Final Report
		6. PERFORMING ORG. REPORT NUMBER
7. AUTHOR(s) James A. White		8. CONTRACT OR GRANT NUMBER(s) DAAJ02-73-C-0017
9. PERFORMING ORGANIZATION NAME AND ADDRESS Bell Helicopter Company P. O. Box 482 Fort Worth, Texas 76101		10. PROGRAM ELEMENT, PROJECT, TASK AREA & WORK UNIT NUMBERS 1G262207AH8902
11. CONTROLLING OFFICE NAME AND ADDRESS Eustis Directorate U. S. Army Air Mobility R&D Laboratory Fort Eustis, Virginia 23604		12. REPORT DATE August 1974
		13. NUMBER OF PAGES ~~173~~ 190
14. MONITORING AGENCY NAME & ADDRESS(*if different from Controlling Office*)		15. SECURITY CLASS. (*of this report*) Unclassified
		15a. DECLASSIFICATION/DOWNGRADING SCHEDULE

16. DISTRIBUTION STATEMENT (*of this Report*)

Approved for public release; distribution unlimited.

17. DISTRIBUTION STATEMENT (*of the abstract entered in Block 20, if different from Report*)

18. SUPPLEMENTARY NOTES

Reproduced by
NATIONAL TECHNICAL
INFORMATION SERVICE
US Department of Commerce
Springfield, VA. 22151

19. KEY WORDS (*Continue on reverse side if necessary and identify by block number*)

Engines
Interfaces
Methods
Test
Airframes
Vibration
Impedance

20. ABSTRACT (*Continue on reverse side if necessary and identify by block number*)

Shake tests and dynamic analyses were conducted on an OH-58A helicopter to define the engine response to airframe vibrations. The objective was to determine the parameters defining the vibratory interaction and to provide a common language for engine/airframe interface analysis and for preparation of engine/airframe specifications.

DD FORM 1 JAN 73 1473 EDITION OF 1 NOV 65 IS OBSOLETE

Unclassified

(190)

SECURITY CLASSIFICATION OF THIS PAGE (*When Data Entered*)

20. Continued.

The shake tests were to determine parameters for use with the data supplied by the engine manufacturer in the impedance/mobility method to calculate engine response to the airframe vibrations. The calculated results showed poor coorelation with the engine response data obtained in shake tests.

The finite element method, NASTRAN, was also used for calculating engine response. There is a lack of data for comparison between the impedance/mobility method and NASTRAN primarily due to the test procedure that was selected at the start of the program. The results do indicate that an optimum test procedure can be developed.

There is no preference to either of the calculation methods. Both are capable of effecting a solution. Both methods have advantages and disadvantages. A combination of the two methods is advantageous.

The present study also reveals the complexity of the problem from the standpoint of both analysis and test. The analytical results, although not conclusive, delineate specific problem areas. The results of the current investigation suggest that analytical methods can be used to gain insight into interface problems at an early stage, while experimental procedures will require a longer period to perfect.

PREFACE

The work presented in this report was performed by Bell Helicopter Company under contract DAAJ02-73-C-0017 for the Eustis Directorate, U. S. Army Air Mobility Research and Development Laboratory, Fort Eustis, Virginia. The program was implemented under the technical direction of Mr. James Gomez, Jr., of the Technology Applications Division.

The study was conducted in two phases. Phase I consisted of the development and evaluation of analytical methods related to the interfacing of airframes and engines and Phase II consisted of the evaluation of experimental procedures for the determination of the mobility parameters developed in Phase I.

The report is presented in two parts. Part I presents the basic theory for the mobility techniques used in the study; the finite element models developed as part of the study; the results of analytical and numerical investigations conducted under Phase I; and a comparison of analytical results from the mobility and modal synthesis (NASTRAN) methods with data from flight test and with results from the experimental investigations conducted in Phase II. Part II presents the results of vibration testing to experimentally determine the mobility parameters for an OH-58A helicopter at the interface locations for the engine. Numerical analysis is also presented using the mobility method developed in Phase I and the data obtained during vibration testing in combination with mobility data for the engine obtained from the engine manufacturer.

TABLE OF CONTENTS

Page

PREFACE iii

LIST OF ILLUSTRATIONS vii

LIST OF TABLES xvi

PART I - ANALYTICAL INVESTIGATION 1

METHODS OF ANALYSIS 2

- Impedance/Mobility 2
  - Theory 2
  - Determination of Parameters 7
  - Analytical Approach 9
  - Experimental Approach 10
- NASTRAN 10

APPLICATION OF THE METHODS 12

- Impedance/Mobility 12
  - Verification of the Theory. 12
  - OH-58A Airframe Model 13
  - T-63 Engine Model. 14
  - Mobility Analysis. 14
- NASTRAN 15

RESULTS, PART I 17

PART II - EXPERIMENTAL INVESTIGATION 22

SHAKE TESTS 23

- Hardware. 23
  - General 23
  - Excitation Hardware 23

Preceding page blank

TABLE OF CONTENTS - cont.

Page

Instrumentation 24

Transducers 24
Data Acquisition System 24

Test Procedure 25

Series A Tests 25
Series B Tests 26
Series C Tests 26

Data Processing 26

NUMERICAL ANALYSIS 29

Determination of Transmission Input Shaft Mobilities. . . 29

Determination of Engine Response 31

RESULTS, PART II 32

Shake Tests 32

Numerical Analysis 33

CONCLUSIONS. 34

REFERENCES 37

LIST OF APPENDIXES 170

GLOSSARY OF TERMS 171

LIST OF ILLUSTRATIONS

Figure		Page
1	Finite Element Model of Simple Beams for Verification of Mobility Method	49
2	Comparison of Computed and Measured Steel Beam Model Tip Transfer Mobility	50
3	Comparison of Computed and Measured Steel Beam Model Transfer Mobility Phase	51
4	Comparison of Computed and Measured Steel Beam Model Driving Point Mobility.	52
5	Comparison of Computed and Measured Steel Beam Model Driving Point Mobility Phase.	53
6	Comparison of NASTRAN and Impedance/Mobility Computed Aluminum Beam Coupled Response, Beam Stations 9.6 and 40.4	54
7	Comparison of NASTRAN and Impedance/Mobility Computed Aluminum Beam Coupled Response, Beam Stations 10.6 and 39.4	55
8	Comparison of NASTRAN and Impedance/Mobility Computed Aluminum Beam Coupled Response, Beam Stations 15.4 and 34.6	56
9	Comparison of NASTRAN and Impedance/Mobility Computed Aluminum Beam Coupled Response, Beam Stations 20.2 and 29.8	57
10	Aluminum Beam Mode Shapes at Each Response Frequency. .	58
11	Two-Dimensional Finite Element Model of OH-58A Airframe With Grid Point Location in Global Reference System . .	59
12	Finite Element Representation of the OH-58A Pylon and Mount Assembly	60
13	Fuselage Mode Shape at 4.6 Hz (Longitudinal Pylon Mode)	61
14	Fuselage Mode Shape at 6.0 Hz (Lateral Pylon Mode) . .	62
15	Fuselage Mode Shape at 7.75 Hz (First Vertical Fuselage Mode)	63

LIST OF ILLUSTRATIONS - Continued

Figure		Page
16	Fuselage Mode Shape at 8.0 Hz (First Lateral Fuselage Mode)	64
17	Fuselage Mode Shape at 11.4 Hz (Baggage Compartment Panel Vertical Mode)	65
18	Fuselage Mode Shape at 22.5 Hz (Second Fuselage Vertical Mode)	66
19	Fuselage Mode Shape at 25.14 Hz (Vertical Fin Lateral Symmetric Bending Mode)	67
20	Fuselage Mode Shape at 28.8 Hz (Second Lateral Fuselage Mode)	68
21	Fuselage Mode Shape at 43.6 Hz (Third Fuselage Vertical Mode)	69
22	Finite Element Representation of the T-63 Engine and OH-58A Engine Mounts	70
23	Comparison of Two-Dimensional NASTRAN Model and Allison Shake Test Engine Mode Shapes	71
24	Three-Dimensional NASTRAN Model of OH-58A Helicopter. .	72
25	Three-Dimensional NASTRAN Model Mode Shapes.	73
26	Three-Dimensional NASTRAN Model Mode Shapes.	74
27	Three-Dimensional NASTRAN Model Mode Shapes.	75
28	Three-Dimensional NASTRAN Model Mode Shapes.	76
29	OH-58A Main Rotor Two-Per-Rev and Four-Per-Rev Vertical Shears	77
30	OH-58A Main Rotor Six-Per-Rev and Eight-Per-Rev Vertical Shears	78
31	OH-58A Main Rotor One-Per-Rev and Three-Per-Rev Inplane Shears	79
32	OH-58A Tail Rotor Vertical and Inplane Shears	80

LIST OF ILLUSTRATIONS - Continued

Figure		Page
33	Comparison of NASTRAN and DRAE02 (Mobility) Computed Engine Forward Compressor Vertical Velocity, Simulated 90-Knot Level Flight Response	81
34	Comparison of NASTRAN and DRAE02 (Mobility) Computed Engine Gearbox Vertical Velocity, Simulated 90-Knot Level Flight Response	82
35	Comparison of NASTRAN and DRAE02 (Mobility) Computed Engine Forward Compressor Vertical Velocity, Simulated 110-Knot Level Flight Response	83
36	Comparison of NASTRAN and DRAE02 (Mobility) Computed Engine Gearbox Vertical Velocity, Simulated 110-Knot Level Flight Response	84
37	Comparison of NASTRAN and DRAE02 (Mobility) Computed Engine Forward Compressor Vertical Velocity, Simulated 130-Knot Level Flight Response	85
38	Comparison of NASTRAN and DRAE02 (Mobility) Computed Engine Gearbox Vertical Velocity, Simulated 130-Knot Level Flight Response	86
39	Comparison of NASTRAN and DRAE02 (Mobility) Computed Engine Forward Compressor Lateral Velocity, Simulated 90-Knot Level Flight Response	87
40	Comparison of NASTRAN and DRAE02 (Mobility) Computed Engine Gearbox Lateral Velocity, Simulated 90-Knot Level Flight Response	88
41	Comparison of NASTRAN and DRAE02 (Mobility) Computed Engine Forward Compressor Lateral Velocity, Simulated 110-Knot Level Flight Response	89
42	Comparison of NASTRAN and DRAE02 (Mobility) Computed Engine Gearbox Lateral Velocity, Simulated 110-Knot Level Flight Response	90
43	Comparison of NASTRAN and DRAE02 (Mobility) Computed Engine Forward Compressor Lateral Velocity, Simulated 130-Knot Level Flight Response	91

LIST OF ILLUSTRATIONS - Continued

Figure		Page
44	Comparison of NASTRAN and DRAE02 (Mobility) Computed Engine Gearbox Lateral Velocity, Simulated 130-Knot Level Flight Response	92
45	Comparison of Analytical and Test Engine Velocities for Simulated 110-Knot Level Flight Forces, Forward Compressor Vertical Response.	93
46	Comparison of Analytical and Test Engine Velocities for Simulated 110-Knot Level Flight Forces, Gearbox Vertical Response	94
47	Comparison of Analytical and Test Engine Velocities for Simulated 110-Knot Level Flight Forces, Turbine Midsplit Vertical Response	95
48	Comparison of Analytical and Test Engine Velocities for Simulated 110-Knot Level Flight Forces, Fuel Nozzle Vertical Response	96
49	Comparison of Analytical and Test Engine Velocities for Simulated 110-Knot Level Flight Forces, Forward Compressor Lateral Response	97
50	Comparison of Analytical and Test Engine Velocities for Simulated 110-Knot Level Flight Forces, Gearbox Lateral Response	98
51	Comparison of Analytical and Test Engine Velocities for Simulated 110-Knot Level Flight Forces, Turbine Midsplit Lateral Response.	99
52	Comparison of Analytical and Test Engine Velocities for Simulated 110-Knot Level Flight Forces, Fuel Nozzle Lateral Response.	100
53	Comparison of Computed Engine Forward Compressor Vertical Velocities for Rigid and Disconnected Input Drive Shaft, 130-Knot Simulated Level Flight.	101
54	Comparison of Computed Engine Gearbox Vertical Velocities for Rigid and Disconnected Input Drive Shaft, 130-Knot Simulated Level Flight	102

LIST OF ILLUSTRATIONS - Continued

Figure		Page
55	Comparison of Computed Engine Turbine Midsplit Vertical Velocities for Rigid and Disconnected Input Drive Shaft, 130-Knot Simulated Level Flight	103
56	Comparison of Computed Engine Fuel Nozzle Vertical Velocities for Rigid and Disconnected Input Drive Shaft, 130-Knot Simulated Level Flight	104
57	Comparison of Computed Engine Forward Compressor Lateral Velocities for Rigid and Disconnected Input Drive Shaft, 130-Knot Simulated Level Flight.	105
58	Comparison of Computed Engine Gearbox Lateral Velocities for Rigid and Disconnected Input Drive Shaft, 130-Knot Simulated Level Flight.	106
59	Comparison of Computed Engine Turbine Midsplit Lateral Velocities for Rigid and Disconnected Input Drive Shaft, 130-Knot Simulated Level Flight.	107
60	Comparison of Computed Engine Fuel Nozzle Lateral Velocities for Rigid and Disconnected Input Drive Shaft, 130-Knot Simulated Level Flight.	108
61	Comparison of Computed and Measured Left-Hand Engine Bipod Longitudinal Driving Point Mobility, Airframe Mobility Element Y_{EE} (1,1)	109
62	Comparison of Computed and Measured Left-Hand Engine Bipod Lateral Driving Point Mobility, Airframe Mobility Element Y_{EE} (2,2)	110
63	Comparison of Computed and Measured Left-Hand Engine Bipod Vertical Driving Point Mobility, Airframe Mobility Element Y_{EE} (3,3)	111
64	Comparison of Computed and Measured Right-Hand Engine Bipod Longitudinal Driving Point Mobility, Airframe Mobility Element Y_{EE} (4,4)	112
65	Comparison of Computed and Measured Right-Hand Engine Bipod Lateral Driving Point Mobility, Airframe Mobility Element Y_{EE} (5,5)	113

LIST OF ILLUSTRATIONS - Continued

Figure		Page
66	Comparison of Computed and Measured Right-Hand Engine Bipod Vertical Driving Point Mobility, Airframe Mobility Element Y_{EE} (6,6)	114
67	Comparison of Computed and Measured Lower Engine Bipod Longitudinal Driving Point Mobility, Airframe Mobility Element Y_{EE} (7,7)	115
68	Comparison of Computed and Measured Lower Engine Bipod Lateral Driving Point Mobility, Airframe Mobility Element Y_{EE} (8,8)	116
69	Comparison of Computed and Measured Lower Engine Bipod Vertical Driving Point Mobility, Airframe Mobility Element Y_{EE} (9,9)	117
70	Comparison of Computed and Measured Left Engine Mount Longitudinal Driving Point Mobility, Engine Mobility Element Y_{EE} (1,1)	118
71	Comparison of Computed and Measured Left Engine Mount Lateral Driving Point Mobility, Engine Mobility Element Y_{EE} (2,2)	119
72	Comparison of Computed and Measured Left Engine Mount Vertical Driving Point Mobility, Engine Mobility Element Y_{EE} (3,3)	120
73	Comparison of Computed and Measured Right Engine Mount Longitudinal Driving Point Mobility, Engine Mobility Element Y_{EE} (4,4)	121
74	Comparison of Computed and Measured Right Engine Mount Lateral Driving Point Mobility, Engine Mobility Element Y_{EE} (5,5)	122
75	Comparison of Computed and Measured Right Engine Mount Vertical Driving Point Mobility, Engine Mobility Element Y_{EE} (6,6)	123
76	Comparison of Computed and Measured Lower Engine Mount Longitudinal Driving Point Mobility, Engine Mobility Element Y_{EE} (7,7)	124

LIST OF ILLUSTRATIONS - Continued

Figure		Page
77	Comparison of Computed and Measured Lower Engine Mount Lateral Driving Point Mobility, Engine Mobility Element Y_{EE} (8,8)	125
78	Comparison of Computed and Measured Lower Engine Mount Vertical Driving Point Mobility, Engine Mobility Element Y_{EE} (9,9)	126
79	Comparison of Computed and Measured Engine Output Shaft Longitudinal Driving Point Mobility, Engine Mobility Element Y_{EE} (10,10).	127
80	Comparison of Computed and Measured Engine Output Shaft Lateral Driving Point Mobility, Engine Mobility Element Y_{EE} (11,11).	128
81	Comparison of Computed and Measured Engine Output Shaft Vertical Driving Point Mobility, Engine Mobility Element Y_{EE} (12,12).	129
82	Installation of the OH-58A Helicopter for Vibration Testing.	130
83	Orientation and Arrangement of Shake Test Hardware for Mechanical Shaker Installation.	131
84	Detailed View of Mechanical Shaker and Hub Installation for Excitation at the Main Rotor	132
85	Arrangement of Impedance Head for Force Measurement Using the Lazan Mechanical Shaker for Longitudinal and Lateral Excitation at the Main Rotor Hub	133
86	Vari-Drive Assembly.	133
87	Arrangement of Electromagnetic Exciter and Hardware for Excitation at the Main Rotor Hub	134
88	Arrangement of Electromagnetic Exciter and Hardware for Excitation at the Tail Rotor Hub	135
89	Installation of Electromagnetic Exciter and Crank Assembly for Typical Excitation at Engine Mounts . . .	136

LIST OF ILLUSTRATIONS - Continued

Figure		Page
90	Arrangement of Exciter and Crank Assembly for Excitation at the Right- or Left-Hand Engine Mount	137
91	Arrangement of Exciter and Crank Assembly for Excitation at Lower Engine Mount	138
92	Arrangement of Exciter and Crank Assembly for Excitation at Main Transmission Input Shaft	139
93	Arrangement of Exciter and Crank Assembly for Excitation at Engine Output Shaft.	140
94	Approximate Location of Fuselage-Mounted Transducers. .	141
95	Approximate Location of Engine-Mounted Transducers . .	142
96	Typical Installations of Vertically Mounted Airframe Transducers	143
97	Typical Installations of Laterally Mounted Airframe Transducers	144
98	Typical Installations of Triaxial Transducers on Engine Bipods and Main Transmission	145
99	Typical Installations of Engine-Mounted Transducers . .	146
100	Data Acquisition System	147
101	Block Diagram of Ground Vibration Test Data Acquisition System	148
102	Test Log Matrix for Airframe Mobility Matrix, $[Y_{EE}]$ . .	149
103	Test Log Matrix for Airframe Mobility Matrix, $[Y_{EI}]$ . .	150
104	Test Log Matrix for Engine Response Check Matrix, $[Y_{CHK}]$	151
105	Coordinate System, Force, and Transducer Orientations. .	152
106	Partitioning for the Airframe Mobility Matrix	153
107	Engine Test Mobility Matrix	154

LIST OF ILLUSTRATIONS - Continued

Figure		Page
108	Engine Response Check Matrix.	155
109	Comparison of Computed and Measured Left-Hand Engine Bipod Vertical Driving Point Mobility.	156
110	Comparison of Computed and Measured Right-Hand Engine Bipod Vertical Driving Point Mobility.	157
111	Comparison of Computed and Measured Lower Engine Bipod Longitudinal Driving Point Mobility	158
112	Comparison of Computed (DRAE04) and Measured Shake Test Engine Forward Compressor Vertical Velocity.	159
113	Comparison of Computed (DRAE04) and Measured Shake Test Engine Gearbox Vertical Velocity	160
114	Comparison of Computed (DRAE04) and Measured Shake Test Engine Turbine Midsplit Vertical Velocity	161
115	Comparison of Computed (DRAE04) and Measured Shake Test Engine Fuel Nozzle Vertical Velocity	162
116	Comparison of Computed (DRAE04) and Measured Shake Test Engine Forward Compressor Lateral Velocity	163
117	Comparison of Computed (DRAE04) and Measured Shake Test Engine Turbine Midsplit Lateral Velocity.	164
118	Comparison of Computed (DRAE04) and Measured Shake Test Engine Fuel Nozzle Lateral Velocity	165
119	Comparison of Computed (DRAE04) and Measured Shake Test Engine Gearbox Longitudinal Velocity	166
120	Comparison of Analytical and Test Engine Velocities for Simulated 110-Knot Level Flight Forces; Forward Compressor Vertical Response.	167
121	Comparison of Analytical and Test Engine Velocities for Simulated 110-Knot Level Flight Forces; Gearbox Vertical Response	168
122	Comparison of Analytical and Test Engine Velocities for Simulated 110-Knot Level Flight Forces; Turbine Midsplit Vertical Response	169

LIST OF TABLES

Table		Page
I	Comparison of NASTRAN Model and OH-58A Shake Test Natural Frequencies	38
II	Center of Gravity Calculation	39
III	Instrumentation for Airframe and Pylon Frequency Response and Mode Shape Determination	40
IV	Instrumentation for Airframe Free Velocity Mobility Determination	41
V	Instrumentation for Internal Airframe Mobility Determination	42
VI	Instrumentation for Engine/Airframe Combined Vibration Tests	44
VII	Schedule of Tests	45
VIII	List of Numerical Analysis Cases	47
IX	Airframe Excitation Frequencies	48

PART I - ANALYTICAL INVESTIGATION

Vibratory interaction between helicopter engines and airframes has been shown in some cases to be a degrader of reliability and performance of operational Army helicopters. Considerable work is being done by the Army and the helicopter industry to determine the extent of the problem and develop analyses and design procedures for mitigating vibration effects.

Combining two dynamically complex machines, the airframe and turbine engine, provides a potential for interface compatibility problems. Excitations can be generated within either of these systems, and the vibratory characteristics of the combination are influenced by the structural dynamics of each of the components, and their interaction. Analytical development is in an early stage because a clear need for the expenditure of the considerable effort was slow in coming. Until recently, little information has been documented and disseminated with regard to vibration environment and its effect on turboshaft engines installed in operational U. S. Army helicopters. Especially perplexing was the wide spread in the vibration magnitudes allowed by the various engine specifications (Reference 1) and the prescribed methods of and parameters for measurement.

Future Army engines such as are presently being developed are characterized by higher rotational speeds and bearing DN values and will, therefore, be more sensitive to adverse engine/airframe vibratory interaction. An immediate need exists to effectively define the helicopter and engine vibration response characteristics in such a way as to reveal the respective contributions of the engine and airframe to the vibratory interaction, and identify and substantiate a set of vibratory parameters which will provide a common language for engine/airframe vibratory specification and analysis.

This report presents the results of an investigation of the OH-58A helicopter and Allison T-63 engine vibration characteristics. The investigation was directed toward the determination of engine response using impedance/mobility methods and NASTRAN. The results of these studies are compared with each other, with results from independent vibration tests of the airframe and engine, and with engine vibration levels measured during flight testing of the OH-58A helicopter.

METHODS OF ANALYSIS

Two independent approaches to analysis of the engine vibration problem were evaluated in pursuing the objectives of this study. The impedance/mobility method was evaluated for determining engine response utilizing test and analytical data. A finite element method, NAsa STRuctural ANalysis (NASTRAN), was evaluated for determining engine vibration utilizing the structural dynamic characteristics of the composite system.

A brief literature survey was conducted to review impedance/mobility methods currently used in the industry for structural dynamics analysis. The method of Flannelly (Reference 2) uses the full mobility matrix of a finite degree-of-freedom primary structure (airframe), the free mobility matrix of a substructure (engine) at the interface, and the interface modal mobility matrix to determine the system response. Flannelly's method is suited to analytical or test input data and uses the mobility method principally to determine the primary structure response. The substructure response is determined by modal synthesis from mobility parameters at the interface. The method of On (Reference 3) is to: (a) reduce the size of finite degree-of-freedom mobility matrices for the primary structure and substructure to mobility matrices with only interface response coordinates in matrix equation form; (b) determine the interface response and force by simultaneous solution of the interface equations, applying boundary conditions at the interface; and (c) determine the subsystem response by modal synthesis of interface modes.

The method of On was initially chosen for the investigation conducted herein since his analysis provides a system of equations in matrix form which leads to a direct determination of interface forces and velocities, and the determination of subsystem response using only impedance/mobility methods.

Initial evaluation of the mobility method with On's equations for a simple beam model gave good results. It was later determined that an inconsistency existed in On's interface equations. However, with minor modifications a system of equations evolved which was consistent with Thevinin's theorem and agreed with the general analysis of the interface problem given in References 4 and 5.

IMPEDANCE/MOBILITY

Theory

The velocity impedance (hereafter called impedance) of a simple mechanical system is defined by the relation

$$Z \equiv F/V \qquad (1)$$

where F is the force acting on the system and V is the resulting system velocity. If the ratio is given for force and velocity at the same location, the term driving point impedance is used; if for two different locations, the term transfer impedance is used.

The mobility of the system is defined by the relation

$$Y \equiv Z^{-1} = V/F \tag{2}$$

Rewriting equation (1) yields

$$VZ = F \tag{3}$$

and dividing both sides of equation (3) by Z gives

$$V = Z^{-1} F = YF \tag{4}$$

For a complex mechanical system, equation (4) in matrix notation is given by

$$\{V\} = [Y]\{F\} \tag{5}$$

The elements Y_{ij} of the mobility matrix are termed driving point mobilities for $i = j$ and transfer mobilities for $i \neq j$. It is understood that [Y] is a matrix derived from a set of frequency dependent functions which describes the dynamic behavior of the system, and that the mobility matrix at a specified frequency is given by $[Y(\omega)]$.

For the purpose of analysis, we shall partition equation (5) in such a way as to isolate coordinates of interest (external coordinates) from other coordinates of the system (internal coordinates), i.e.,

$$\left\{\begin{array}{c} V_E \\ \hdashline V_I \end{array}\right\} = \left[\begin{array}{c:c} Y_{EE} & Y_{EI} \\ \hdashline Y_{IE} & Y_{II} \end{array}\right] \left\{\begin{array}{c} F_E \\ \hdashline F_I \end{array}\right\} \tag{6}$$

where

$\{V_E\}$ - system velocities at external coordinates

$\{V_I\}$ - system velocities at internal coordinates

$[Y_{EE}]$ - driving point and transfer mobilities at external coordinates due to externally applied forces

$[Y_{EI}]$ - transfer mobilities at external coordinates due to internally applied forces

$[Y_{IE}]$ - transfer mobilities at internal coordinates due to externally applied forces

$[Y_{II}]$ - driving point and transfer mobilities at internal coordinates due to internally applied forces

$\{F_E\}$ - forces applied at external coordinates

$\{F_I\}$ - forces applied at internal coordinates

It is assumed that force generators of the system are always located at internal coordinates.

Expanding equation (6) gives

$$\{V_E\} = [Y_{EE}]\,\{F_E\} + [Y_{EI}]\,\{F_I\} \qquad (7)$$

and

$$\{V_I\} = [Y_{IE}]\,\{F_E\} + [Y_{II}]\,\{F_I\} \qquad (8)$$

Equation (7) gives the velocity of the system at external coordinates, i.e., at the coordinates of interest, and equation (8) gives the system velocities at all other coordinates.

For the particular case where the external forces are zero, the first of the matrix products on the right side of equations (7) and (8) vanishes, and the system velocities are given by

$$\{V_E\} = [Y_{EI}]\{F_I\} \qquad (9)$$

and

$$\{V_I\} = [Y_{II}]\{F_I\} \qquad (10)$$

The velocities given by equation (10) are termed the free velocities, $\{V_o\}$.

Substitution of $\{V_o\}$ into equation (7) yields

$$\{V_E\} = [Y_{EE}]\{F_E\} + \{V_o\} \qquad (11)$$

Equation (11) gives the system response at the external coordinates in terms of external velocities and external forces only.

Consider two systems with common external coordinates.

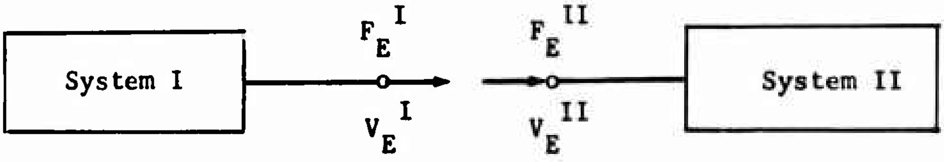

It is desired to determine the forces exerted on system II, $\{F_E^{II}\}$, at the external coordinates and the resultant internal velocities of system II, $\{V_I^{II}\}$, when the systems are connected together to form a composite system. Writing equation (11) for each system yields

$$\begin{aligned} \{V_E^{\ I}\} &= \{V_o^{\ I}\} + [Y_{EE}^{\ I}]\,\{F_E^{\ I}\} \\ \{V_E^{\ II}\} &= \{V_o^{\ II}\} + [Y_{EE}^{\ II}]\{F_E^{\ II}\} \end{aligned} \tag{12}$$

When the systems are connected together, equation (12) must satisfy a force equilibrium condition given by

$$\{F_E^{\ I}\} + \{F_E^{\ II}\} = 0 \Rightarrow \{F_E^{\ I}\} = - \{F_E^{\ II}\} \tag{13}$$

and a velocity compatibility condition given by

$$\{V_E^{\ I}\} = \{V_E^{\ II}\} \tag{14}$$

Substituting equations (13) and (14) into equation (12) and subtracting the first of equations (12) from the second yields

$$\left([Y_{EE}^{\ I}] + [Y_{EE}^{\ II}]\right)\{F_E^{\ II}\} + \{V_o^{\ II} - V_o^{\ I}\} = 0 \tag{15}$$

from which it follows that

$$\{F_E^{\ II}\} = \left([Y_{EE}^{\ I}] + [Y_{EE}^{\ II}]\right)^{-1}\{V_o^{\ I} - V_o^{\ II}\} \tag{16}$$

Equation (8) for system II gives

$$\{V_I^{\ II}\} = [Y_{IE}^{\ II}]\{F_E^{\ II}\} + [Y_{II}^{\ II}]\{F_I^{\ II}\} \tag{17}$$

Substituting equation (16) into equation (17) yields

$$\{V_I^{\ II}\} = [Y_{IE}^{\ II}]\left\{\left([Y_{EE}^{\ I}] + [Y_{EE}^{\ II}]\right)^{-1}\{V_o^{\ I} - V_o^{\ II}\}\right\} + [Y_{II}^{\ II}]\{F_I^{\ II}\} \tag{18}$$

Remembering that $\{F_E^{\ I}\} = - \{F_E^{\ II}\}$, the internal velocities of system I are given by

$$\{V_I^{\ I}\} = [Y_{IE}^{\ I}]\left\{\left([Y_{EE}^{\ I}] + [Y_{EE}^{\ II}]\right)^{-1}\{V_o^{\ II} - V_o^{\ I}\}\right\} + [Y_{II}^{\ I}]\{F_I^{\ I}\} \tag{19}$$

Equation (18) yields the response at internal coordinates of system II, and equation (19) yields the response at internal coordinates of system I, for normal operations of both systems after the connection. Equation (16) yields the interconnection or interface forces. The interface velocities of systems I and II, i.e., $\{V_E^{I}\}$ and $\{V_E^{II}\}$, can be obtained by substitution of equation (16), and equation (16) with superscripts I and II exchanged, into equation (7) for systems II and I, respectively.

In the above analysis, both systems I and II are active. If system II is passive, i.e., $\{F_I^{II}\} = 0$, then equation (16) reduces to

$$\{F_E^{II}\} = \left([Y_{EE}^{I}] + [Y_{EE}^{II}]\right)^{-1} \{V_o^{I}\} \qquad (20)$$

and equation (18) reduces to

$$\{V_I^{II}\} = [Y_{IE}^{II}] \left([Y_{EE}^{I}] + [Y_{EE}^{II}]\right)^{-1} \{V_o^{I}\} \qquad (21)$$

By application of Thevinin's equivalent theorem and the definitions of mechanical impedance and mobility, it can be shown (Reference 4) that the response, V_N, at a desired point on a simple passive system which has been connected to a simple active system is given by

$$V_N = \left[Y_N/(Y_1 + Y_2)\right] V_o = Y_N (Y_1 + Y_2)^{-1} V_o \qquad (22)$$

where Y_N is the transfer mobility of the passive system (due to forces at the connection), Y_1 is the driving point mobility of the active system as observed at the connection, Y_2 is the driving point mobility of the passive system as observed at the connection, and V_o is the velocity of the active system at the point of connection, prior to the connection.

For a complex system, equation (22) in matrix notation becomes

$$\{V_N\} = [Y_N] \left([Y_1] + [Y_2]\right)^{-1} \{V_o\} \qquad (23)$$

In terms of the notation given in the analysis above,

$\{V_N\} = \{V_I^{II}\}$, $[Y_N] = [Y_{IE}^{II}]$, $[Y_1] = [Y_{EE}^{I}]$, $[Y_2] = [Y_{EE}^{II}]$, and

$$\{V_o\} = \{V_o^{I}\}$$

where the superscripts I and II correspond to the active and passive systems, respectively. Substitution of these equalities into equation (23) yields

$$\{V_I^{II}\} = [Y_{IE}^{II}] \left([Y_{EE}^{I}] + [Y_{EE}^{II}]\right)^{-1} \{V_o^{I}\} \qquad (24)$$

which is identical to equation (21).

The governing equations for the connection of two complex, active dynamic systems are given by equations (16) and (18). The matrices given in these equations can be determined directly by test or by analysis using methods to be shown after digressing to comment on On's method.

Using the method of On, equation (21) is of the form

$$\{V_I{}^{II}\} = [Y_{IE}{}^{II}] \left([Y_E{}^{I}] + [Y_E{}^{II}]\right)^{-1} \{V_o{}^{I}\} \tag{25}$$

where

$$[Y_E] = [Y_{EE}] - [Y_{EI}][Y_{II}]^{-1} [Y_{IE}] \tag{26}$$

and

$$\{V_o\} = [Y_{EI}][Y_{II}]^{-1} \{V_I\} \tag{27}$$

The superscript is omitted with the understanding that equations (26) and (27) are identical in form for either system. Equation (25) compares exactly with equation (23) if $\{V_N\}$, $[Y_N]$, $[Y_1]$, $[Y_2]$, and $\{V_o\}$ are substituted for $\{V_I{}^{II}\}$, $[Y_{IE}{}^{II}]$, $[Y_E{}^{I}]$, $[Y_E{}^{II}]$, and $\{V_o{}^{I}\}$, respectively. However, $[Y_E{}^{I}]$ and $[Y_E{}^{II}]$ differ conceptually from $[Y_1]$ and $[Y_2]$ and must be analytically determined, along with $\{V_o{}^{J}\}$, from a measurement of the full mobility matrix $[Y]$ given in equation (5). From the pure analytical standpoint, equation (25) in combination with equations (26) and (27) for each system results in a dilemma brought about by the fact that On's interface equations involve three unknowns: $\{V_E\}$, $\{F_E\}$, and $\{V_I\}$.

Determination of Parameters

The equation of motion of a complex mechanical system, in matrix form, is given by

$$[M] \{\ddot{x}(t)\} + [C] \{\dot{x}(t)\} + [K] \{x(t)\} = \{f(t)\} \tag{28}$$

Let

$$\left.\begin{aligned} f(t) &= Fe^{i\omega t} \\ \dot{x}(t) &= \dot{X}e^{i\omega t} \end{aligned}\right\} \tag{29}$$

Assume steady-state harmonic motion, i.e., $\dot{X}$ = constant; then

$$\left.\begin{aligned} \ddot{x}(t) &= \frac{d}{dt}\,\dot{x}(t) = \frac{d}{dt}\,\dot{X}e^{i\omega t} = i\omega\dot{X}e^{i\omega t} \\ \text{and} \\ x(t) &= \int^{\tau}\dot{x}(t)dt = \int^{\tau}\dot{X}e^{i\omega t} = \frac{1}{i\omega}\,\dot{X}e^{i\omega t} \end{aligned}\right\} \qquad (30)$$

where τ is the period of the harmonic motion. Substitution of equations (29) and (30) into equation (28) and arranging terms in real and imaginary components yields

$$\left(i\omega[M] + \frac{1}{i\omega}\,[K] + [C]\right)\,\{\dot{X}e^{i\omega t}\} = \{Fe^{i\omega t}\} \qquad (31)$$

The Fourier transforms of $\dot{X}e^{i\omega t}$ and $Fe^{i\omega t}$ are given by $V(\omega)$ and $F(\omega)$, respectively. It follows that

$$\left(i\omega[M] + \frac{1}{i\omega}\,[K] + [C]\right)\,\{V(\omega)\} = \{F(\omega)\} \qquad (32)$$

Dividing both sides of equation (32) by $\{V(\omega)\}$ gives

$$\left(i\omega[M] + \frac{1}{i\omega}\,[K] + [C]\right) = \frac{\{F(\omega)\}}{\{V(\omega)\}} \qquad (33)$$

By definition (equation (1)),

$$Z(\omega) = \frac{F(\omega)}{V(\omega)} \qquad (34)$$

Therefore

$$[Z(\omega)] = \left(i\omega[M] + \frac{1}{i\omega}\,[K] + [C]\right) \qquad (35)$$

Furthermore

$$[Y(\omega)] \equiv [Z(\omega)]^{-1} = \left(i\omega[M] + \frac{1}{i\omega}\,[K] + [C]\right)^{-1} \qquad (36)$$

Substituting equation (35) into equation (32) and premultiplying both sides of the resultant equation by $[Z(\omega)]^{-1}$ gives

$$\{V(\omega)\} = [Z(\omega)]^{-1}\,\{F(\omega)\} \qquad (37)$$

From equation (36) it follows that

$$\{V(\omega)\} = [Y(\omega)]\,\{F(\omega)\} \qquad (38)$$

Partitioning (38) in terms of internal and external coordinates gives

$$\begin{Bmatrix} V_E \\ \hdashline V_I \end{Bmatrix} = \left[\begin{array}{c:c} Y_{EE} & Y_{EI} \\ \hdashline Y_{IE} & Y_{II} \end{array}\right] \begin{Bmatrix} F_E \\ \hdashline F_I \end{Bmatrix} \qquad (39)$$

where the ω subscript is dropped for simplicity. Equation (39) is identical to equation (6). In order to determine the matrices of the foregoing sections, analytical and experimental procedures are given in the following sections.

Analytical Approach

The basic procedures for analytical evaluation of the response of two complex dynamic systems, for which at least one of the systems is active, may be summarized as follows.

A. Choose a set of appropriate coordinates of the systems and form the equation of motion of each system, i.e.,

$$[M_1]\ \{\ddot{x}_1(t)\} + [C_1]\ \{\dot{x}_1(t)\} + [K_1]\ \{x_1(t)\} = f_1(t)$$

$$[M_2]\ \{\ddot{x}_2(t)\} + [C_2]\ \{\dot{x}_2(t)\} + [K_2]\ \{x_2(t)\} = f_2(t)$$

The equations of motion may be formed by any rational analysis. It is recommended, however, that finite element procedures be utilized for large complex systems, since these procedures are well documented and are especially suited to automatic data processing techniques of current high speed digital computers.

B. Using coordinate reduction procedures, reduce the number of coordinates to the desired level and determine the reduced mass, [M], damping, [C], and stiffness, [K], matrices for each system.

C. Determine the impedance matrices, $[Z^I]$ and $[Z^{II}]$, by application of the Fourier transforms.

D. Partition the impedance matrix for each system in terms of internal and external coordinates.

E. Establish the frequency range (or discrete frequencies) for which the analysis is to be conducted.

F. For the initial frequency, determine the impedance matrix, $[Z(\omega)]$, and its inverse, $[Y(\omega)]$, for each system.

G. Determine the submatrices, $[Y_{EE}]$, $[Y_{EI}]$, $[Y_{IE}]$, and $[Y_{II}]$, and the column vector of internal forces, $\{F_I\}$, and free velocities, $\{V_o\}$, for each system.

H. Determine the interface forces, $\{F_E^{II}\}$, from equation (16), the internal velocities of system II, $\{V_I^{II}\}$, from equation (18) and the internal velocities of system I, $\{V_I^{I}\}$, from equation (19).

I. If the interface velocities, $\{V_E^{I}\} = \{V_E^{II}\} = \{V_E\}$, are of interest, determine $\{V_E\}$ from a combination of equation (16) with equation (7) for system II.

J. Repeat procedures F through I for each frequency of interest.

Experimental Approach

Both analytical and experimental evaluations of the impedance/mobility method described by the theory presented in preceding sections were conducted. The experimental approach used for this evaluation is presented in Part II.

NASTRAN

Finite element methods using the NASTRAN were evaluated, and the results are reported herein. The theoretical development of NASTRAN is beyond the scope of this report. However, the general aspects of the program and the general data requirements for dynamic analysis are discussed in the following paragraphs.

NASTRAN is a general-purpose, structural analysis computer program, based on finite element theory and methods. The program can be used for static and dynamic structural analysis with several subanalyses under each of these broad categories. For example, static analysis can include inertia relief and/or differential stiffness, buckling analysis, piecewise linear analysis, etc., while dynamic analysis may include direct complex eigenvalue analysis, direct frequency and random response, modal eigenvalue analysis and response, and direct transient response. Only the natural frequency and forced response analyses were evaluated in this study.

The basic inputs for dynamic analysis are

- grid point identification and location
- element identification, grid point connectivity, and orientation
- element physical and/or geometrical properties
- grid point mass (lumped) or density (distributed mass)
- degrees of freedom omitted at each grid point

- type of solution desired; frequency and mode shapes, forced response, etc.

- location, magnitude and orientation of excitation forces

The program formulates the stiffness, mass and damping matrices for the combined structure and performs coordinate reductions defined by input. From the reduced stiffness and mass matrices, the program formulates and solves the general eigenvalue problem and computes the system natural frequencies, generalized mass and stiffness and mode shapes. If required, the program then computes the response at predetermined coordinates to specified forces by modal synthesis.

APPLICATION OF THE METHODS

IMPEDANCE/MOBILITY

Verification of the Theory

The simple beam models shown in Figure 1 were used to substantiate the mobility analysis. The dimensions of the steel beam were 50 by 2 by 1/2 inches and of the aluminum beam 30.8 by 2 by .46 inches. The beam masses were determined by lumped parameter methods using the beam cross-sectional area, and material density. The stiffness matrix for each beam was determined using NASTRAN. The stiffness and mass matrices were then used in the mobility and NASTRAN methods to compute mobility matrices of the beams and the response of the aluminum beam to forces exerted on the steel beam.

At the conclusion of the shake test program the response of the steel beam was determined for grid point 2 and 12 locations. The driving force was located at grid point 12 for the shake test. The transfer mobility magnitude (response at grid point 2 to a force at grid point 12) computed by the mobility and NASTRAN methods is compared with shake test results in Figure 2. The mobility phase is compared in Figure 3. For the computed cases, the system damping was zero. Good agreement between analysis and test is shown, ignoring the asymmetric mode responses at 15 and 137 Hertz. The disagreement at the 15 Hertz frequency is due to a support system mode. The analytical models were symmetrical in both stiffness and mass, while the actual beam tested was asymmetrical in mass, due to the location of an accelerometer 1 inch from the beam tip (model grid point 2). Thus, the asymmetric bending mode shown at 137 Hertz would not be shown in these models for forced excitation at the beam center. The phase difference (Figure 3) is due to structural damping characteristics of the beam which were omitted in the computed cases. The phase angle for computed data had to be indexed by 180 degrees, to account for the difference in reference between analysis and test.

A similar comparison is given for driving point mobility (response and force at the same location), at the beam center, in Figures 4 and 5. For excitation frequencies below 130 Hertz, good agreement is shown between all cases. From 130 Hertz to 190 Hertz, the location of the response minima and the magnitudes of response are slightly different for all three cases. This difference is attributed to mass condensation procedures, omission of grid point inertias, and difference in the methods of analysis.

The coupled response of the aluminum beam was computed using the mobility and NASTRAN methods for a 5-pound and 10-pound force applied at grid points 2 and 22 of the steel beam. The mobility and NASTRAN aluminum beam responses for this case are compared in Figures 6 through 9 for a frequency range of from 30 to 50 Hertz. The computed response is given for all beam stations except at the connection. The NASTRAN and mobility methods produce exactly the same response in this frequency range. Mode shapes of the beam response are given in Figure 10 for each response frequency. The mode shapes demonstrate that the aluminum beam experiences only vertical translational motion in the frequency band shown which brackets the resonance of the steel beam. The above comparisons demonstrate that the mobility and NASTRAN methods produce the same results over a significant frequency range. It is concluded, therefore, that the impedance/mobility theory given in the preceding sections presents a rational analysis.

The NASTRAN input data, computed natural frequencies and mode shapes, and the stiffness and mass distributions for each beam are tabulated in Appendix A. The NASTRAN computed responses, the mobility matrices, and the beam responses for the mobility method are also tabulated in this appendix. Appendixes to the report are on file at USAAMRDL, Eustis Directorate and will be furnished on request.

OH-58A Airframe Model

The two-dimensional finite element model of the OH-58A helicopter given in Figure 11 was used in both the mobility and NASTRAN methods. The grid point locations of each of the principal mass points in fuselage coordinates are presented in the figure. The finite element elastic axis model of the Allison T-63 engine is shown installed.

A detailed finite element model of the pylon assembly and pylon mounts is presented in Figure 12. The grid point attachment to the airframe model is shown in the figure.

The models shown in these figures were assembled using bar elements, pin-ended bar elements, and linear elastic springs. The properties of these elements were determined from detailed drawings of the OH-58A airframe and subsystems. The weight distribution by grid point was determined from a detailed weight statement for the helicopter, for the empty weight configuration. Useful load items, i.e., pilot, copilot, fuel, ballast, etc., and the engine distributed weight were added to produce the gross weight/center of gravity configuration corresponding to the flight and shake test cases.

Natural frequencies of the helicopter were computed (with the engine installed) and compared with shake test results. Approximately ten iterations, varying element stiffnesses at selected locations, were required to produce model natural modes at the same frequencies as shown by shake test. The fuselage mode shapes for the first nine flexible modes of the helicopter are given in Figures 13 through 21. The generalized mass, generalized stiffness, and the engine out, engine in, and shake test natural frequencies are presented in the figures. Agreement between analysis and test was good. The element data and computed frequencies and mode shapes for the above model are tabulated in Appendix B.

T-63 Engine Model

A detailed finite element representation of the T-63 engine and OH-58A engine mounts is presented in Figure 22. The element properties for the mounts were determined from detailed drawings. The element stiffness and mass distributions for the T-63 elastic axis engine model were furnished by Detroit Diesel Allison Division, General Motors Corporation. The mass distribution furnished did not include supported weight items, i.e., fuel lines, trapped fuel, engine oil, starter-generator, fuel control, etc.; these were added. The total engine weight for the model was 196.2 pounds, which agrees with the Bell weights statement.

The elastic axis model furnished Bell was used by Allison to determine pin-ended engine and shaft modes. The double diaphragm connection between the engine case and forward compressor was represented by a single bending spring element between grid points 216 and 217 of Figure 22. The stiffness of the element was varied for inplane and out-of-plane bending until the desired frequencies were obtained. The completed model mode shapes and natural frequencies are compared with Allison shake test results in Figure 23. Agreement between analysis and test was good.

To provide attachment of the elastic axis engine model to the airframe model at the engine mounts, the massless, rigid T-element (shown in Figure 22) was used to represent the engine gear case. This element also provided the required interface points.

The element data and computed frequencies and mode shapes for the engine model are tabulated in Appendix C.

Mobility Analysis

The stiffness and mass matrices for the OH-58A and T-63 models described in the preceding sections were determined using NASTRAN. The matrices were determined for the engine and airframe independently and were provided in punched card form by the program. This data is tabulated in Appendixes B and C for the OH-58A and T-63 model, respectively.

An impedance/mobility analysis, BHC computer program DRAE02, was developed based on the mobility theory previously discussed. The program was coded to accept mass and stiffness matrices in card form for one or two mechanical systems not exceeding seventy-five degrees of freedom each. For the single-system case, the program computes the impedance/mobility parameters for all degrees of freedom at each frequency desired, up to a maximum of 150 frequencies. For the two-system case, system I must be described by the first set of input data and must be active. Two active systems are permitted. The program computes impedance/mobility parameters for each system, forms the connection, and computes the response of system II due to forces applied at system I coordinates.

Options are provided by input to plot system I or system II mobility coordinates, interconnection forces as observed by system II, and/or response of specified coordinates of system II for the combined system. A linearly scaled response versus frequency graph was selected for forced response data to provide interfacing with flight test data and because discrete frequency analysis is generally required in this case. Both mobility amplitude and phase are plotted. A linearly scaled phase and logarithmically scaled amplitude versus frequency graph is provided for interfacing with shake test data (continuous frequency case). A FORTRAN listing of the program, including all subroutines, and users guide is given in tabular form in Appendix D.

The finite element models described in the preceding sections were analyzed using program DRAE02. The mobility matrices for the airframe and engine models are presented in Appendixes B and C, respectively. The results are discussed in a later section.

NASTRAN

The three-dimensional NASTRAN model of the OH-58A helicopter shown in Figure 24 was developed to evaluate the efficacy of the modal synthesis method for coupling the airframe and engine. This type of model, although not required, was desirable because the topology discretely retains the engine interface location and provides coupling of vertical, lateral, and torsional airframe modes. In developing the OH-58A dynamics three-dimensional model from a NASTRAN stress model of an Aerial Scout helicopter, it was necessary to make several major modifications. These included: the nose structure, main rotor pylon support structure, tail-boom/vertical-fin elastic axis structure, tail rotor support structure, and basic fuselage structural properties. Extensive grid point and connectivity modifications were required. A model having 374 grid points with 2038 degrees of freedom was condensed in NASTRAN to 245 degrees of freedom. Even though compressed, this analysis required the entire storage of the IBM 360 computer. Five passes, at two and one-half hours per pass, were made to remove singularities and obtain a set of natural frequencies. The three-dimensional model could not be justified, and it was dropped in favor of a two-dimensional model.

The first eight flexible modes of the three-dimensional NASTRAN model are presented in Figures 25 through 28. The generalized mass, generalized stiffness and natural frequency for each mode are given in the figures. The three-dimensional model frequencies and the two-dimensional model and shake test frequencies are compared in Table I. Close agreement (obtained by iteration of stiffness properties) between the two-dimensional NASTRAN model and shake test frequencies is shown. All frequencies of the three-dimensional model, however, are low in comparison to either of these, except for the baggage compartment floor, main rotor mast lateral, and second fuselage lateral modes. The element data, natural frequencies, and mode shape data for the three-dimensional model are tabulated in Appendix D.

The two-dimensional NASTRAN model was used in subsequent analyses in lieu of the more complex three-dimensional model. Engine response, however, was computed with the three-dimensional model for comparison with impedance/mobility and two-dimensional model results. Response cases were computed with force levels for 90-knot, 110-knot, and 130-knot airspeeds at the discrete frequencies related to the main rotor, tail rotor, and input drive shaft excitations. The results are discussed and compared with two-dimensional NASTRAN and impedance/mobility results in the following section. Computed engine response data for all models and cases is tabulated in Appendix E.

RESULTS, PART I

The methods used to compute engine vibration were discussed in the preceding sections. Also presented was substantiation of the analyses by simple model tests, and substantiation of the analytical models by mode shape and natural frequency correlation. To evaluate the NASTRAN and impedance/mobility methods, engine vibration levels were computed for three level flight conditions. The driving point mobilities of the free systems at the interface were determined for a frequency range of from 5 to 60 Hertz for the airframe and from 5 to 220 Hertz for the engine.

It was assumed that engine response in the frequency range of investigation is due to excitation sources related to the airframe alone. A review of data measured during flight test of the OH-58A helicopter (Reference 6) supports this assumption and provides a base from which to evaluate computed results. To compare computed data with test results and to track the engine response due to the individual excitation sources, the spectral amplitude versus frequency format was selected for data presentation.

A set of discrete frequencies was specified and engine response was computed using the NASTRAN and mobility methods for level flight airspeeds of 90, 110, and 130 knots for an approximate gross weight and center of gravity of 3000 pounds and 109 inches, respectively. Engine response was computed for 90, 100, and 110 percent of the following discrete frequencies:

Main Rotor	Two-Per-Rev	11.8 Hz
Main Rotor	Four-Per-Rev	23.6 Hz
Main Rotor	Six-Per-Rev	35.4 Hz
Main Rotor	Eight-Per-Rev	47.2 Hz
Tail Rotor	Two-Per-Rev	87.6 Hz
Input Shaft	One-Per-Rev	103.0 Hz
Input Shaft	Two-Per-Rev	206.0 Hz

Tail rotor and main rotor one-per-rev responses were evaluated during the experimental phase but were omitted for the analytical study. Since airframe and directional control pedal vibration levels at these frequencies (main rotor and tail rotor one-per-rev, respectively) are highly objectionable for reasons of comfort, acceptable force levels producing these vibrations are negligible in comparison to force levels at the higher rotor harmonics. Experimental evaluation of engine response sensitivity to these frequencies was therefore considered adequate for the purpose of this study.

Tail rotor and main rotor hub shear forces were determined from measured rotor bending moments for the discrete frequency harmonics presented above. These forces were computed for 100 percent rotor speed only, and are considered invariant for the range of rotor speeds indicated, i.e., ±10 percent. The computed rotor hub shears are presented in Figures 29 and 30 for the main rotor vertical components, in Figure 31 for the main rotor inplane components, and in Figure 32 for the tail rotor vertical and inplane components.

The main rotor vertical shears transmit directly to the fixed system at the frequency of excitation, i.e., two-, four-, six-, and eight-per-rev. The main rotor inplane shears transmit to the fixed system at the frequency of excitation ± one-per-rev. Thus the one- and three-per-rev inplane shears result in steady and two-per-rev longitudinal and lateral hub shears in the fixed system. The magnitude of each of these components depends on the phase angle (with respect to rotor azimuth) of the force resultant. The tail rotor two-per-rev vertical shear results in a two-per-rev lateral fixed system force, while the one-per-rev inplane shear results in a two-per-rev longitudinal and vertical fixed system force. The phase angles in Figures 29 to 32 give the rotor azimuth at which the shears are maximum in the rotating system. Zero degree phase angle for the main rotor indicates reference blade over the tailboom; for the tail rotor indicates reference blade down vertically.

Engine responses for the two-dimensional and three-dimensional models computed by NASTRAN and impedance/mobility are compared in Figures 33 through 44. Based on engine mode shape data, the forward compressor vertical and lateral vibrations would be the most severe in the frequency range of interest, and the accessory gearbox vertical and lateral vibrations provide a measure of the interface velocities over this frequency range. Thus, the data is presented for these locations only. The comparison is presented for 90-knot, 110-knot, and 130-knot simulated flight conditions at the discrete frequencies indicated above in Figures 33 through 38 for engine vertical response and in Figures 39 through 44 for engine lateral response.

Good agreement between the mobility and NASTRAN methods for the two-dimensional model is shown for vertical engine response through 50 Hertz. From this frequency upward, the NASTRAN data does not include the higher frequency airframe modes (by selection). The mobility method retains all airframe and engine degrees of freedom and produces engine velocities as a result of fuselage flexible modes through the applicable frequency range. The two methods therefore cannot be directly compared for frequencies above 50 Hertz. The two-dimensional and three-dimensional NASTRAN data show fair agreement from 50 to 200 Hertz. Since the response in this region is primarily rigid body fuselage (flexible modes above 45 Hertz are rejected), this is the expected result. The differences in the two-dimensional and three-dimensional NASTRAN computed velocities for frequencies below 50 Hertz are due to the differences in the model natural frequencies. For the same frequency placement, it is anticipated that both models would produce the same results. For the cases presented above, the data was computed without damping.

For engine lateral response (Figures 38 through 43) the comments above apply, except for the comparison between the NASTRAN and mobility responses for the two-dimensional model below 50 Hertz. In this case, poor agreement between the two methods is shown, except for the main rotor two-per-rev responses (10.6, 11.8., and 13.0 Hertz). In the lateral direction, the forces are applied at main rotor two-per-rev, tail rotor two-per-rev, and at the input drive shaft frequencies. The mobility method shows lateral response to vertical forces, while the NASTRAN method shows little coupling in this regard. This difference is due to analytical differences in the mobility and NASTRAN analyses.

In the NASTRAN analysis, the engine is considered a part of the total system structure and restraints at the airframe/engine interface are specified in the modeling procedure. For this analysis the engine mounts are modeled to perform as axial structural members for any application of shears and/or moments to the engine. For example, a lateral shear force applied to the engine center of gravity (statically or dynamically) results in a lateral shear force and a yaw and roll moment at the engine mount locations. The lateral shear force is reacted by the two horizontal members of the lower engine mount bipod, i.e., axial loads are produced in these members as a result of the applied lateral shear. The yaw and roll moments are reacted by the vertical members of the left and right engine mount bipods. In this case too, axial loads are produced as a result of the applied loads. Thus, for the NASTRAN application, out-of-plane bending of the structural members comprising the engine mounts is not considered in the modeling process and for the assembled structure these members react only axial loads.

In the mobility method, there are several choices for formulating the airframe mobility at the interface (reference Figure 22). One formulation is to determine the airframe mobility at the lower mount points (grid points 202, 204, 205, 207, 208, and 210) and the mobility of the engine mounts separately and superpose the results. This formulation presents a direct measurement of airframe and engine mount mobilities independently. A second formulation is to treat the engine mounts as a single unit and connect the mounts by means of rigid massless structure at grid points 203, 206, and 209. This formulation leads to airframe/engine mount mobilities representative of a single effective mount. A third formulation is to determine the airframe/mount mobilities at grid points 203, 206, and 209 for an independent representation of each mount as part of the basic airframe structure. For this formulation, the system mobilities are representative of the free system. The third formulation was chosen for this study. In the formulation of the impedance/mobility analysis, the above representations would produce identical results since no restraints are imposed on the method of separating the systems except that the separation is accomplished at interface locations. It was assumed that satisfying the conditions of force equilibrium and velocity compatibility at the interface provided sufficient conditions for the analysis of the combined system behavior. The test results have shown that reaction restraints at the interface to forces applied to either system must also be specified. That is, care must be taken to assure that the individual system behavior after separation satisfies design reaction restraints imposed on the systems by the connecting element, in this case the engine mounting system.

Computed data (all methods) is compared with measured flight data and with shake test data in Figures 45 through 52. Vertical and lateral response at the forward compressor and gearbox is presented for airspeeds of 110 knots (Figures 45 through 48) and 130 knots (Figures 49 through 52).

Very little agreement is shown between analytical and test results, and between flight test and shake test results. For frequencies below 50 Hertz, the mobility and two-dimensional NASTRAN results are generally greater than flight test results. For frequencies above 50 Hertz, the two-dimensional and three-dimensional NASTRAN data is considerably lower than flight test results. The mobility method, in general, produces higher analytical responses for frequencies above 50 Hertz than shown for the flight test data, but is comparable in some instances. Experimentally determined engine responses are greater in most instances than flight test or computed data. This is a result of the measurement and testing techniques employed and is discussed in greater detail in Part II.

For all comparisons presented in the above discussion, the computed data were generated from finite element models with no connection between the engine and main transmission (disconnected transmission input shaft). A comparison between computed response for the disconnected case with computed response for a rigid transmission input shaft is given for each engine response location in Figures 53 through 60. The comparison is presented for computed data using the NASTRAN (two-dimensional) and mobility methods. For the forward compressor and engine gearbox vertical responses (Figures 53 and 54), the system response with a rigid input shaft (solid symbols) is lower at most frequencies than the disconnected system response. For all other locations, the rigid input shaft response is greater than the disconnected case at most frequencies. For lateral response (Figures 57 through 60), a greater disagreement between the methods of computation is shown.

Computed data for the forced response cases discussed above is given in tabular form, for all engine coordinates, in Appendix D. The mobility matrices for the airframe and engine are presented in tabular form in Appendixes B and C, respectively.

Computed and measured airframe driving point mobilities at interface coordinates are compared in Figures 61 through 69. The airframe driving point mobilities are presented for a frequency range of from 5 through 60 Hertz. This covers the range of fuselage modes correlated in the development of the analytical model. This data is presented primarily to compare equivalence of the model with the actual system.

The airframe driving point mobilities are presented for the left engine mount in Figures 61 to 63, for the right engine mount in Figures 64 to 66, and for the lower engine mount in Figures 67 to 69. The mobility data for the analytical model is given by the solid curves, and shake test results are given by the dashed curves. The driving point mobilities of the analytical model for the left and right mounts (all degrees of freedom, Figures 61 to 66) and the lower mount lateral degree of freedom (Figure 68) do not compare favorably with shake test results. The disagreement between the two sets of data is due to the bending stiffness of the mounts and the system damping with respect to airframe modes at the interface.

The comparison of airframe driving point mobilities for the lower mount longitudinal and vertical degrees of freedom, Figures 67 and 69, shows reasonable agreement between analysis and test. The mobility data presented in Figure 67 clearly identifies the difference in modal frequency placement between the analytical model and the full-scale airframe. The effect of damping omission in the analytical model is also demonstrated. The mobility data presented in Figure 69 shows good agreement between analysis and test (ignoring the support system mode shown in the test data). The difference in this case is due entirely to system inertia as observed at the interface.

Computed and measured engine driving point mobilities are compared in Figures 70 through 81. In this case, shake test data is presented by the curves and analytical data is given by the triangular symbols. The analytical model of the engine used for the mobility analysis and NASTRAN was a simple elastic axis model as discussed in an earlier section. In the development of the model, inertia coupling of vertical and lateral modes was ignored, and a vertical mode of the forward compressor cantilevered off the gearbox was not simulated. Considering these differences, and the lack of damping in the various engine bending modes, good agreement between analysis and test is shown. A clear indication is given, however, for two discrepancies between the engine model used in the mobility analysis and the NASTRAN free-free engine model. In the first place, the lateral engine natural frequency used in the mobility analysis was approximately 180 Hertz (see Figures 70, 71, 73, 74, 77, and 80). This yields frequencies which are approximately 24 Hertz higher than shown by NASTRAN. Secondly, the rigid body roll inertia of the engine was apparently omitted in the mass condensation process (see Figures 72, 75, and 77). These figures show that excitation of the engine at the lower mount location in the lateral direction, or excitation at the left or right mount locations in the vertical direction, produce only mass-like response of the engine (in translation) which is greater than rigid body motion. The system motion is the result of a vertical (or lateral) force applied at the engine elastic axis which is proportional to the inertia of the very small masses ($\approx 3 \mathrm{X} \cdot 10^{-6}$ lb-sec^2/in.) at each interface point, i.e., a very low translational force. Unlike the case of the mount bending stiffness, this latter effect is overcome by the equilibrium and compatibility conditions after connection. The computed mobility data for the above cases is tabulated in Appendix B for the airframe and in Appendix C for the engine.

PART II - EXPERIMENTAL INVESTIGATION

In the past several years, a number of matrix structural analyses (References 2, 3 and 7) using impedance/mobility (sometimes called impedance, sometimes mobility) formulations have been developed. Although wide variations in the analytical techniques are used, most of these analyses use modal synthesis techniques with regard to the interfacing of one system with another, and all reportedly are applicable to experimental determination of system parameters. In at least one case (Reference 3), experimental procedures are outlined and recommended for determination of mobility parameters.

A brief survey of impedance/mobility literature failed to produce even one instance in which experimental methods were actually used to determine the mobility characteristics of a complex system such as the helicopter for any significant frequency range. In one case, well-behaved "simulated" test data was reported (Reference 7) for a very wide frequency range (zero to 600 Hertz), showing that the analytical method was insensitive to experimental error. The simulated test data were reportedly representative of a full-scale helicopter structure.

During the conduct of the present investigation, analytical procedures were developed which demonstrated that the mobility method can predict the combined response of two complex dynamic systems from the mobilities of the separate systems and the simultaneous solution of interface mobility equations. For identical analytical models, the above procedures produced the same results as NASTRAN, a well-documented matrix structural analysis.

The impedance/mobility method developed for this study is also applicable for use with experimentally determined mobility parameters. To obtain such parameters for evaluating this concept, a lengthy vibration test of the OH-58A airframe was conducted by Bell Helicopter Company and a similar vibration test of the T-63 turbine engine was conducted by Detroit Diesel Allison Division of General Motors Corporation. The results of the Bell Helicopter Company tests and the results of a numerical analysis using Bell and Allison experimental data are reported herein.

SHAKE TESTS

HARDWARE

General

An OH-58A helicopter, S/N 40611, was provided by the Government for the conduct of ground vibration testing required by the contract. The main rotor and tail rotor hub assemblies were removed and replaced with test hub assemblies. The main and tail rotor blades were replaced with equivalent weights rigidly attached to the test hubs. The helicopter was configured for a gross weight of 3005 pounds with a center of gravity at fuselage station 109.1. The configuration was obtained using full fuel and ballast as shown in Table II. The helicopter was supported on a low frequency (below 5 Hertz) suspension system. The helicopter installation and suspension system for a typical test is shown in Figure 82.

Excitation Hardware

A Lazan mechanical shaker was installed in the main rotor hub assembly to provide vertical, lateral and longitudinal excitation of the helicopter for the determination of airframe natural frequencies. Photographs of the orientation and arrangement of the exciter and associated hardware are presented in Figure 83 for vertical and longitudinal excitation. Detailed views of the exciter and hub assembly are presented in Figure 84 for vertical, longitudinal and lateral excitation at the main rotor hub. The arrangement of the impedance head for longitudinal and lateral tests is shown in Figure 85. The mechanical shaker was driven through a flexible cable and Vari-Drive assembly powered by an electric motor. A photograph of the Vari-Drive assembly is presented in Figure 86. The mechanical shaker was operated over a frequency range of from 2 to 45 Hertz.

An MB model C10 electromagnetic exciter was used for excitation of the helicopter during mobility tests. The arrangement of the exciter and associated hardware for excitation at the main rotor hub is shown in Figure 87 and for excitation at the tail rotor hub is shown in Figure 88.

To facilitate excitation of the system at the engine mounts, main transmission, and at the engine output shaft, a crank assembly was used with the electromagnetic exciter. A detailed view of the arrangement of exciter and crank assembly for a typical test is shown in Figure 89. Whenever possible, the direct application of exciter force was utilized. The arrangement of exciter and crank assembly is shown in Figure 90 for excitation at the left- or right-hand engine bipod, in Figure 91 for excitation at the lower engine bipod, in Figure 92 for excitation at the main transmission input shaft, and in Figure 93 for excitation at the engine output shaft. In each of the above figures the general arrangement of exciter and crank assembly is shown with close-ups of the exciter input for vertical, lateral and longitudinal tests, where available.

INSTRUMENTATION

Transducers

Endevco piezoelectric accelerometers were used at all response locations specified for the tests. The type, laboratory serial number and calibration date of each accelerometer are presented in tabular form in Appendix G. Endevco, type 2110, impedance transducers (Z-head) were used to monitor force and acceleration at the driving point for each test. The laboratory serial number and calibration curves for each impedance transducer used are furnished in Appendix G. The approximate locations of fuselage-mounted transducers are shown in Figure 94 and of engine-mounted transducers in Figure 95. Typical transducer installations are shown in Figures 96 and 97 for airframe vertically and laterally mounted accelerometers. Transducer installations on the engine mounts and transmission are shown in Figure 98; engine-mounted transducers are shown in Figure 99.

For airframe vibration tests conducted to identify fuselage natural frequencies and mode shapes, transducers were installed as indicated in Table III. For conducting mobility tests, transducers were located and recorded for main rotor and tail rotor hub excitations as indicated in Table IV. For excitation at the engine bipods or at the main transmission, input shaft transducers were located and recorded as shown in Table V. Due to limitations of the data acquisition system, each of the mobility measurement tests had to be performed twice. The reference letter, A or B, given in Tables IV and V indicates the transducers recorded during the first and second test, respectively. Transducers installed during the combined airframe and engine vibration tests are shown in Table VI.

Data Acquisition System

A photograph of the data acquisition system employed during the shake tests is presented in Figure 100. A flow diagram of the system is given in Figure 101. Acceleration mobility magnitude for a selected transducer location was monitored using an X-Y plotter for all tests conducted to determine airframe natural frequencies and mode shapes; however, mobility phase was not monitored. All other transducer locations were monitored using a BHC developed mode shape meter display. Airframe mode shapes were recorded for each natural frequency using a video recorder in combination with the mode shape meters.

Velocity mobility magnitude and phase for a selected transducer location were monitored using two X-Y plotters for all tests conducted to determine mobilities. Velocity was obtained by integrating the acceleration output signal from the charge amplifier for a specified transducer location. The characteristics of the integrator, i.e., output amplitude and phase angle as a function of frequency, are presented in Appendix G. During the conduct of the mobility tests all other transducers were monitored using the mode shape meter display.

For all tests, the output signals from the charge amplifiers, i.e., force or acceleration, were recorded directly on tape and simultaneously monitored using the mode shape meter display. Velocity and/or acceleration mobilities for all required transducer locations were obtained via playback from magnetic tape through the data acquisition system.

TEST PROCEDURE

Tests were conducted to determine airframe natural frequencies and response characteristics, airframe internal and free mobilities at the engine mount locations (triaxial), and coupled engine/airframe response. The general procedure for each test was essentially the same: the excitation hardware and instrumentation were installed; the helicopter was lifted on its suspension; and an excitation frequency sweep was conducted at a constant force level, where possible, for the applicable frequency range. The T-63 engine was installed during tests conducted to determine the airframe natural frequencies and engine coupled response. For all other tests, the engine was removed.

A schedule of required tests is presented in Table VII. The purpose, orientation and location of the exciter, applicable instrumentation, and frequency range for each test are shown in the table. Tests were not performed in the sequence shown, but rather in the order of minimum conversion time from one set of excitation hardware and instrumentation to the next. However, each series of tests, A, B or C, was completed in order. Additional tests were conducted to establish force level and charge amplifier sensitivities for the specified frequency ranges, to repeat tests aborted due to mechanical or instrumentation failures, and to check the repeatability of the data acquisition system at regular intervals.

A test log was maintained by the test engineer, and instrumentation setup sheets were filed for each instrumentation change. The instrumentation setup sheets are presented in Appendix G. Specific test procedures for series A, B, and C tests are discussed below.

Series A Tests

Series A tests were conducted to identify airframe natural frequencies and mode shapes. A Lazan mechanical exciter was employed for these tests. Frequency sweeps were conducted for each test from 2 or 5 Hertz to 45 Hertz, using one force level up to 20 Hertz and a lower force level from 20 to 45 Hertz. At the completion of each frequency sweep, the exciter was set at a frequency corresponding to each substantial peak shown on the acceleration mobility curves recorded on the X-Y plotter. Each of these frequencies was identified as to modal characteristics, and the principal airframe mode shapes were recorded using the video recorder in combination with the mode shape meter display. The natural frequencies corresponding to empennage and/or local absorber modes were identified primarily by feel. All principal response peaks were identified and noted on the acceleration mobility curves.

Series B Tests

Series B tests were conducted to determine the airframe internal and free velocity mobilities at engine interface coordinates. Excitation for these tests was provided by an electromagnetic exciter for a frequency range of from 5 to 200 Hertz. Prior to each data test, a frequency sweep was conducted and transducer output for each of the six locations was monitored on the mode shape meter display. Variations in mobility parameters exceeding 4 cycles (log paper) or a recording range greater than 80 db were observed. Since the dynamic range of the data acquisition system, in cascade, was 40 db, this required the establishment of force levels and charge amplifier sensitivities to guarantee that no loss of data would occur during the conduct of a given test. Thus, each test was conducted in from two to four frequency sweep increments with a different constant level force and instrumentation setup sheet for each increment.

During the initial tests, efforts were made to identify as many peak response points as possible. This proved to be futile for frequencies greater than 40 Hertz, since a large number of control tube, panel, and absorber-type modes were found to exist, and the effort was abandoned.

Series C Tests

These tests were conducted to determine engine response due to main rotor, tail rotor, and engine output shaft forces. Tests were conducted for a frequency range of from 5 to 200 Hertz. The test procedure for this series was identical to the series B tests.

DATA PROCESSING

Acceleration and velocity mobility data were generated during the above tests for use in evaluating engine response and engine/airframe compatibility using mobility techniques. The data were accumulated in graphical form, i.e., mobility magnitude and phase graphs. Each graph contains information for a single element of the total airframe mobility matrix. A test log, in matrix form, giving the run number and plot number for a given response location due to a specified force location is presented in Figures 102, 103, and 104. For each matrix element, the upper number indicates the test run number and the lower number indicates the plot number. The matrix row and column numbers specify the excitation I.D. and response I.D., respectively. Negative row (excitation) and column (response) numbers indicate force and/or accelerometer orientations opposite to the assigned coordinate reference.

Digital processing of the data was required to obtain mobility amplitude and phase values at each of 26 discrete frequencies related to airframe excitation sources. A Gerber oscillograph reader was used to obtain punched IBM cards with mobility amplitude and phase at each of the desired frequencies in terms of inches from graph reference. A computer program, DRAE01, was generated to transform the punched card data to mobility amplitude and phase and to store the information on magnetic tape for further processing. The data were stored in terms of the test run number, plot number, excitation I.D., and response I.D. indicators given in Figures 102 to 104 at each of the 26 discrete frequencies.

A schematic diagram of the coordinate system reference and force and transducer orientations for the shake test is presented in Figure 105. Positive force was determined by an up-scale signal for a compressive load on the impedance head, and positive acceleration was determined by an up-scale signal for transducer motion in the positive coordinate sense. The mobility phase was plotted for velocity lag with respect for force. This is 180 degrees out of phase with the normal mobility phase reference. During processing of the data in program DRAE01, 180 degrees was added to each mobility phase angle, and mobility magnitude sign errors due to force or transducer orientation were corrected.

A partitioning of the measured airframe mobilities based on the theory presented in Part I of this report was performed as shown in Figure 106. The cross-hatched submatrices indicate element data obtained during the shake test. Partitioning given by the heavy solid lines in the figure indicates the required airframe mobilities for a disconnected transmission input shaft. For this case, data for rows and columns 10, 11, and 12 do not exist, and only 9 interface coordinates are required. Partitioning given by the heavy dashed lines in the figure indicates the airframe mobilities for the inclusion of the transmission input shaft. For this case, twelve interface coordinates are required, and data for rows and columns 10, 11, and 12 were determined analytically. The determination of these data is discussed in a later section. The matrix partitioning was performed to be compatible with the theory and with engine mobility data furnished on magnetic tape by the engine manufacturer. The engine mobility data thus provided is shown in matrix form in Figure 107.

During the combined airframe/engine shake test, engine response was measured in terms of engine transfer mobilities (due to airframe excitation sources) at engine response coordinates specified by the engine installation drawing. The data were arranged for analytical use in matrix form as shown in Figure 108. The matrix equation form given in the figure demonstrates the utility of these data; i.e., the engine velocity at a given location is determined by

$$V_i = \sum_{j=1}^{k} Y_{CHK_{ij}} F_j$$

where the subscript i indicates the selected response coordinate, and the summation is performed for the k products of mobilities of the i^{th} row with the j^{th} forces of the airframe internal force vector, $\{F_I\}$. Engine velocities computed in this way provide a basis for evaluating the mobility method presented in Part I using experimentally determined airframe and engine mobility data.

The mobility magnitude and phase graphs recorded during the shake tests are presented in Appendix H. The data are arranged in the appendix in matrix element order for the matrices and submatrices presented in Figures 106 and 108.

NUMERICAL ANALYSIS

DETERMINATION OF TRANSMISSION INPUT SHAFT MOBILITIES

The contract required the evaluation of engine response using experimentally determined mobilities for the OH-58A airframe with a pin-connected transmission input shaft and with a rigidly connected transmission input shaft. The objective was to "bracket" the upper and lower limits of the engine response due to the type of connection for the transfer of power from the engine to the airframe rotating components. During shake tests, the transmission input shaft was removed. To comply with contract requirements it was necessary, therefore, to add the transmission input shaft mobilities to the airframe mobility matrix analytically. Computer program DRAE03 was used to accomplish this task and to provide the proper partitioning of mobility data obtained during the shake tests.

To determine mobility data for the transmission input shaft, the shaft was treated as a subsystem of the airframe. The free system mobilities of the shaft with pinned couplings at each end, and with rigidly attached couplings at each end, were determined using finite element NASTRAN models. For the pinned shaft, rotational degrees of freedom between the couplings and shaft were unstrained except in the θ_x (torque) coordinate. In each case, the model was symmetrical, and the driving point and transfer mobilities for unit forces were determined for one end of the shaft, and the remaining data determined on the basis of symmetry and system linearity. With the shaft mobility data determined in this fashion, and the airframe mobility data determined from test, the desired coupled airframe/input shaft mobilities were determined using program DRAE03 which is based on the theory and methods described in Part I, wherein system I is the airframe and system II is the transmission input shaft. In terms of the mobility matrices given in Figure 106, this results in the determination of the elements of the airframe submatrices $[Y_{EE_2}]$, $[Y_{EE_3}]$, $[Y_{EE_4}]$ and $[Y_{EI_3}]$.

Program DRAE03 is essentially the same as program DRAE02 discussed in Part I. The basic difference is that program DRAE03 was coded to accept direct matrix input, and special subroutines were added to complete the transmission input shaft mobility matrices, determine the coupled airframe/input shaft mobilities, and create a magnetic tape with all required data, properly partitioned, including engine mobilities furnished by the engine manufacturer. A copy of the resulting tape was furnished to the engine manufacturer.

The elements of the submatrices $[Y_{EE_2}]$ and $[Y_{EE_4}]$ were determined (via program DRAE03) by computing the velocities at the left, right and lower engine mount bipods and at the free end of the transmission input shaft due to triaxial unit loads applied at the free end of the shaft. The elements of the submatrices $[Y_{EE_3}]$ and $[Y_{EI_3}]$ were determined by computing the velocities at the free end of the shaft due to unit triaxial forces applied at the respective airframe coordinates.

To determine the mobilities for the submatrix $[Y_{EI_4}]$, the theory had to be revised since external forces applied at interface coordinates—in this case, coordinates at the transmission end of the shaft—are not allowed. This was accomplished by treating the airframe and transmission input shaft as passive systems and determining the velocity at the interface of these systems due to an external force applied at the interface. For unit forces this is equivalent to determining the driving point mobility of the combined system at the interface coordinate. Thus,

$$[Y_{EI_4}] = [Y_{EE}{}^{I}][Y_{EE}{}^{II}] \Big/ \left([Y_{EE}{}^{I}] + [Y_{EE}{}^{II}]\right)$$

where the matrices $[Y_{EE}{}^{I}]$ and $[Y_{EE}{}^{II}]$ are the free system mobilities of the airframe and input shaft at the interface, and the notation is the same as that used in the mobility theory presented in Part I.

The required matrices were determined as described above for the pinned and rigid transmission input shaft cases. This permitted the evaluation of engine response for three cases:

1. Disconnected transmission input shaft
   - Only the first 9 rows and columns of the airframe $[Y_{EE}]$ matrix are required. Data computed for this case can be directly compared with shake test results given by the $[Y_{CHK}]$ mobility matrix.
2. Pinned transmission input shaft
   - Computed engine response can be compared with results given by the $[Y_{CHK}]$ mobility matrix if interface forces at the engine output shaft coordinates are used, or if transmission input shaft forces are not applied at all. Note that the $[Y_{CHK}]$ matrix (Figure 27) does not include engine responses due to forces applied on the transmission side of the input shaft.
3. Rigid transmission input shaft
   - The same comparison criterion established for the pinned-shaft case is applicable.

The mobility matrices determined from test and the above analytical procedure are presented in Appendix J. The data is presented in the appendix in tabular matrix form using complex number notation. Matrices are presented for each of the twenty-six discrete frequencies related to airframe excitation sources.

DETERMINATION OF ENGINE RESPONSE

Program DRAE04 was developed to determine engine response using the mobility matrices determined from Bell and Allison shake tests and modified as indicated in the preceding section. This program simply reads the data from the tape generated by Program DRAE03 for the applicable transmission input shaft, i.e., disconnected, pinned, or rigid, and performs the required matrix operations indicated below:

$$\{F_E^{II}\} = \left([Y_{EE}^{I}] + [Y_{EE}^{II}]\right)^{-1} [Y_{EI}^{I}] \{F_I^{I}\}$$

and

$$\{V_E^{II}\} = [Y_{IE}^{II}] \{F_E^{II}\}$$

where $\{F_E^{II}\}$ is a column vector of interface forces at engine interface coordinates, $\{V_E^{II}\}$ is a column vector of engine velocities at the desired engine response coordinates, $[Y_{EE}^{I}]$ and $[Y_{EE}^{II}]$ are the free system airframe and engine mobility matrices due to interface forces, $[Y_{EI}^{I}]$ is the airframe internal mobility matrix as observed at the interface, $[Y_{IE}^{II}]$ is the engine transfer mobility matrix at internal coordinates due to force applied at the interface, and $\{F_I^{I}\}$ is a column vector of forces applied at internal airframe coordinates. The column vector $\{F_I^{I}\}$ is determined by input and specifies the operating condition of the helicopter for which the engine responses are determined.

Engine response was computed for each of the cases and conditions indicated in Table VIII. The discrete frequencies and corresponding airframe excitation sources related to the above analysis are presented in Table IX. The results of this analysis and results of the shake test are discussed in the following section. Utilization instructions and listings of each of the computer programs discussed above are presented in Appendix K.

Listing of the computer programs used for the evaluation and processing of experimental data is presented in Appendix K.

RESULTS, PART II

SHAKE TESTS

The results of shake tests conducted under this contract are presented in graphical form in Appendix H. Mobility magnitude and phase graphs for each test are presented in matrix element order and are identified by matrix element number pairs. The element order is based on the matrix partitioning given in Figure 106. It was often necessary to shift the mobility magnitude scale up or down one decade. To call attention to this, vertical lines are drawn on the appropriate graphs, and scale multipliers are given on the graph for the regions affected. Scale multipliers with positive exponents result in a downward shift of the printed scale; i.e., for a scale factor of 10^1, a scale value of .01 becomes .1, .001 becomes .01, etc. Negative exponents result in an upward shift of the printed scale.

For most of the mobility graphs, a substantial number of resonance peaks are shown. Identification of the peaks above 15 Hertz, in most cases, was not practicable due to lack of instrumentation and time. Furthermore, many of these peaks are related to vibrating shafts, bellcranks, unloaded support structure, and absorber type modes which under load are at different frequencies and have appreciable damping. Consequently, the measured responses are not considered to be representative of the engine environment for normal operating conditions and are inadequate for evaluating operating engine/airframe compatibility. For the direct evaluation of the mobility method, however, this is not considered a critical problem since the majority of these modes exist with the engine removed or installed.

In the development of the mobility theory, no restrictions or assumptions were imposed on interface coordinates for the free system. The force equilibrium and motion compatibility equations were assumed to be adequate to establish boundary conditions at the interface. In actual design practice, however, the lateral motion of the left and right engine mount bipods is restrained by lateral characteristics of the lower engine mount bipod and the vertical characteristics of the left and right bipods. Vertical motion of the lower engine mount bipod is restrained by the vertical characteristics of the left and right bipods and the longitudinal characteristics of the lower bipod. Thus, for the OH-58A helicopter, the engine mounts are designed to act as a single unit and the system mobility characteristics should be representative of this case. The mobility representation chosen at the start of this study and upon which all test plans and procedures were predicated was not the optimum choice and the test results are essentially inadequate with regard to verification of the mobility approach.

A comparison of shake test and computed vertical driving point mobility for the left and right engine mount bipods is presented in Figures 109 and 110, respectively. A similar comparison for the lower engine mount bipod is presented in Figure 111. Note that in Figures 109 and 110 the airframe mobility is representative of the mount lateral stiffness properties for both the analytical and test cases, even though the excitation is applied vertically. The airframe modes in the experimental data are completely masked by the mount characteristics for the frequency range shown. In contrast, the airframe mobility at the lower mount bipod (Figure 111), for similar loading, i.e., force applied in the plane of the mount, is characteristic of the airframe structure and clearly shows response of airframe modes. If the mounts were properly restrained to act as a single unit, the response characteristics shown for the left and right bipods due to vertical excitation should be similar to that shown for the lower bipod with longitudinal excitation, i.e., response representative of airframe structure. For the correct representation of the mounts, lateral stiffness properties should not be identifiable for the frequency range applicable to this study, even for excitation in the lateral direction. The computed data for the above comparisons were generated using a two-dimensional finite element model of the airframe and engine mounts.

NUMERICAL ANALYSIS

Engine response was computed using program DRAE04 with Bell Helicopter Company and Allison measured mobility data for the cases presented in Table IX. For the original computation of case one, it was observed that little agreement existed between the computed responses and the measured coupled system response. Several analytical and experimental errors were found and corrected without improving the degree of correlation, as evidenced in Figures 112 through 119 which compare computed (using measured mobilities) with shake test measured engine velocities. The principal remaining error source is due to improperly restraining the engine mounts when measuring the free mobility of the airframe.

A comparison of engine velocities computed using experimentally measured mobilities and finite element models with flight test measured response is presented in Figures 120, 121, and 122 for vertical engine responses at the forward compressor, engine gearbox, and turbine midsplit coordinates, respectively. Computed engine velocities (from test results) are greater than analytically determined velocities using finite element models for all locations at most frequencies. The lack of agreement between computed test responses and flight test results is attributed to engine/airframe mount interface definition, unrealistic resonances reflected in the airframe mobility data, and uncertainty in the magnitude and phase angles of the shear forces deduced from flight data. Only the two-per-rev vertical shears are known with any degree of certainty. Data for the numerical analysis cases are tabulated in Appendix J.

CONCLUSIONS

The results of this investigation have shown that:

- Engine response computed using the mobility method or the modal synthesis (NASTRAN) method is the same for the same analytical model over a given frequency range. This substantiates the mobility method as an analytical tool.
- Computation of engine response is feasible using either method if reasonable representation of each system, airframe and engine, is provided for the full frequency range of interest.
- Engine/airframe interface analysis is possible using finite element models with as few as seventy-five degrees of freedom.
- Problem areas requiring further study include evaluation and development of adequate test methods, and identification and resolution of problems involving interfacing finite element stiffness and mass matrices with impedance/mobility transformation equations.
- Due to insufficient data, a preference of one analytical method over the other (NASTRAN versus impedance/mobility) cannot be demonstrated. However, significantly shorter run times are anticipated for subsystem evaluation using the mobility method.
- Force equilibrium and displacement compatibility equations at the interface are not sufficient to guarantee free choice with regard to system separation. Physical restraints imposed by design, particularly for a statically unstable free system, must also be considered.
- Experimental measurement of mobilities for complex systems such as the helicopter requires pretest modifications to remove or restrain loosely attached shafts, bellcranks, etc., if realistic parameters are to be obtained.
- Although adequately demonstrated by the analytical methods reported herein, the impedance/mobility theory applicable to this study could not be verified on the basis of the experimental results.

In the brief literature survey conducted for this study, no references were found which indicated that impedance testing of a full-scale helicopter over a very wide frequency range had ever been performed. Developers of matrix structural analyses using impedance formulations have used "simulated" test results to demonstrate the experimental application of the theory. The effort reported herein was overly ambitious in regard to the experimental aspect of the program, and it is believed that a considerable effort, over several years, will be required before adequate methods and procedures for the experimental determination of full-scale helicopter mobility parameters are developed. Adequate prediction methods, using mobility concepts, are likely to precede experimental methods by a wide time span.

Experimental methods and procedures could be realized in the most expeditious manner as outlined below:

1. Verify the mobility analysis by conducting vibration tests using four or five simple tractable systems, increasing the complexity of the systems and the number of interface coordinates with each new system.

2. Demonstrate the degree to which mobility methods are dependent on the way systems are disconnected, or develop analyses which <u>are</u> independent of the method of separation as an alternative.

3. Determine by experiment with relatively complex systems whether acceleration mobility would be more advantageous than velocity mobility in producing the desired result. One obvious advantage is a reduced dynamic range of the data acquisition system.

4. Determine first-order airframe mobility parameters by conducting vibration tests of an airframe in various stages of assembly, including the evaluation of principal substructures in each stage.

5. Determine the effect of control tubes and other discrete systems on the airframe mobility under simulated loading for these systems.

6. Determine if direct evaluation and successive addition of subsystems will produce an adequate description of the total helicopter dynamics, including the engine.

The following related areas may also require investigation and/or development:

- Data acquisition systems

  with increased dynamic range (up to a 120 decibel range), improved and expanded recording techniques, and direct computer interfacing to limit data processing.

- Vibration test hardware

  with improved exciter and/or system suspensions to minimize hardware manufacture and changeover periods, and

  evaluation of random vibration techniques to minimize the lengths of tests for large frequency ranges.

The results of the study conducted under this contract fall somewhat short of the desired goal. However, this initial thrust into the investigation of engine/airframe interface has demonstrated a few of the problems which must be considered.

A continuing effort is required to obtain the eventual goal, i.e., the specification of parameters and analytical or test procedures for assuring improved engine/airframe vibratory compatibility and realistic engine vibration limits. In particular, the determination of airframe mobility parameters for the proper formulation of engine mounting and the identification of primary structural modes of the airframe for the full frequency range should be pursued. A further evaluation of the impedance/mobility method should be conducted to identify and resolve the problems of mobility parameter determination using finite element stiffness and mass distributions.

REFERENCES

1. Balke, R. W., A REVIEW OF TURBINE ENGINE VIBRATION CRITERIA FOR VTOL AIRCRAFT, AHS Journal, Volume 16, No. 4, October 1973, pp. 29-38.

2. Giasante, N., Flannelly, W. G., Berman, A., RESEARCH ON STRUCTURAL DYNAMIC TESTING BY IMPEDANCE METHODS - VOLUME IV, SUBSYSTEMS, Kaman Aerospace Corporation; USAAMRDL Technical Report 72-63D, U. S. Army Air Mobility Research and Development Laboratory, Fort Eustis, Virginia, November 1972.

3. On, F. J., MECHANICAL IMPEDANCE ANALYSIS FOR LUMPED PARAMETER MULTI-DEGREE OF FREEDOM/MULTI-DIMENSIONAL SYSTEMS, Goddard Space Flight Center, NASA TN D-3865, National Aeronautics and Space Administration, Washington, D. C., May 1967.

4. Gomez, J. Jr., Vance, J. M., VIBRATORY COMPATIBILITY OF ROTARY-WING AIRCRAFT PROPULSION COMPONENTS, Presented at the 29th Annual National Forum of the American Helicopter Society, Washington, D. C., AHS Preprint No. 774, May 1973.

5. Church, A. H., MECHANICAL VIBRATIONS, John Wiley and Sons, Inc., 2nd Ed., New York, 1963.

6. Lewis, W. I., ENGINE INSTALLATION VIBRATION SURVEY OF THE MODEL 206A-1 HELICOPTER, Bell Helicopter Company, Report No. 206-099-179, Fort Worth, Texas, November 1969.

7. Flannelly, W. G., Berman, A., Giasante, N., RESEARCH ON STRUCTURAL DYNAMIC TESTING BY IMPEDANCE METHODS - VOLUME II, STRUCTURAL SYSTEM IDENTIFICATION FROM SINGLE-POINT EXCITATION, Kaman Aerospace Corporation; USAAMRDL Technical Report 72-63B, U. S. Army Air Mobility Research and Development Laboratory, Fort Eustis, Virginia, November 1972.

TABLE I. COMPARISON OF NASTRAN MODEL AND OH-58A SHAKE TEST NATURAL FREQUENCIES

Mode	Identification	Natural Frequency, Hz			
		2-D NASTRAN Model		3-D NASTRAN Model	OH-58A Shake Test
		Engine Out	Engine In		
1	Pylon Longitudinal (F/A)	4.60	4.60	3.98	4.6
2	Pylon Lateral	6.91	5.95	4.45	6.0
3	1st Fuselage Vertical	7.98	7.75	7.37	7.8
4	1st Fuselage Lateral	8.75	8.05	7.66	8.0
5	Baggage Compartment Vertical	11.44	11.29	13.69	11.4
6	Main Rotor Mast Longitudinal	-	-	-	16.6
7	Main Rotor Mast Lateral	-	-	20.95	16.6
8	2nd Fuselage Vertical	23.96	22.17	16.93	22.5
9	Vertical Fin Lateral Symmetric Bending	25.93	25.14	18.72	25.0
10	2nd Fuselage Lateral	29.14	28.79	28.00	26.5
11	Engine Vertical (Pitch)	-	-	24.45	29.0
12	Engine Lateral (Yaw)	-	-	-	31.4
13	3rd Fuselage Lateral	37.03	35.89	-	34.4
14	3rd Fuselage Vertical	46.35	43.55	-	41.4
	The Following Modes Were Computed But Not Observed During Shake Test				
15	Windshield Support Mode	-	-	14.96	-
16	Upper Vertical Fin Lateral Bending (Cantilevered)	14.54	14.54	17.75	20.3
17	Lower Vertical Fin Lateral Bending (Cantilevered)	23.55	23.67	-	21.4

TABLE II. CENTER OF GRAVITY CALCULATION

PURPOSE: Shake Test CONFIGURATION: Ballast for 3000 lb at Neutral CG	HELICOPTER NO.: 40611 FLIGHT NO.: N/A DATE: 14 Feb 1973

ITEM	WEIGHT (lb)	LONGITUDINAL	
		ARM (in)	MOMENT (in-Lb)
REFERENCE WEIGHT SHEET DATED: 2-13-73			
Left Forward Jack Point	449	55.2	
Right Forward Jack Point	499	55.2	
Aft Jack Point	894	180.6	
AS WEIGHED:	1842	116.06	213,786.0
CHANGES:			
(a) Dummy M/R Hub/Blade	279	107.1	29,880.9
(b) Dummy T/R Hub/Blade	9	352.2	3,169.8
Fuel: Full			
Pilot/Copilot	400	65.0	26,000.0
Crew:	200	164.0	20,800.0
Ballast: (a)	100	85.0	8,500.0
(b)	175	148.0	25,900.0
(c)			
ENGINE START WEIGHT AND CENTER OF GRAVITY	3005	109.16	328,036.7

TABLE III. INSTRUMENTATION FOR AIRFRAME AND PYLON FREQUENCY RESPONSE AND MODE SHAPE DETERMINATION

No.	Transducer	Location	STA	W/L	B/L	M/R Hub Excitation		
						F/A	LAT	VERT
						①	②	③
1	Impedance Head, Force	M/R Hub				X	X	X
2	Impedance Head, Accel	M/R Hub				X	X	X
3	Accelerometer	M/R Mast	-	95	0	X	X	-
4	Accelerometer	Main Xmsn Case (Top)	-	-	-	X	X	-
5	Accelerometer	Main Xmsn Case (Bot)	-	-	-	X	X	-
6	Accelerometer	Work Deck	110	72	0	X	X	-
7	Accelerometer	Lower Fuselage	110	20	0	X	X	-
						④	⑤	③
8	Accelerometer	Fuselage Nose	10	32	0	Vert	X	X
9	Accelerometer	Pilot Floor	67	30	18	Vert	-	X
10	Accelerometer	Copilot Floor	67	30	-18	Vert	X	X
11	Accelerometer	Left Passenger Seat	105	30	18	Vert	X	X
12	Accelerometer	Right Passenger Seat	105	30	-18	Vert	-	X
13	Accelerometer	Fuselage Floor	167	35	0	Vert	X	X
14	Accelerometer	Tail Boom at Fus Joint	205	60	0	Vert	X	X
15	Accelerometer	Tail Boom at Elevator	85*	-	0	Vert	X	X
16	Accelerometer	Tail Boom at 90° Gearbox	352	-	0	X	X	X
17	Accelerometer	Vertical Fin (Top)	-	-	-	X	X	X
18	Accelerometer	Vertical Fin (Bot)	-	-	-	X	X	X

* Tail Boom Station

TABLE IV. INSTRUMENTATION FOR AIRFRAME FREE VELOCITY MOBILITY DETERMINATION

No.	Transducer	Location	Ref. Test	EXCITATION					
				M/R HUB			T/R HUB		
				F/A ①	LAT ②	VERT ③	F/A ④	LAT ⑤	VERT ⑥
1	Impedance Head, Force	Main Rotor Hub	A and B	X	X	X	-	-	-
2		Tail Rotor Hub		-	-	-	X	X	X
3	Impedance Head, Acceleration	Main Rotor Hub	A and B	X	X	X	-	-	-
4		Tail Rotor Hub		-	-	-	X	X	X
				Transducer response in the plane of orientation will be recorded for the test points indicated below.					
5	Accelerometer	Left Engine Bipod, F/A	A	X	X	X	X	X	X
6		Left Engine Bipod, Lat		X	X	X	X	X	X
7		Left Engine Bipod, Vert		X	X	X	X	X	X
8		Right Engine Bipod, F/A		X	X	X	X	X	X
9		Right Engine Bipod, Lat		X	X	X	X	X	X
10		Right Engine Bipod, Vert		X	X	X	X	X	X
11	Accelerometer	Lower Engine Bipod, F/A	B	X	X	X	X	X	X
12		Lower Engine Bipod, Lat		X	X	X	X	X	X
13		Lower Engine Bipod, Vert		X	X	X	X	X	X
14		Xmsm, Input Shaft, F/A		X	X	X	X	X	X
15		Xmsm, Input Shaft, Lat		X	X	X	X	X	X
16		Xmsm, Input Shaft, Vert		X	X	X	X	X	X

TABLE V. INSTRUMENTATION FOR INTERNAL AIRFRAME MOBILITY DETERMINATION

No.	Transducer	Location	Ref. Test	EXCITATION								
				LEFT ENG BIPOD			RIGHT ENG BIPOD			LOWER ENG BIPOD		
				F/A ①	LAT ②	VERT ③	F/A ④	LAT ⑤	VERT ⑥	F/A ⑦	LAT ⑧	VERT ⑨
1	Impedance Head, Force	Lt Eng Bipod	A and B	X	X	X	-	-	-	-	-	-
2		Rt Eng Bipod		-	-	-	X	X	X	-	-	-
3		Low Eng Bipod		-	-	-	-	-	-	X	X	X
4		Xmsn, Input Shaft		-	-	-	-	-	-	-	-	-
5	Impedance Head, Acceleration	Lt Eng Bipod	A and B	X	X	X	-	-	-	-	-	-
6		Rt Eng Bipod		-	-	-	X	X	X	-	-	-
7		Low Eng Bipod		-	-	-	-	-	-	X	X	X
8		Xmsn, Input Shaft		-	-	-	-	-	-	-	-	-
				Transducer response in the plane of orientation will be recorded for the test points indicated below.								
9	Accelerometer	Lt Eng Bipod, F/A	A	-	X	X	X	X	X	X	X	X
10		Lt Eng Bipod, Lat		X	-	X	X	X	X	X	X	X
11		Lt Eng Bipod, Vert		X	X	-	X	X	X	X	X	X
12		Rt Eng Bipod, F/A		X	X	X	-	X	X	X	X	X
13		Rt Eng Bipod, Lat		X	X	X	X	-	X	X	X	X
14		Rt Eng Bipod, Vert		X	X	X	X	X	-	X	X	X
15	Accelerometer	Low Eng Bipod, F/A	B	X	X	X	X	X	X	-	X	X
16		Low Eng Bipod, Lat		X	X	X	X	X	X	X	-	X
17		Low Eng Bipod, Vert		X	X	X	X	X	X	X	X	-
18		Xmsn Shaft, F/A		X	X	X	X	X	X	X	X	X
19		Xmsn Shaft, Lat		X	X	X	X	X	X	X	X	X
20		Xmsn Shaft, Vert		X	X	X	X	X	X	X	X	X

TABLE V. (Continued)

No.	Transducer	Location	Ref. Test	EXCITATION		
				XMSN INPUT SHAFT		
				F/A ⑩	LAT ⑪	VERT ⑫
1	Impedance Head, Force	Left Engine Bipod	A and B	-	-	-
2		Right Engine Bipod		-	-	-
3		Lower Engine Bipod		-	-	-
4		Xmsn, Input Shaft		X	X	X
5	Impedance Head, Acceleration	Left Engine Bipod	A and B	-	-	-
6		Right Engine Bipod		-	-	-
7		Lower Engine Bipod		-	-	-
8		Xmsn, Input Shaft		X	X	X
				Transducer response in the plane of orientation will be recorded for the test points indicated below.		
9	Accelerometer	Left Eng Bipod, F/A	A	X	X	X
10		Left Eng Bipod, Lat		X	X	X
11		Left Eng Bipod, Vert		X	X	X
12		Right Eng Bipod, F/A		X	X	X
13		Right Eng Bipod, Lat		X	X	X
14		Right Eng Bipod, Vert		X	X	X
15	Accelerometer	Lower Eng Bipod, F/A	B	X	X	X
16		Lower Eng Bipod, Lat		X	X	X
17		Lower Eng Bipod, Vert		X	X	X
18		Xmsn Shaft, F/A		-	X	X
19		Xmsn Shaft, Lat		X	-	X
20		Xmsn Shaft, Vert		X	X	-

TABLE VI. INSTRUMENTATION FOR ENGINE/AIRFRAME COMBINED VIBRATION TESTS

No.	Transducer	Location	EXCITATION SOURCE AND PLANE								
			M/R HUB			T/R HUB			ENGINE AT INPUT SHAFT		
			F/A ①	LAT ②	VERT ③	F/A ④	LAT ⑤	VERT ⑥	F/A ⑦	LAT ⑧	VERT ⑨
1	Impedance Head Force	Main Rotor Hub	X	X	X	-	-	-	-	-	-
2		Tail Rotor Hub	-	-	-	X	X	X	-	-	-
3		Engine, Input Shaft	-	-	-	-	-	-	X	X	X
4	Impedance Head Acceleration	Main Rotor Hub	X	X	X	-	-	-	-	-	-
5		Tail Rotor Hub	-	-	-	X	X	X	-	-	-
6		Engine, Input Shaft	-	-	-	-	-	-	X	X	X
			Transducer response in the plane of orientation will be recorded for the test points indicated below.								
7	Accelerometer	Front Compressor, Vert	X	X	X	X	X	X	X	X	X
8		Front Compressor, Lat	X	X	X	X	X	X	X	X	X
9		Turbine Midsplit, Vert	X	X	X	X	X	X	X	X	X
10		Turbine Midsplit, Lat	X	X	X	X	X	X	X	X	X
11		Eng Gearbox, F/A	X	X	X	X	X	X	X	X	X
12		Eng Gearbox, Vert	X	X	X	X	X	X	X	X	X
13		Eng Gearbox, Lat	X	X	X	X	X	X	X	X	X
14		Fuel Nozzle, Vert	X	X	X	X	X	X	X	X	X
15		Fuel Nozzle, Lat	X	X	X	X	X	X	X	X	X

TABLE VII. SCHEDULE OF TESTS

SERIES	TEST NO.	PURPOSE	EXCITATION		Freq (Hz)	APPLICABLE INSTRUMENTATION	
			Location	Plane		Table	Column
A	I	Identify Pylon F/A Frequencies	M/R	F/A	2-42	I	1
	II	Identify Pylon Lateral Frequencies		Lat	2-42	I	2
	III	Identify Fuselage Vertical Modes		Vert	5-45	I	3
	IV	Identify Fuselage F/A Frequency Response		F/A	5-45	I	4
	V	Identify Fuselage Lateral Modes		Lat	5-45	I	5
B	VIa	Determine Airframe Internal Mobility due to Main Rotor Forces	M/R	F/A	5-200	II	1A
	b				5-200		1B
	c			Lat	5-200	II	2A
	d				5-200		2B
	e			Vert	5-200	II	3A
	f				5-200		3B
B	VIIa	Determine Airframe Internal Mobility due to Tail Rotor Forces	T/R	F/A	5-200	II	4A
	b				5-200		4B
	c			Lat	5-200	II	5A
	d				5-200		5B
	e			Vert	5-200	II	6A
	f				5-200		6B
B	VIIIa	Determine Left Bipod Driving Point and Transfer Mobility	Lt Bipod	F/A	5-200	III	1A
	b				5-200		1B
	c			Lat	5-200	III	2A
	d				5-200		2B
	e			Vert	5-200	III	3A
	f				5-200		3B

TABLE VII.- Continued

SERIES	TEST NO.	PURPOSE	EXCITATION		Freq (Hz)	APPLICABLE INSTRUMENTATION	
			Location	Plane		Table	Column
B	IXa	Determine Right Bipod Driving Point and Transfer Mobility	Rt Bipod	F/A	5-200	III	4A
	b				5-200		4B
	c			Lat	5-200	III	5A
	d				5-200		5B
	e			Vert	5-200	III	6A
	f				5-200		6B
B	Xa	Determine Lower Bipod Driving Point and Transfer Mobility	Low Bipod	F/A	5-200	III	7A
	b				5-200		7B
	c			Lat	5-200	III	8A
	d				5-200		8B
	e			Vert	5-200	III	9A
	f				5-200		9B
B	XIa	Determine Transmission Input Shaft Driving Point and Transfer Mobility	Xmsn Input Shaft	F/A	5-200	III	10A
	b				5-200		10B
	c			Lat	5-200	III	11A
	d				5-200		11B
	e			Vert	5-200	III	12A
	f				5-200		12B
C	XIIa	Determine Engine Frequency Response to Main Rotor Hub Forces	M/R Hub	F/A	5-200	IV	1
	b			Lat	5-200	IV	2
	c			Vert	5-200	IV	3
C	XIIIa	Determine Engine Frequency Response to Tail Rotor Hub Forces	T/R Hub	F/A	5-200	IV	4
	b			Lat	5-200	IV	5
	c			Vert	5-200	IV	6
C	XIVa	Determine Engine Frequency Response to Input Shaft Forces	Engine Input Shaft	F/A	5-200	IV	7
	b			Lat	5-200	IV	8
	c			Vert	5-200	IV	9

TABLE VIII. LIST OF NUMERICAL ANALYSIS CASES

Case	Description
1	Compute engine response at all frequencies* using shake test level forces for direct comparison with shake test results.
2	Compute engine response at 5.9, 11.8, and 23.6 Hertz using shake test level forces and all airframe mobility phase angles at the above frequencies shifted 180 degrees to evaluate the possibility of a phase reference error.
3	Compute engine response at all frequencies related to 100% normal operating speeds using longitudinal unit forces only to evaluate engine sensitivity to longitudinal forces.
4	Compute engine response at all frequencies related to 100% normal operating speeds using lateral unit forces only, at all applicable airframe coordinates, to evaluate engine response sensitivity to lateral forces.
5	Compute engine response at all frequencies related to 100% normal operating speeds using vertical unit forces only, at all applicable airframe coordinates, to evaluate engine response sensitivity to vertical forces.
6-8	Compute engine response for combined triaxial unit loads at all frequencies and a) disconnected shaft b) pinned shaft c) rigid shaft
9	Compute engine response for combined level flight forces at 90 knots, disconnected shaft for comparison with flight test data.
10	Compute engine response for combined level flight forces at 110 knots, disconnected shaft for comparison with flight test data.
11-13	Compute engine for combined level flight forces at 130 knots and a) disconnected shaft b) pinned shaft c) rigid shaft for comparison with flight test data, and to evaluate shaft restraint.

* See Table IX.

TABLE IX. AIRFRAME EXCITATION FREQUENCIES

Source	Percent Normal Operating Speed		
	90%	100%	110%
Main Rotor			
1/Rev	5.3	5.9	6.5
2/Rev	10.6	11.8	13.0
4/Rev	21.2	23.6	26.0
6/Rev	31.8	35.4	39.0
8/Rev	42.4	47.2	52.0
Tail Rotor			
1/Rev	39.4	43.8	48.2
2/Rev	78.8	87.6	96.4
Transmission Input Drive Shaft			
1/Rev	92.7	103.0	113.3
2/Rev	185.4	206.0	226.6

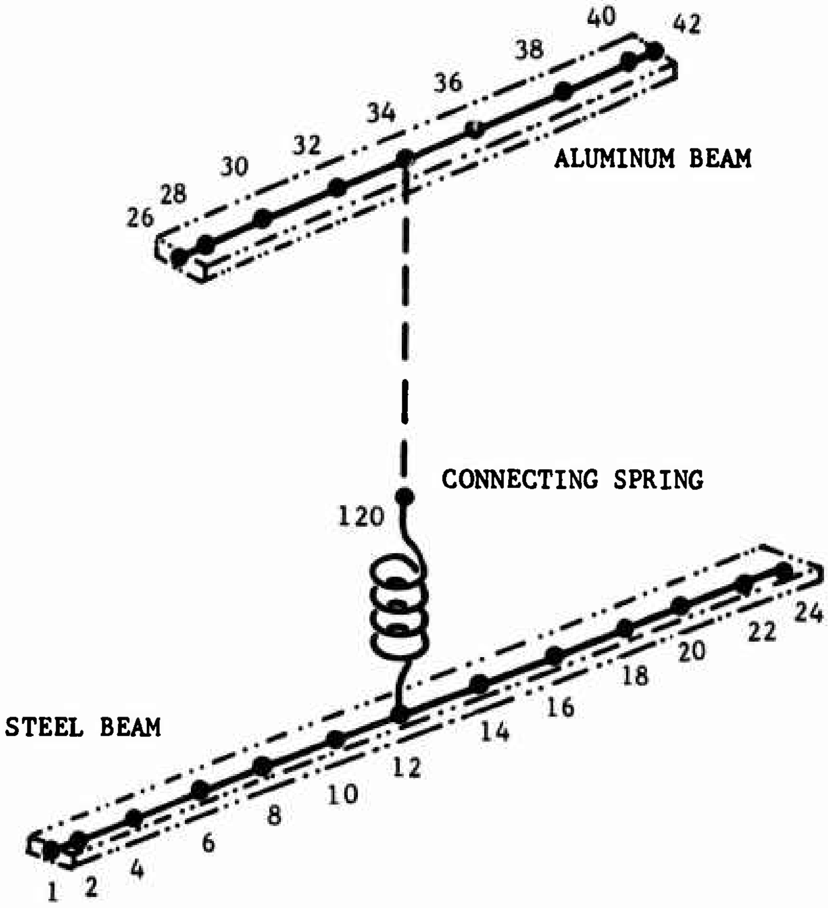

Figure 1. Finite Element Model of Simple Beams for Verification of Mobility Method.

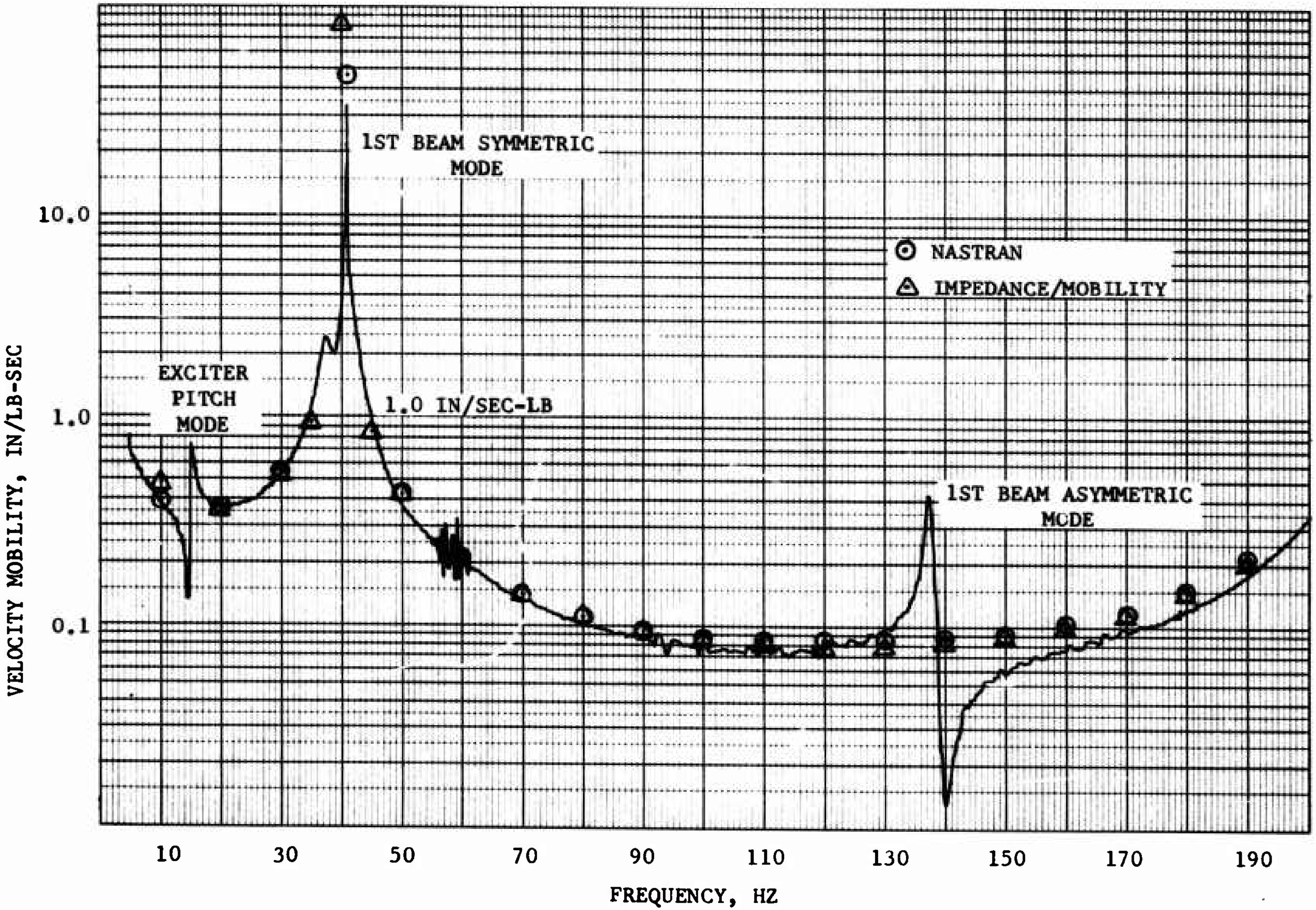

Figure 2. Comparison of Computed and Measured Steel Beam Model Tip Transfer Mobility.

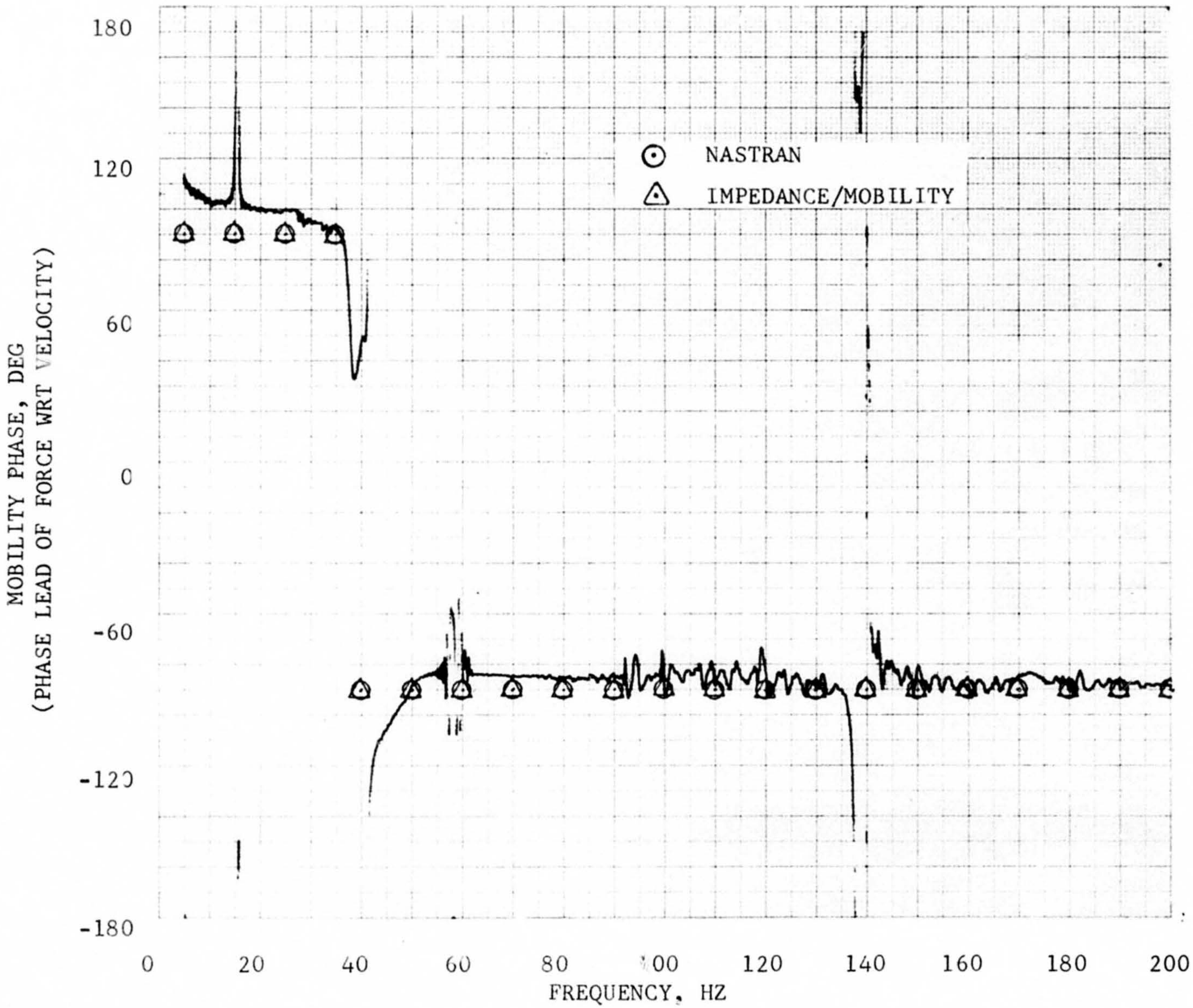

Figure 3. Comparison of Computed and Measured Steel Beam Model Transfer Mobility Phase.

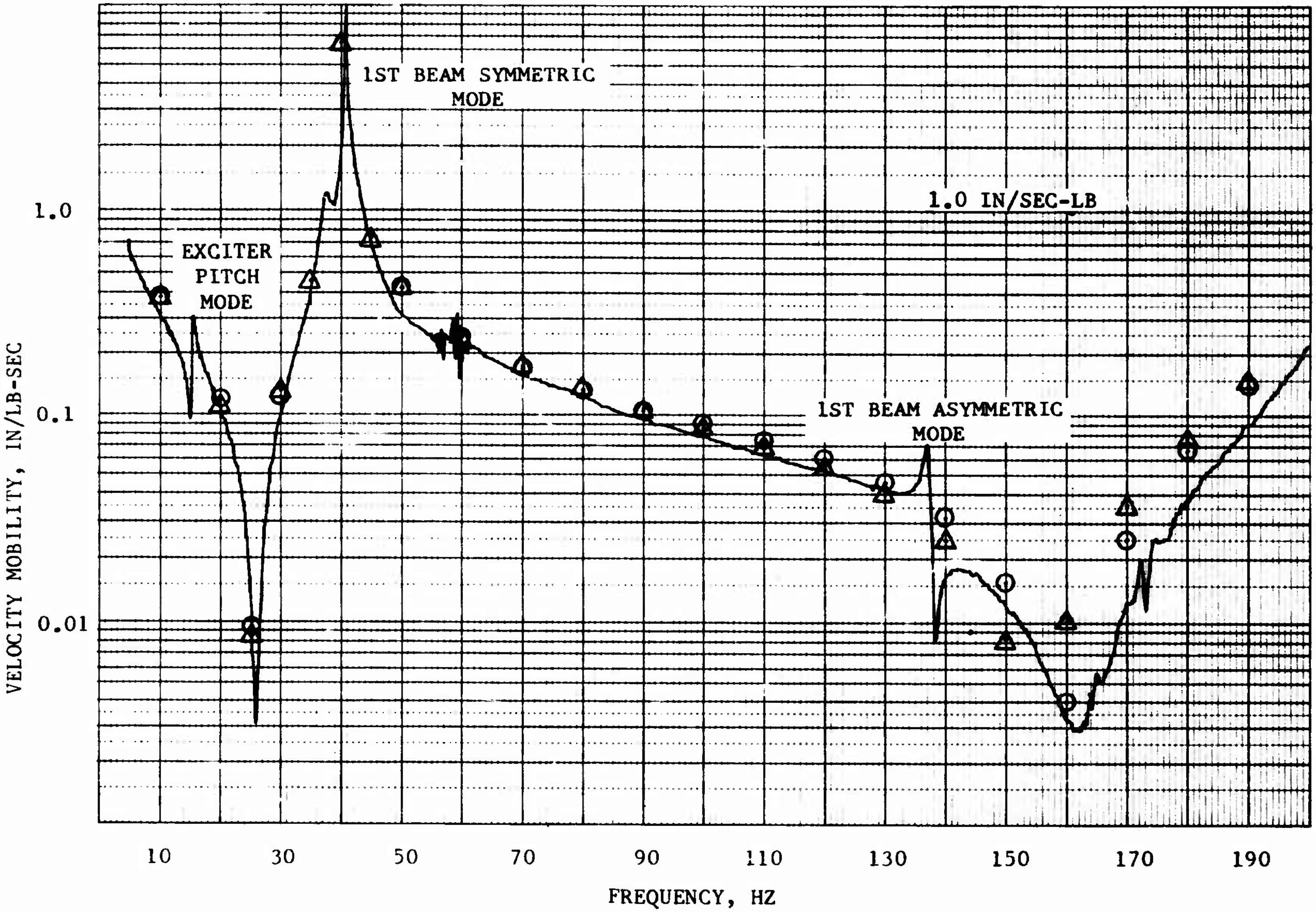

Figure 4. Comparison of Computed and Measured Steel Beam Model Driving Point Mobility.

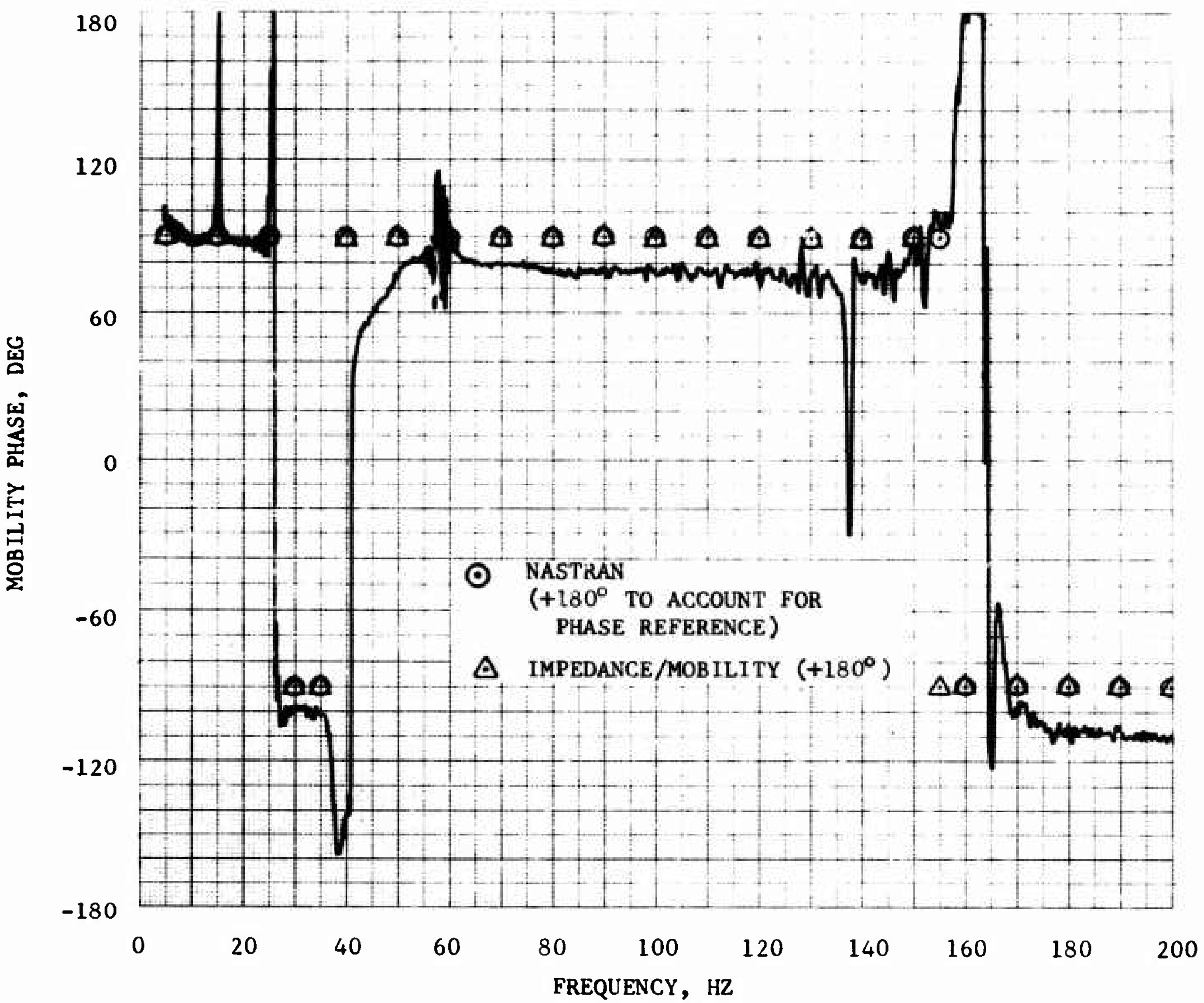

Figure 5. Comparison of Computed and Measured Steel Beam Model Driving Point Mobility Phase.

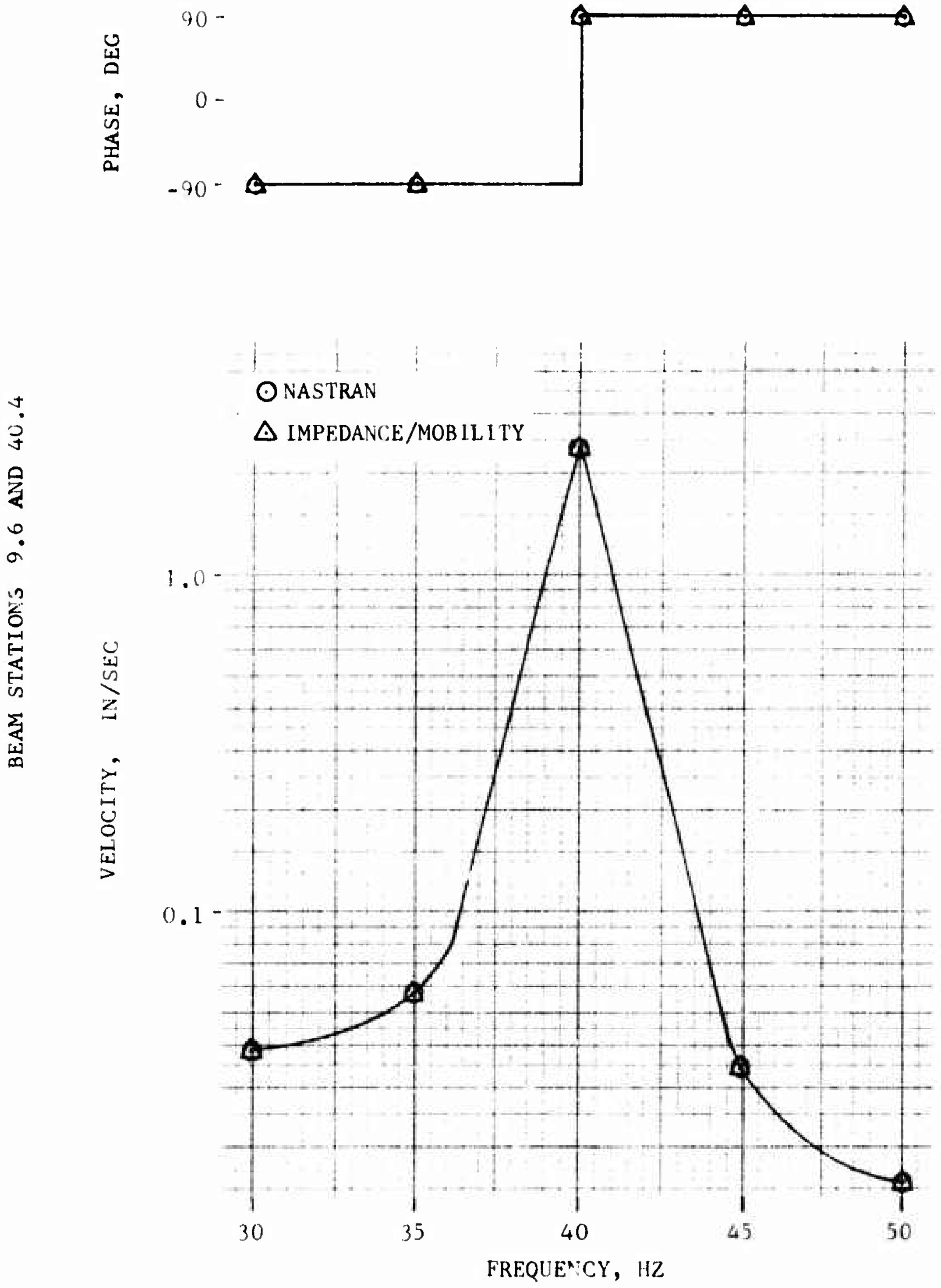

Figure 6. Comparison of NASTRAN and Impedance/Mobility Computed Aluminum Beam Coupled Response, Beam Stations 9.6 and 40.4.

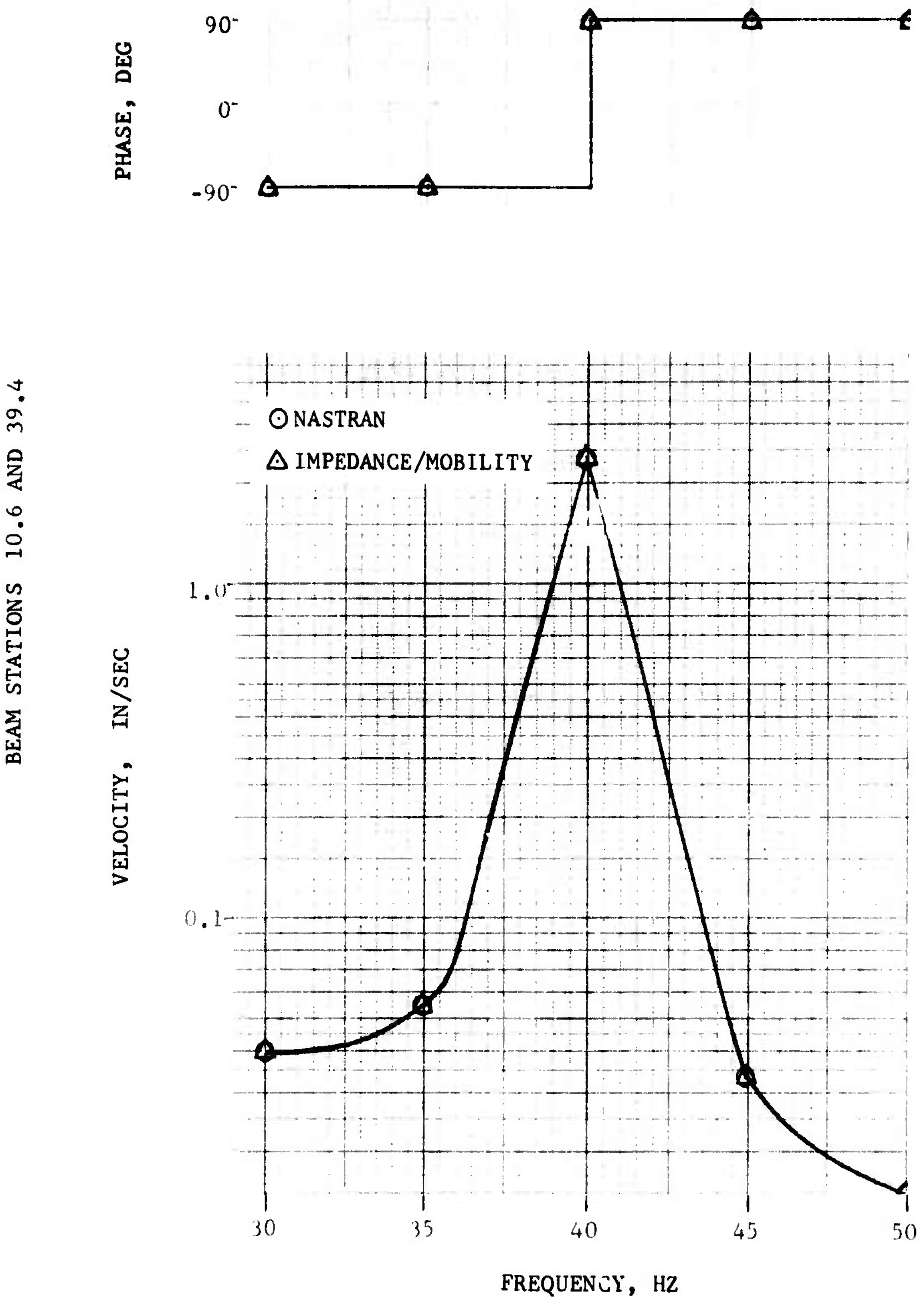

Figure 7. Comparison of NASTRAN and Impedance/Mobility Computed Aluminum Beam Coupled Response, Beam Stations 10.6 and 39.4.

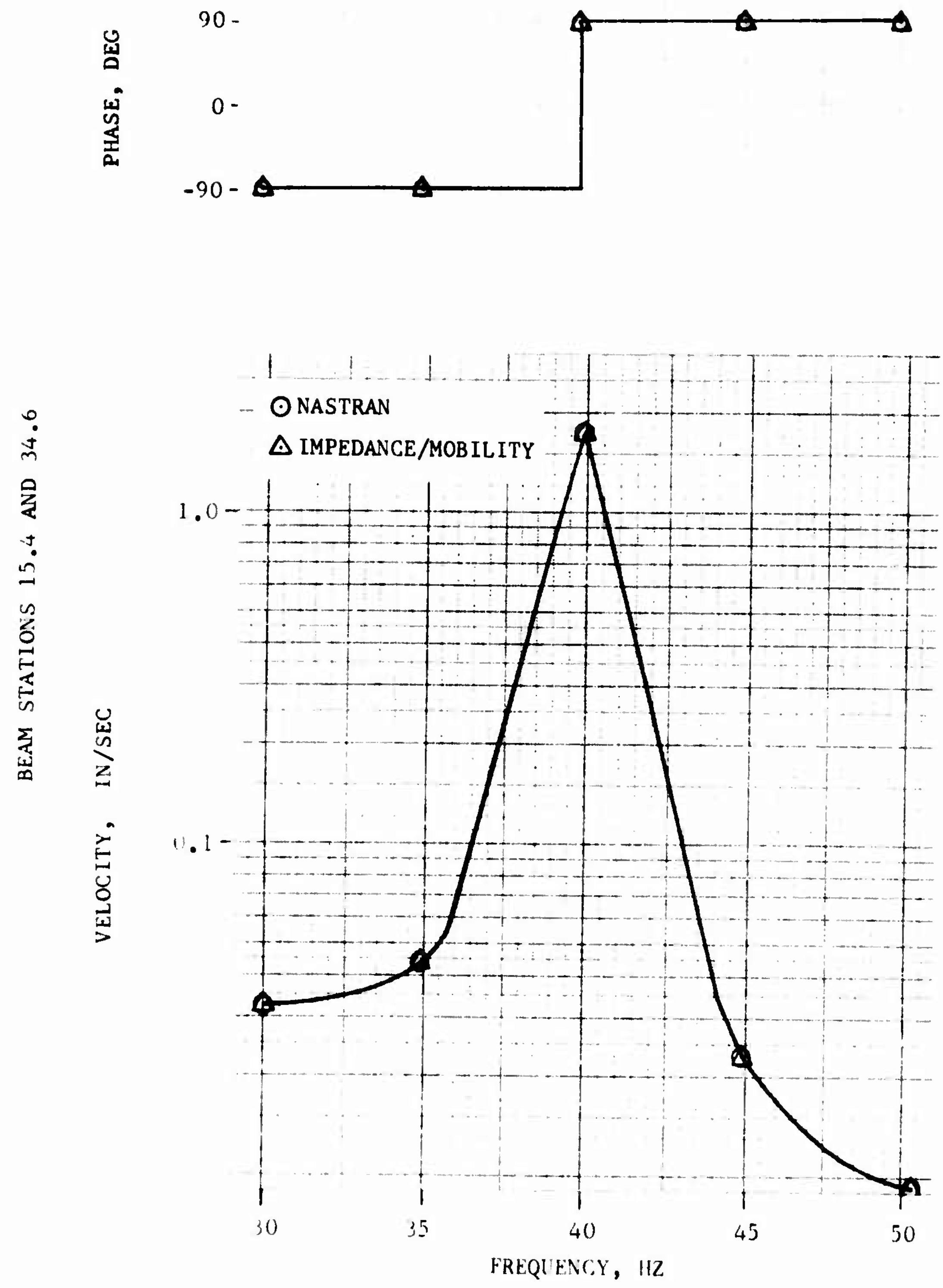

Figure 8. Comparison of NASTRAN and Impedance/Mobility Computed Aluminum Beam Coupled Response, Beam Stations 15.4 and 34.6.

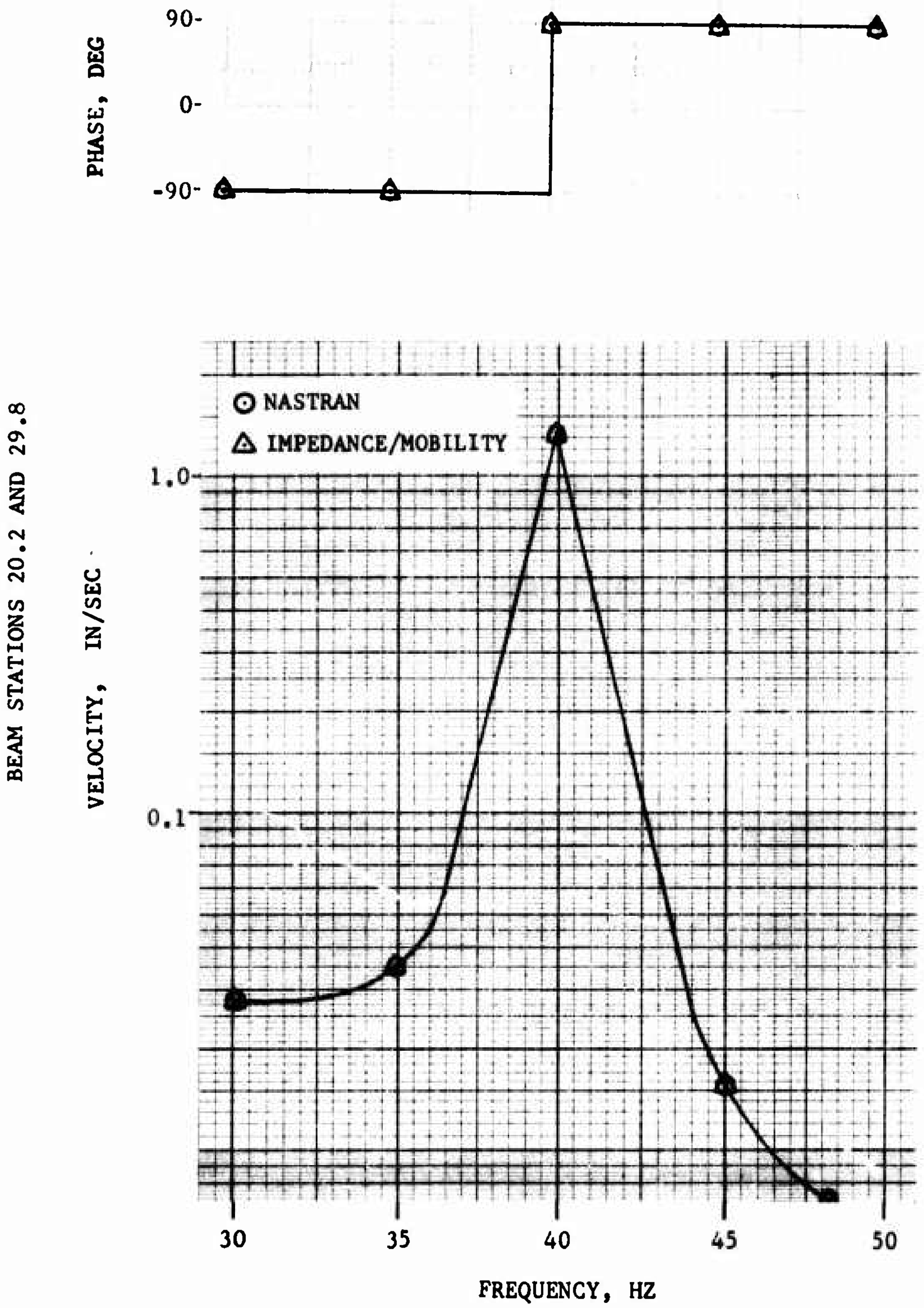

Figure 9. Comparison of NASTRAN and Impedance/Mobility Computed Aluminum Beam Coupled Response, Beam Stations 20.2 and 29.8.

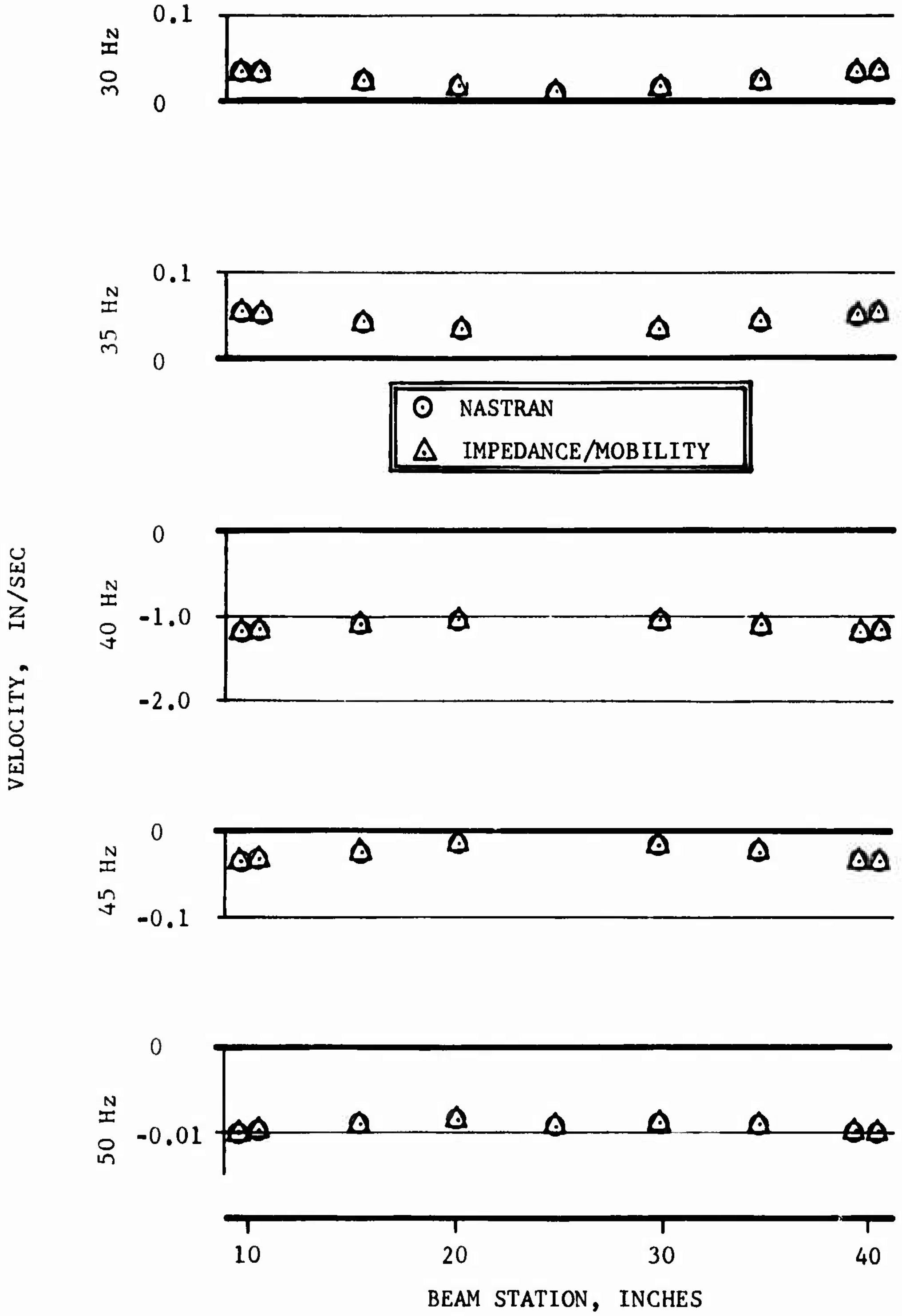

Figure 10. Aluminum Beam Mode Shapes at Each Response Frequency.

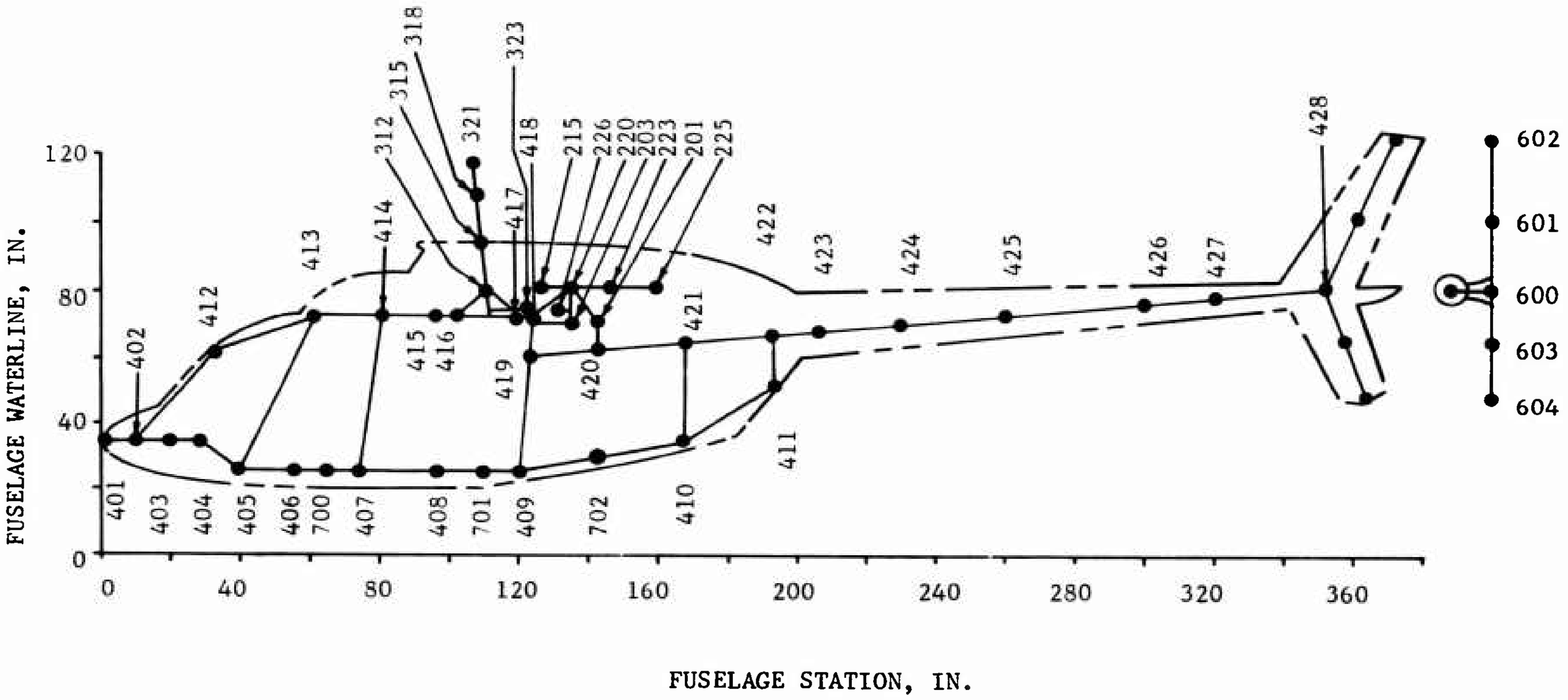

Figure 11. Two-Dimensional Finite Element Model of OH-58A Airframe With Grid Point Location in Global Reference System.

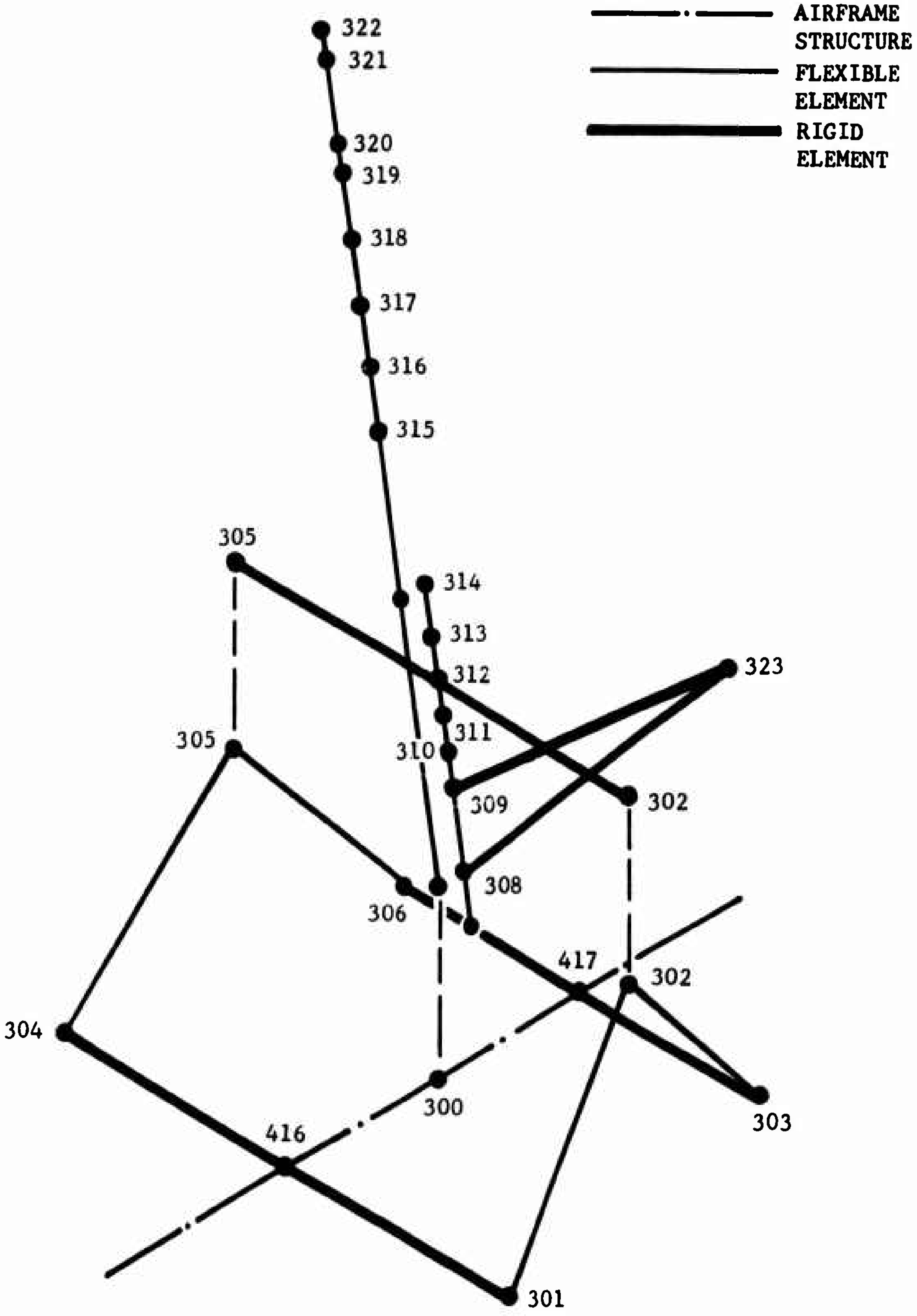

Figure 12. Finite Element Representation of the OH-58A Pylon and Mount Assembly.

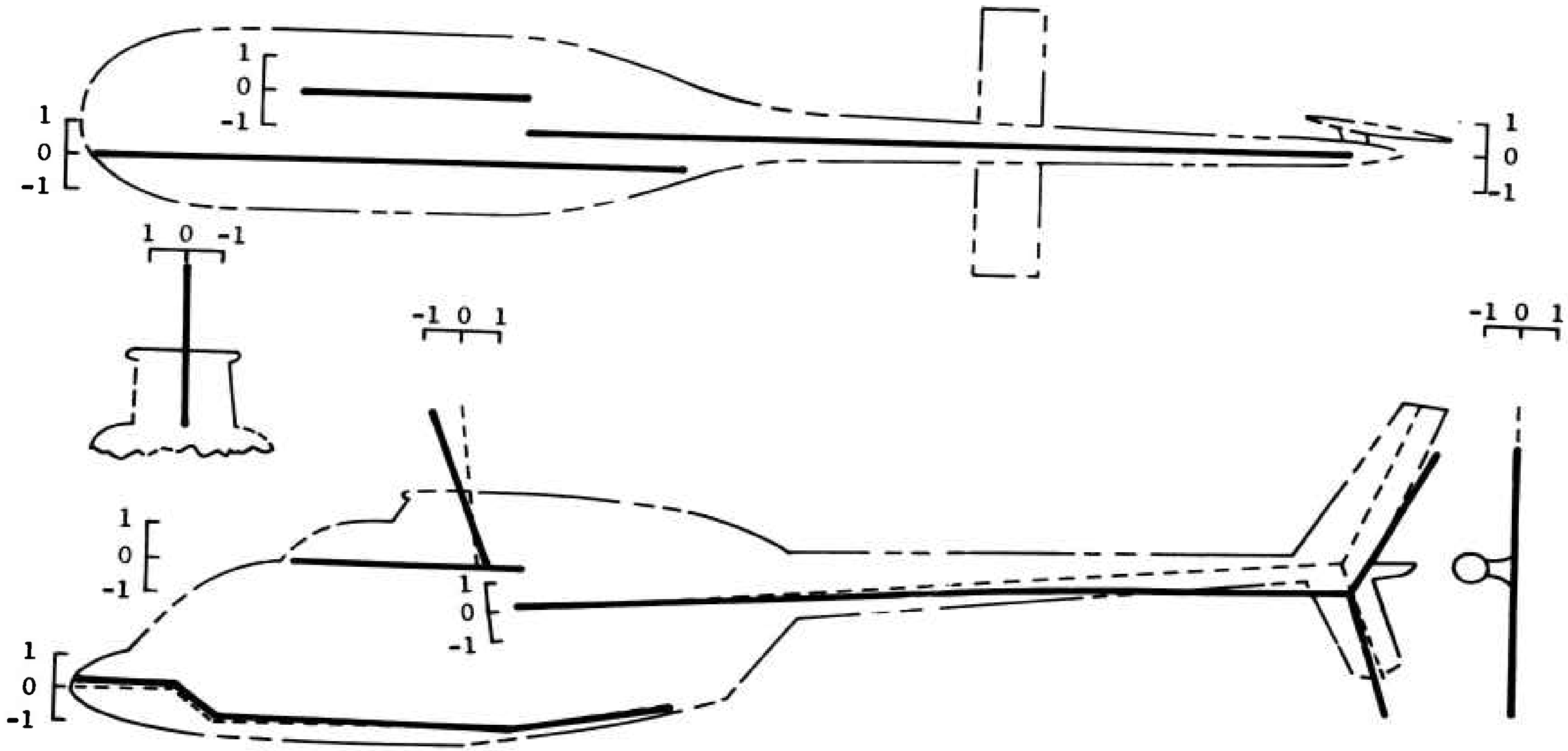

GENERALIZED MASS	.8059
GENERALIZED STIFFNESS	673.
NATURAL FREQUENCY	4.6 Hz ENGINE OUT 4.6 Hz ENGINE IN 4.6 Hz SHAKE TEST

Figure 13. Fuselage Mode Shape at 4.6 Hz (Longitudinal Pylon Mode).

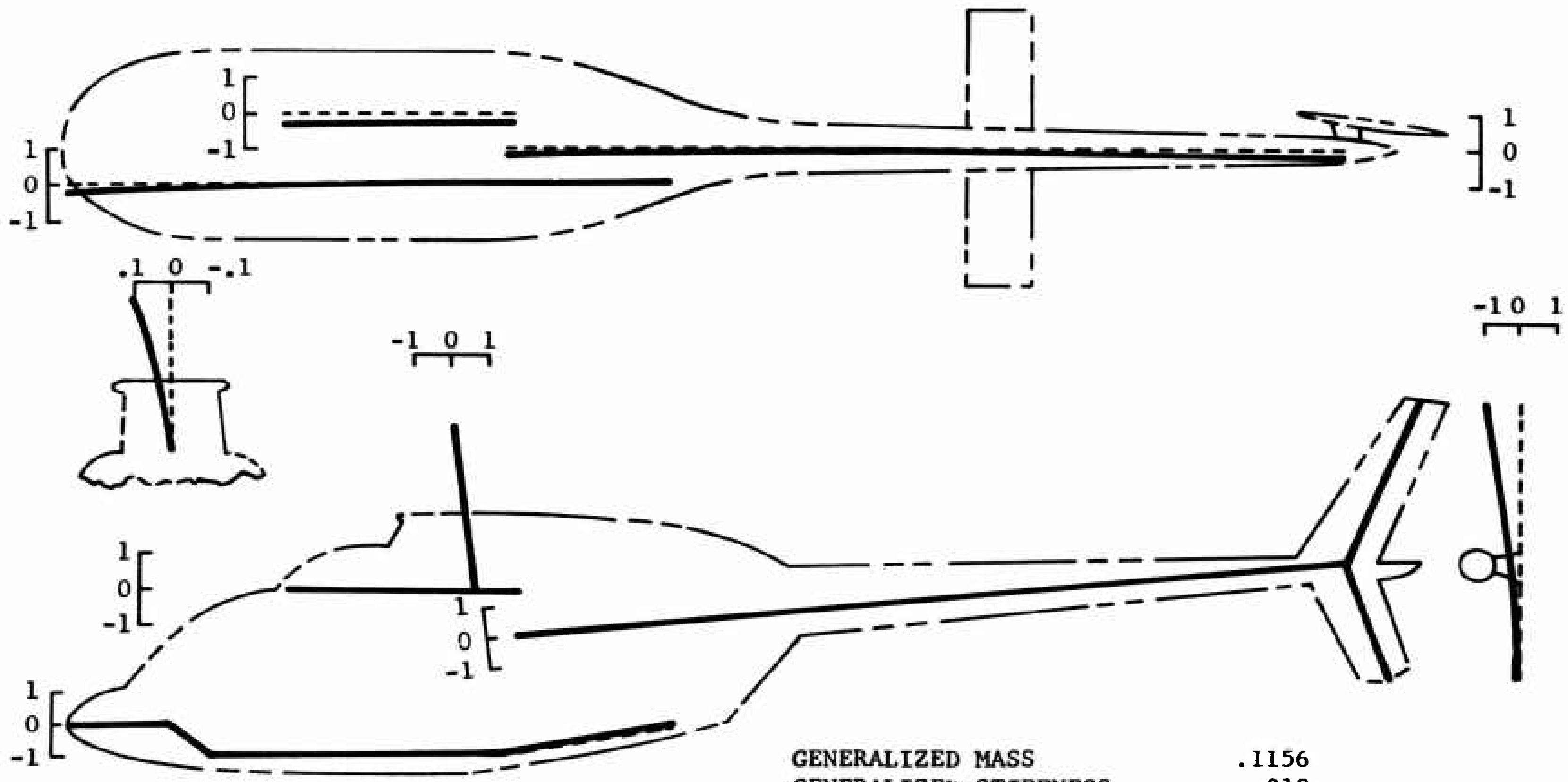

GENERALIZED MASS	.1156
GENERALIZED STIFFNESS	218
NATURAL FREQUENCY	6.91 Hz ENGINE OUT 6.05 Hz ENGINE IN 4.0 Hz SHAKE TEST

Figure 14. Fuselage Mode Shape at 6.0 Hz (Lateral Pylon Mode).

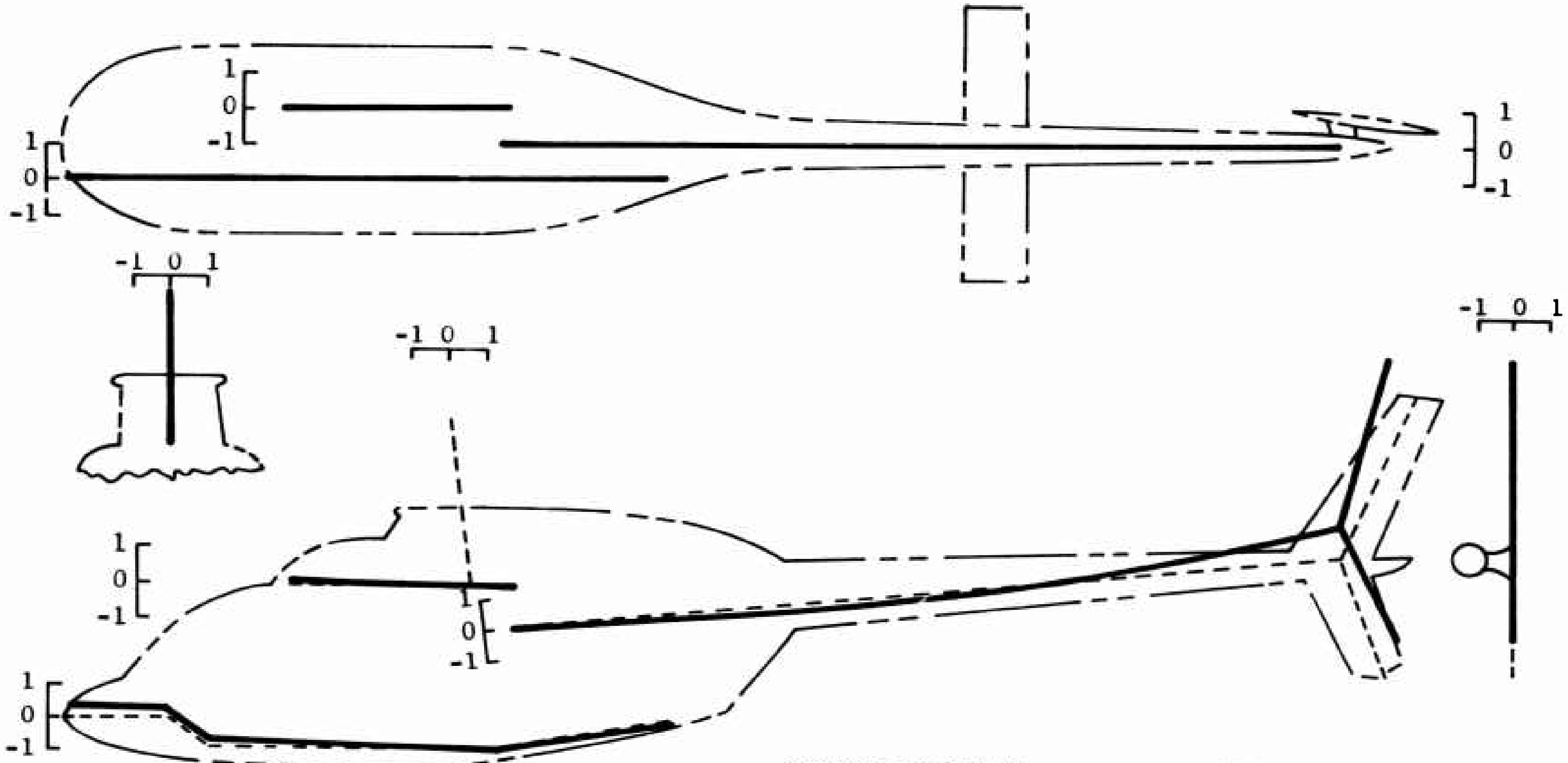

GENERALIZED MASS	.2886
GENERALIZED STIFFNESS	726.
NATURAL FREQUENCY	7.98 Hz ENGINE OUT
	7.75 Hz ENGINE IN
	7.8 Hz SHAKE TEST

Figure 15. Fuselage Mode Shape at 7.75 Hz (First Vertical Fuselage Mode).

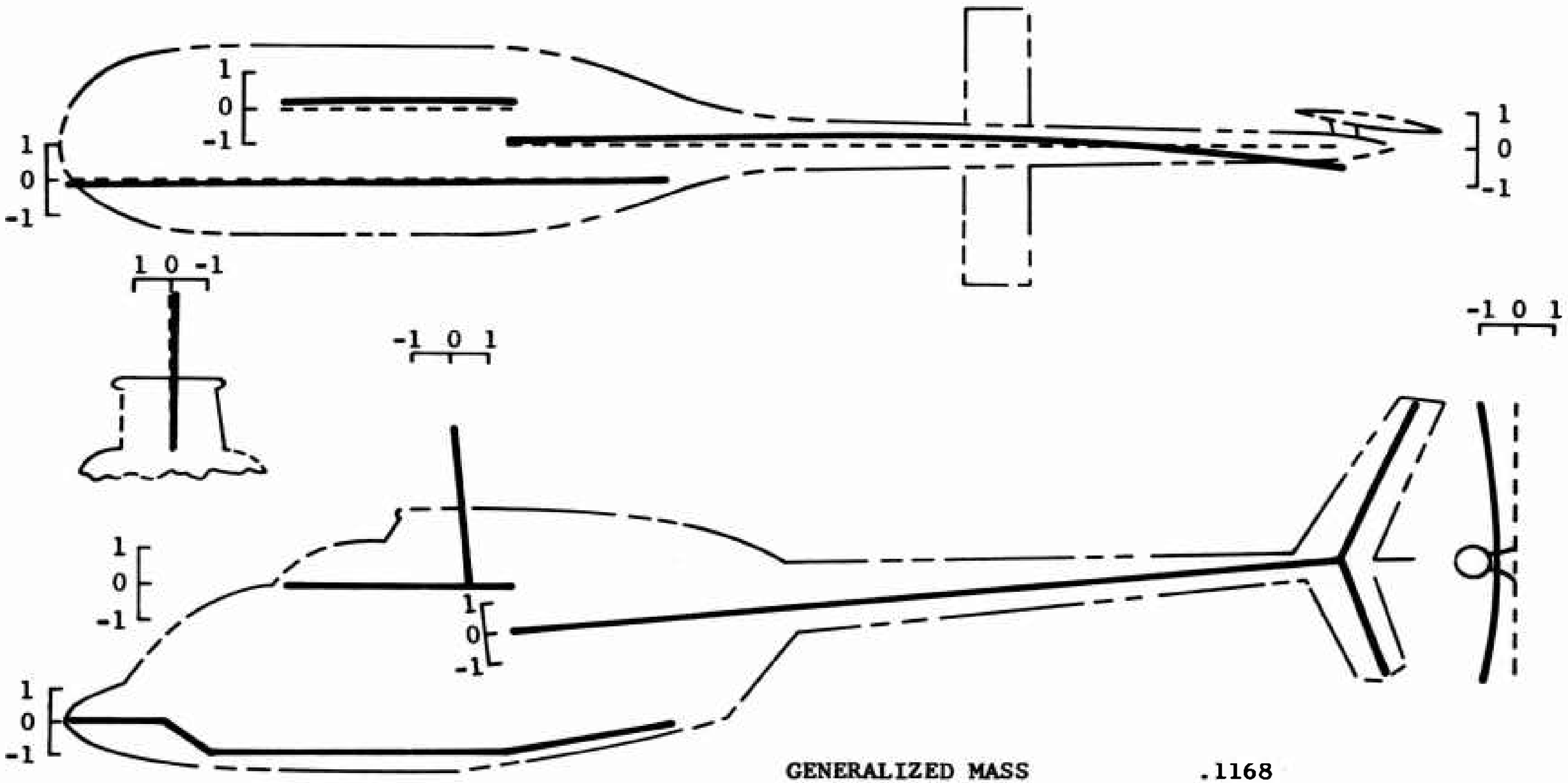

GENERALIZED MASS	.1168
GENERALIZED STIFFNESS	353.
NATURAL FREQUENCY	8.75 Hz ENGINE OUT
	8.0 Hz ENGINE IN
	8.0 Hz SHAKE TEST

Figure 16. Fuselage Mode Shape at 8.0 Hz (First Lateral Fuselage Mode).

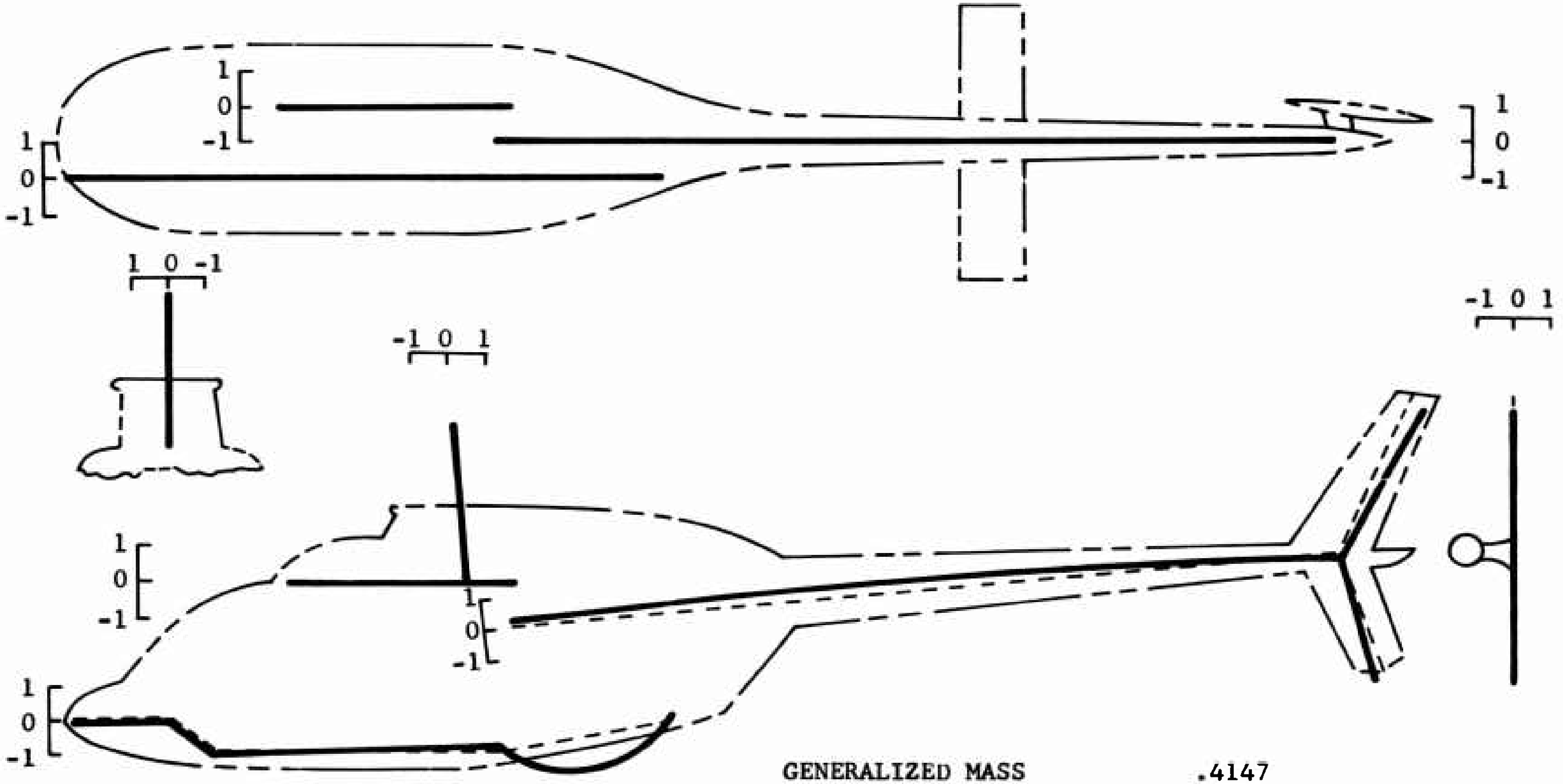

GENERALIZED MASS	.4147
GENERALIZED STIFFNESS	214.
NATURAL FREQUENCY	11.44 Hz ENGINE OUT 11.29 Hz ENGINE IN 11.4 Hz SHAKE TEST

Figure 17. Fuselage Mode Shape at 11.4 Hz (Baggage Compartment Panel Vertical Mode).

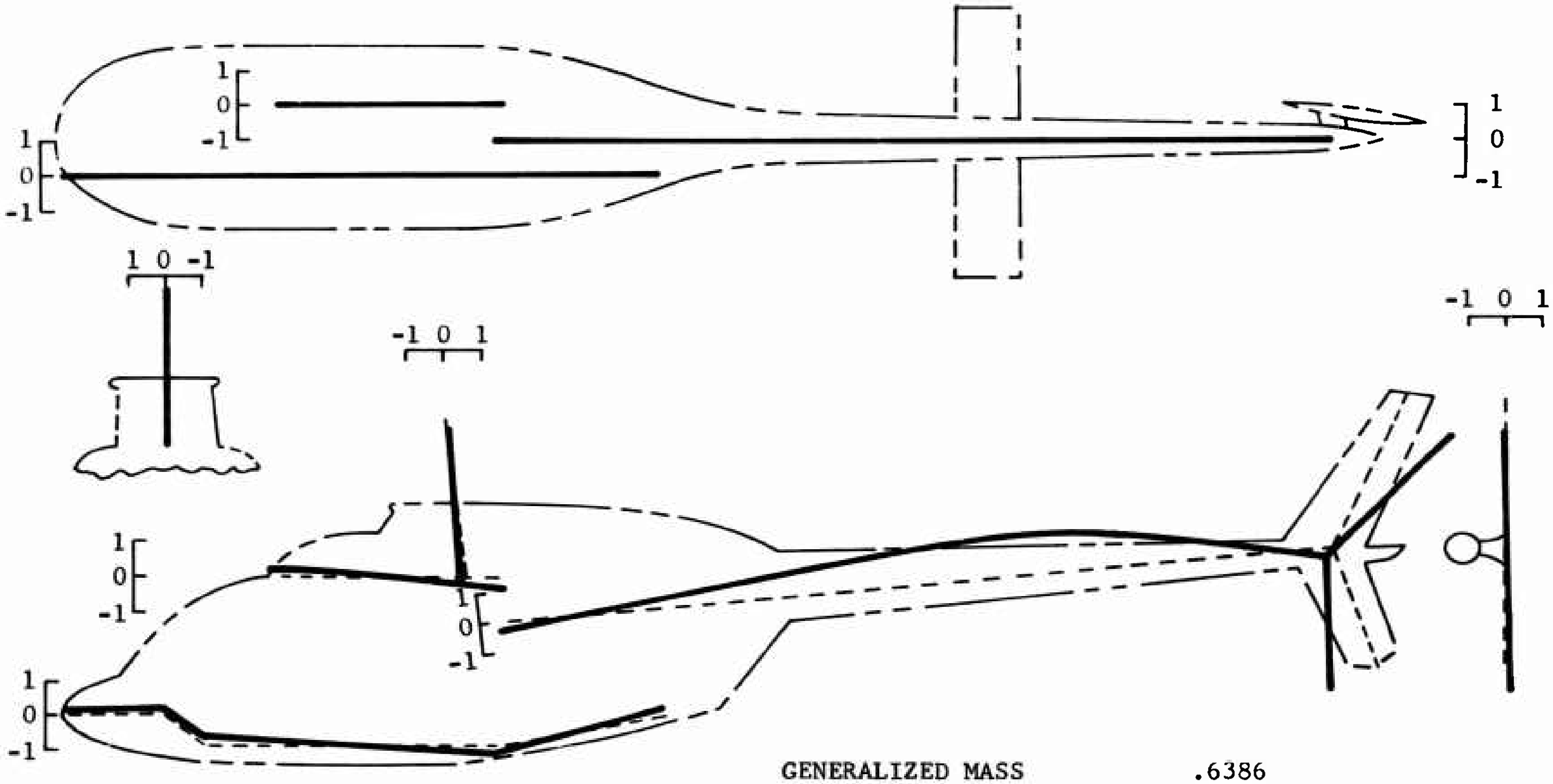

GENERALIZED MASS	.6386
GENERALIZED STIFFNESS	14468.
NATURAL FREQUENCY	23.96 Hz ENGINE OUT
	22.17 Hz ENGINE IN
	22.5 Hz SHAKE TEST

Figure 18. Fuselage Mode Shape at 22.5 Hz (Second Fuselage Vertical Mode).

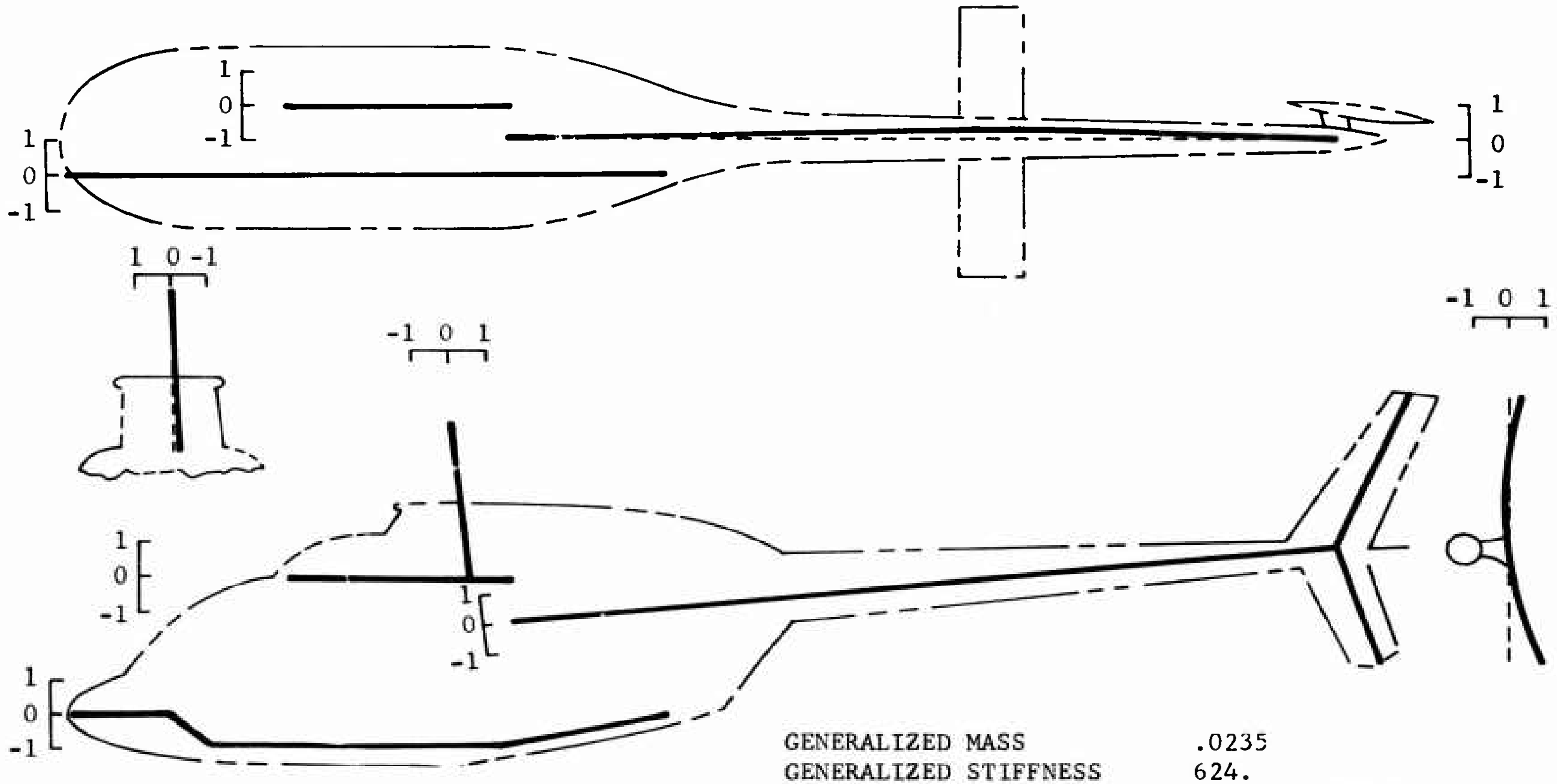

GENERALIZED MASS	.0235
GENERALIZED STIFFNESS	624.
NATURAL FREQUENCY	25.93 Hz ENGINE OUT
	25.14 Hz ENGINE IN
	25.0 Hz SHAKE TEST

Figure 19. Fuselage Mode Shape at 25.14 Hz (Vertical Fin Lateral Symmetric Bending Mode).

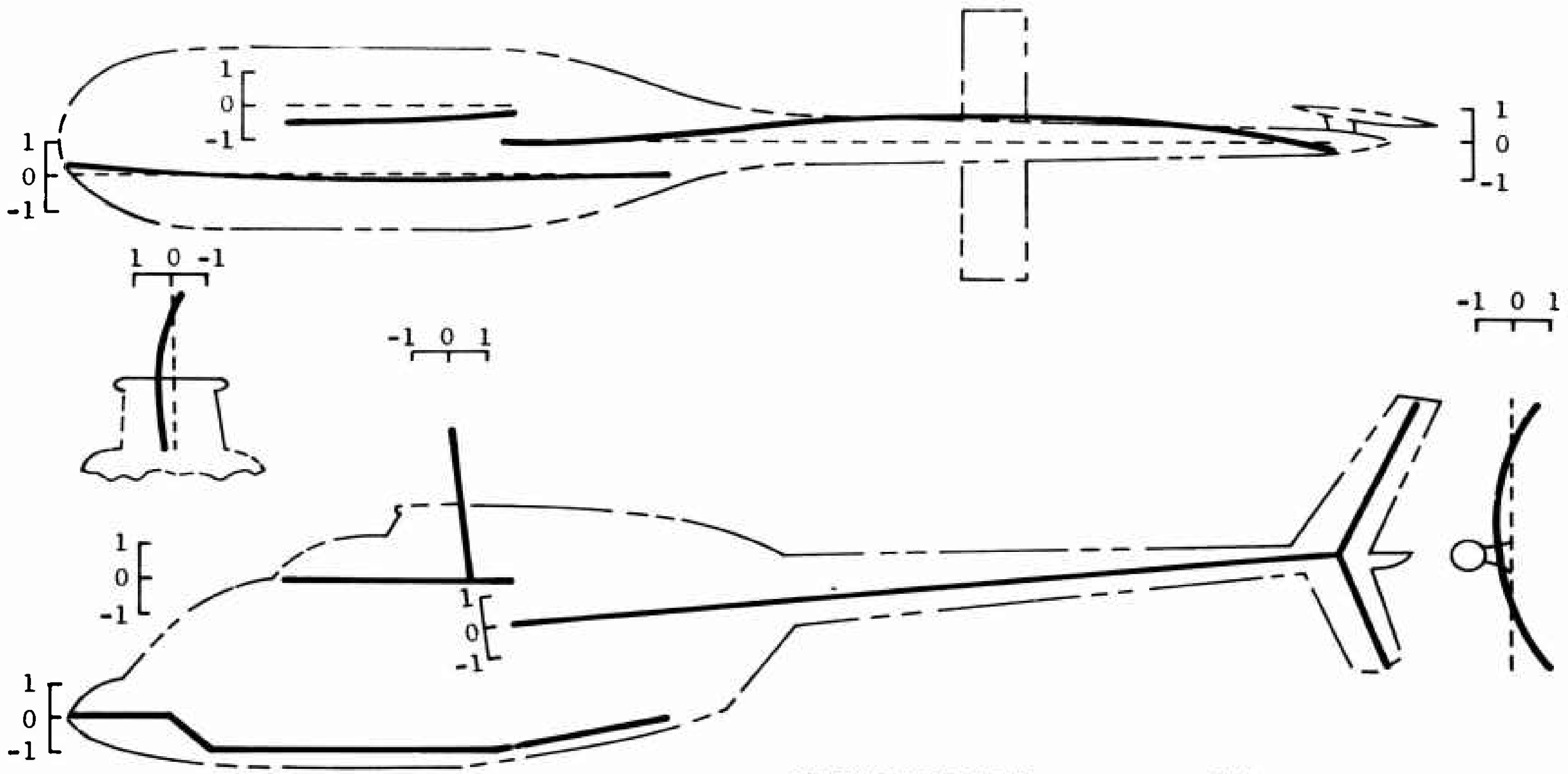

GENERALIZED MASS	.294	
GENERALIZED STIFFNESS	9857	
NATURAL FREQUENCY	29.14 Hz	ENGINE OUT
	28.79 Hz	ENGINE IN
	26.5 Hz	SHAKE TEST

Figure 20. Fuselage Mode Shape at 28.8 Hz (Second Lateral Fuselage Mode).

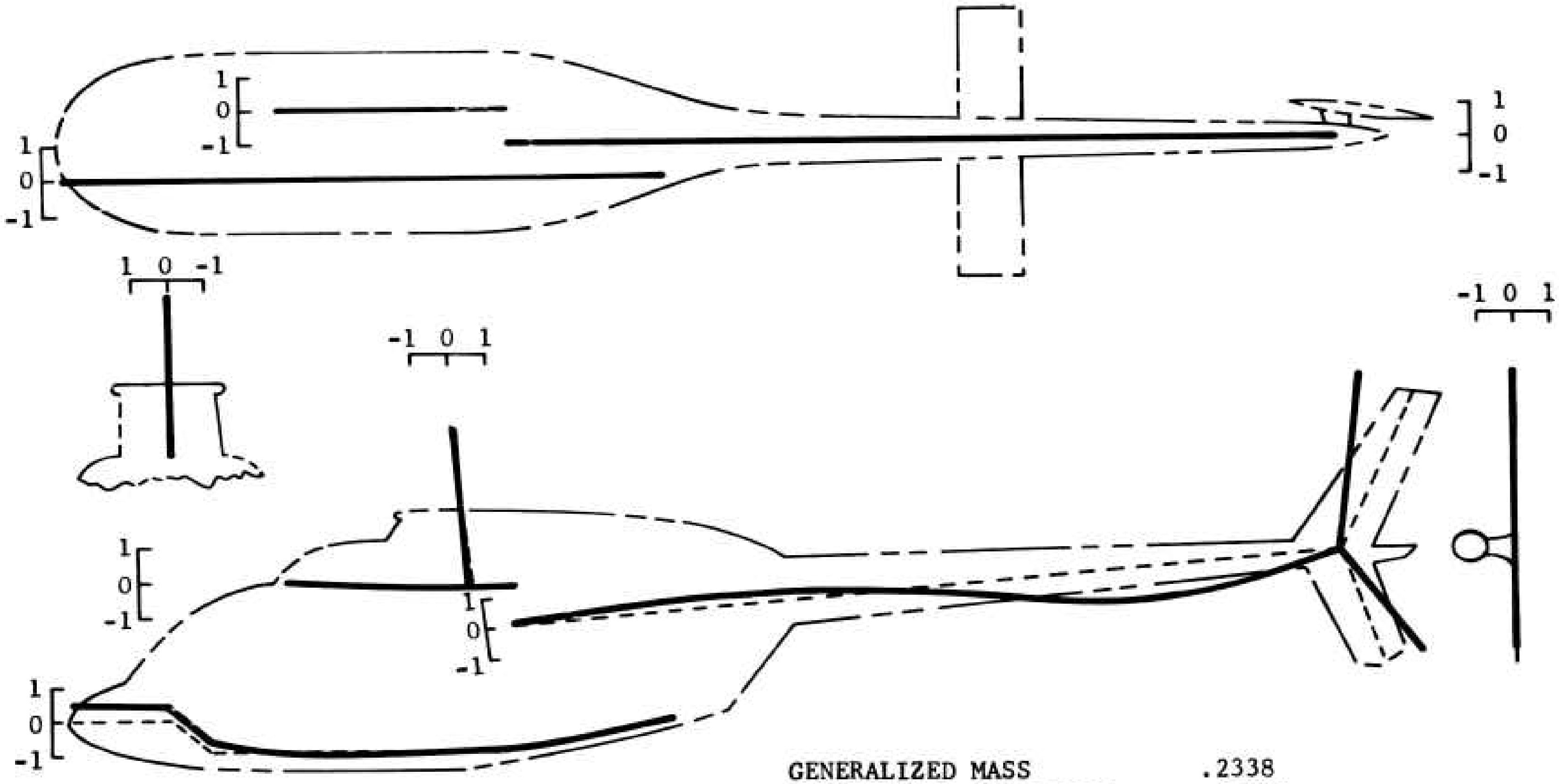

GENERALIZED MASS	.2338
GENERALIZED STIFFNESS	19828.
NATURAL FREQUENCY	46.35 Hz ENGINE OUT
	43.55 Hz ENGINE IN
	41.4 Hz SHAKE TEST

Figure 21. Fuselage Mode Shape at 43.6 Hz (Third Fuselage Vertical Mode).

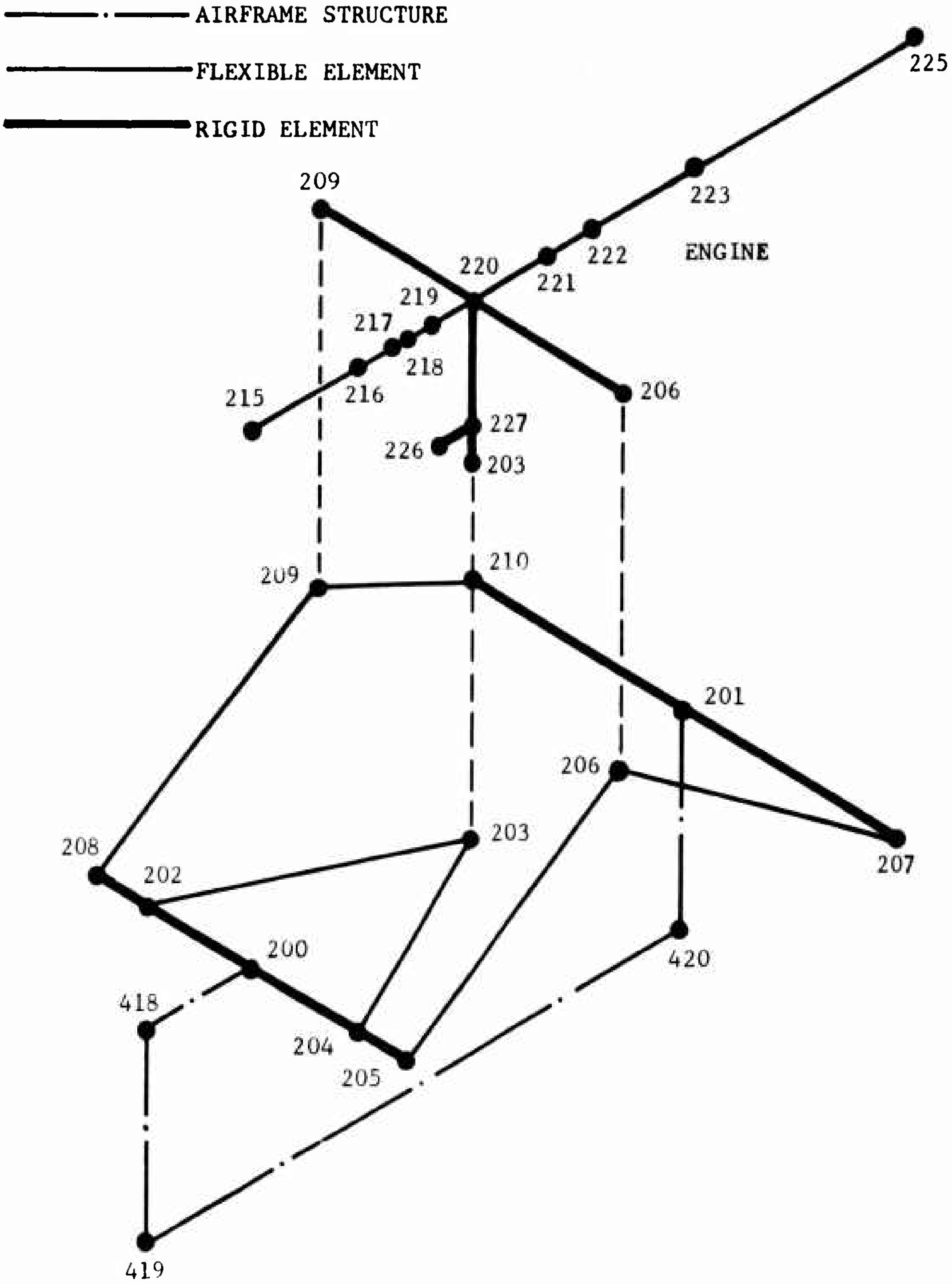

Figure 22. Finite Element Representation of the T-63 Engine and OH-58A Engine Mounts.

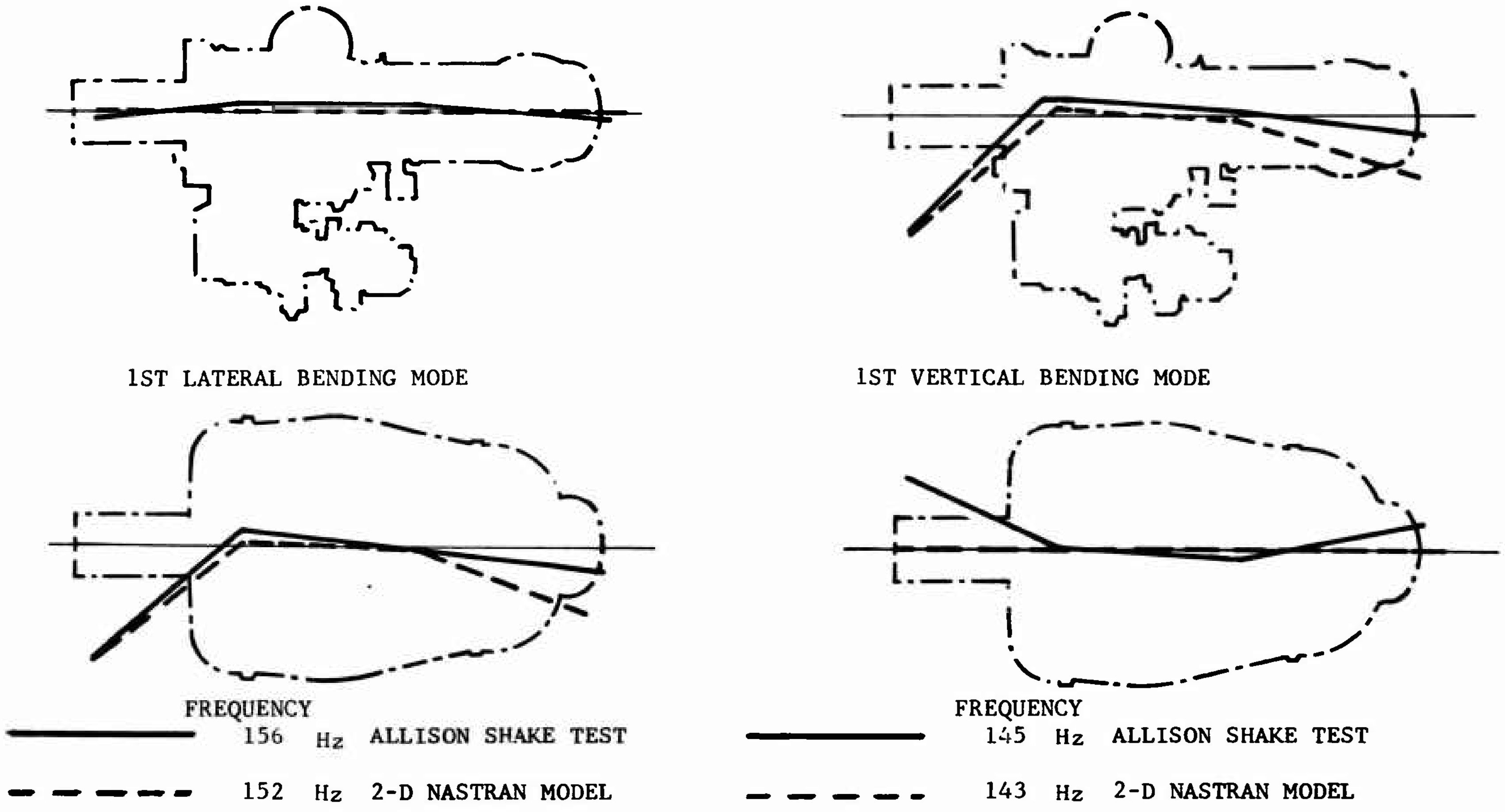

1ST LATERAL BENDING MODE

1ST VERTICAL BENDING MODE

Figure 23. Comparison of Two-Dimensional NASTRAN Model and Allison Shake Test Engine Mode Shapes.

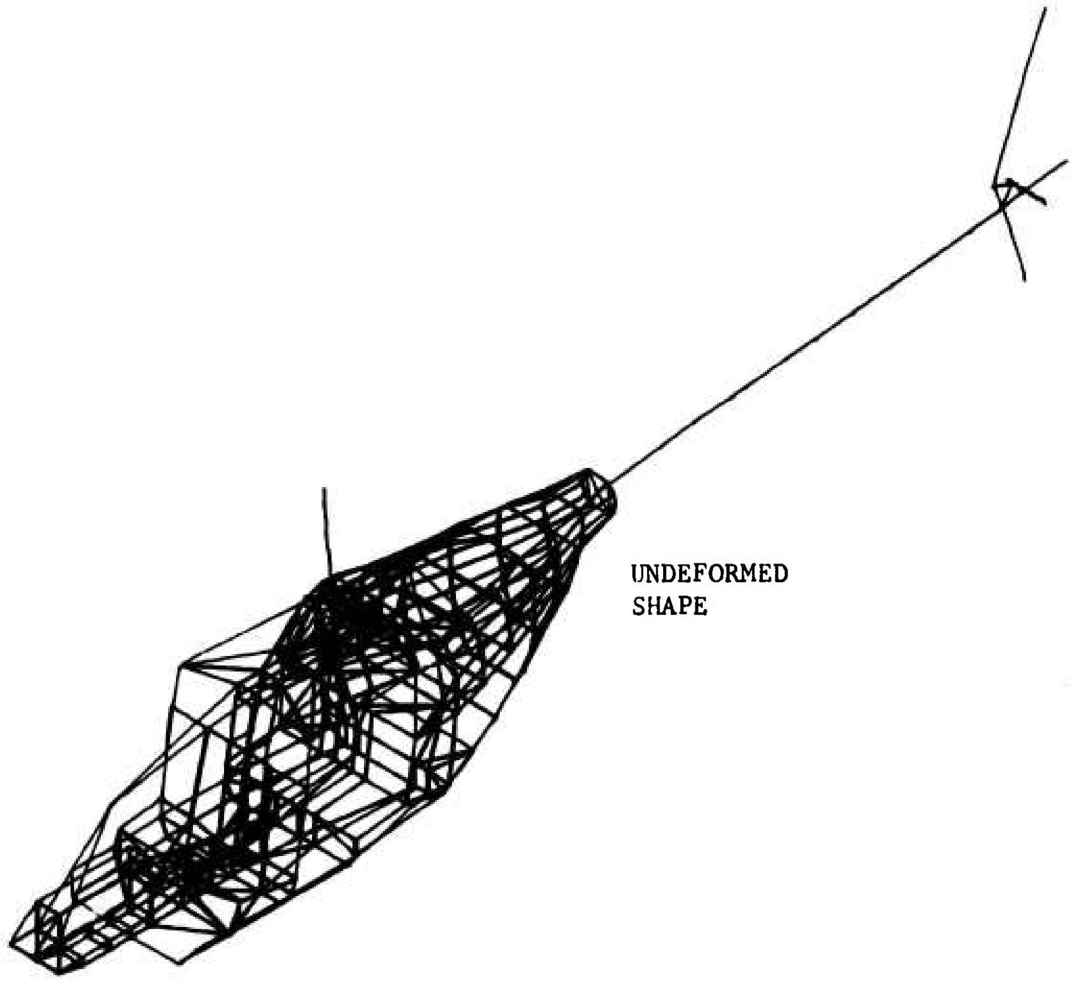

Figure 24. Three-Dimensional NASTRAN Model of OH-58A Helicopter.

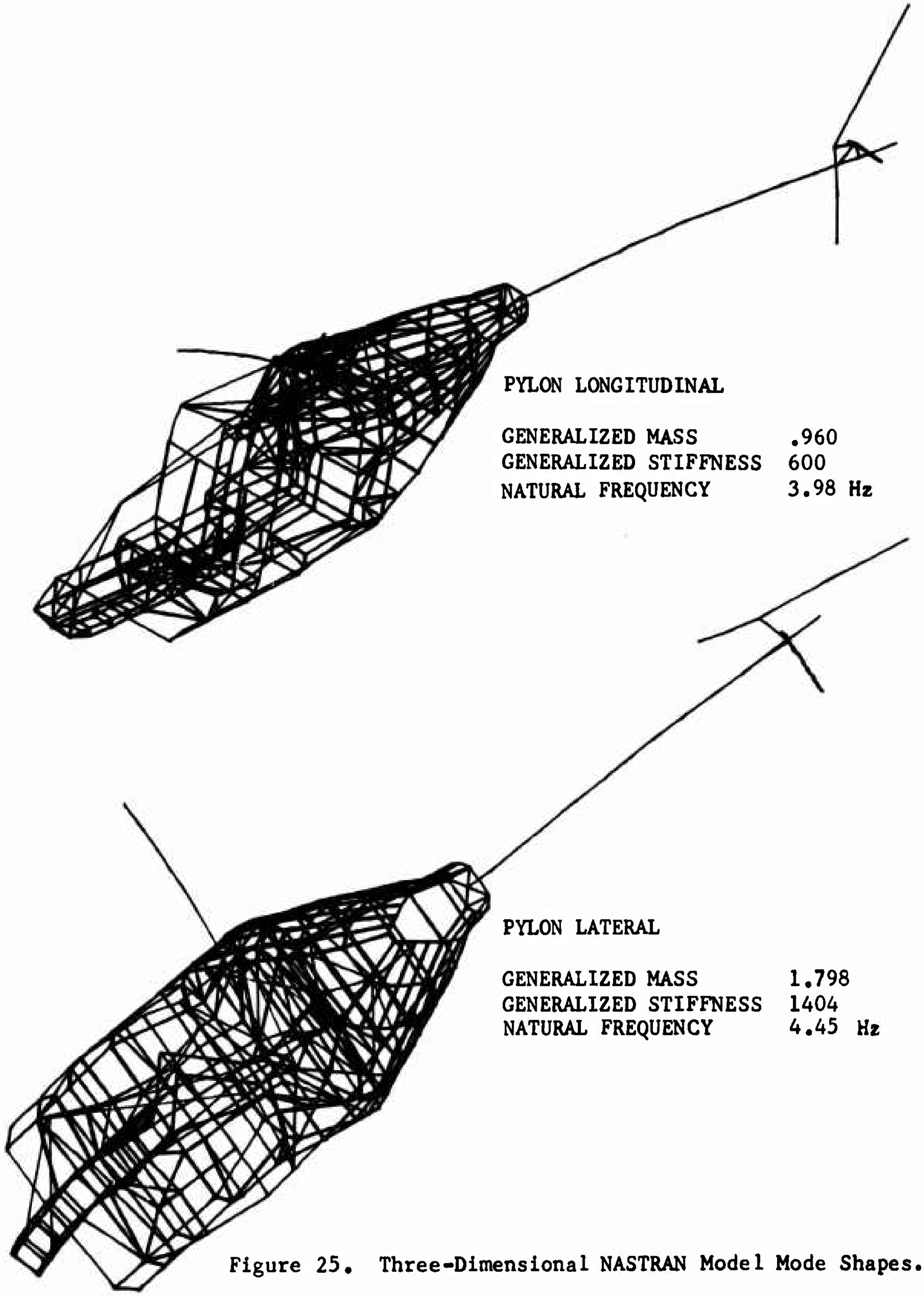

PYLON LONGITUDINAL

GENERALIZED MASS	.960
GENERALIZED STIFFNESS	600
NATURAL FREQUENCY	3.98 Hz

PYLON LATERAL

GENERALIZED MASS	1.798
GENERALIZED STIFFNESS	1404
NATURAL FREQUENCY	4.45 Hz

Figure 25. Three-Dimensional NASTRAN Model Mode Shapes.

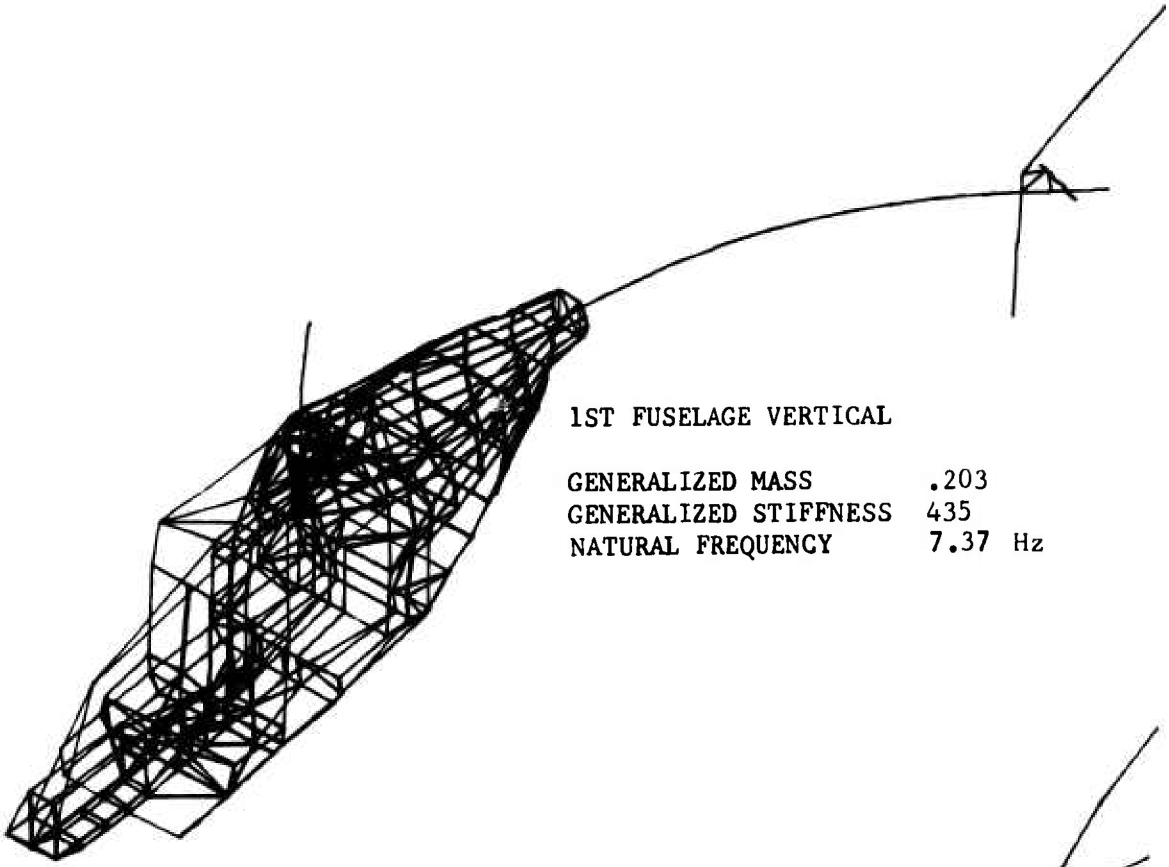

1ST FUSELAGE VERTICAL

GENERALIZED MASS	.203
GENERALIZED STIFFNESS	435
NATURAL FREQUENCY	7.37 Hz

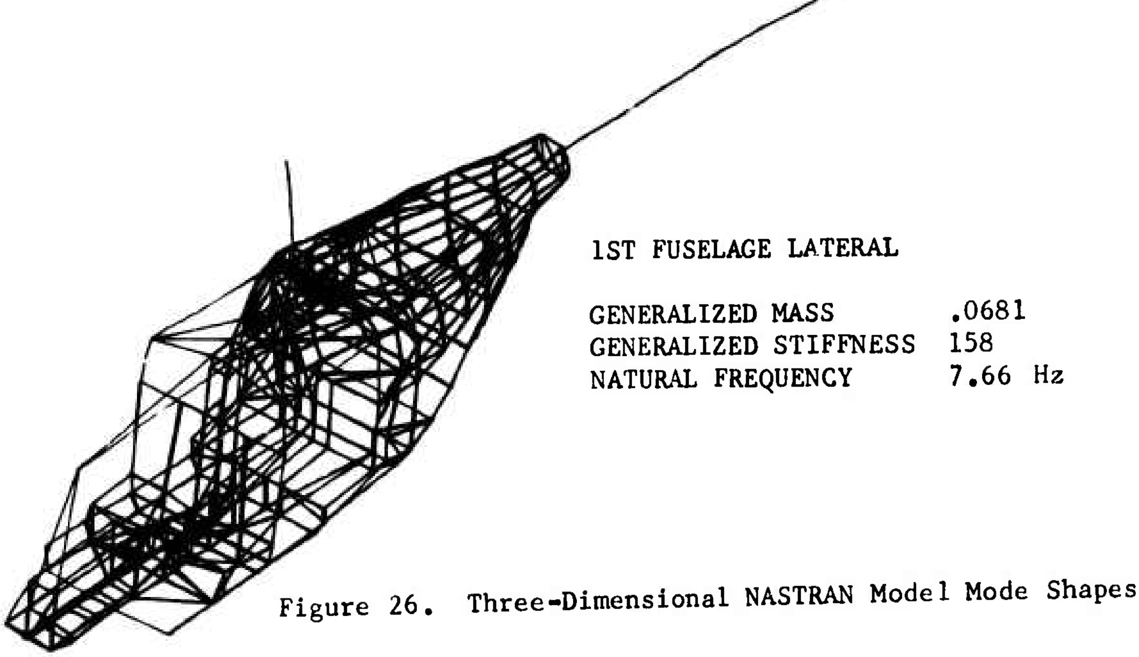

1ST FUSELAGE LATERAL

GENERALIZED MASS	.0681
GENERALIZED STIFFNESS	158
NATURAL FREQUENCY	7.66 Hz

Figure 26. Three-Dimensional NASTRAN Model Mode Shapes.

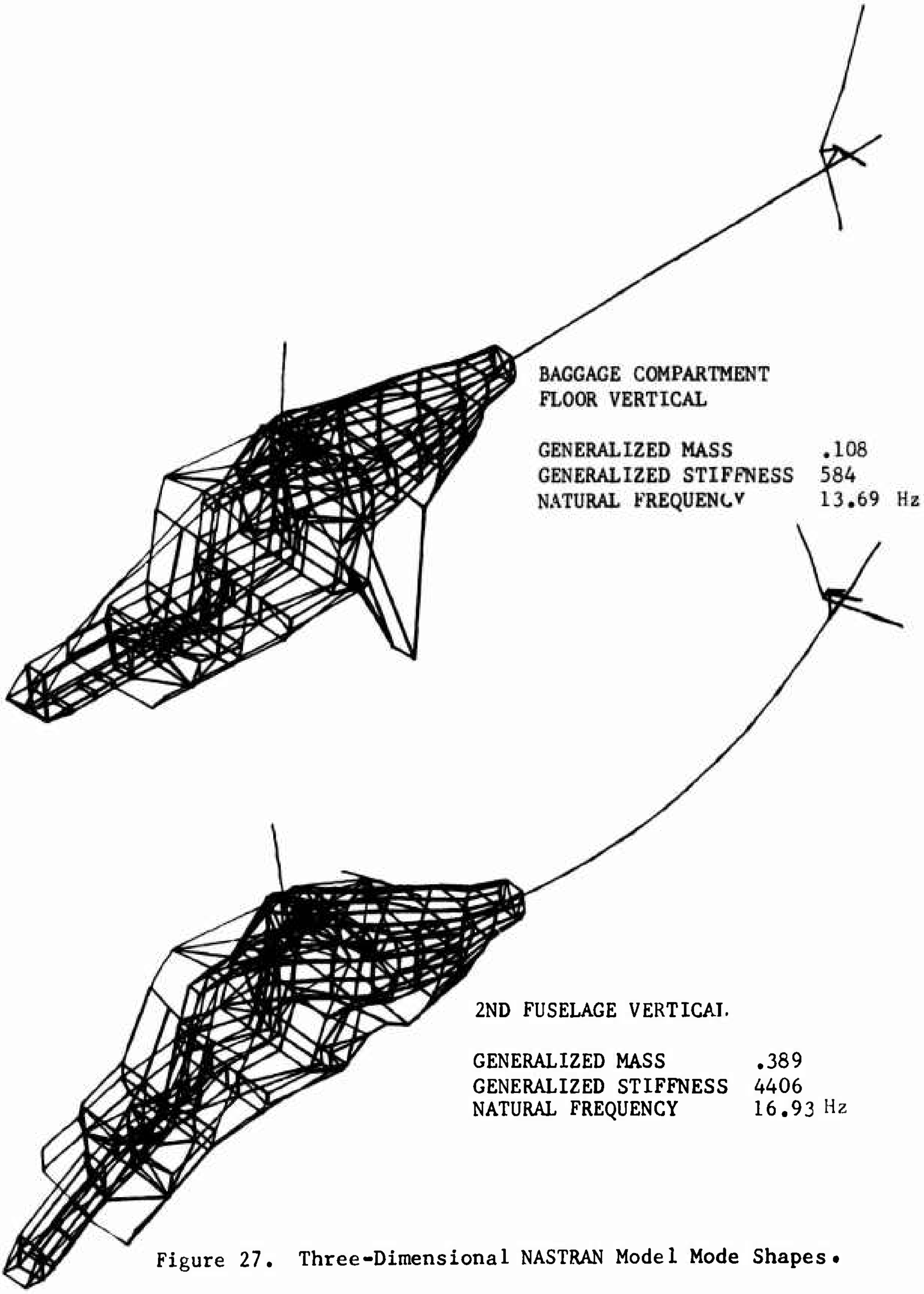

Figure 27. Three-Dimensional NASTRAN Model Mode Shapes.

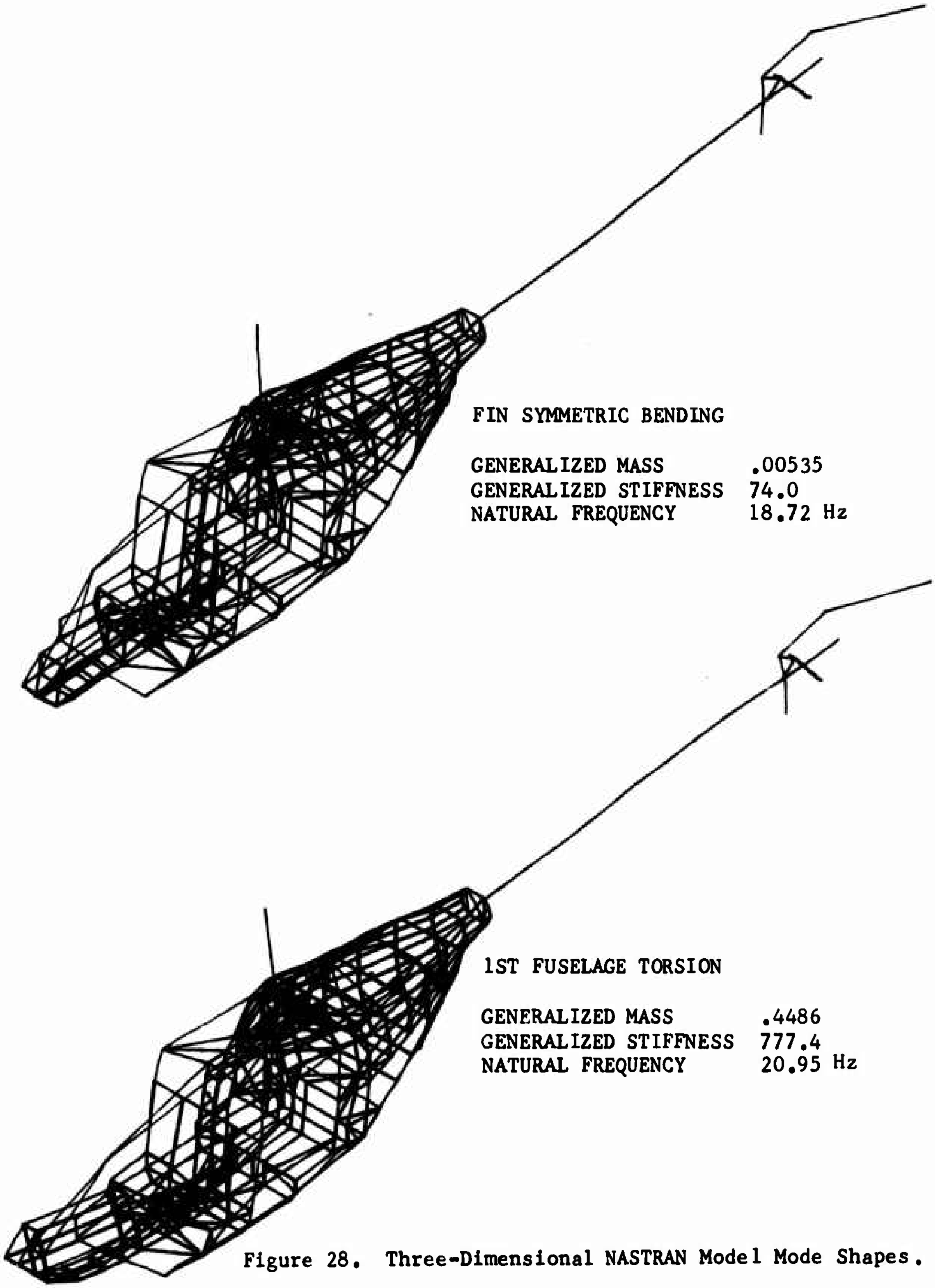

FIN SYMMETRIC BENDING

GENERALIZED MASS	.00535
GENERALIZED STIFFNESS	74.0
NATURAL FREQUENCY	18.72 Hz

1ST FUSELAGE TORSION

GENERALIZED MASS	.4486
GENERALIZED STIFFNESS	777.4
NATURAL FREQUENCY	20.95 Hz

Figure 28. Three-Dimensional NASTRAN Model Mode Shapes.

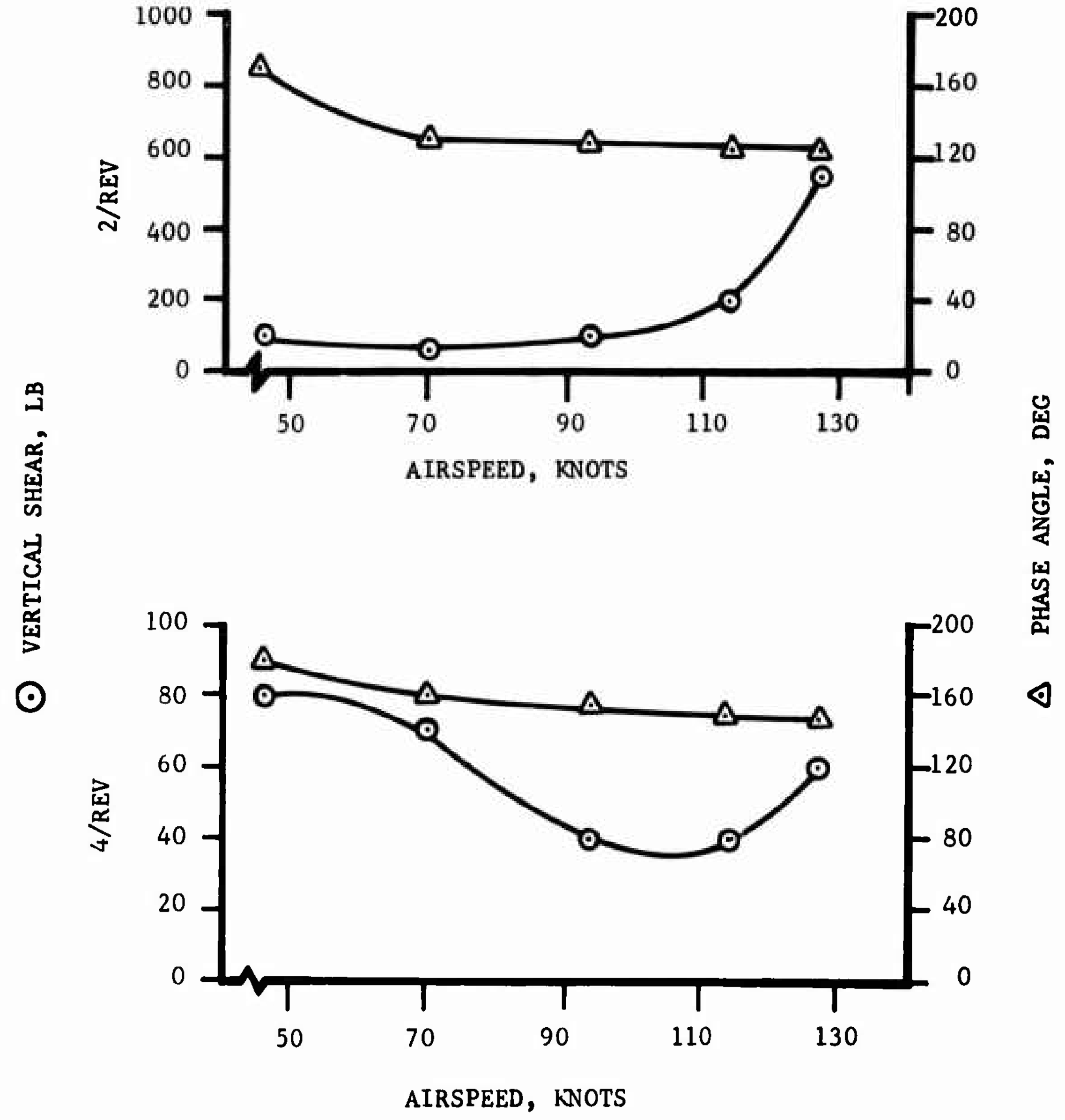

Figure 29. OH-58A Main Rotor Two-Per-Rev and Four-Per-Rev Vertical Shears.

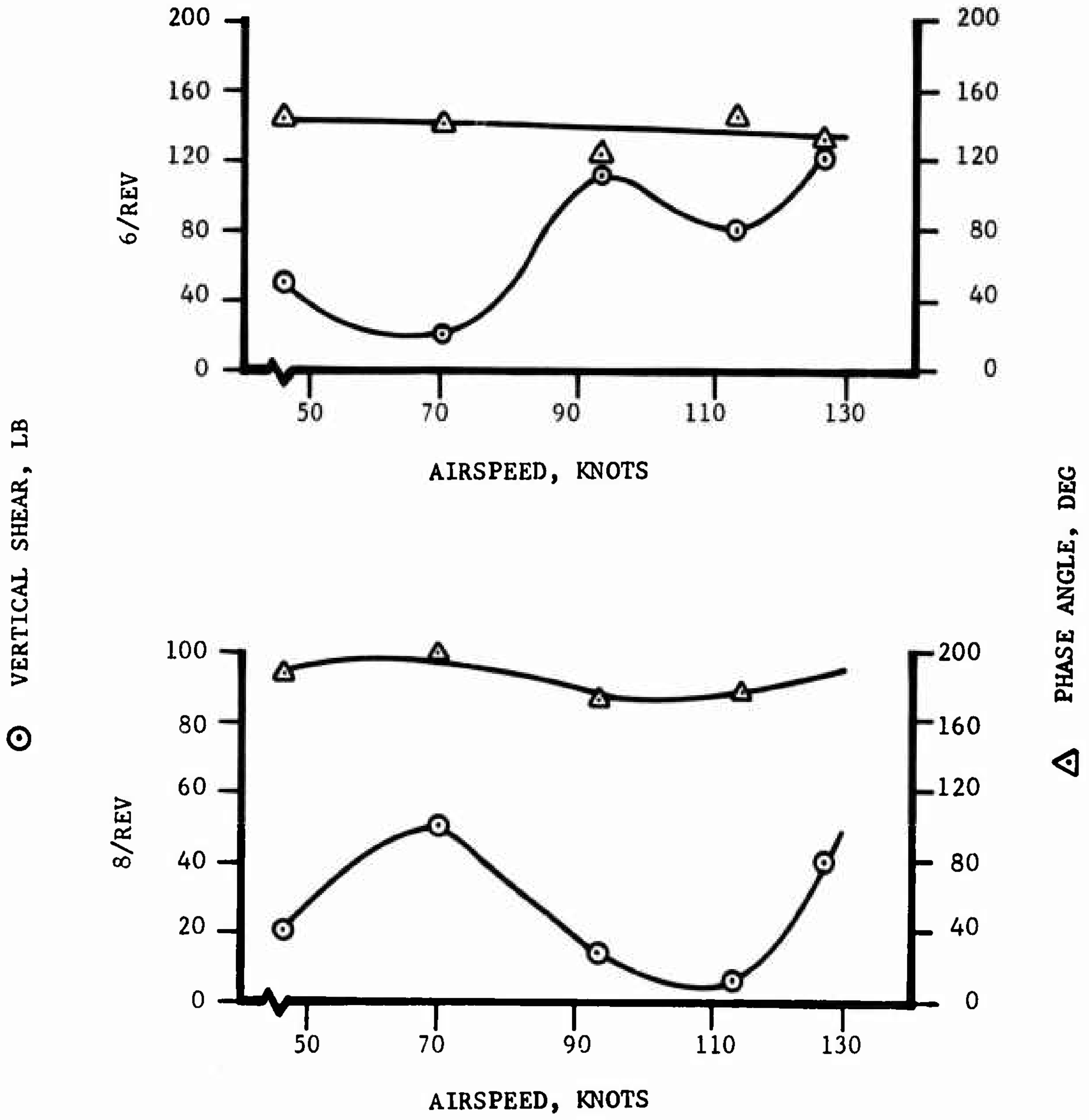

Figure 30. OH-58A Main Rotor Six-Per-Rev and Eight-Per-Rev Vertical Shears.

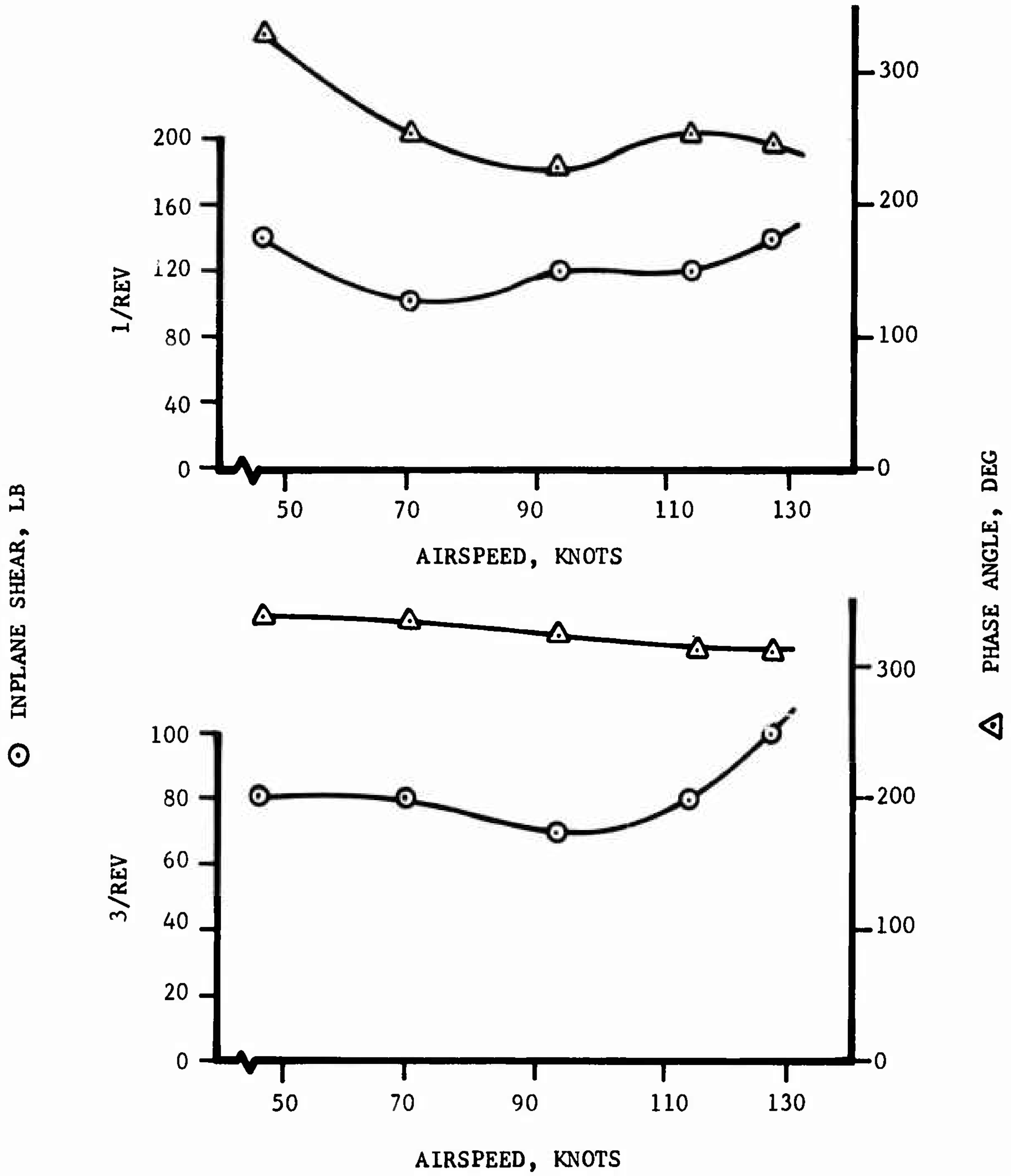

Figure 31. OH-58A Main Rotor One-Per-Rev and Three-Per-Rev Inplane Shears.

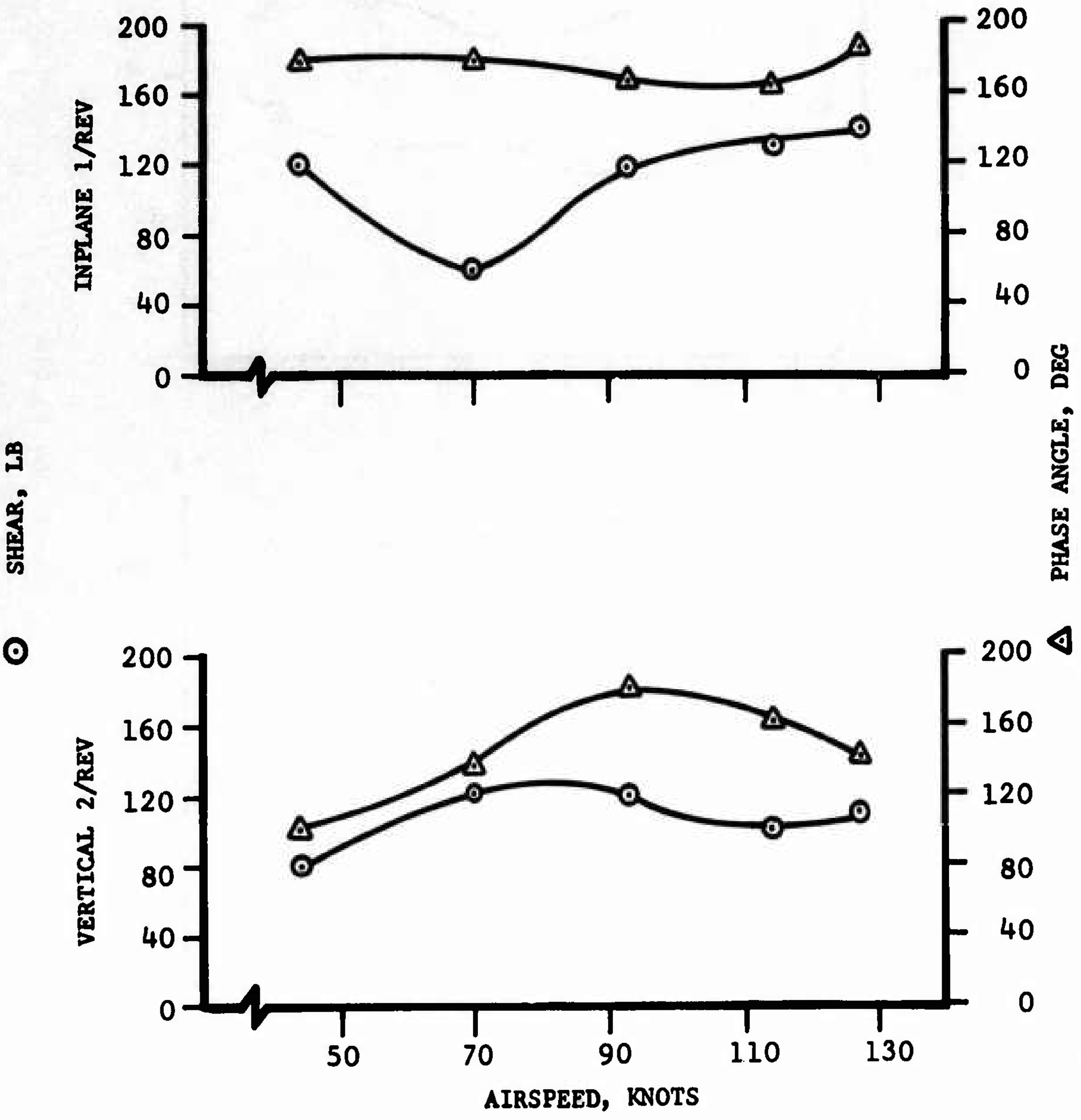

Figure 32. OH-58A Tail Rotor Vertical and Inplane Shears.

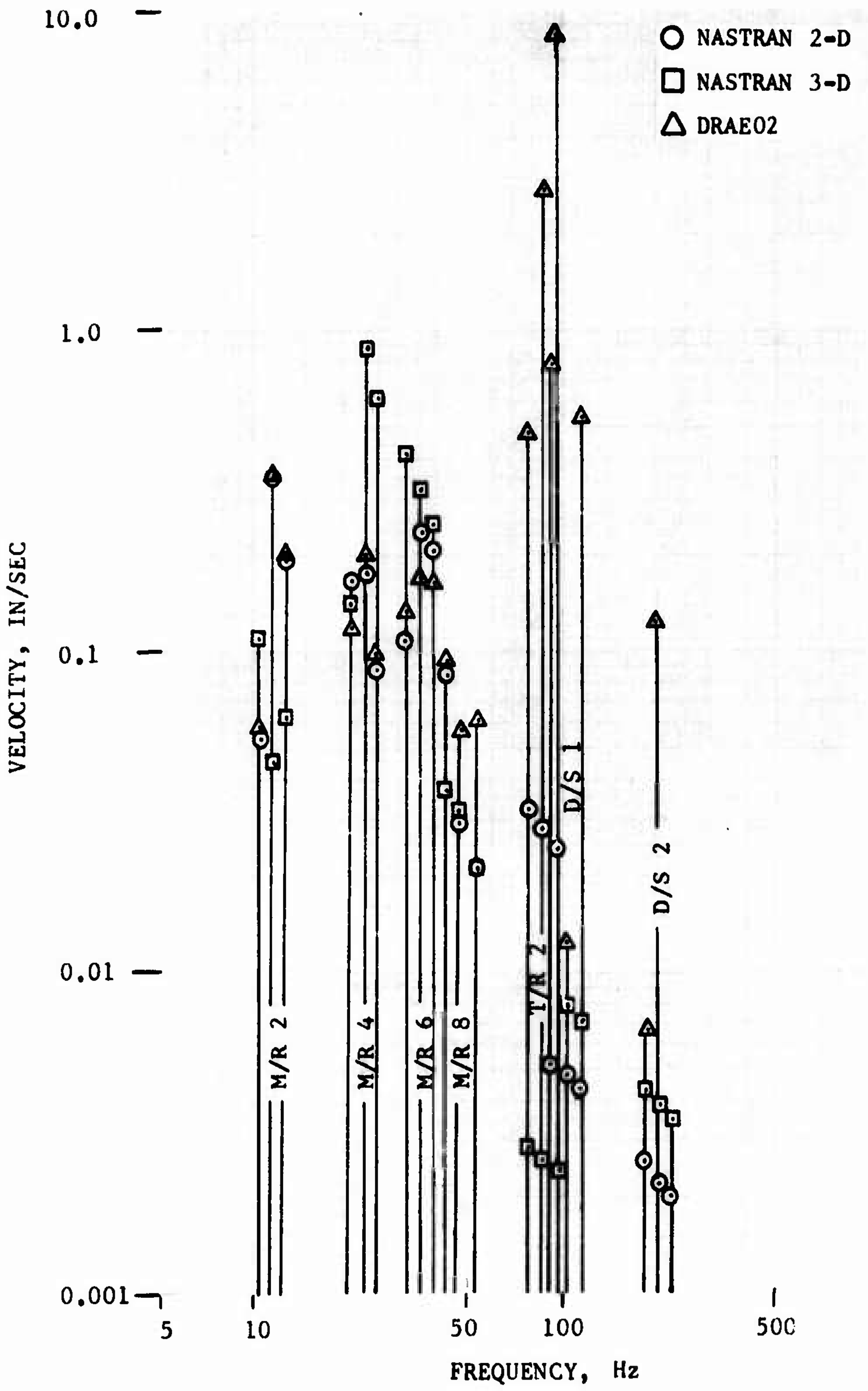

Figure 33. Comparison of NASTRAN and DRAE02 (Mobility) Computed Engine Forward Compressor Vertical Velocity, Simulated 90-Knot Level Flight Response.

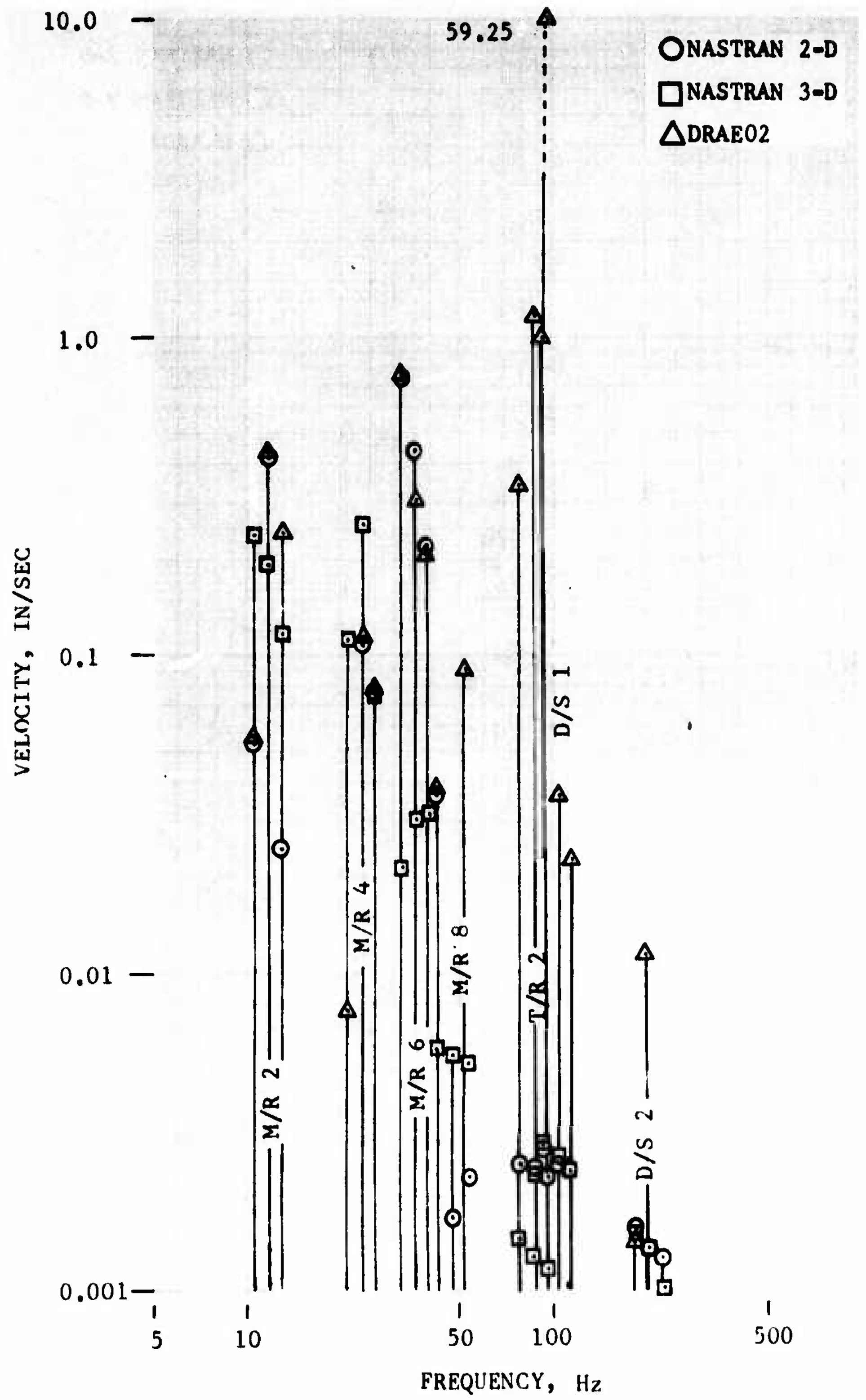

Figure 34. Comparison of NASTRAN and DRAE02 (Mobility) Computed Engine Gearbox Vertical Velocity, Simulated 90-Knot Level Flight Response.

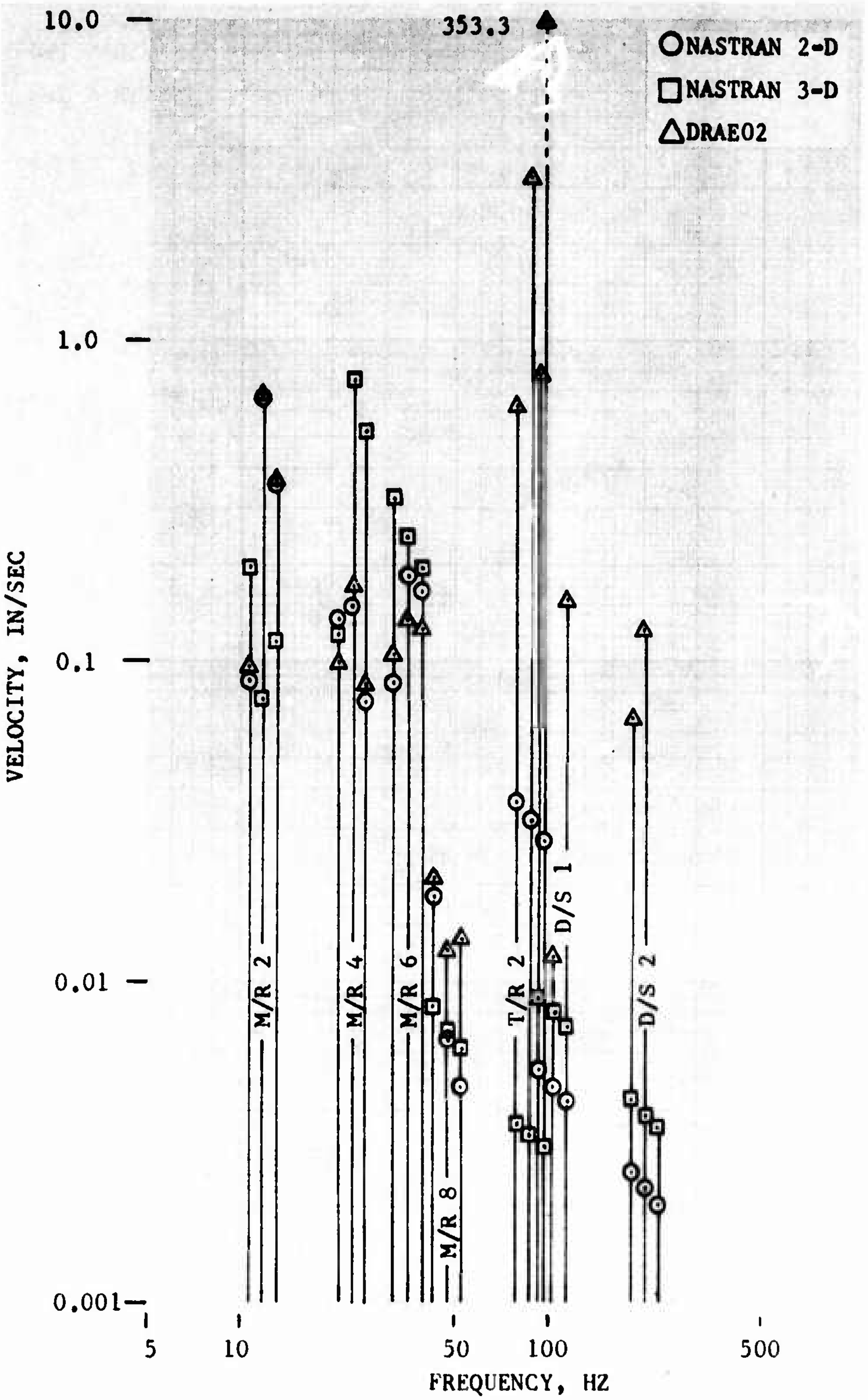

Figure 35. Comparison of NASTRAN and DRAE02 (Mobility) Computed Engine Forward Compressor Vertical Velocity, Simulated 110-Knot Level Flight Response.

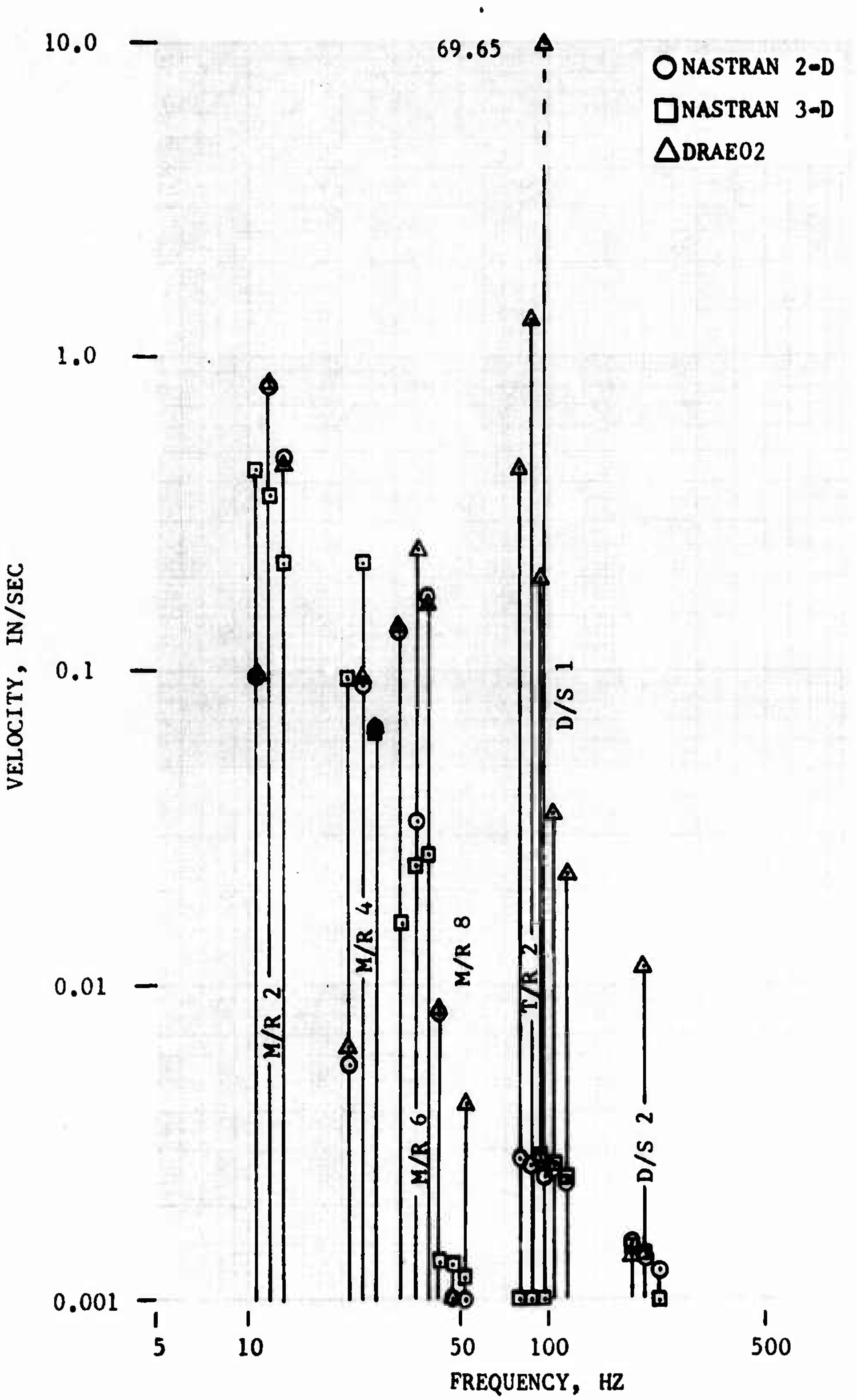

Figure 36. Comparison of NASTRAN and DRAE02 (Mobility) Computed Engine Gearbox Vertical Velocity, Simulated 110-Knot Level Flight Response.

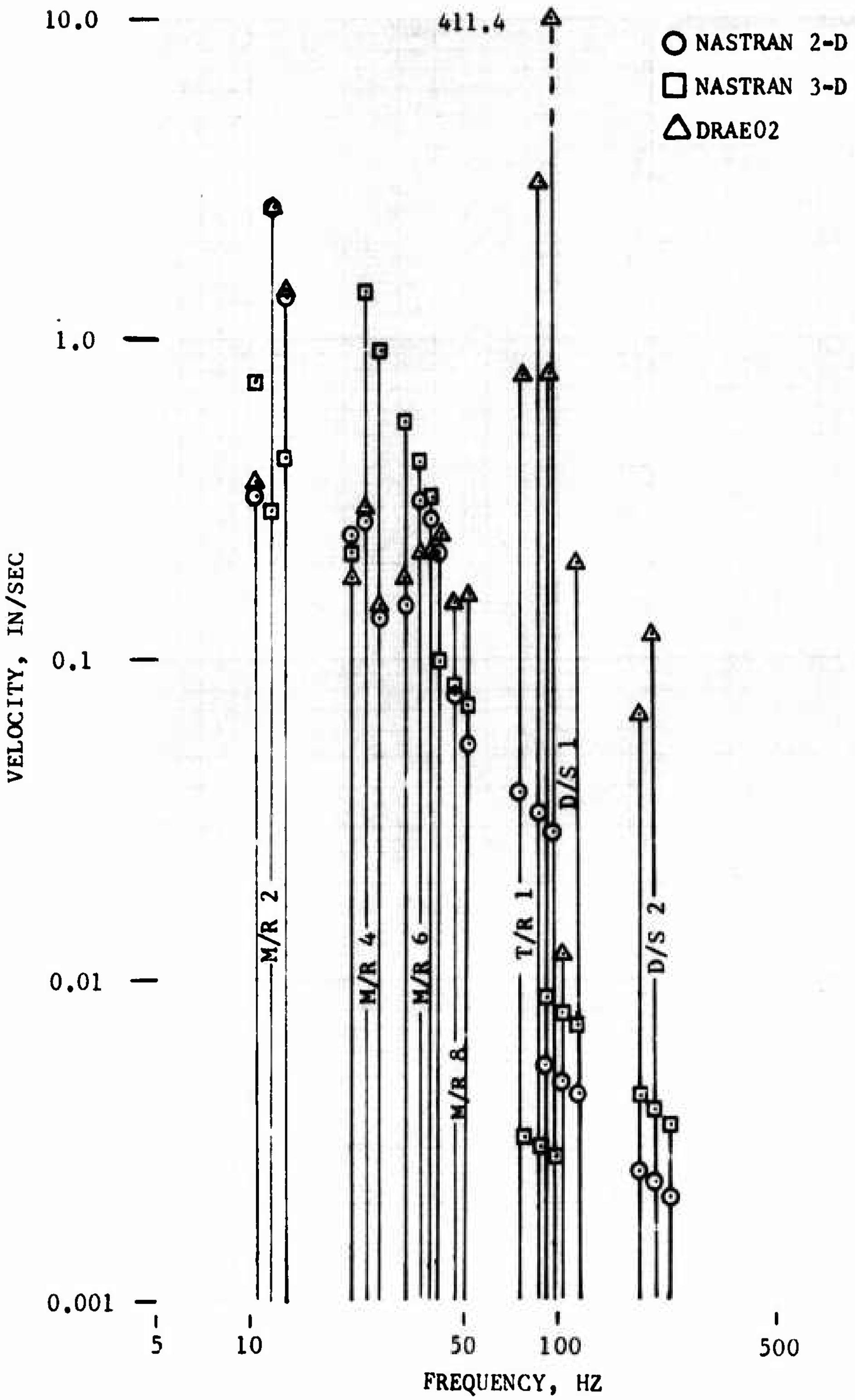

Figure 37. Comparison of NASTRAN and DRAE02 (Mobility) Computed Engine Forward Compressor Vertical Velocity, Simulated 130-Knot Level Flight Response.

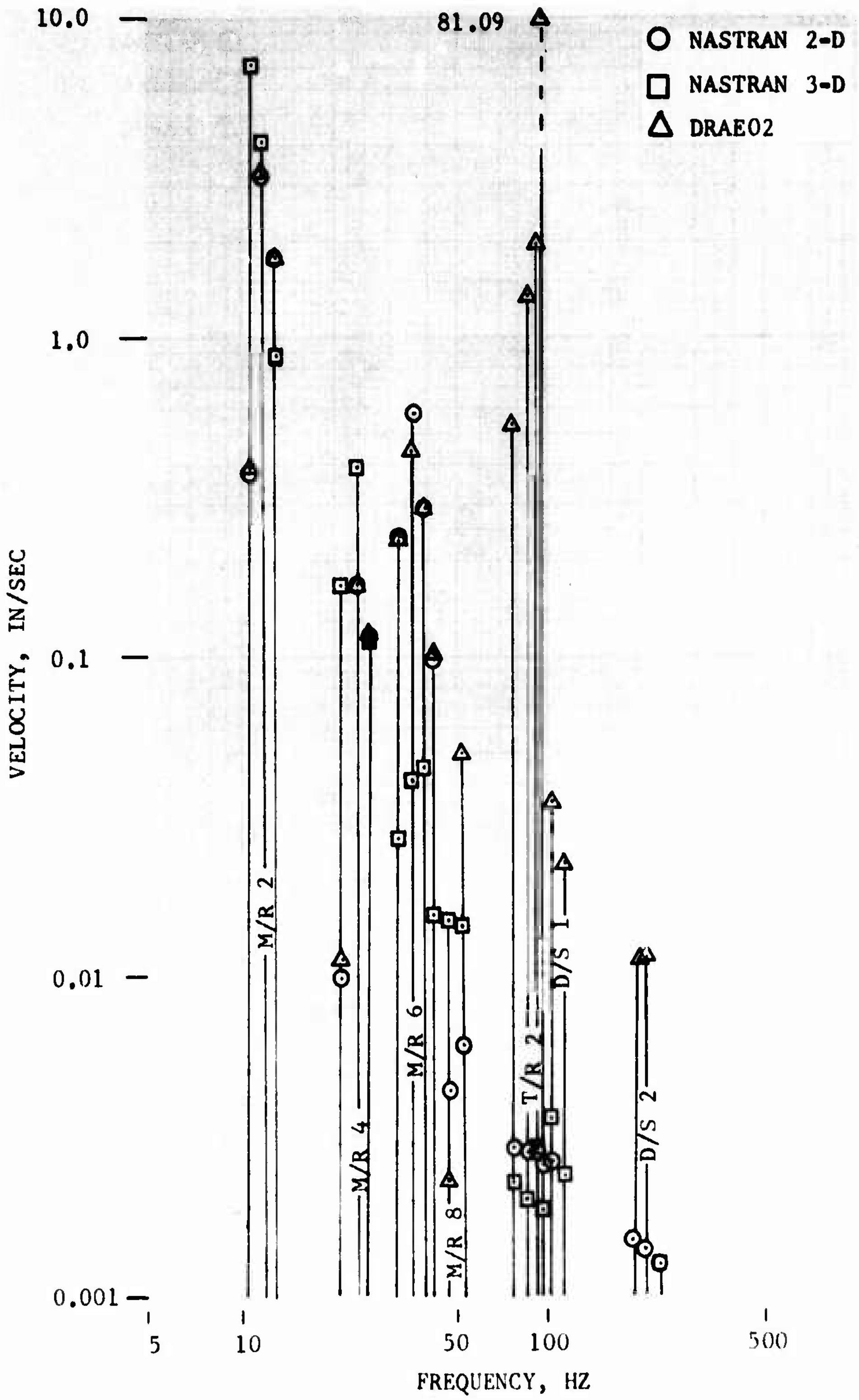

Figure 38. Comparison of NASTRAN and DRAE02 (Mobility) Computed Engine Gearbox Vertical Velocity, Simulated 130-Knot Level Flight Response.

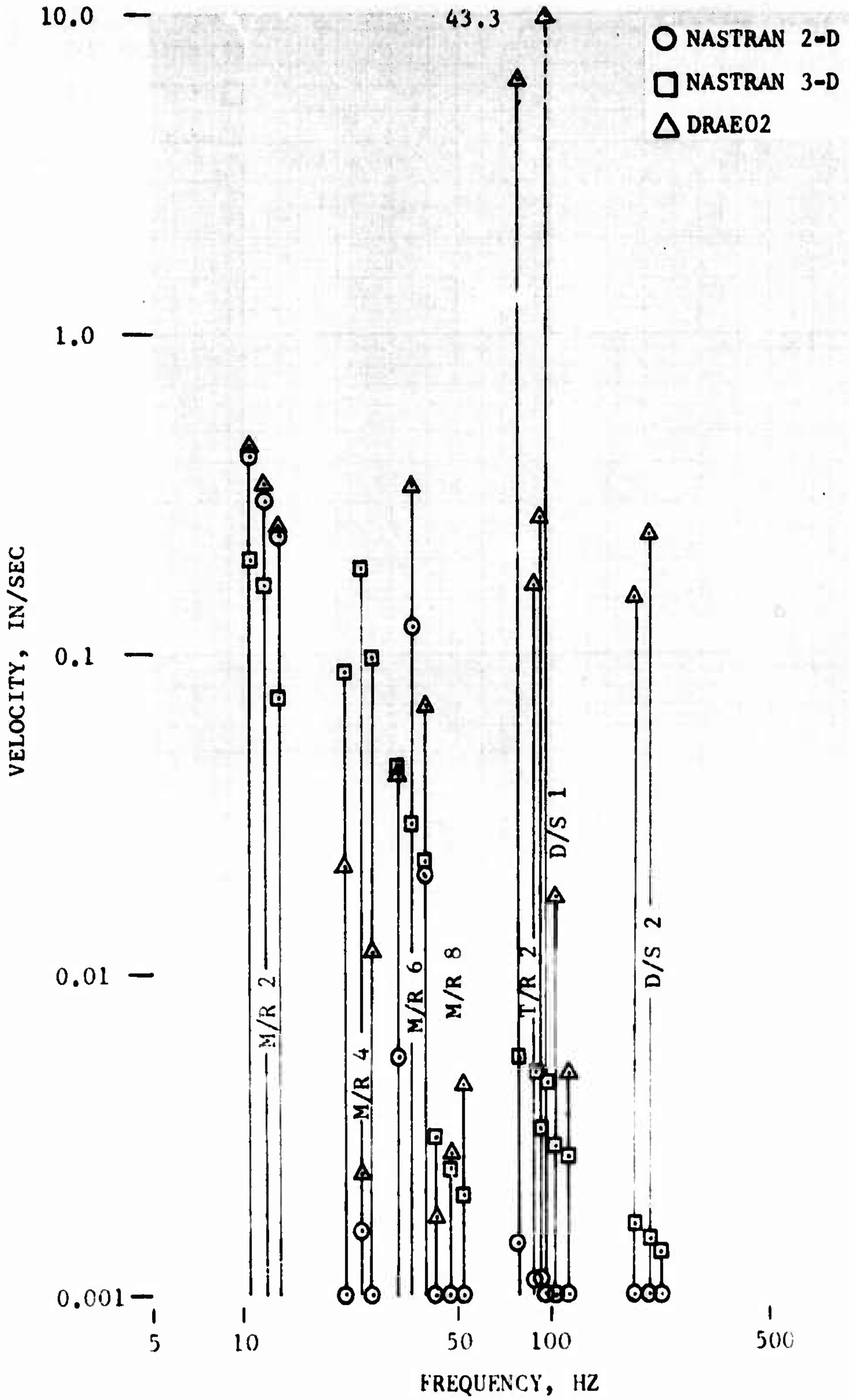

Figure 39. Comparison of NASTRAN and DRAE02 (Mobility) Computed Engine Forward Compressor Lateral Velocity, Simulated 90-Knot Level Flight Response.

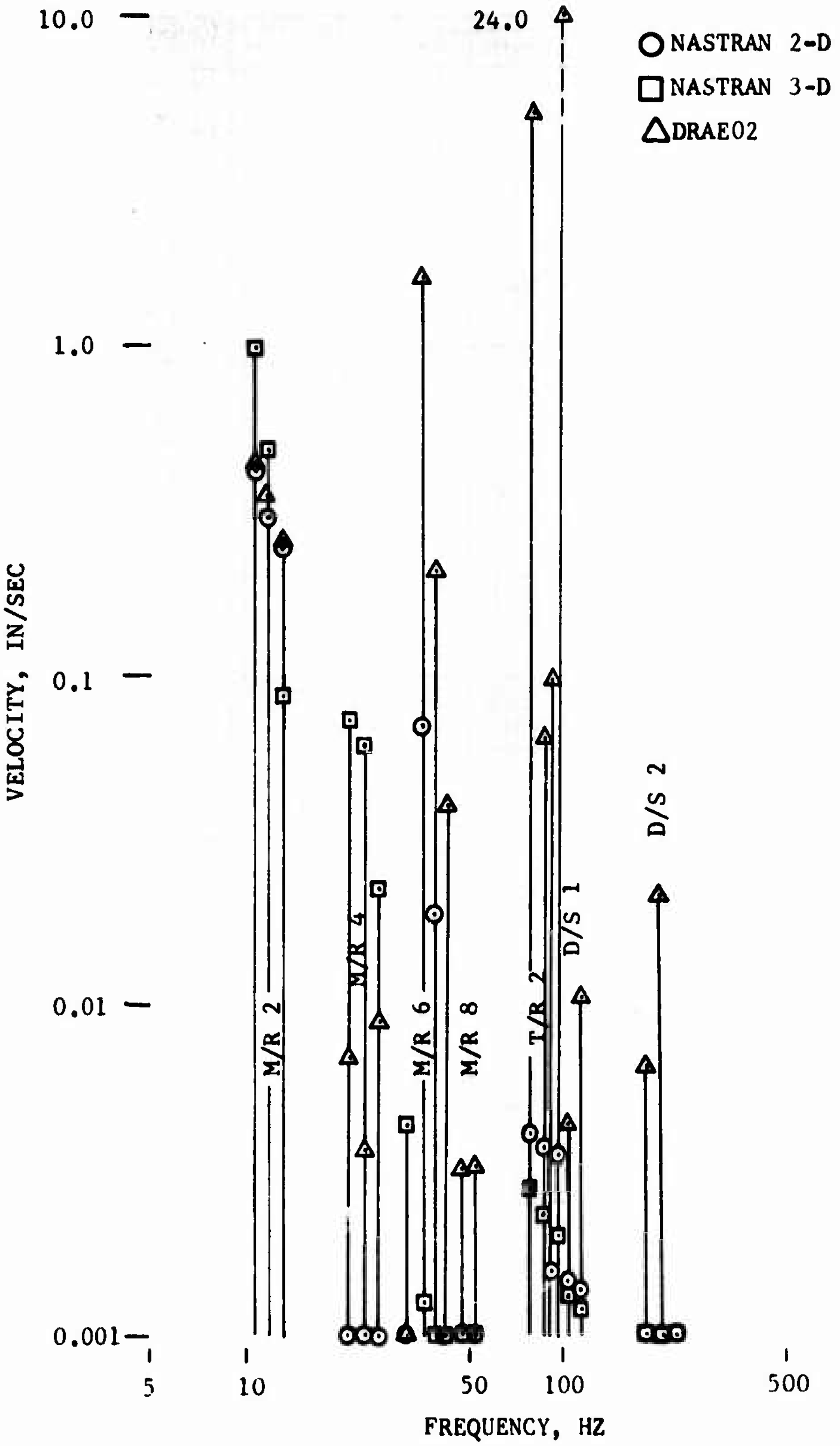

Figure 40. Comparison of NASTRAN and DRAE02 (Mobility) Computed Engine Gearbox Lateral Velocity, Simulated 90-Knot Level Flight Response.

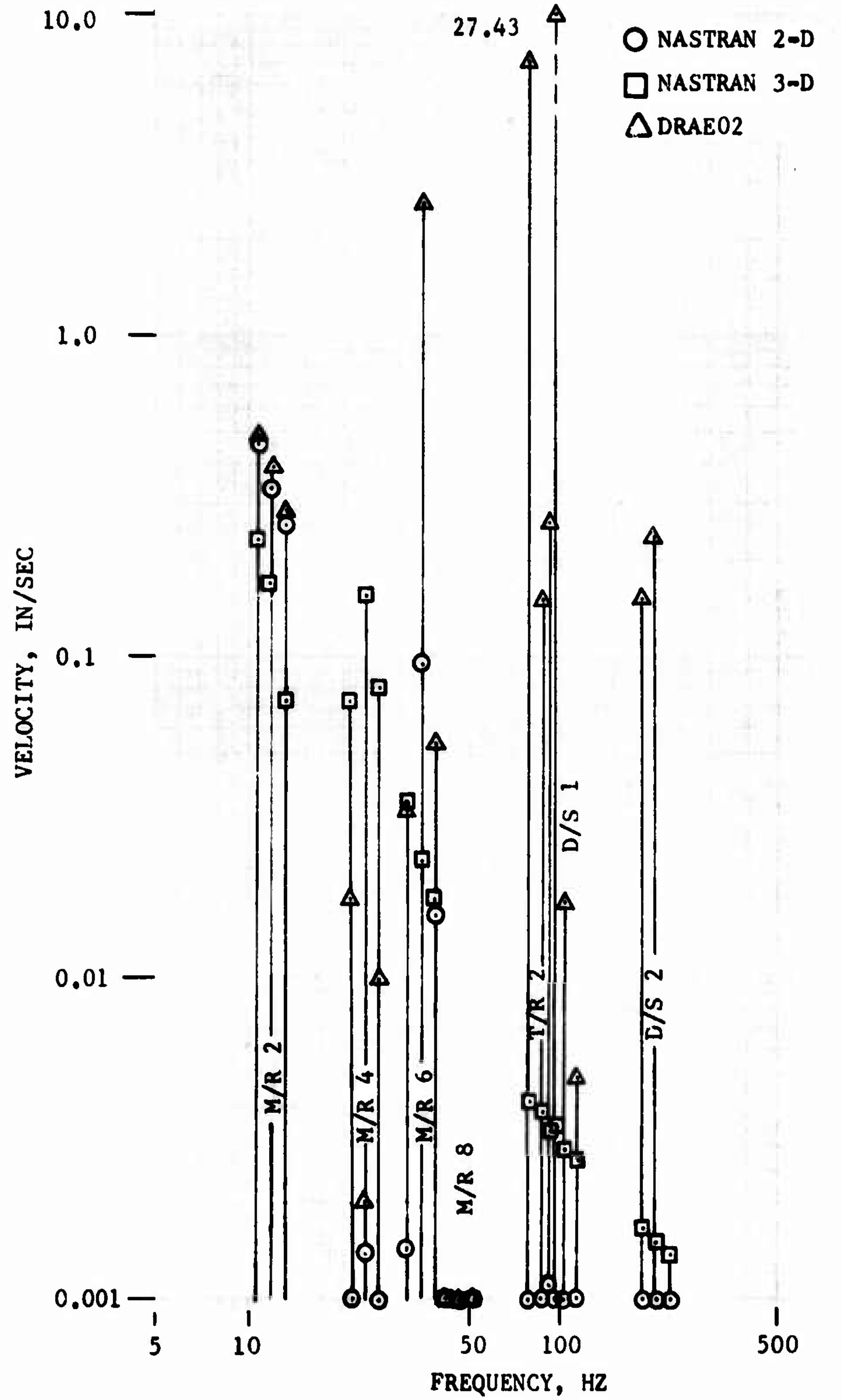

Figure 41. Comparison of NASTRAN and DRAE02 (Mobility) Computed Engine Forward Compressor Lateral Velocity, Simulated 110-Knot Level Flight Response.

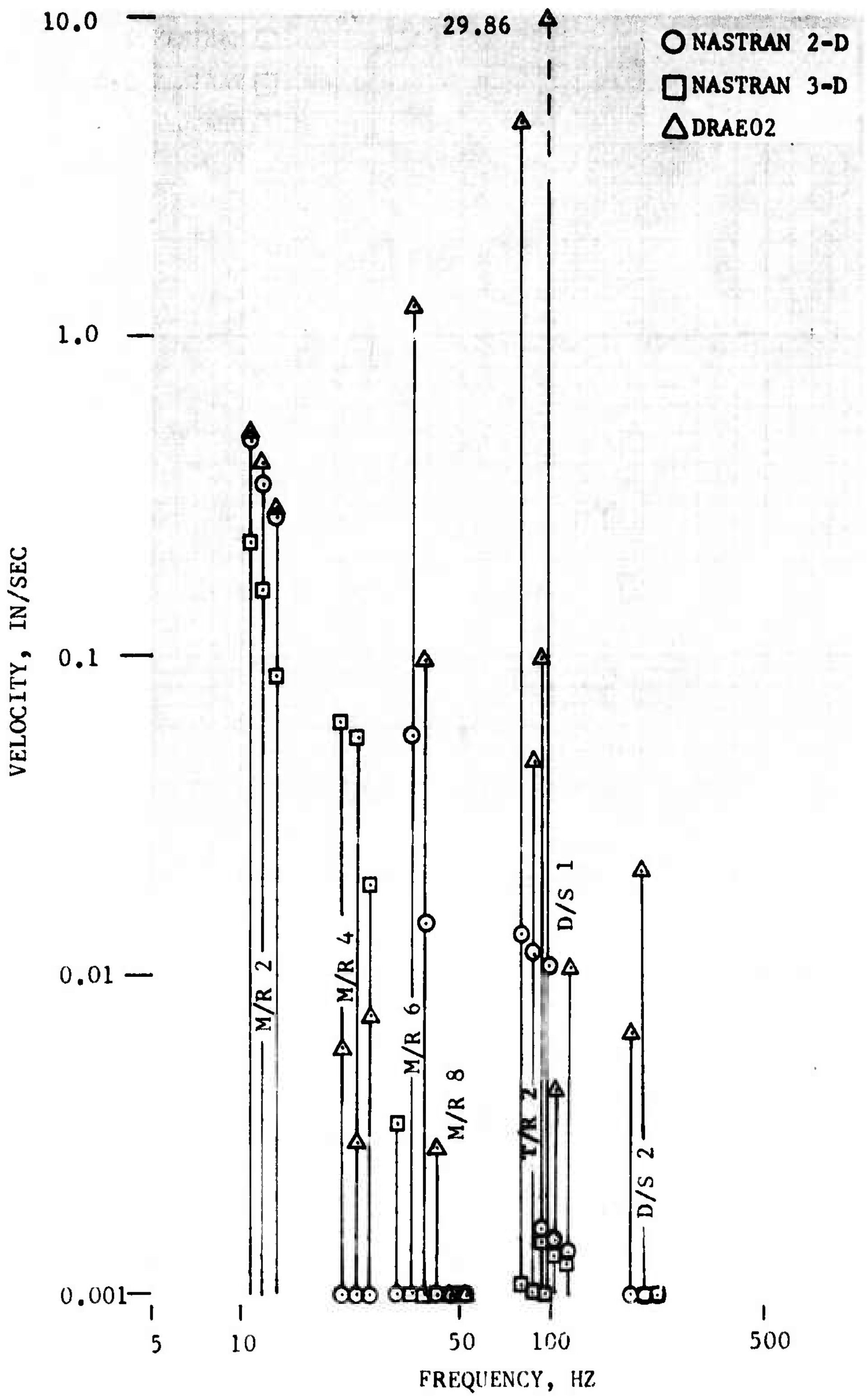

Figure 42. Comparison of NASTRAN and DRAE02 (Mobility) Computed Engine Gearbox Lateral Velocity, Simulated 110-Knot Level Flight Response.

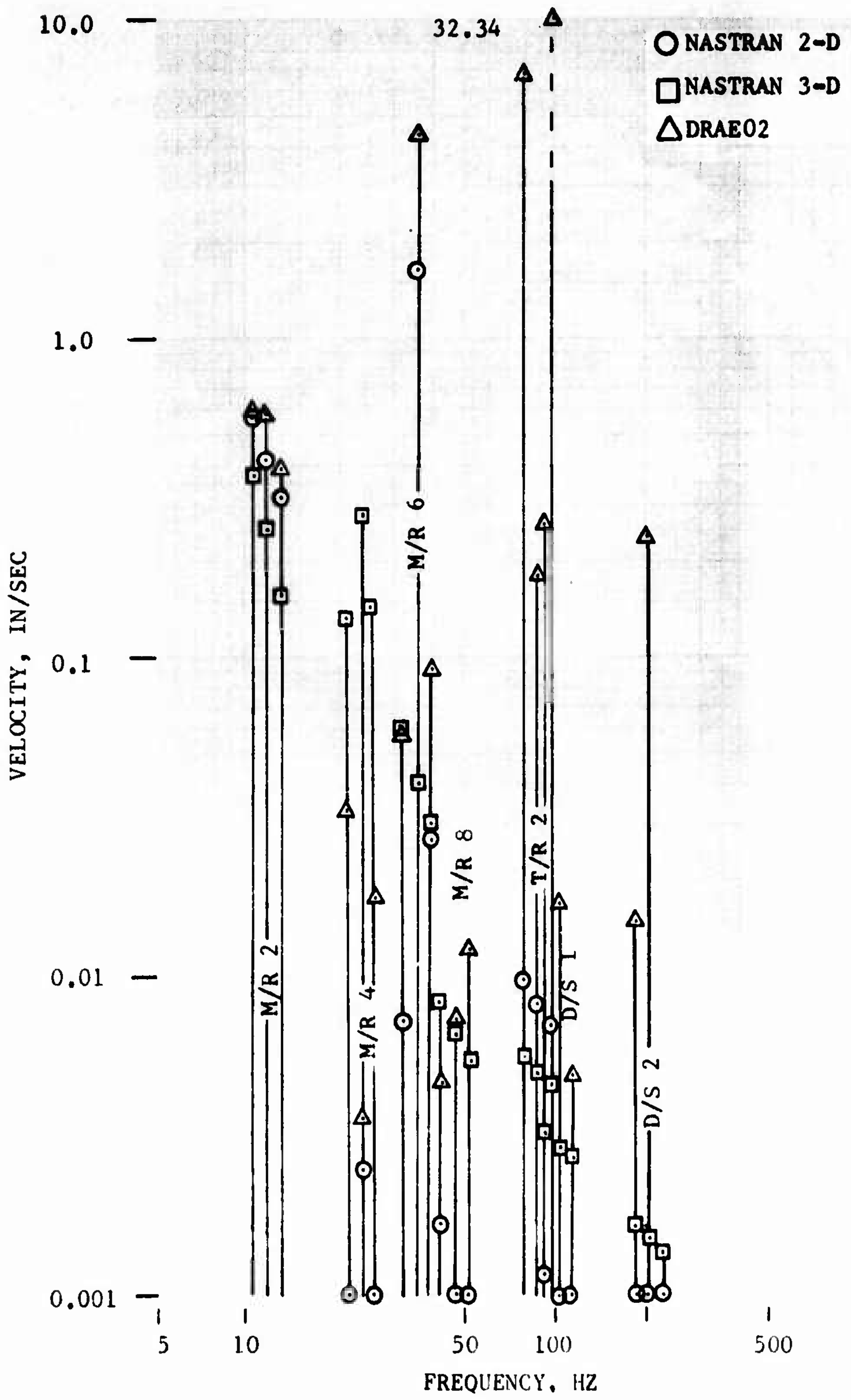

Figure 43. Comparison of NASTRAN and DRAE02 (Mobility) Computed Engine Forward Compressor Lateral Velocity, Simulated 130-Knot Level Flight Response.

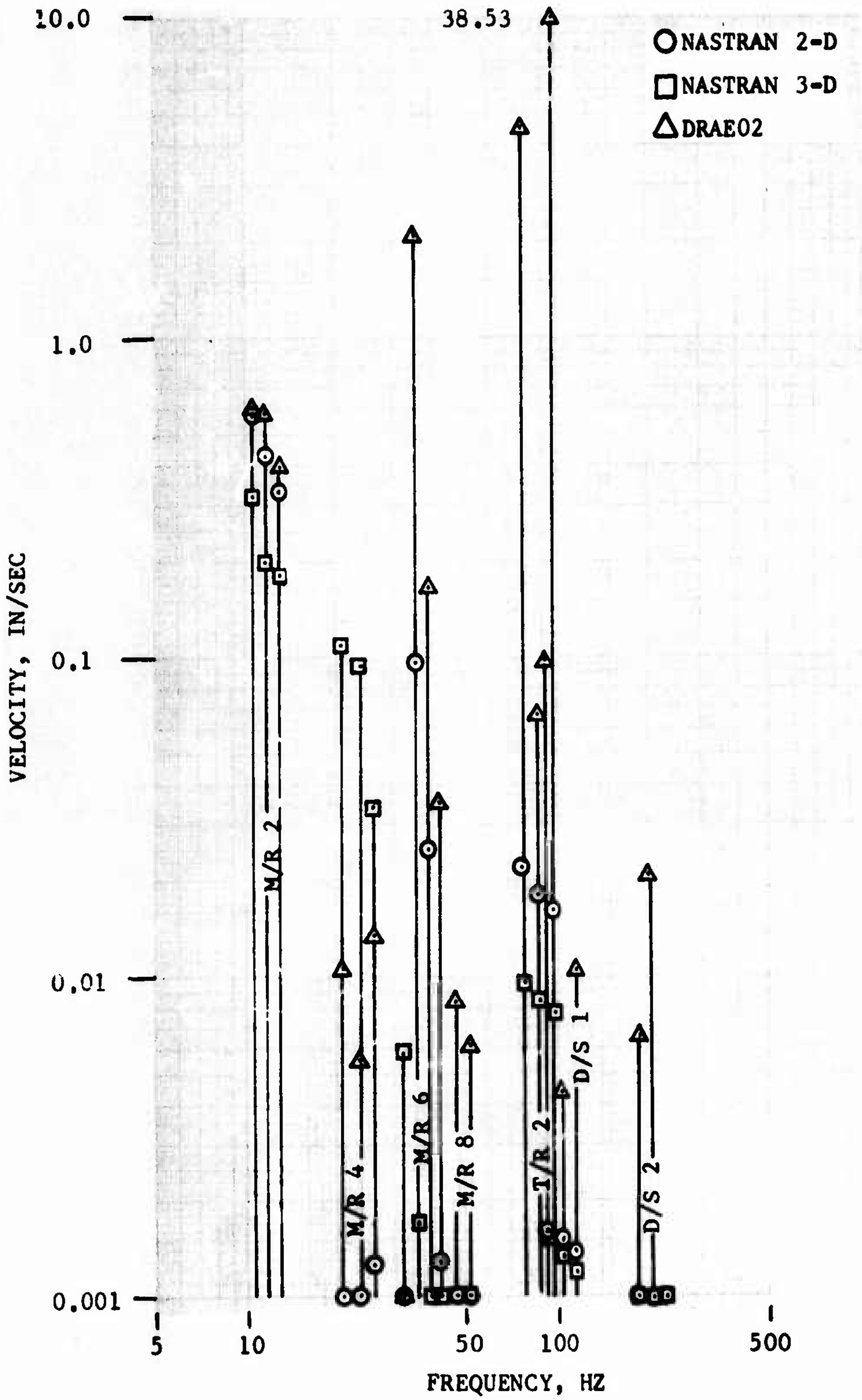

Figure 44. Comparison of NASTRAN and DRAE02 (Mobility) Computed Engine Gearbox Lateral Velocity, Simulated 130-Knot Level Flight Response.

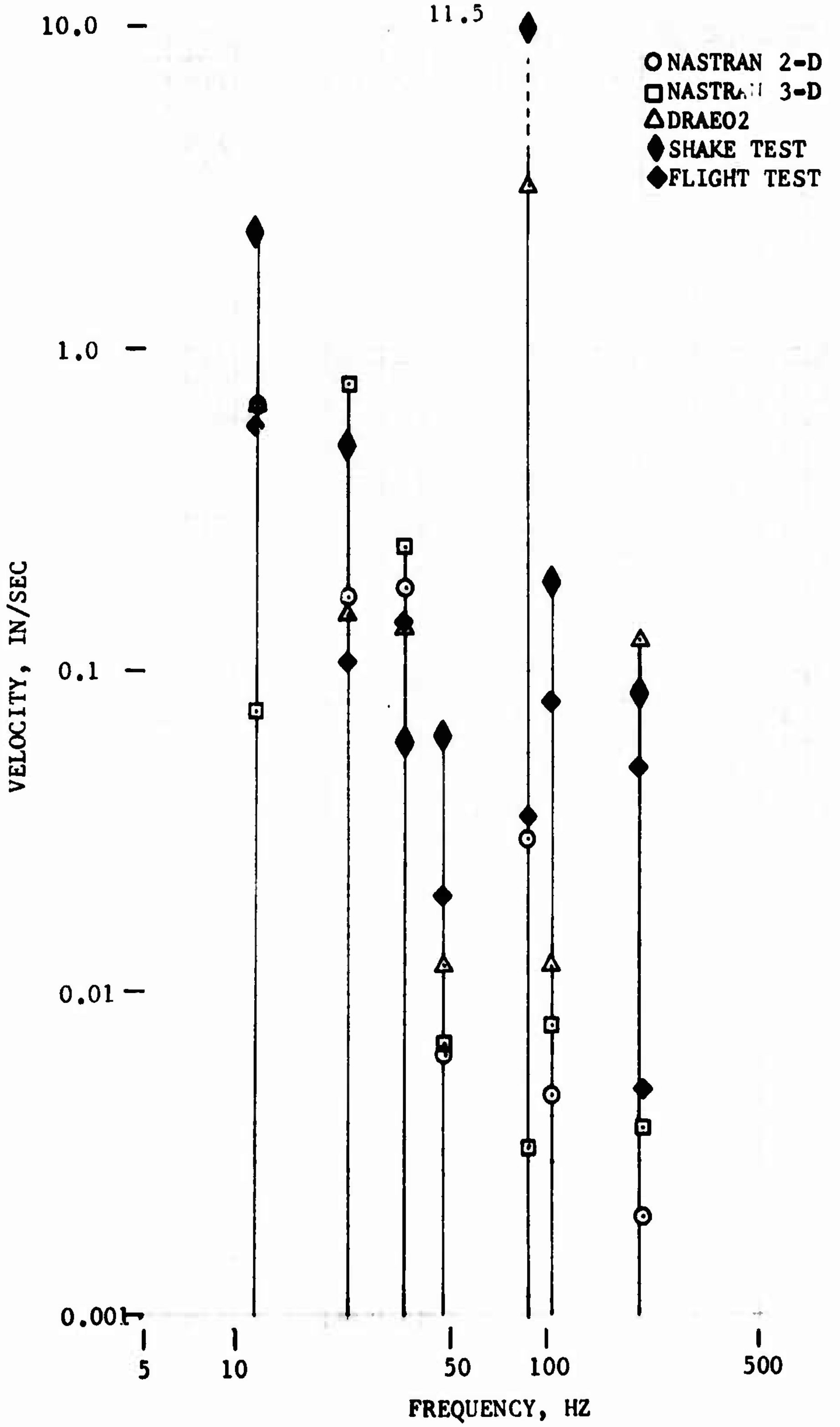

Figure 45. Comparison of Analytical and Test Engine Velocities for Simulated 110-Knot Level Flight Forces, Forward Compressor Vertical Response.

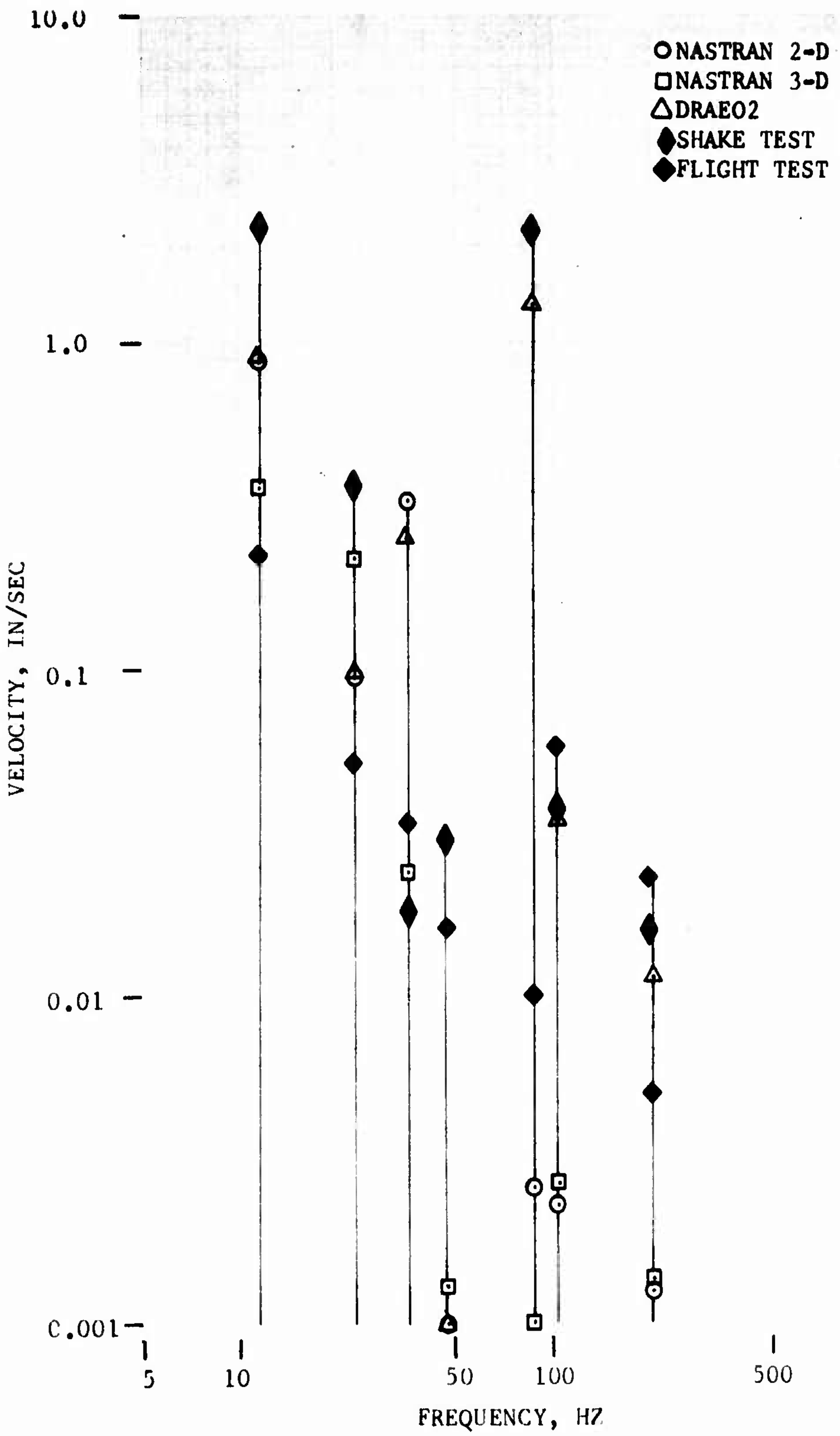

Figure 46. Comparison of Analytical and Test Engine Velocities for Simulated 110-Knot Level Flight Forces, Gearbox Vertical Response.

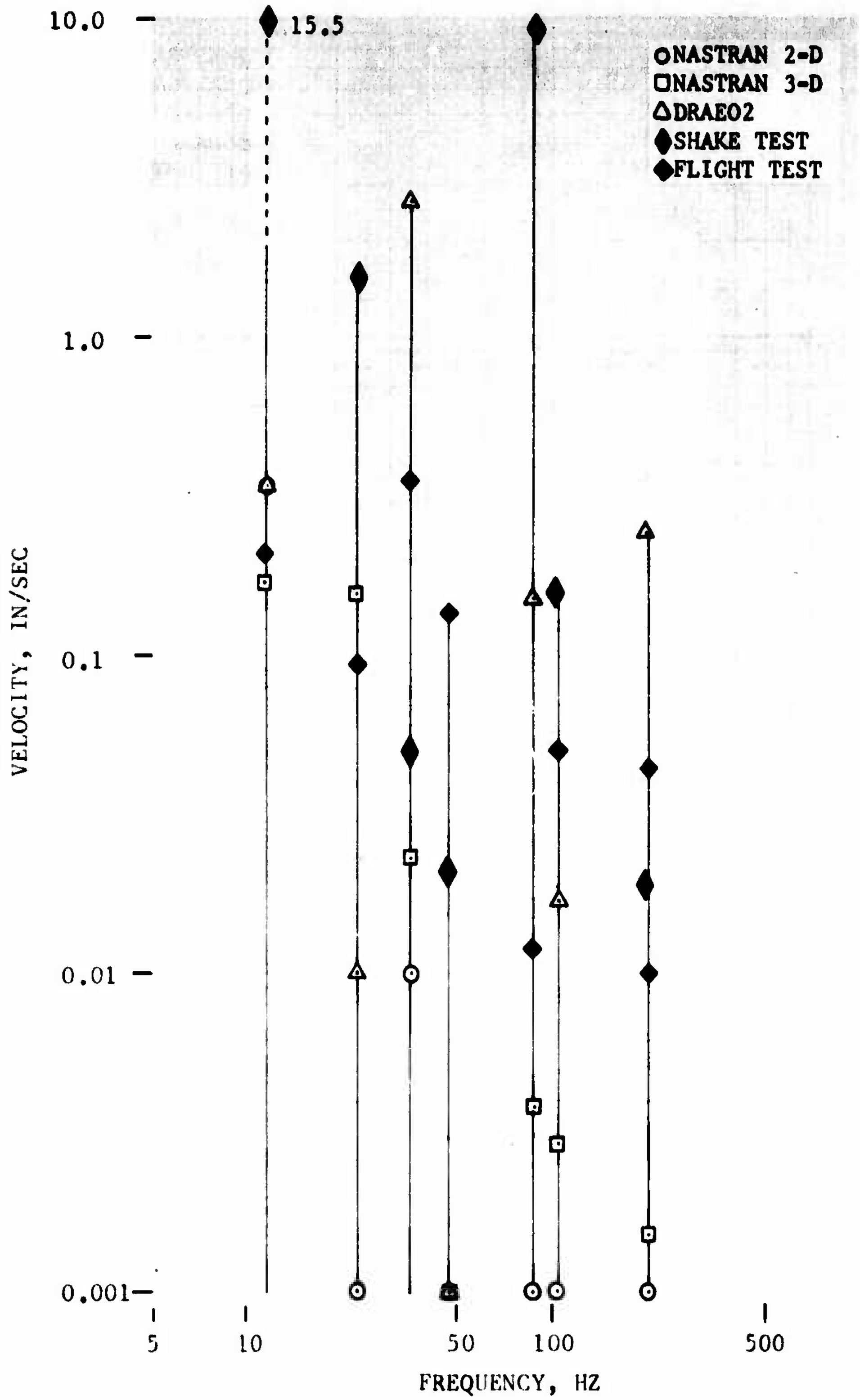

Figure 47. Comparison of Analytical and Test Engine Velocities for Simulated 110-Knot Level Flight Forces, Turbine Midsplit Vertical Response.

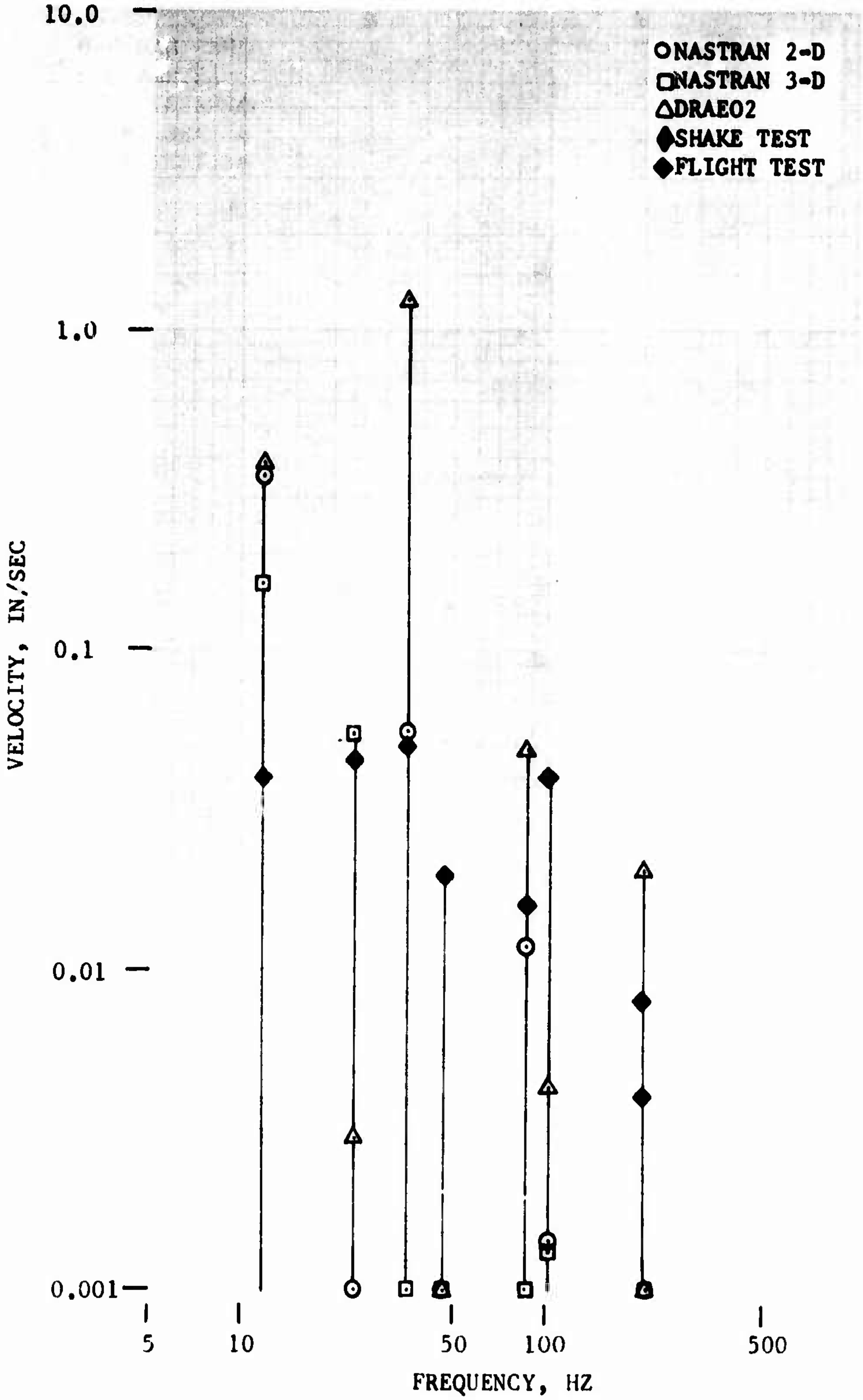

Figure 48. Comparison of Analytical and Test Engine Velocities for Simulated 110-Knot Level Flight Forces, Fuel Nozzle Vertical Response.

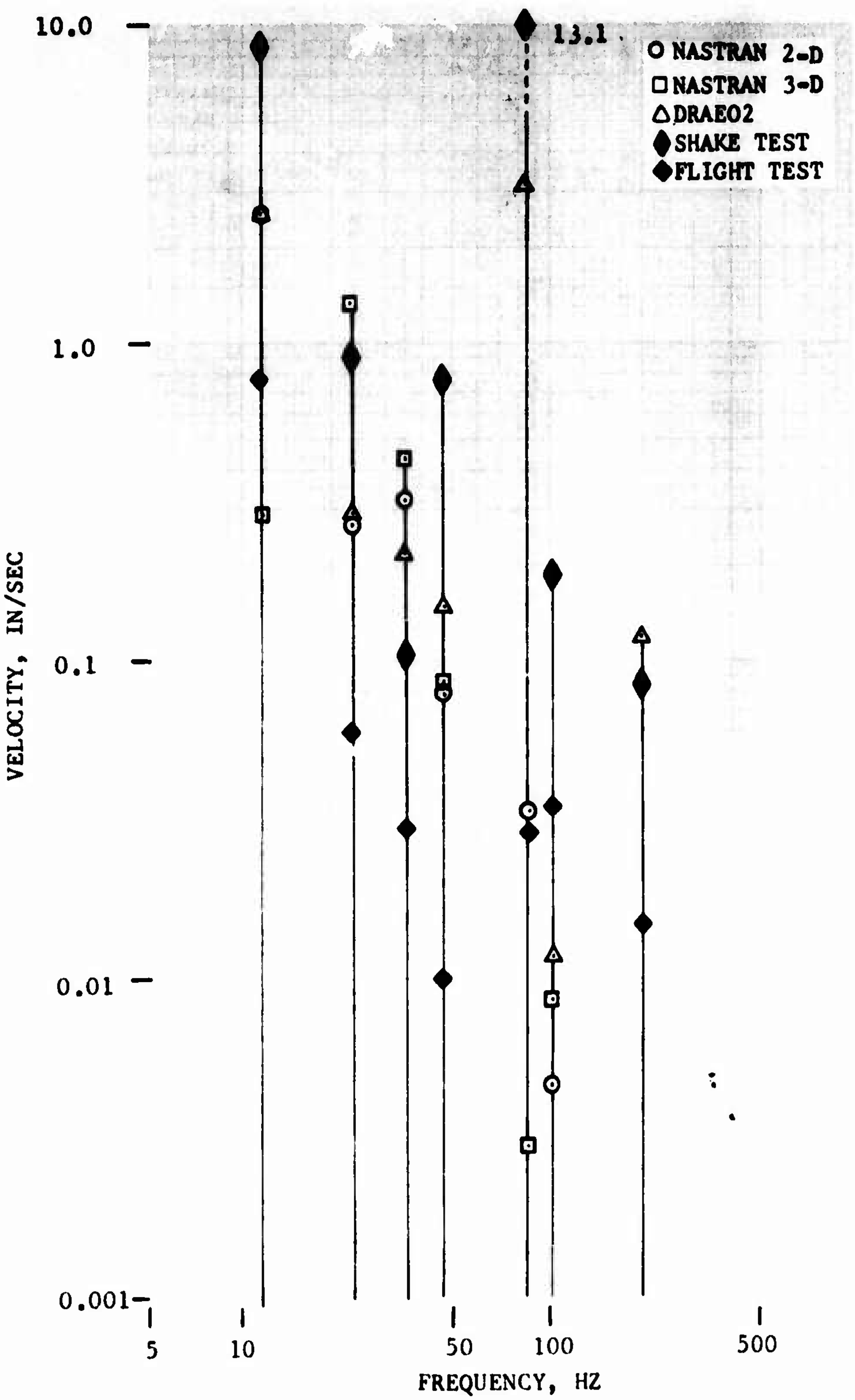

Figure 49. Comparison of Analytical and Test Engine Velocities for Simulated 110-Knot Level Flight Forces, Forward Compressor Lateral Response.

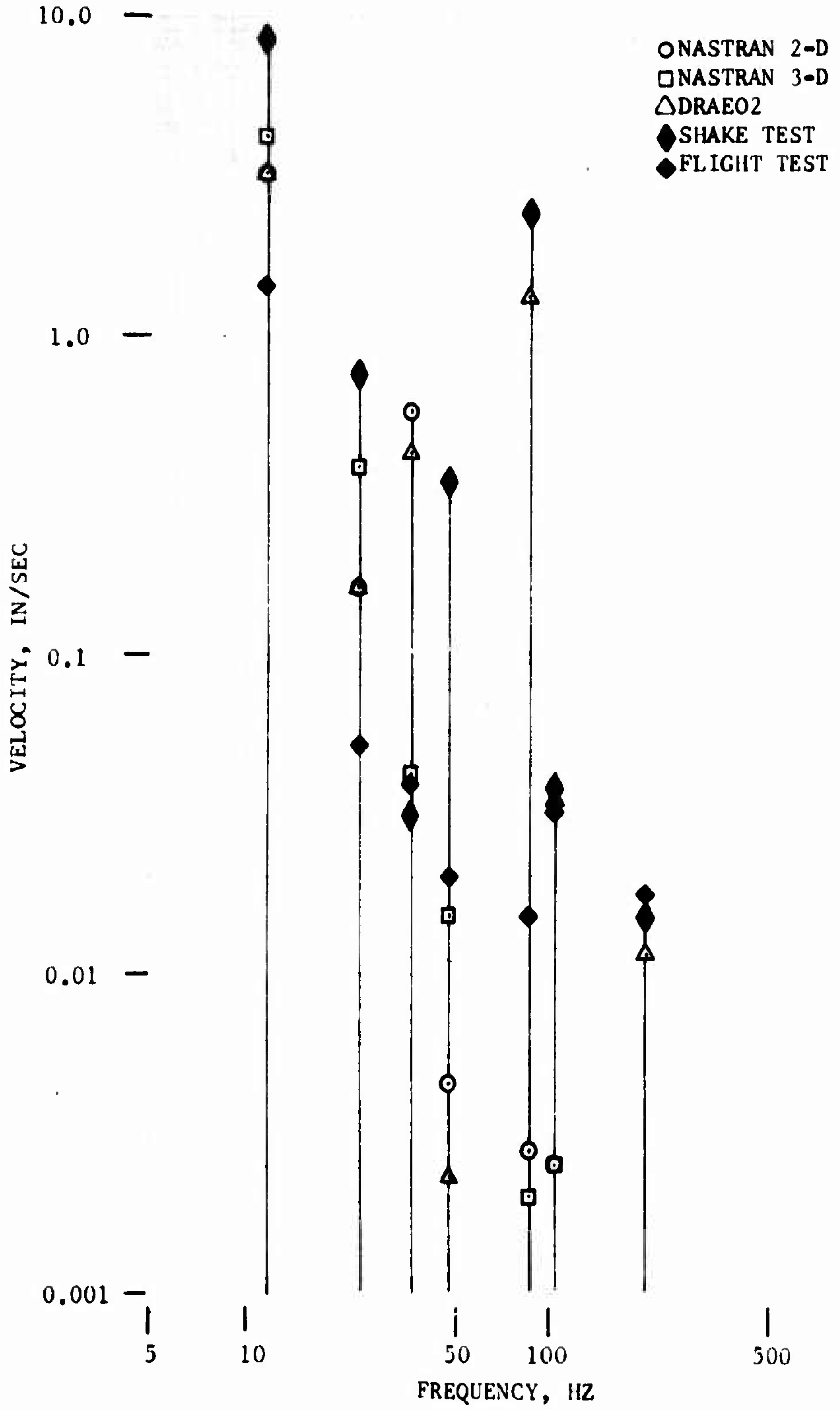

Figure 50. Comparison of Analytical and Test Engine Velocities for Simulated 110-Knot Level Flight Forces, Gearbox Lateral Response.

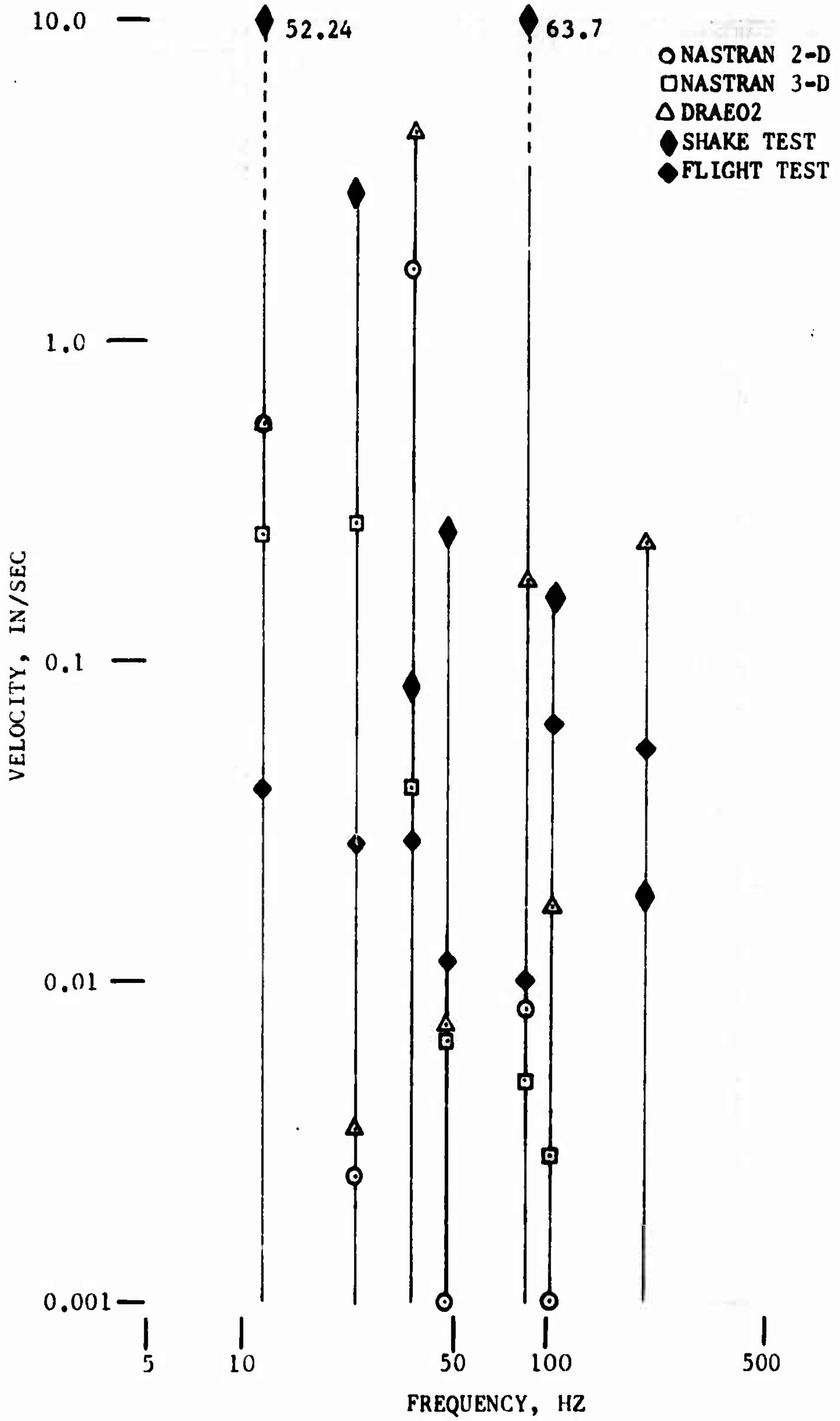

Figure 51. Comparison of Analytical and Test Engine Velocities for Simulated 110-Knot Level Flight Forces, Turbine Midsplit Lateral Response.

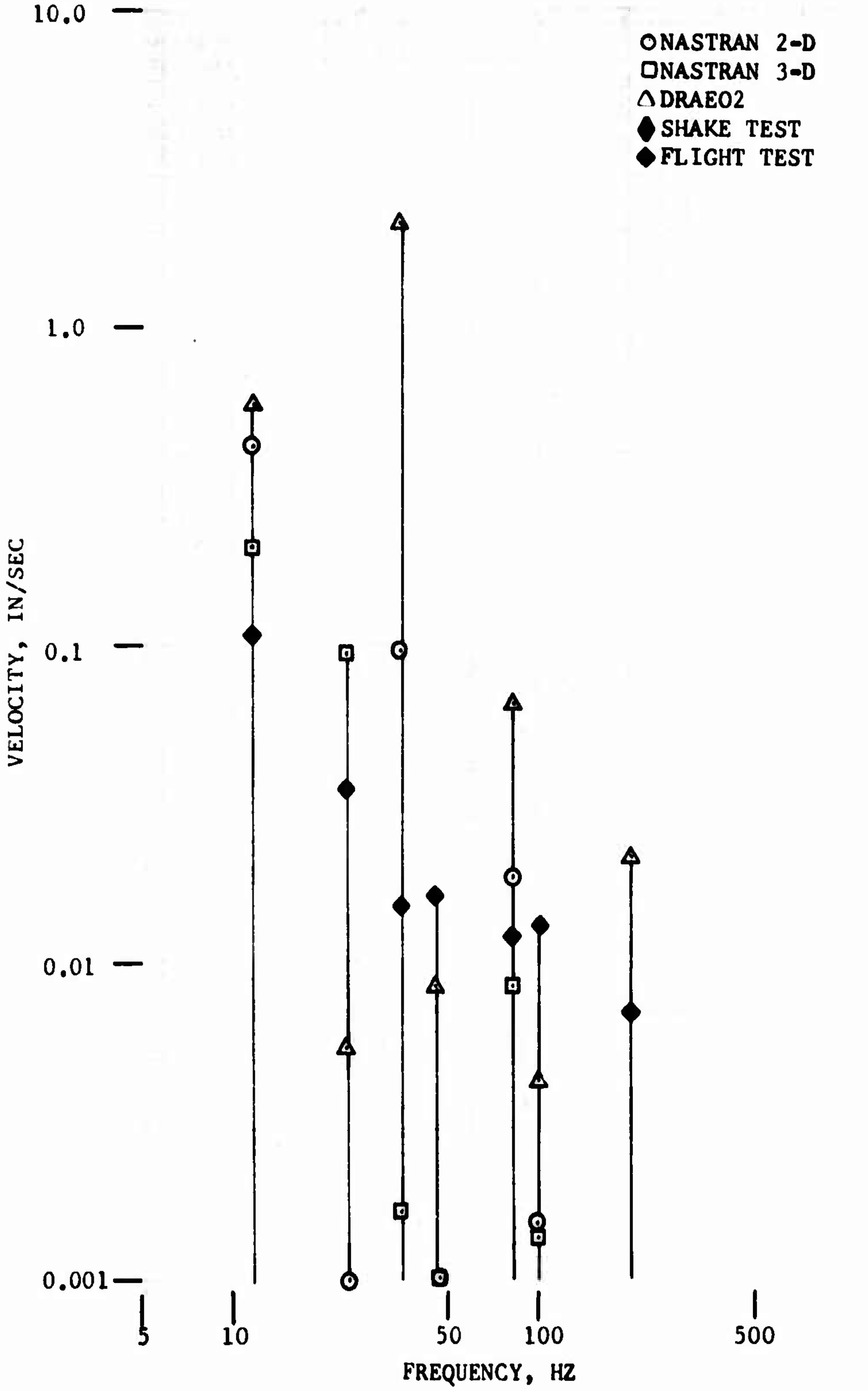

Figure 52. Comparison of Analytical and Test Engine Velocities for Simulated 110-Knot Level Flight Forces, Fuel Nozzle Lateral Response.

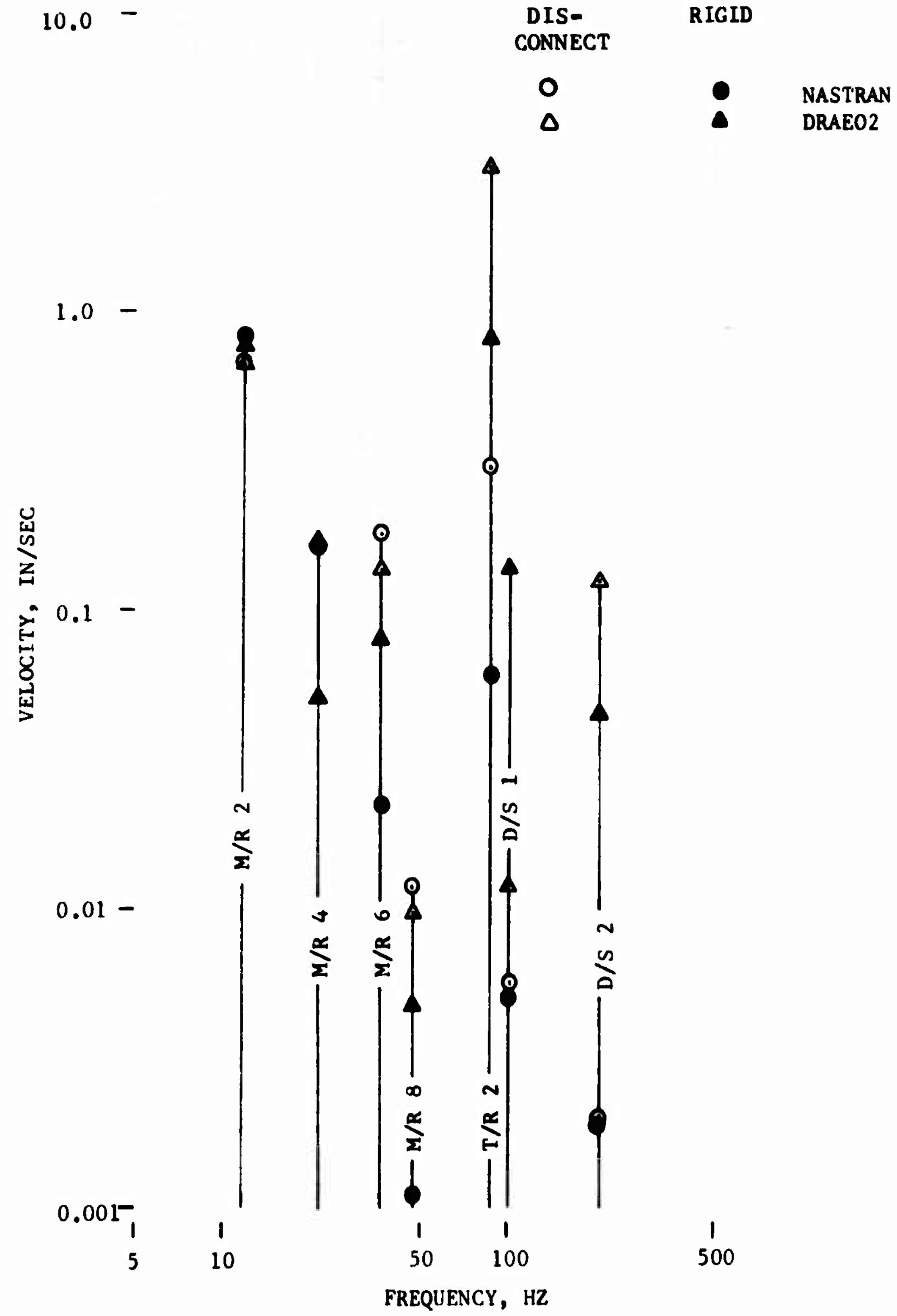

Figure 53. Comparison of Computed Engine Forward Compressor Vertical Velocities for Rigid and Disconnected Input Drive Shaft, 130-Knot Simulated Level Flight.

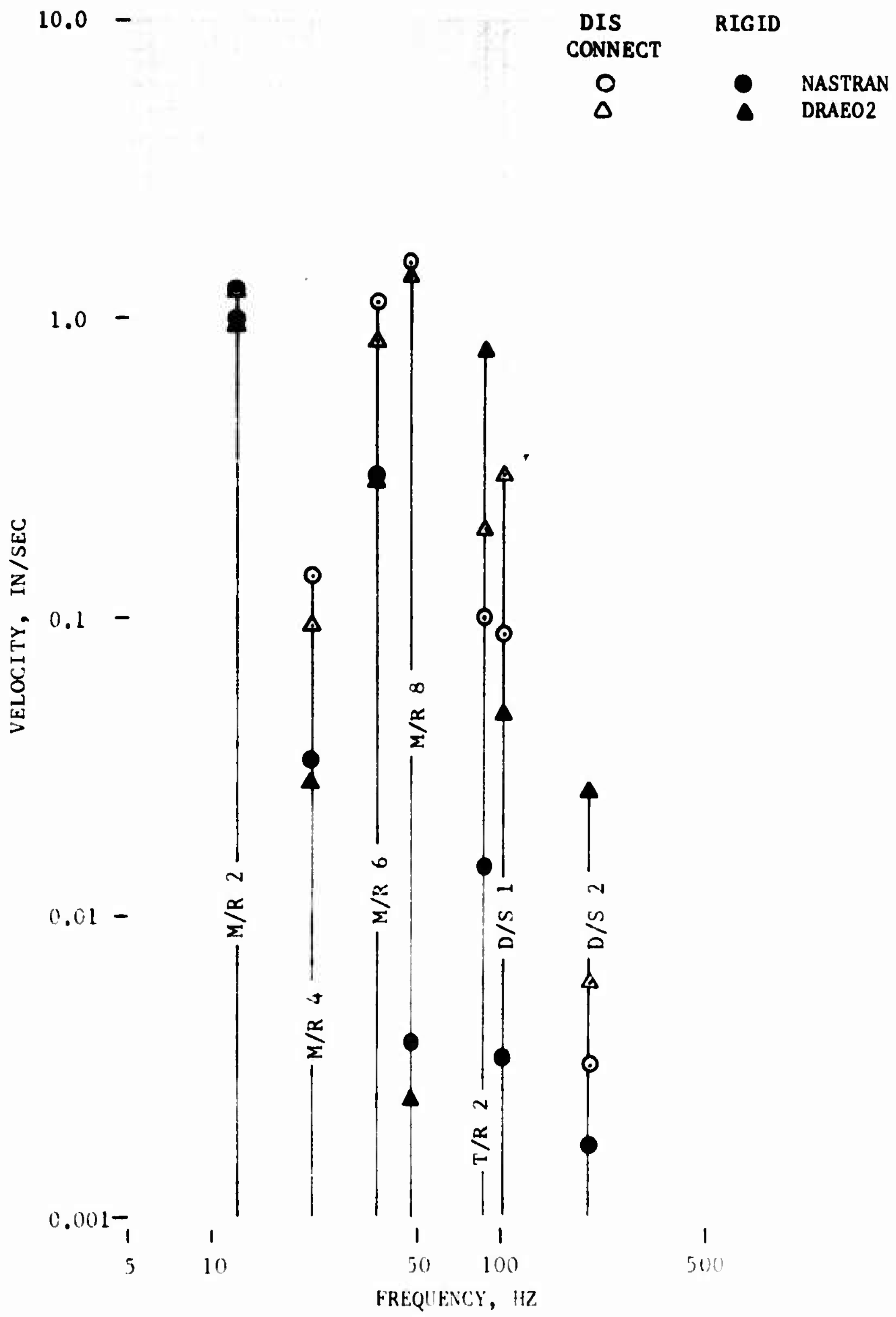

Figure 54. Comparison of Computed Engine Gearbox Vertical Velocities for Rigid and Disconnected Input Drive Shaft, 130-Knot Simulated Level Flight.

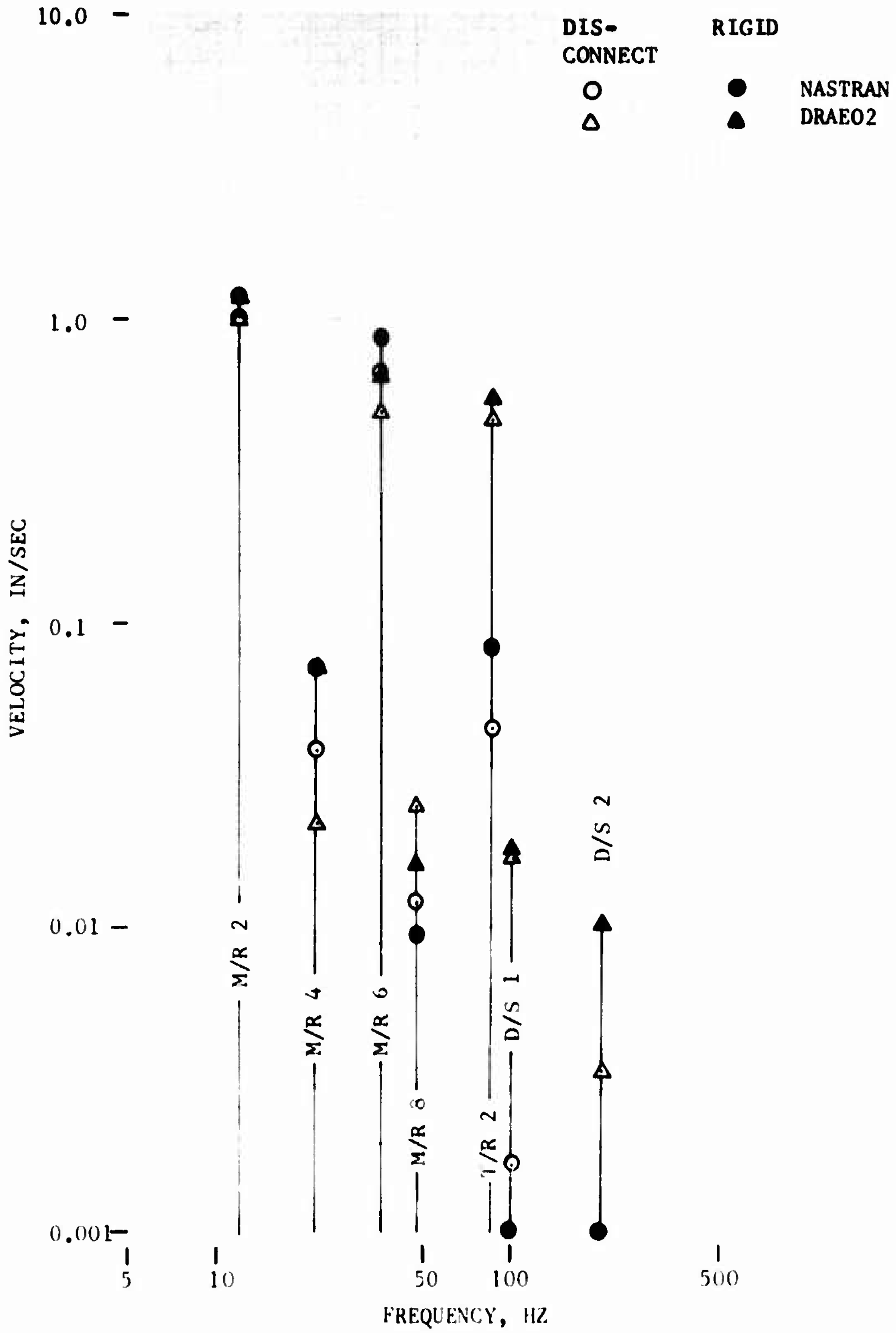

Figure 55. Comparison of Computed Engine Turbine Midsplit Vertical Velocities for Rigid and Disconnected Input Drive Shaft, 130-Knot Simulated Level Flight.

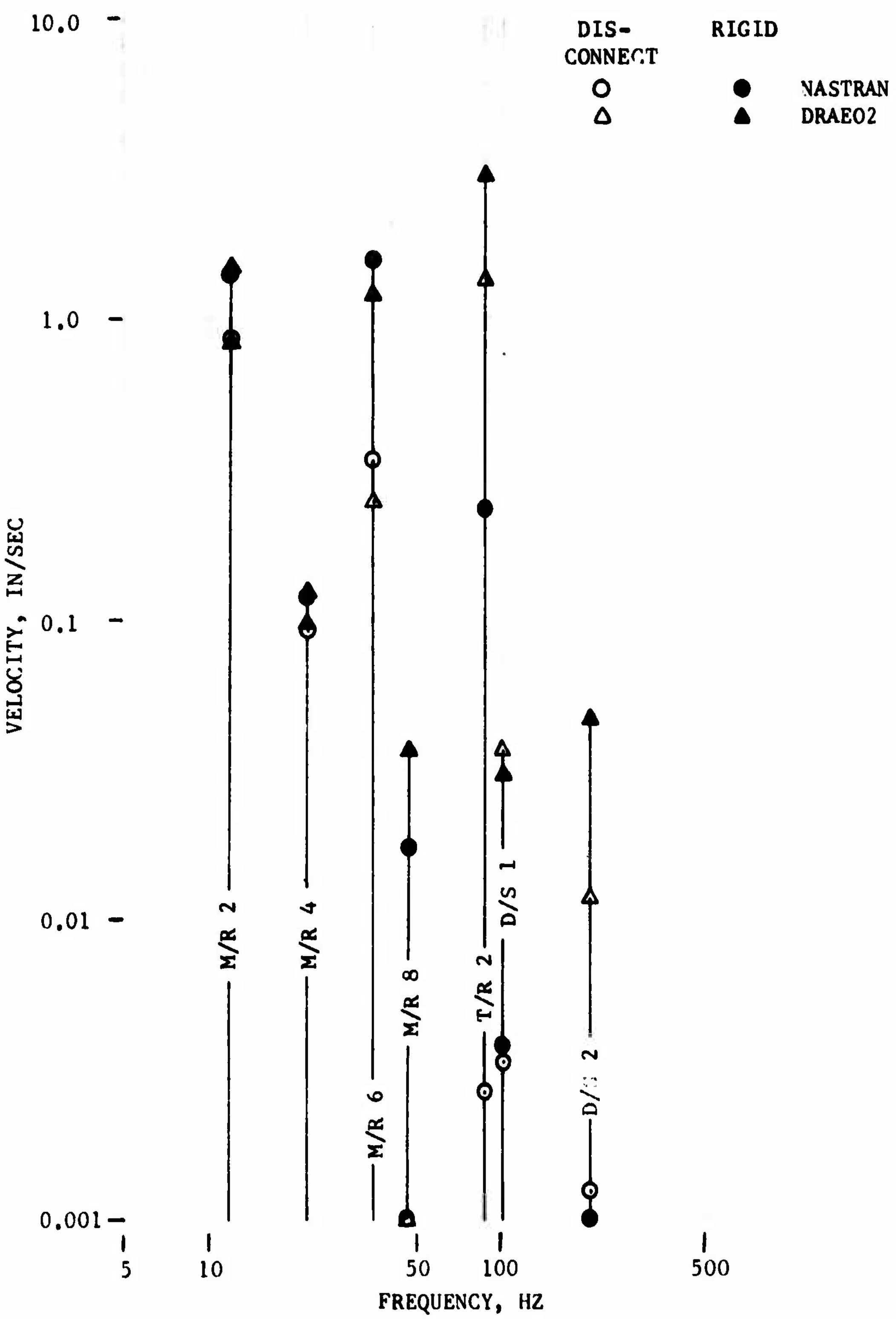

Figure 56. Comparison of Computed Engine Fuel Nozzle Vertical Velocities for Rigid and Disconnected Input Drive Shaft, 130-Knot Simulated Level Flight.

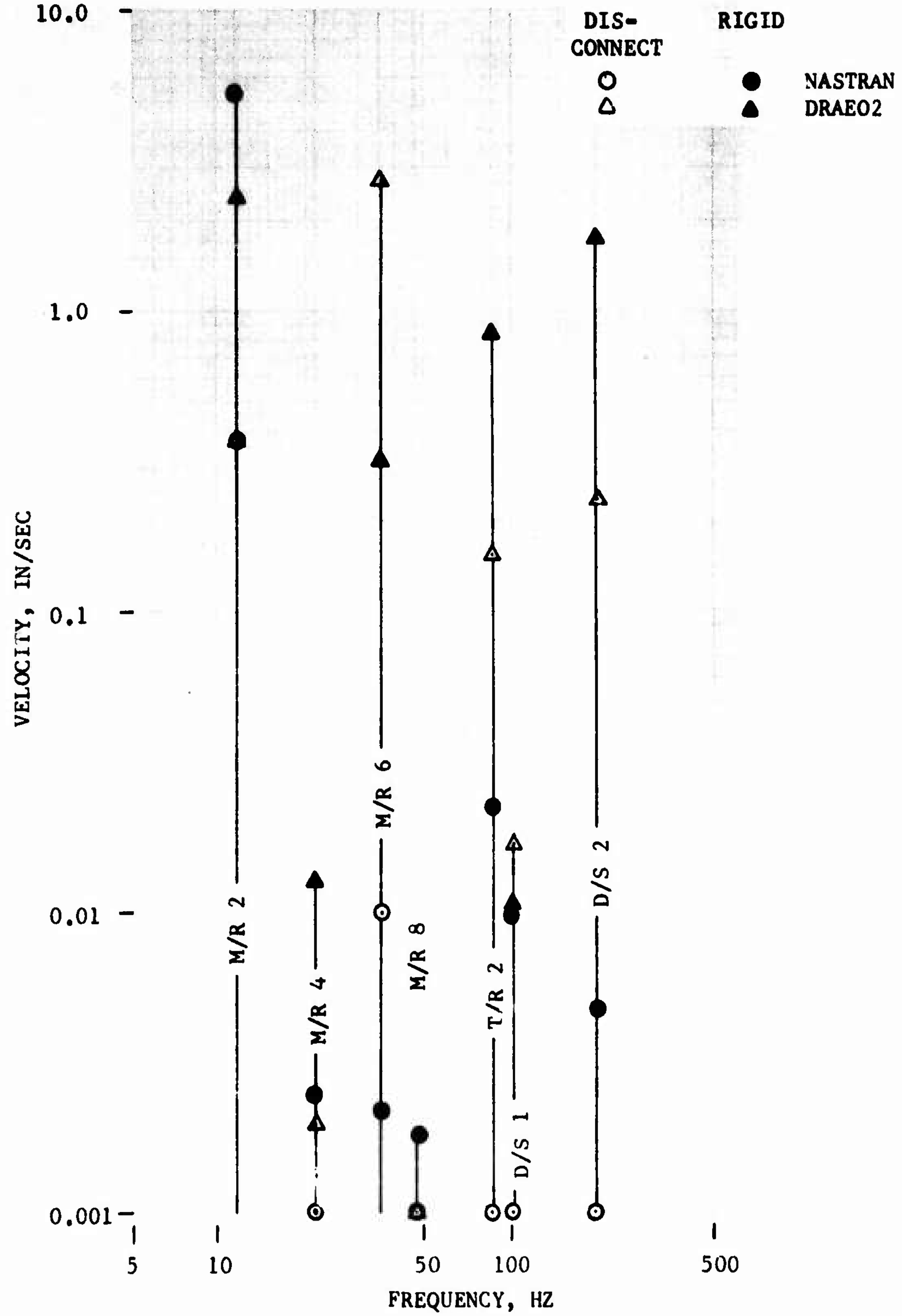

Figure 57. Comparison of Computed Engine Forward Compressor Lateral Velocities for Rigid and Disconnected Input Drive Shaft, 130-Knot Simulated Level Flight.

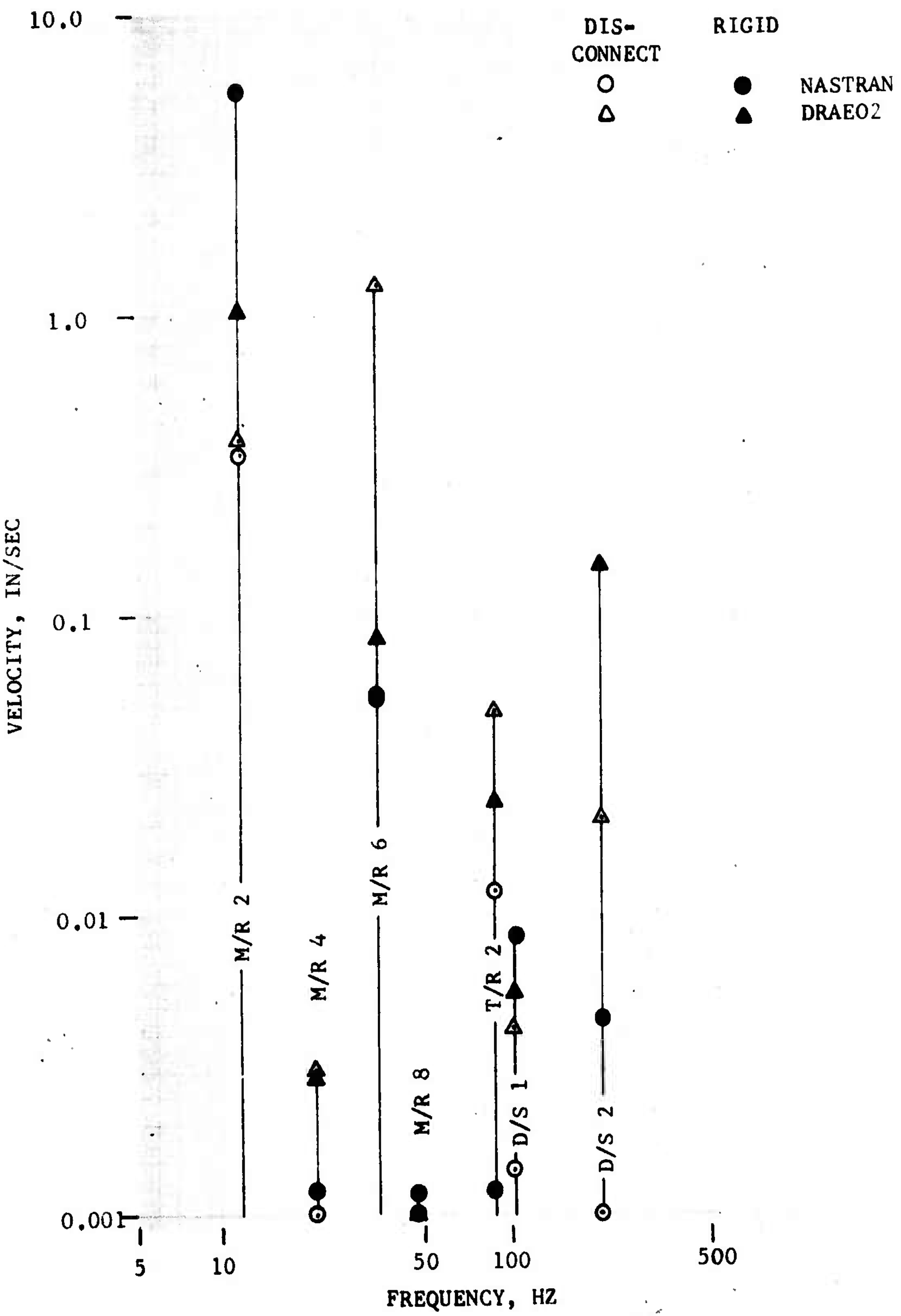

Figure 58. Comparison of Computed Engine Gearbox Lateral Velocities for Rigid and Disconnected Input Drive Shaft, 130-Knot Simulated Level Flight.

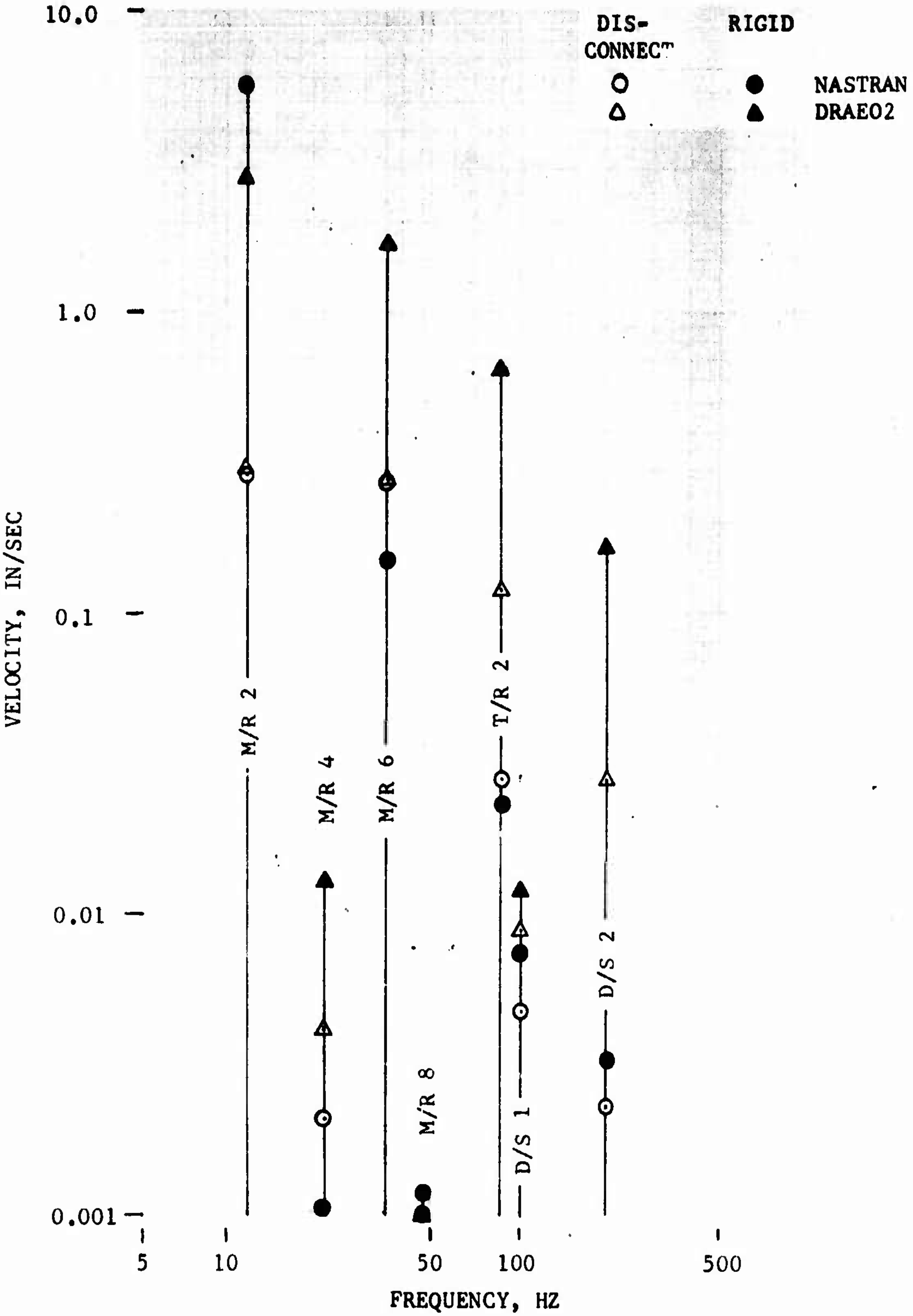

Figure 59. Comparison of Computed Engine Turbine Midsplit Lateral Velocities for Rigid and Disconnected Input Drive Shaft, 130-Knot Simulated Level Flight.

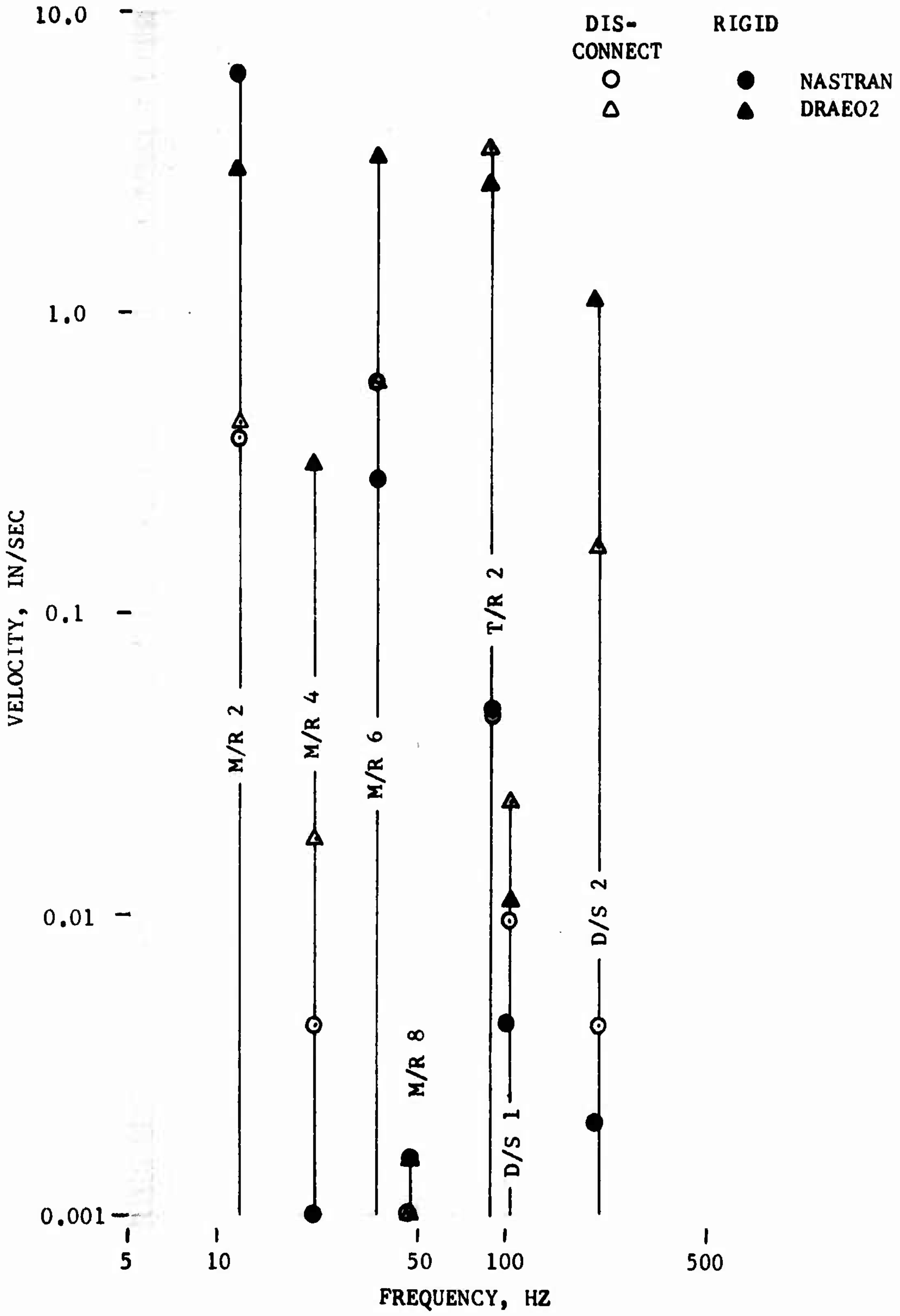

Figure 60. Comparison of Computed Engine Fuel Nozzle Lateral Velocities for Rigid and Disconnected Input Drive Shaft, 130-Knot Simulated Level Flight.

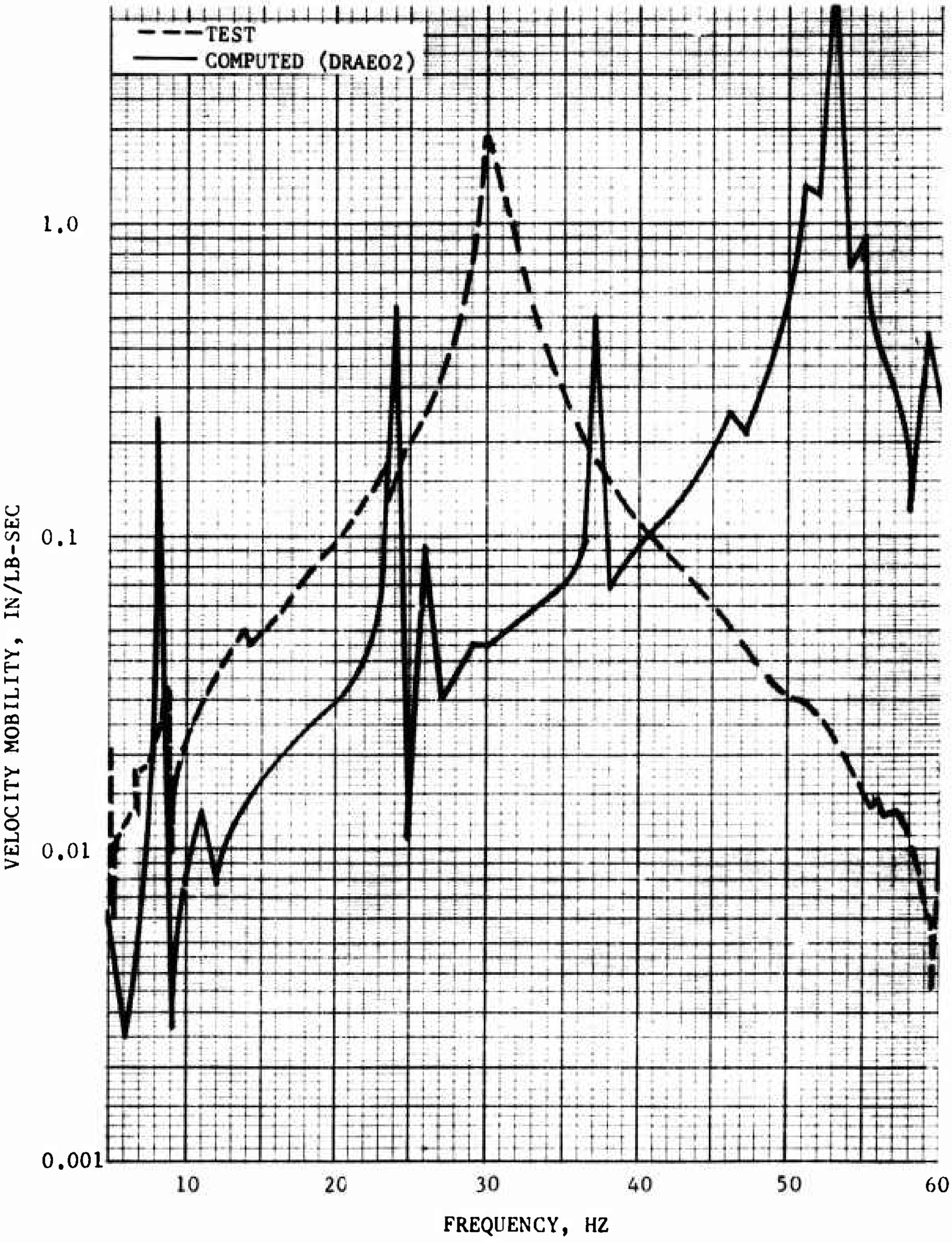

Figure 61. Comparison of Computed and Measured Left-Hand Engine Bipod Longitudinal Driving Point Mobility, Airframe Mobility Element Y_{EE} (1,1).

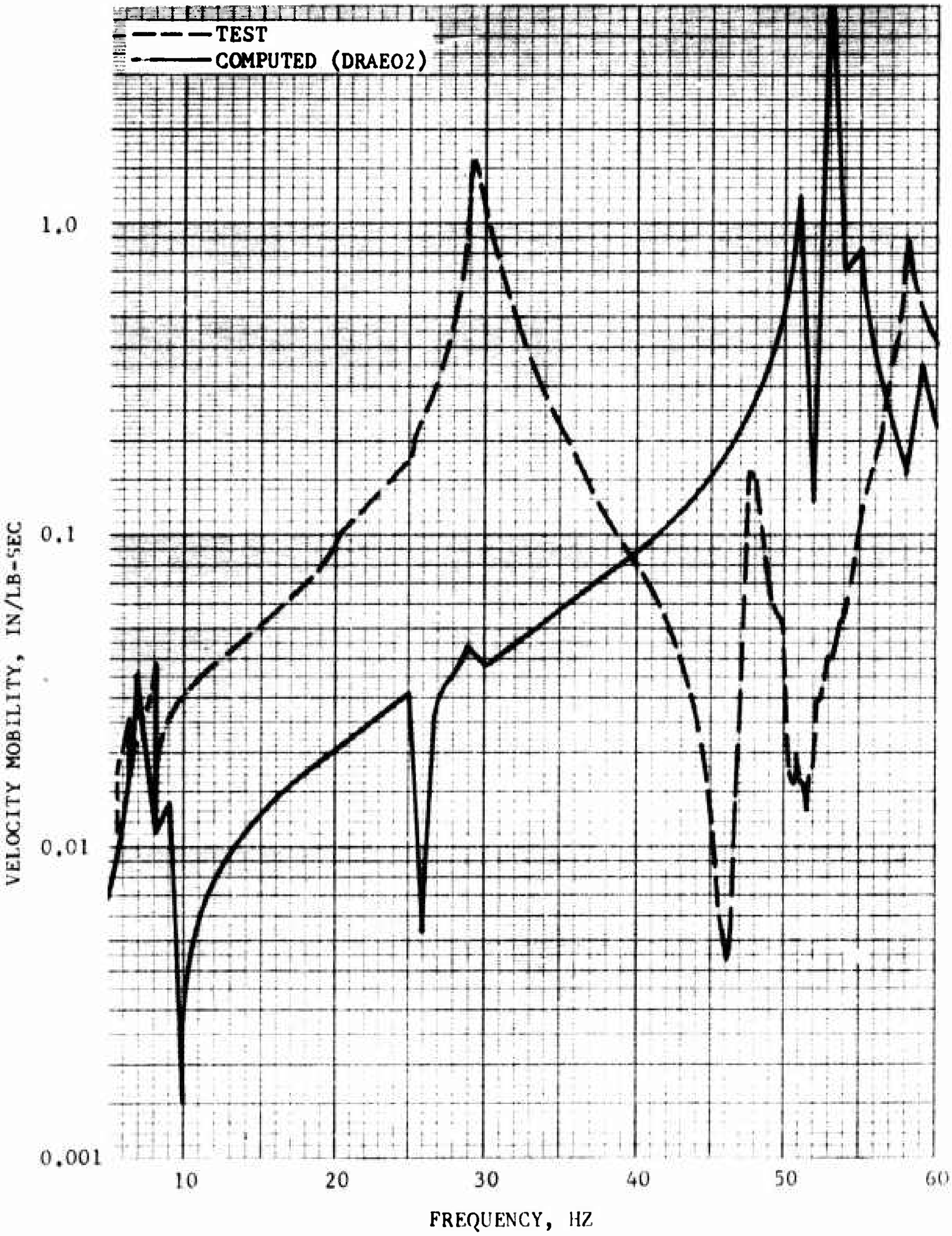

Figure 62. Comparison of Computed and Measured Left-Hand Engine Bipod Lateral Driving Point Mobility, Airframe Mobility Element Y_{EE} (2,2).

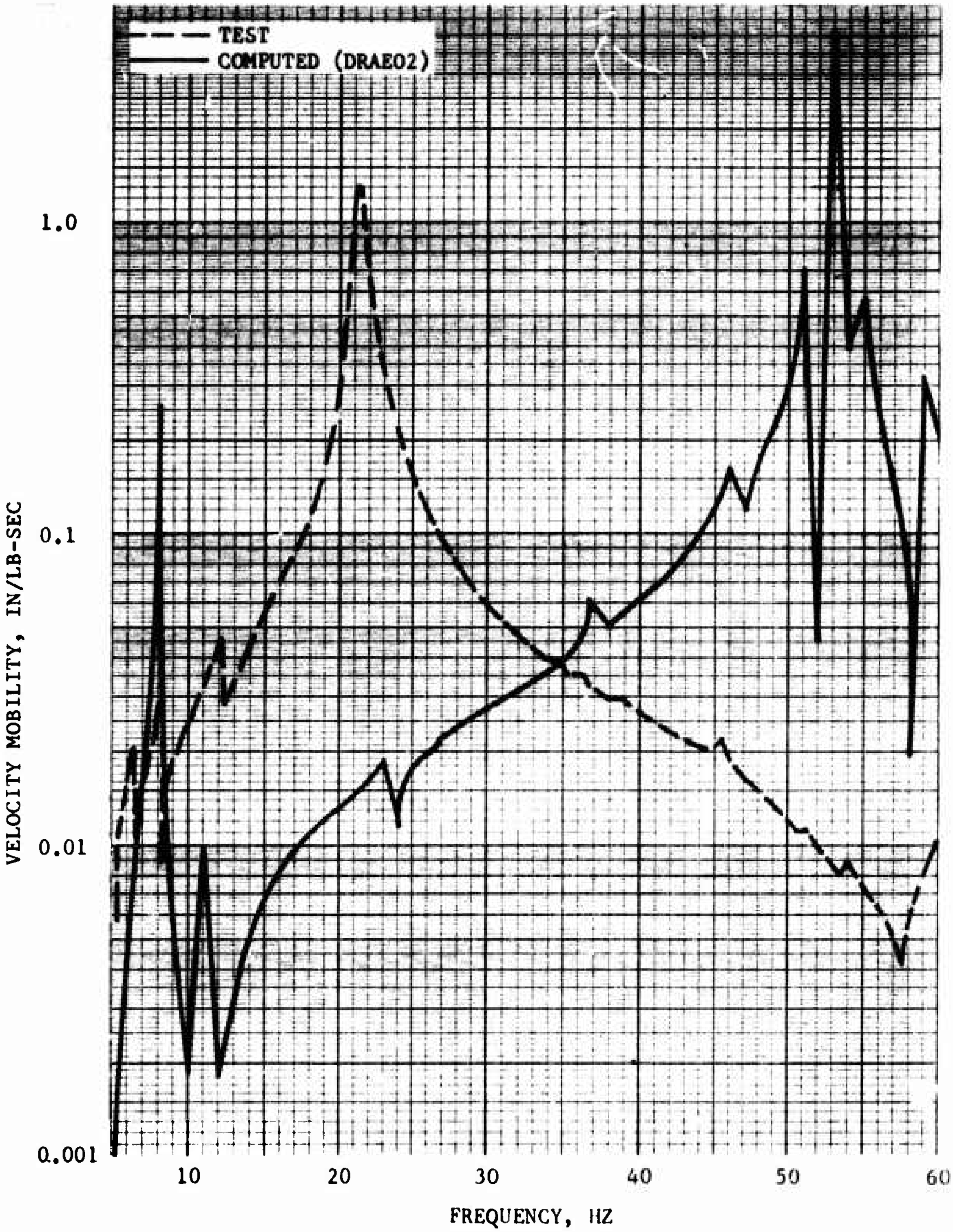

Figure 63. Comparison of Computed and Measured Left-Hand Engine Bipod Vertical Driving Point Mobility, Airframe Mobility Element Y_{EE} (3,3).

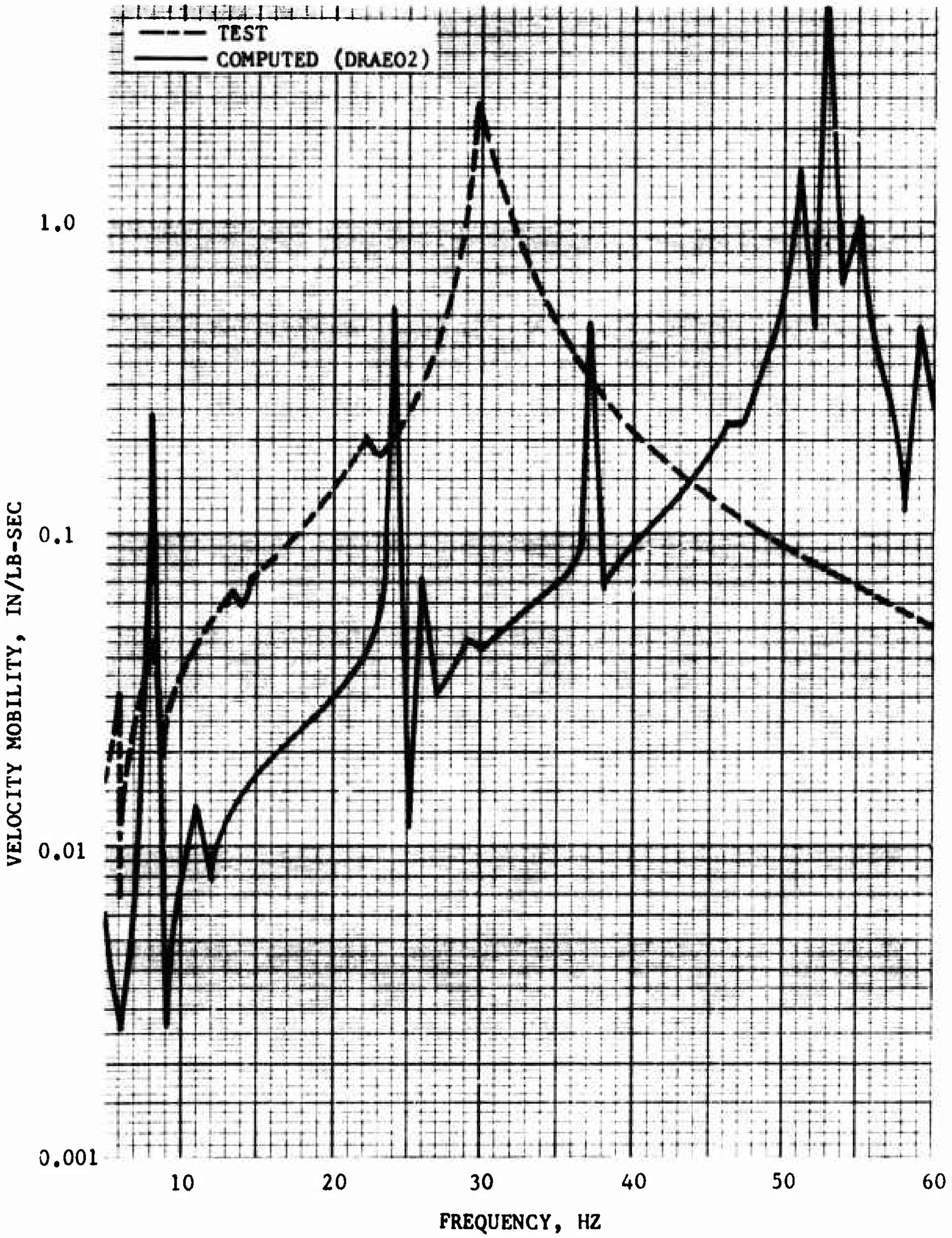

Figure 64. Comparison of Computed and Measured Right-Hand Engine Bipod Longitudinal Driving Point Mobility, Airframe Mobility Element Y_{EE} (4,4).

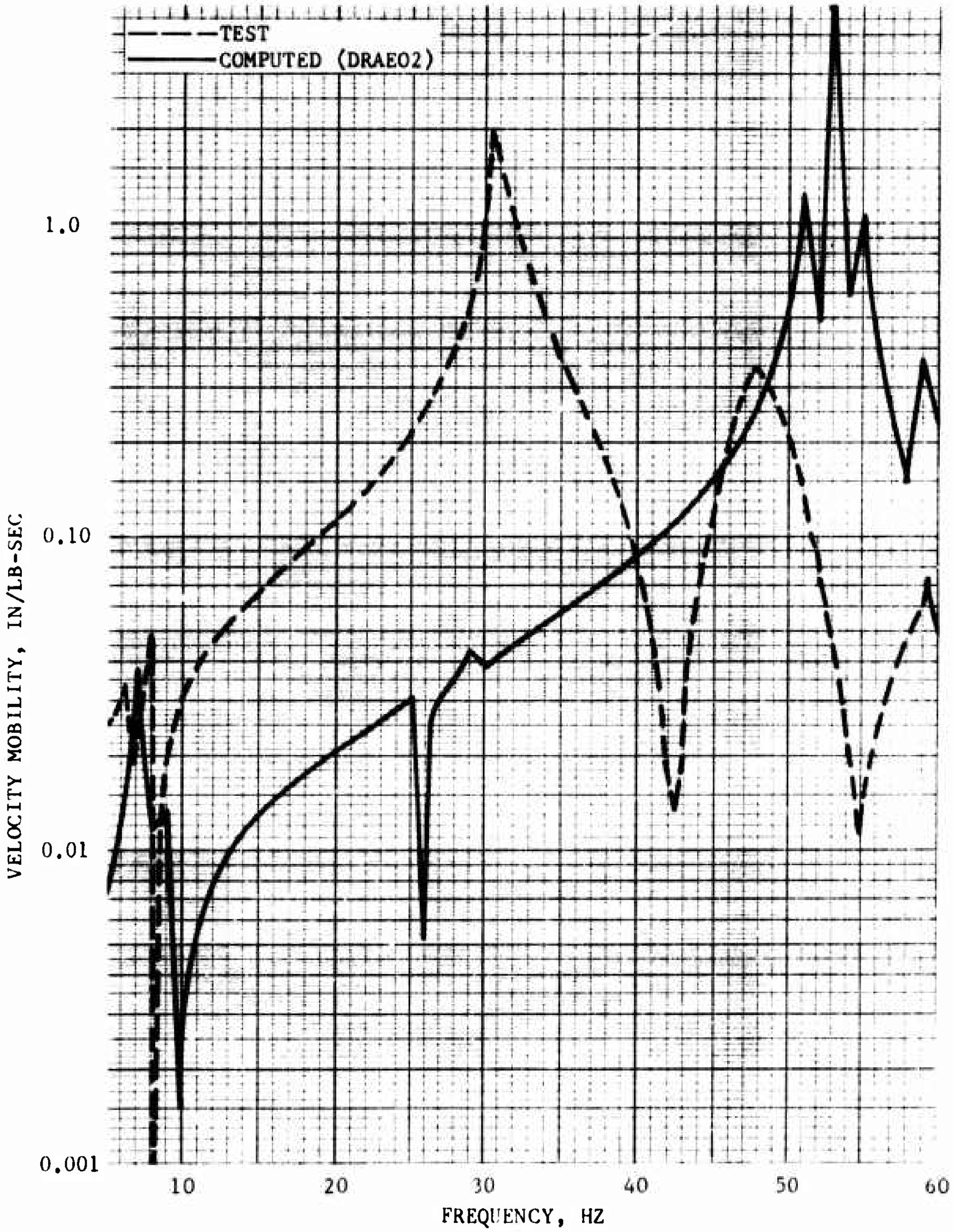

Figure 65. Comparison of Computed and Measured Right-Hand Engine Bipod Lateral Driving Point Mobility, Airframe Mobility Element Y_{EE} (5,5).

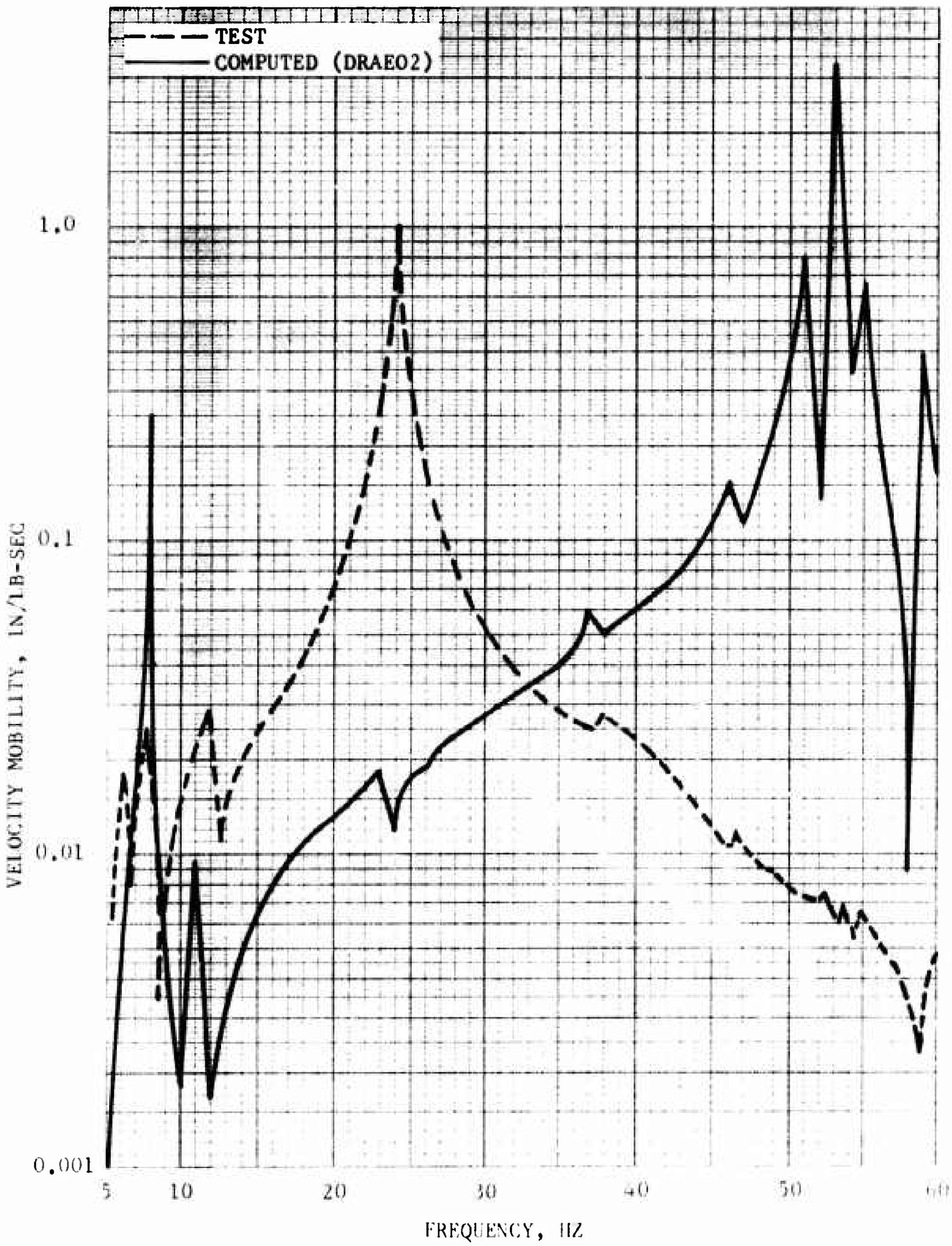

Figure 66. Comparison of Computed and Measured Right-Hand Engine Bipod Vertical Driving Point Mobility, Airframe Mobility Element Y_{EE} (6,6).

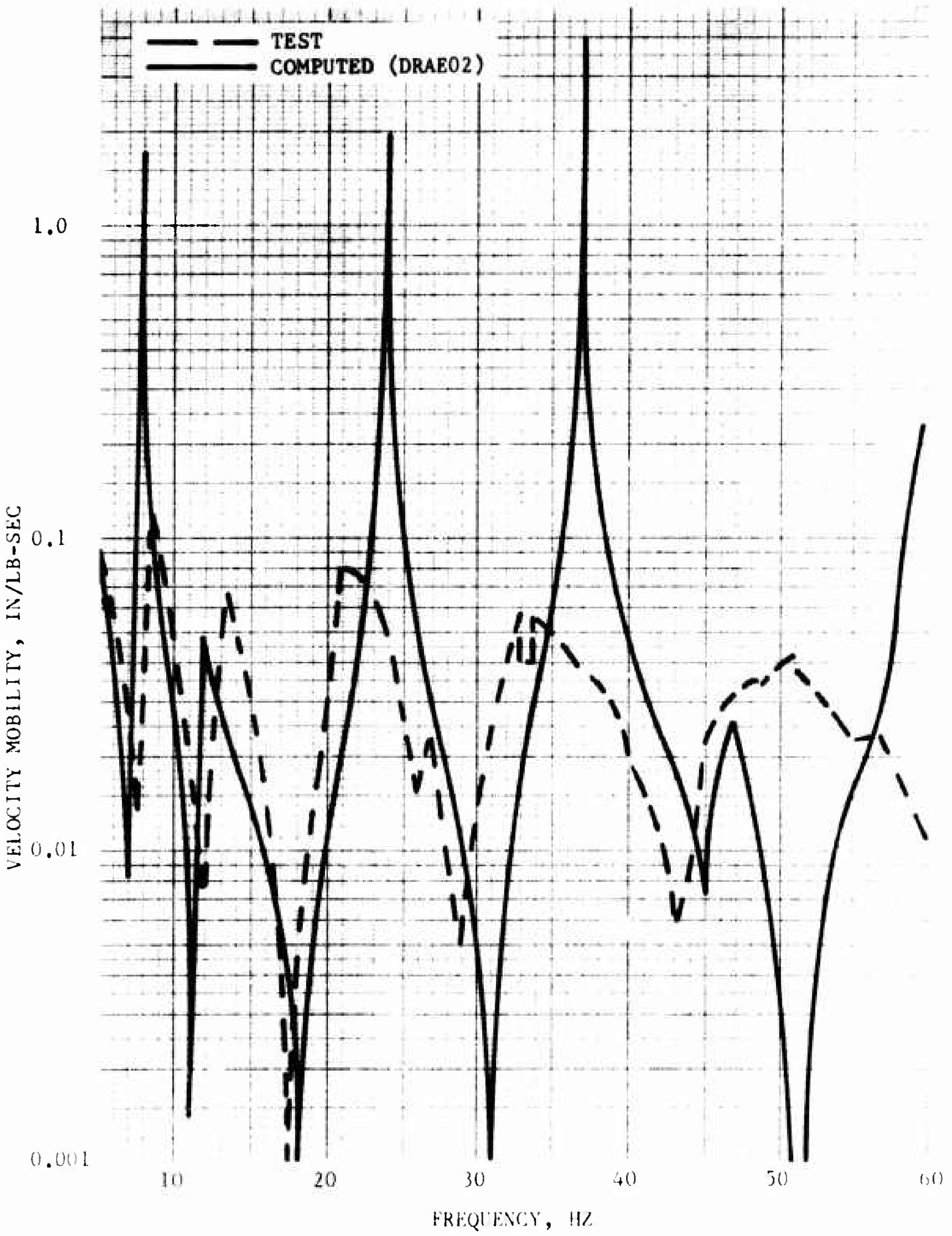

Figure 67. Comparison of Computed and Measured Lower Engine Bipod Longitudinal Driving Point Mobility, Airframe Mobility Element Y_{EE} (7,7).

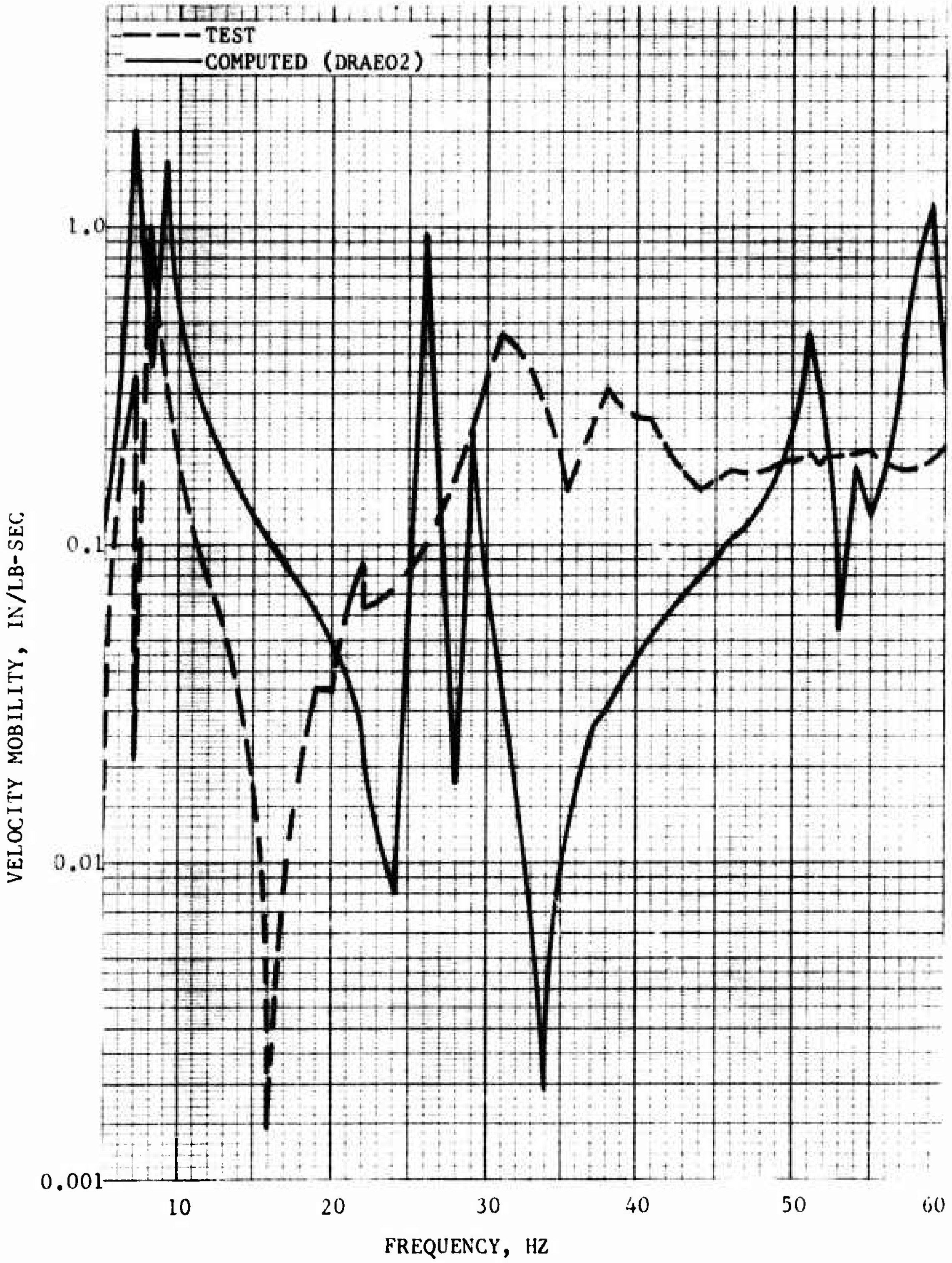

Figure 68. Comparison of Computed and Measured Lower Engine Bipod Lateral Driving Point Mobility, Airframe Mobility Element Y_{EE} (8,8).

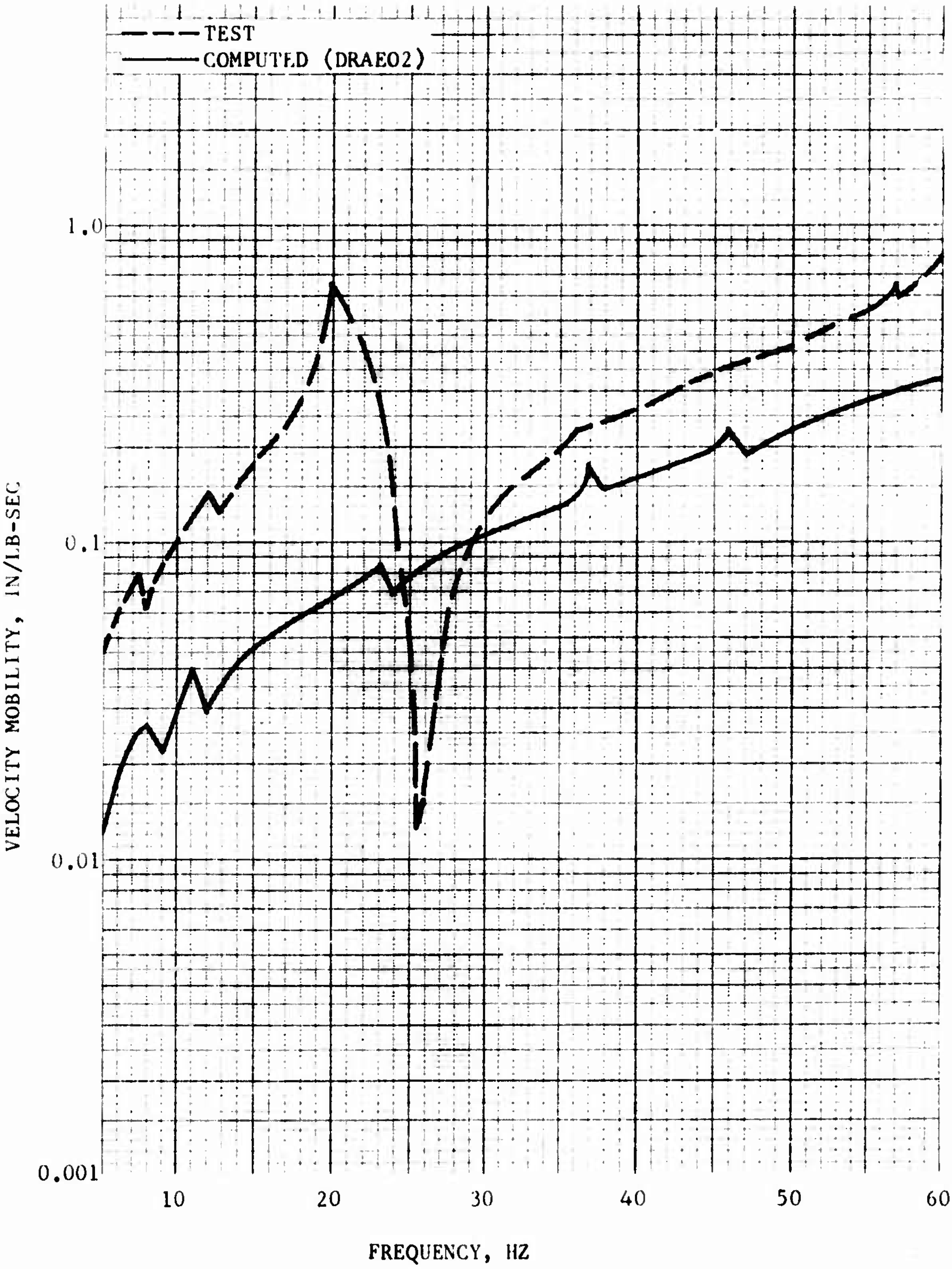

Figure 69. Comparison of Computed and Measured Lower Engine Bipod Vertical Driving Point Mobility, Airframe Mobility Element Y_{EE} (9,9).

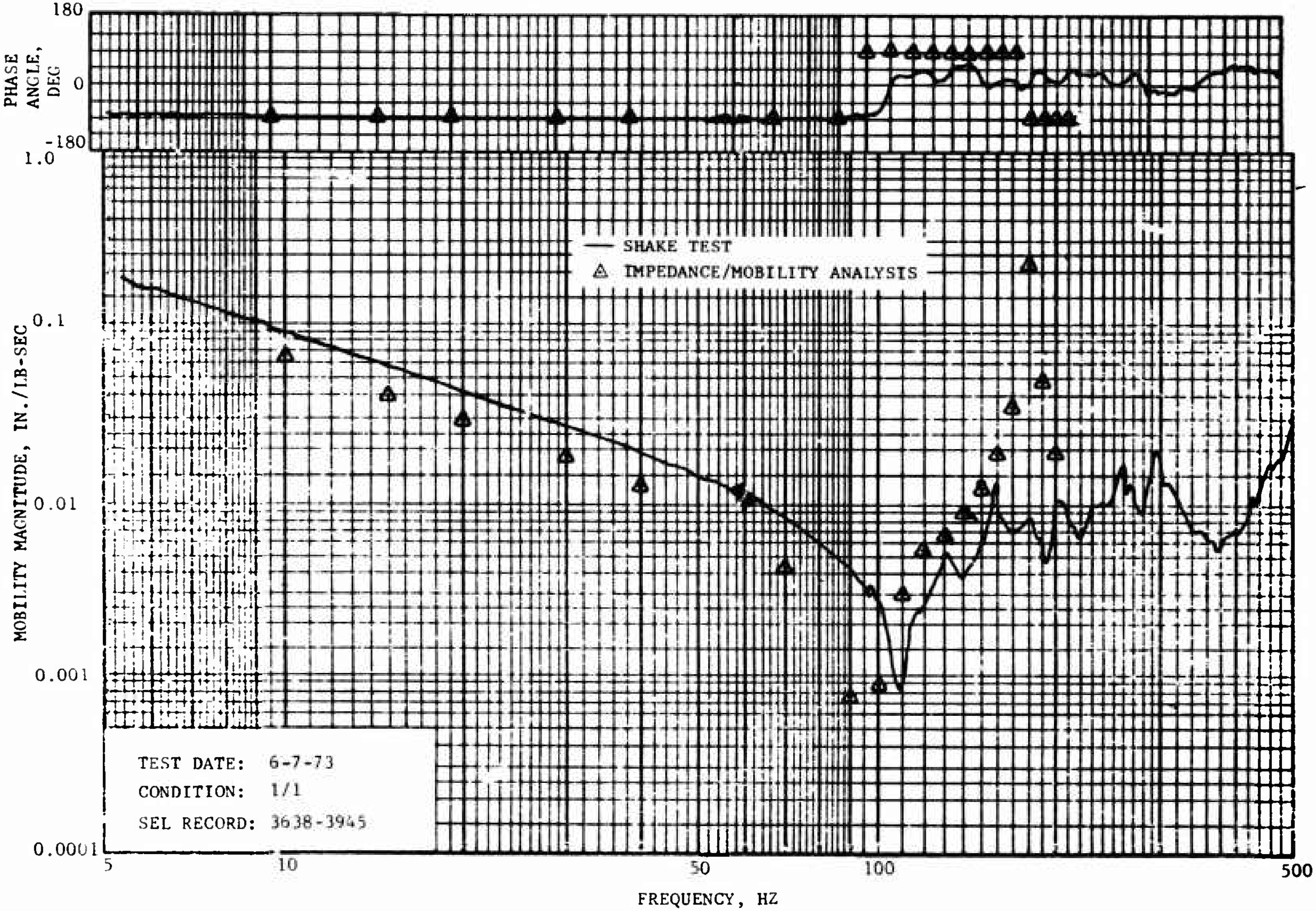

Figure 70. Comparison of Computed and Measured Left Engine Mount Longitudinal Driving Point Mobility, Engine Mobility Element Y_{EE} (1,1).

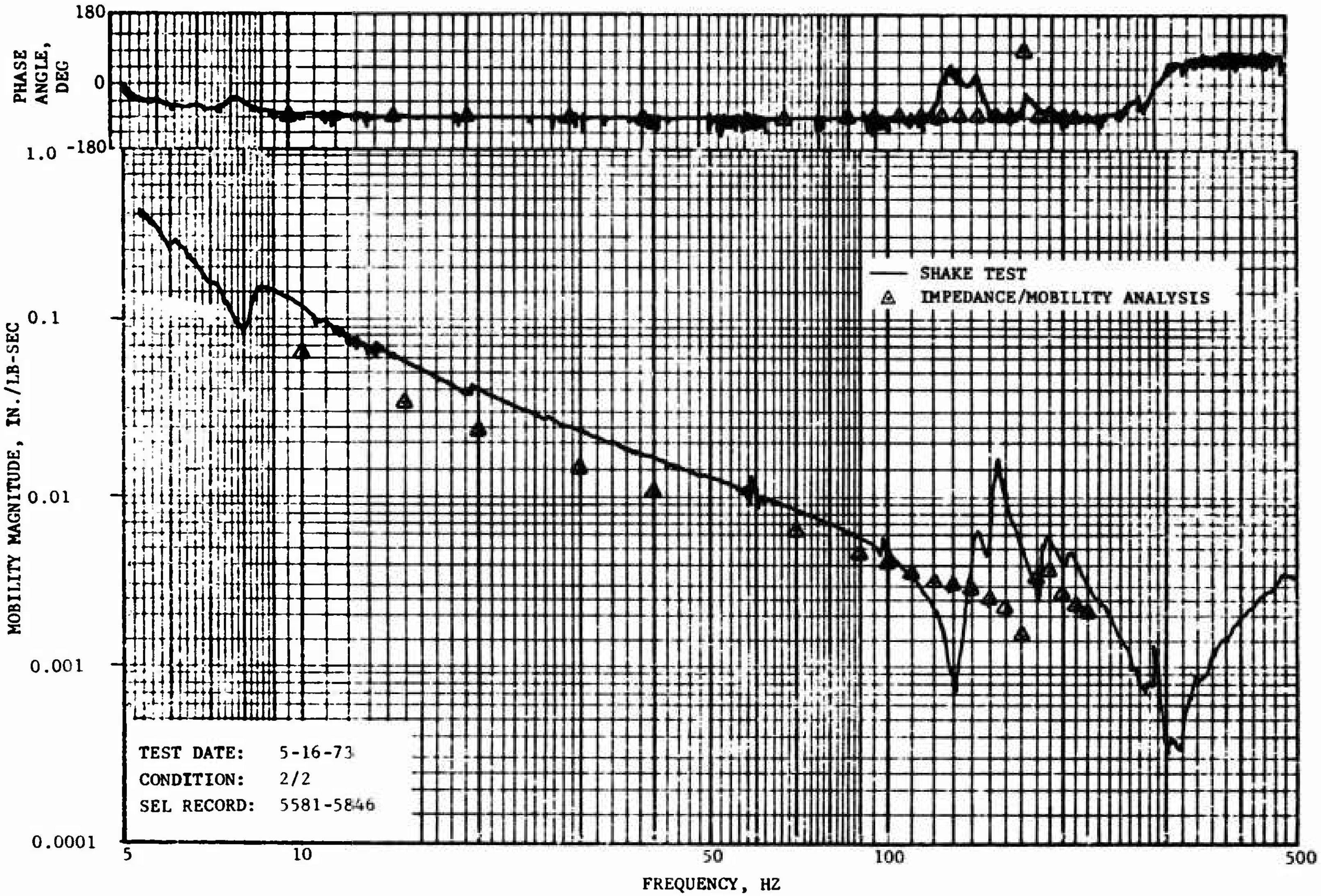

Figure 71. Comparison of Computed and Measured Left Engine Mount Lateral Driving Point Mobility, Engine Mobility Element Y_{EE} (2,2).

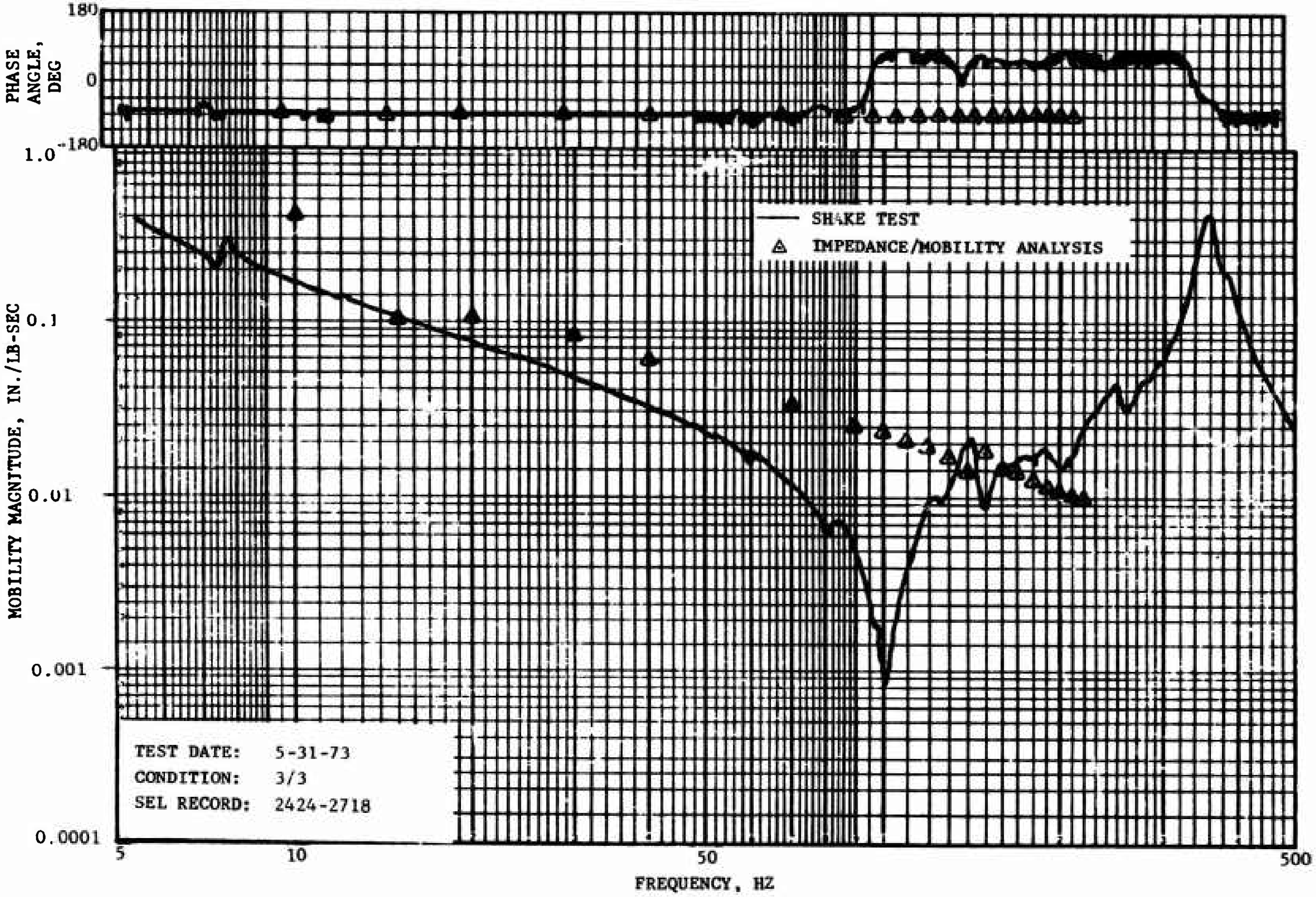

Figure 72. Comparison of Computed and Measured Left Engine Mount Vertical Driving Point Mobility, Engine Mobility Element Y_{EE} (3,3).

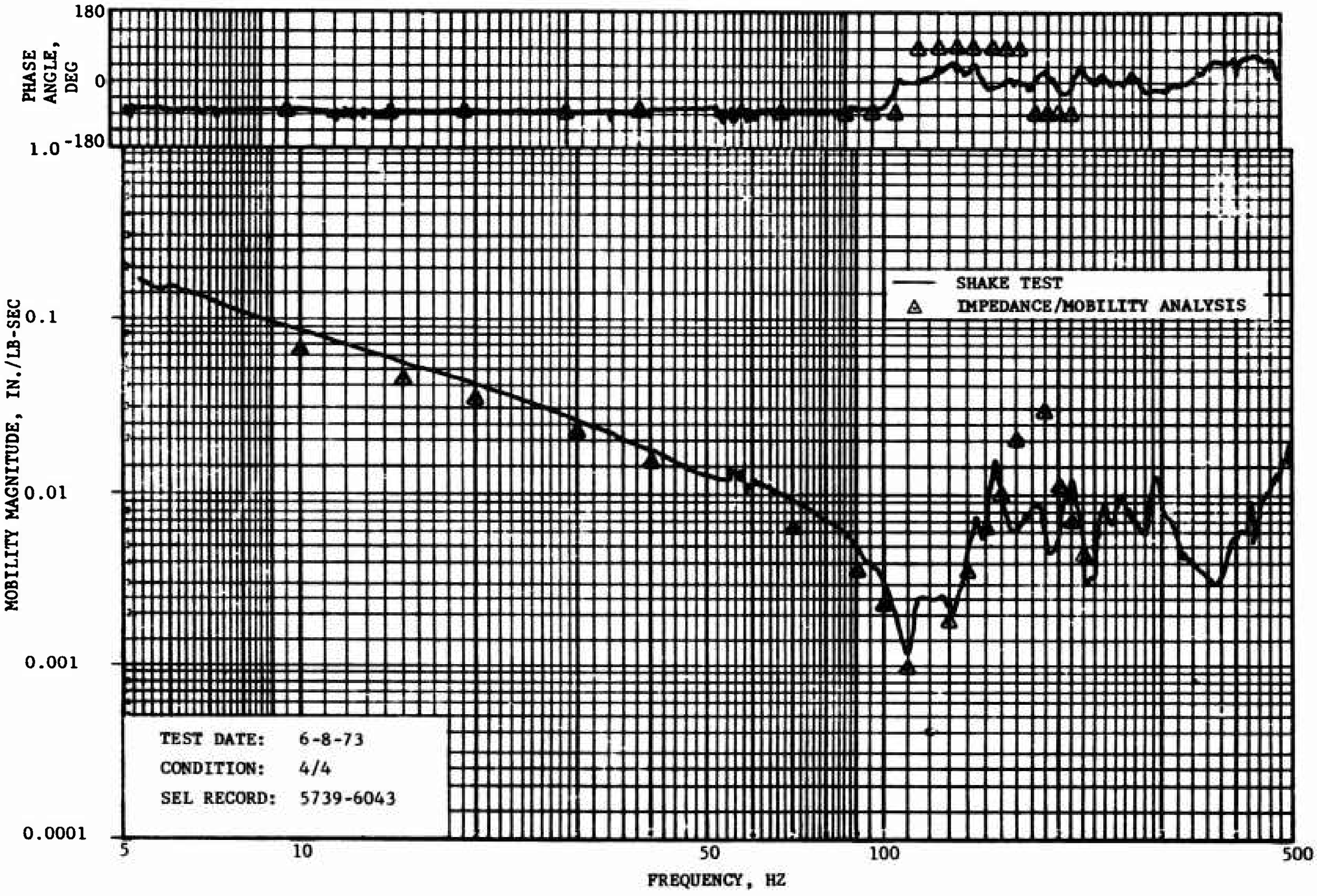

Figure 73. Comparison of Computed and Measured Right Engine Mount Longitudinal Driving Point Mobility, Engine Mobility Element Y_{EE} (4,4).

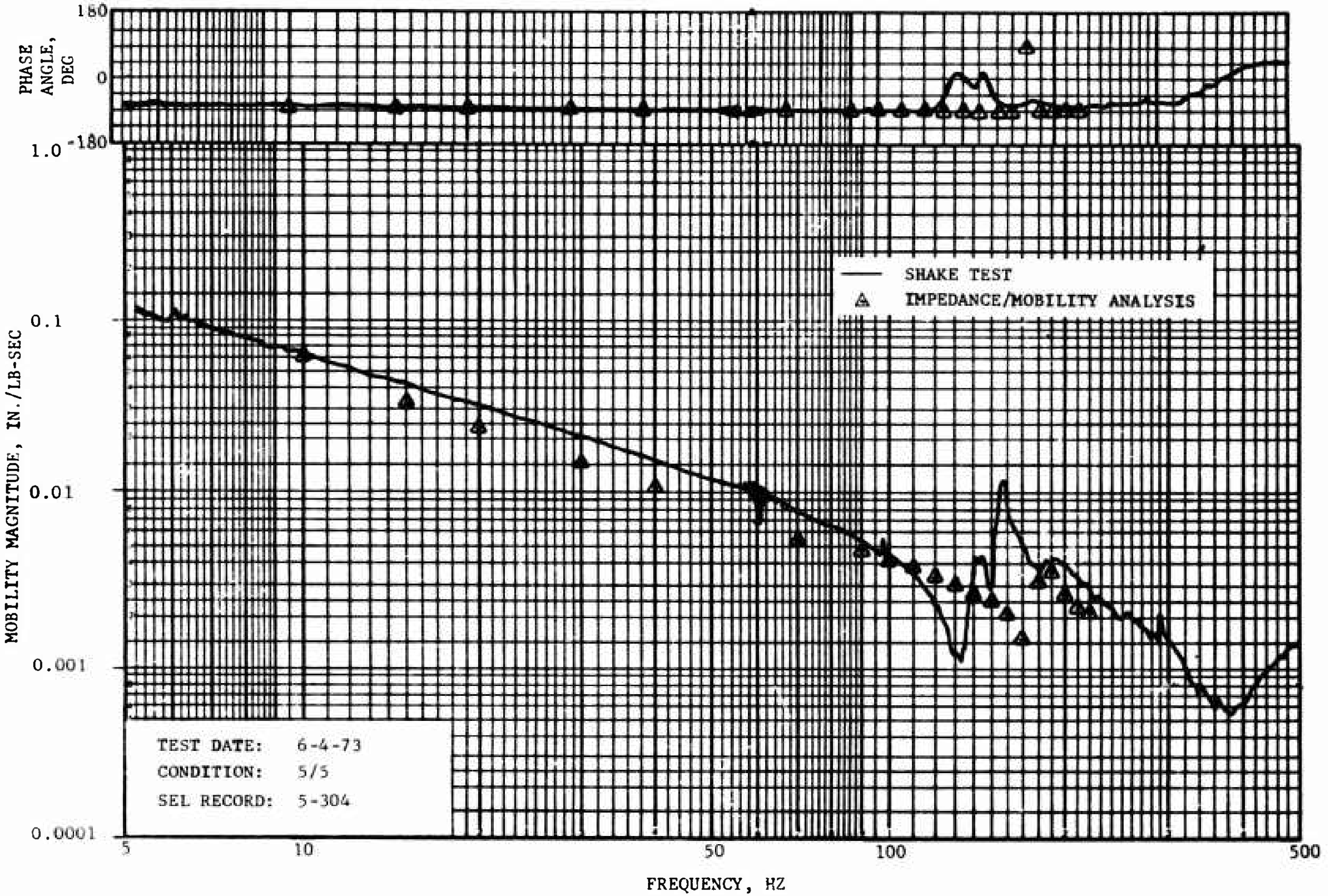

Figure 74. Comparison of Computed and Measured Right Engine Mount Lateral Driving Point Mobility, Engine Mobility Element Y_{EE} (5,5).

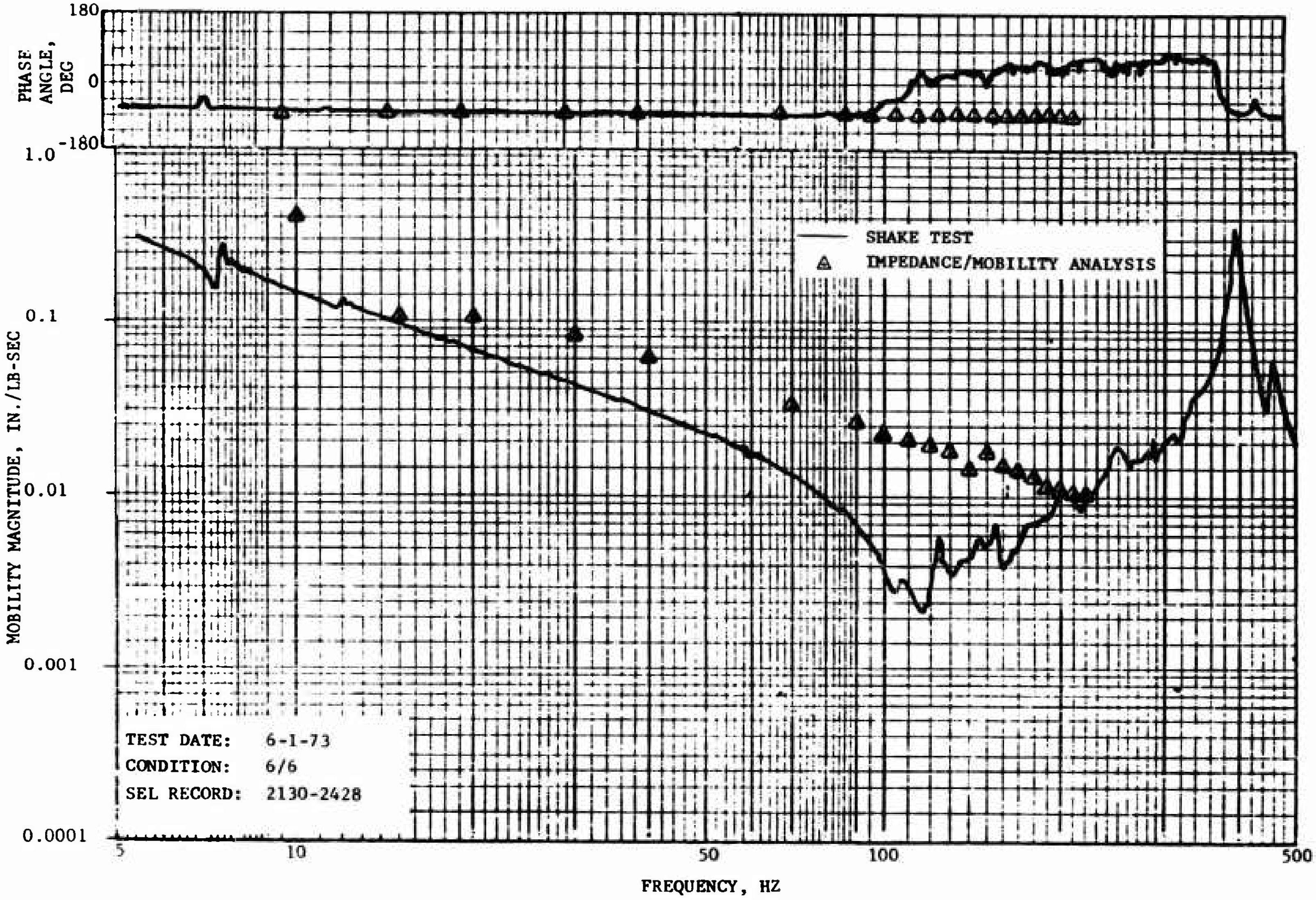

Figure 75. Comparison of Computed and Measured Right Engine Mount Vertical Driving Point Mobility, Engine Mobility Element Y_{EE} (6,6).

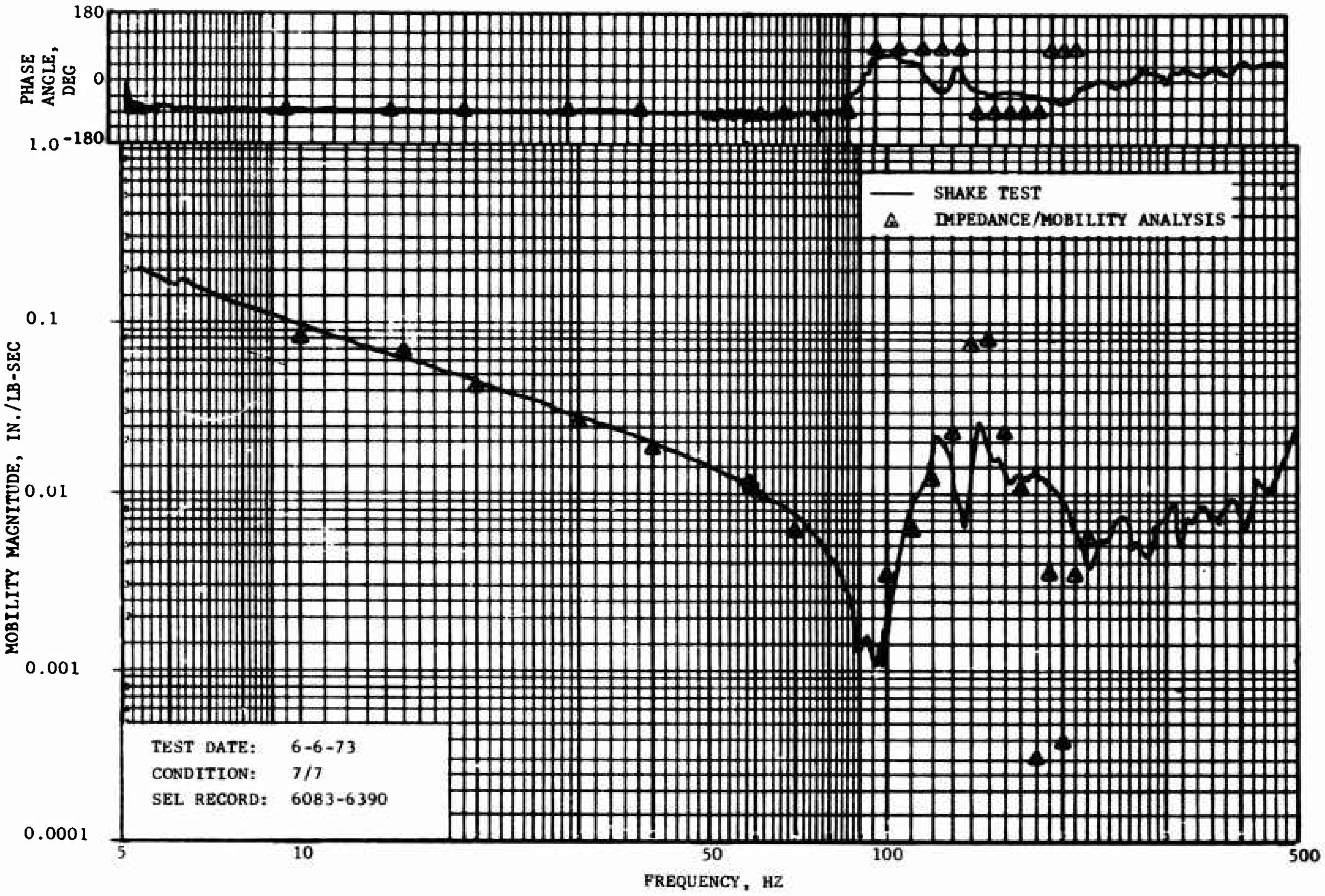

Figure 76. Comparison of Computed and Measured Lower Engine Mount Longitudinal Driving Point Mobility, Engine Mobility Element Y_{EE} (7,7).

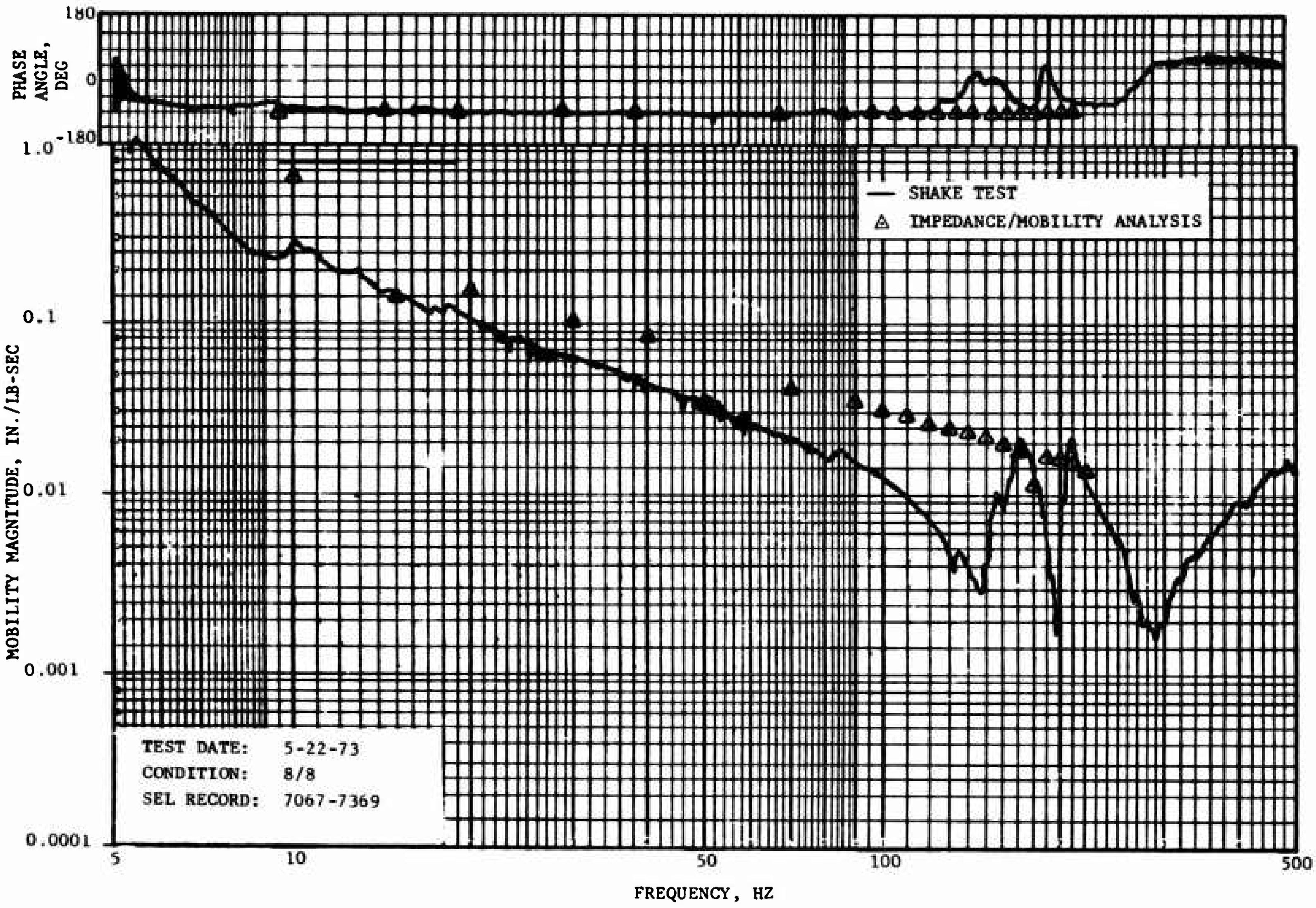

Figure 77. Comparison of Computed and Measured Lower Engine Mount Lateral Driving Point Mobility, Engine Mobility Element Y_{EE} (8,8).

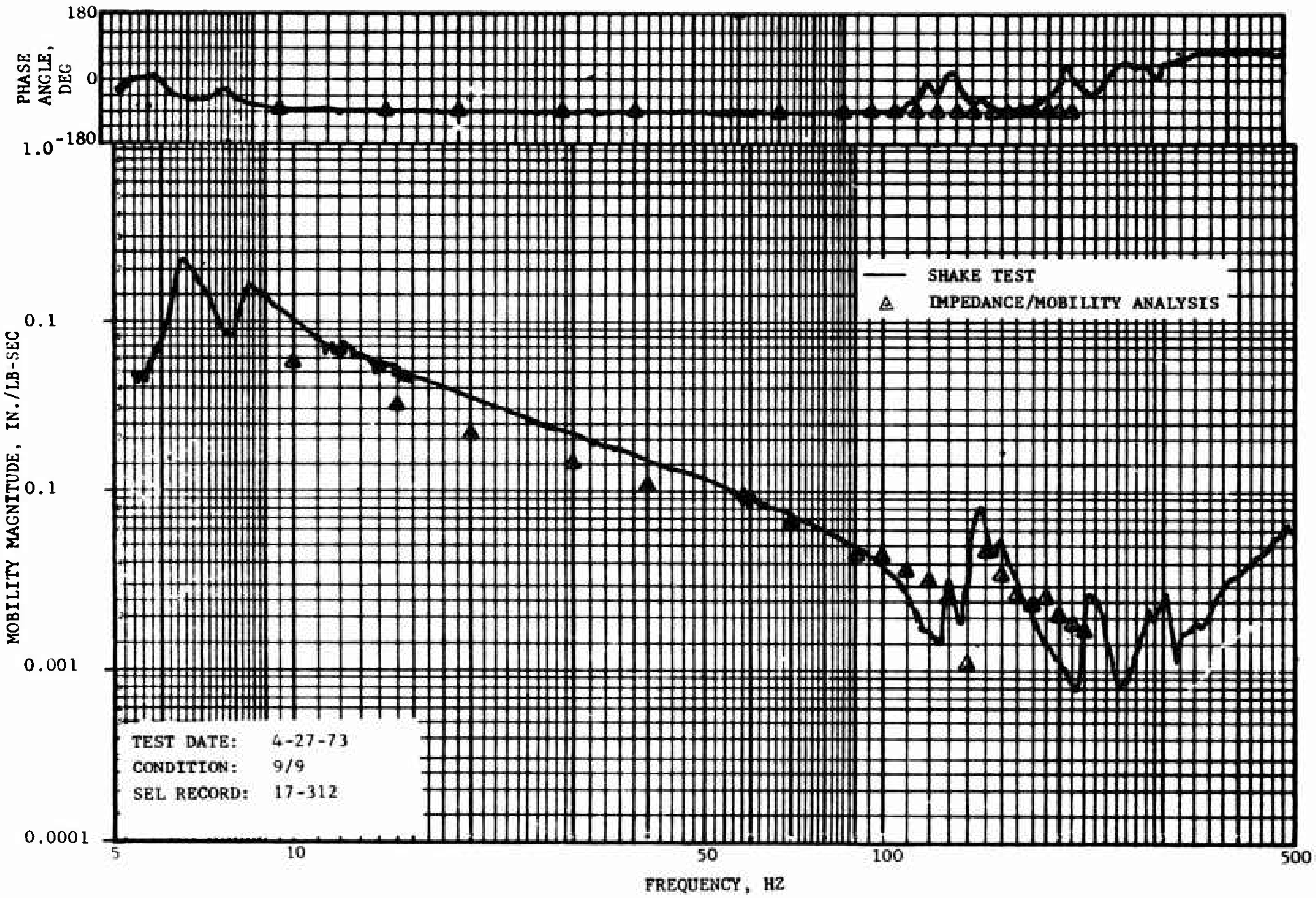

Figure 78. Comparison of Computed and Measured Lower Engine Mount Vertical Driving Point Mobility, Engine Mobility Element Y_{EE} (9,9).

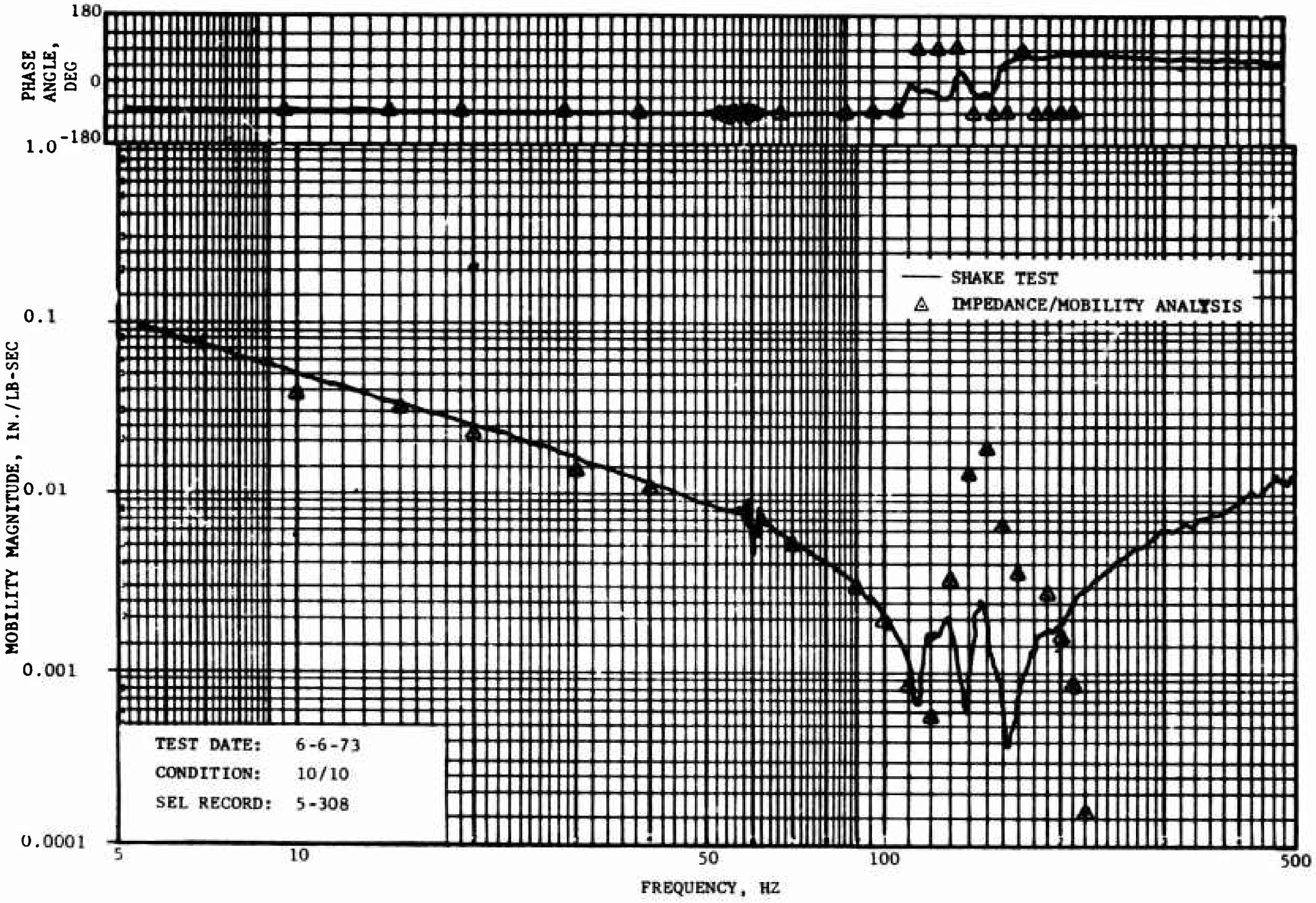

Figure 79. Comparison of Computed and Measured Engine Output Shaft Longitudinal Driving Point Mobility, Engine Mobility Element Y_{EE} (10,10).

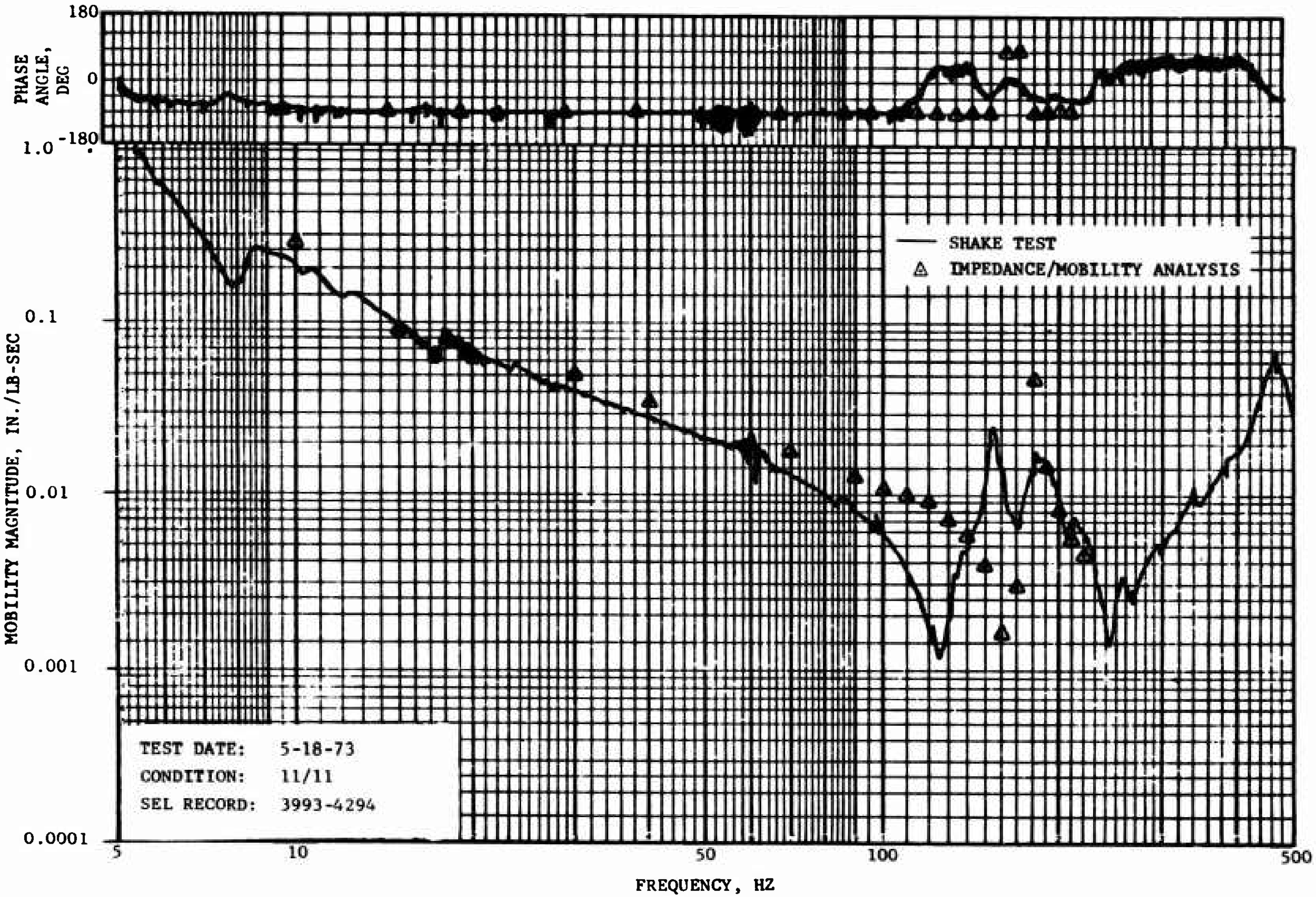

Figure 80. Comparison of Computed and Measured Engine Output Shaft Lateral Driving Point Mobility, Engine Mobility Element Y_{EE} (11,11).

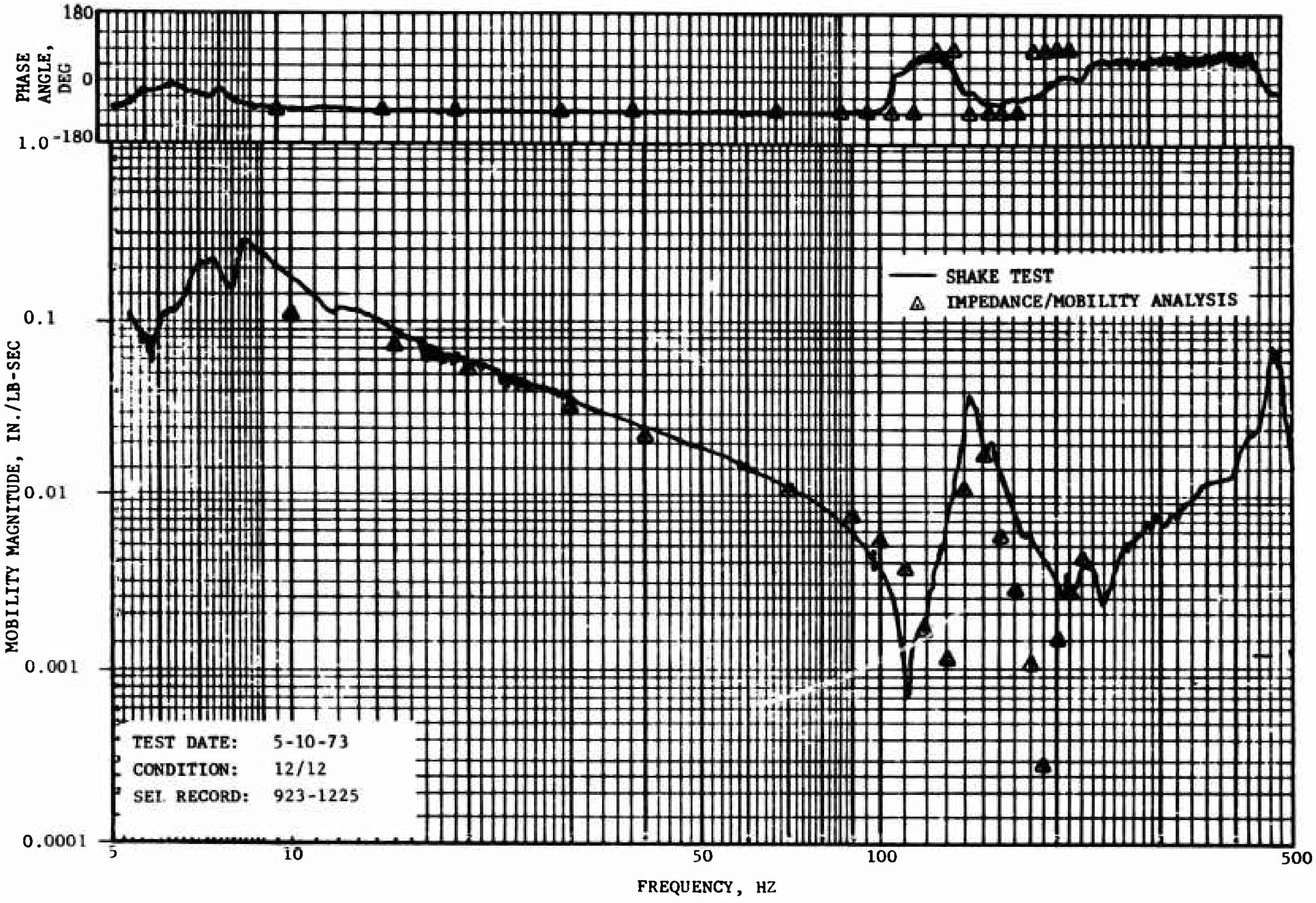

Figure 81. Comparison of Computed and Measured Engine Output Shaft Vertical Driving Point Mobility, Engine Mobility Element Y_{EE} (12,12).

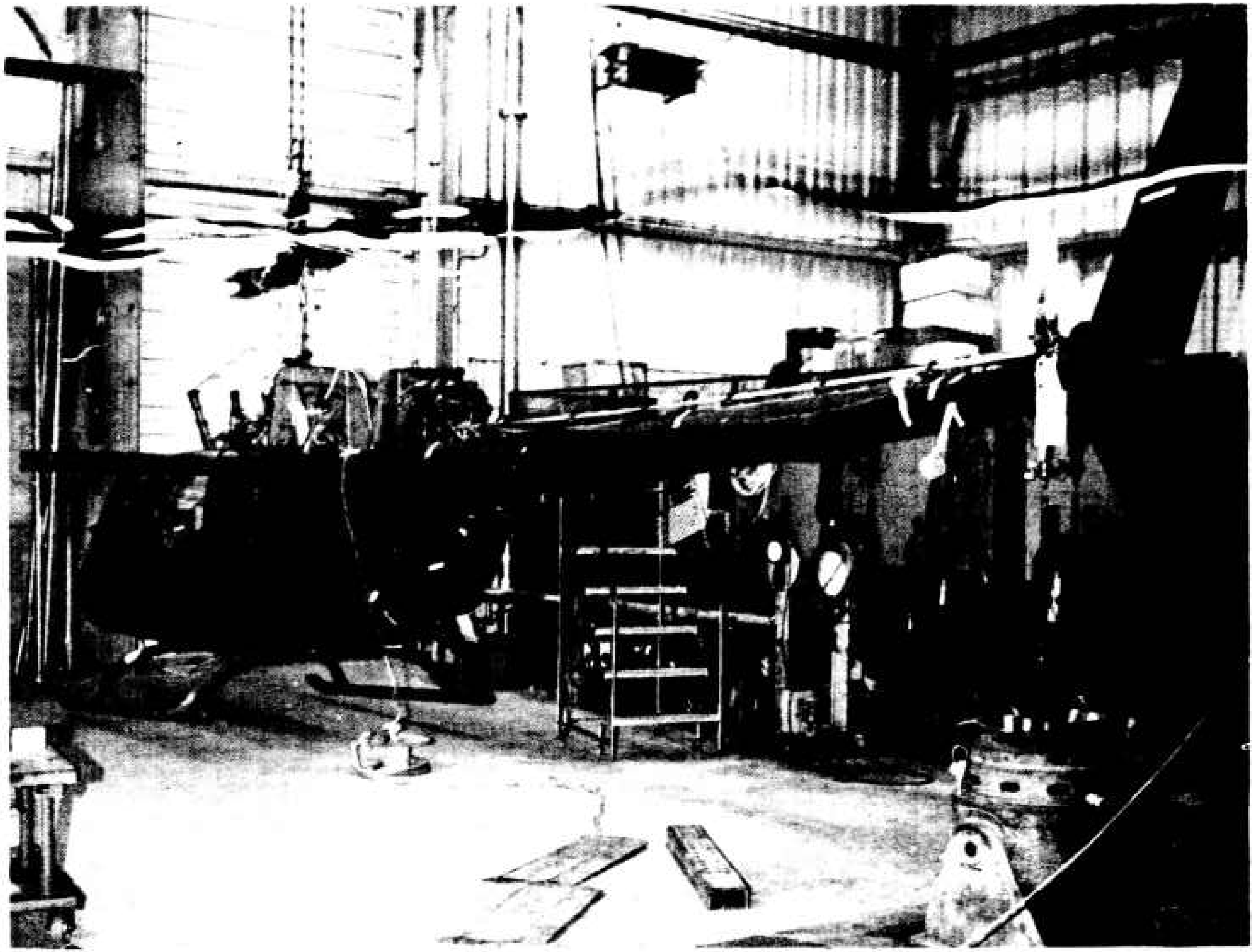

Figure 52. Installation of the OH-58A Helicopter for Vibration Testing.

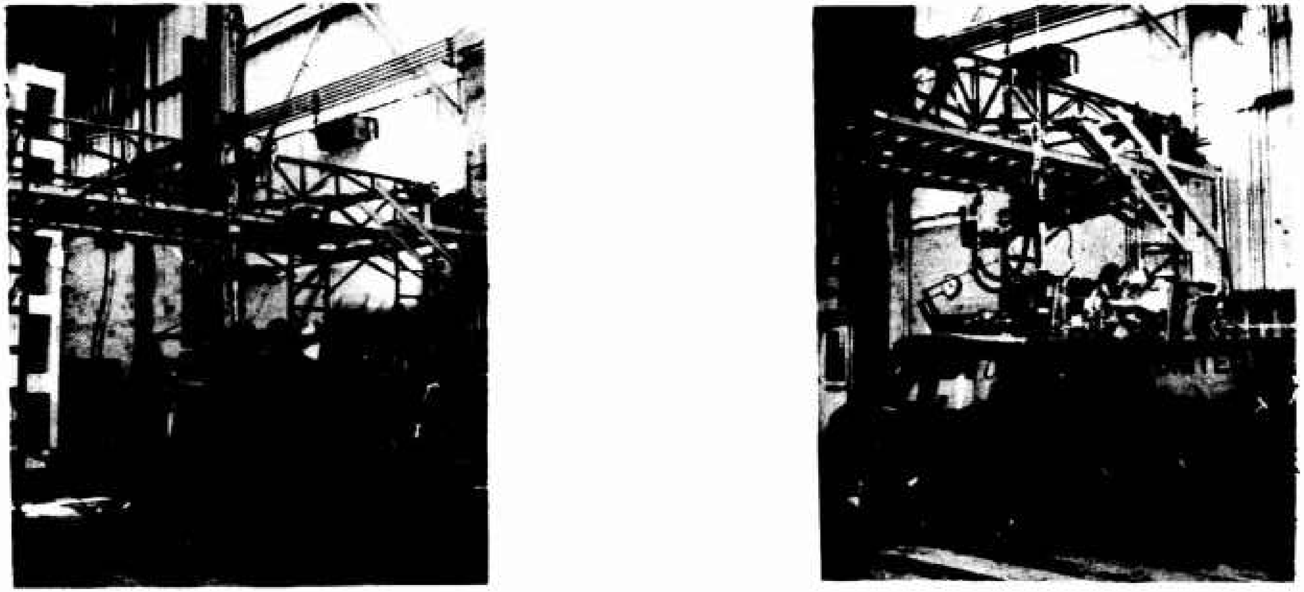

a) Vertical Excitation

b) Longitudinal Excitation

Figure 83. Orientation and Arrangement of Shake Test Hardware for Mechanical Shaker Installation.

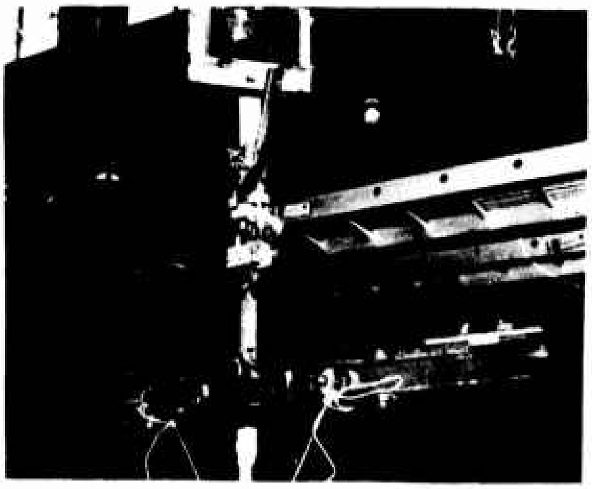

a) Vertical Excitation

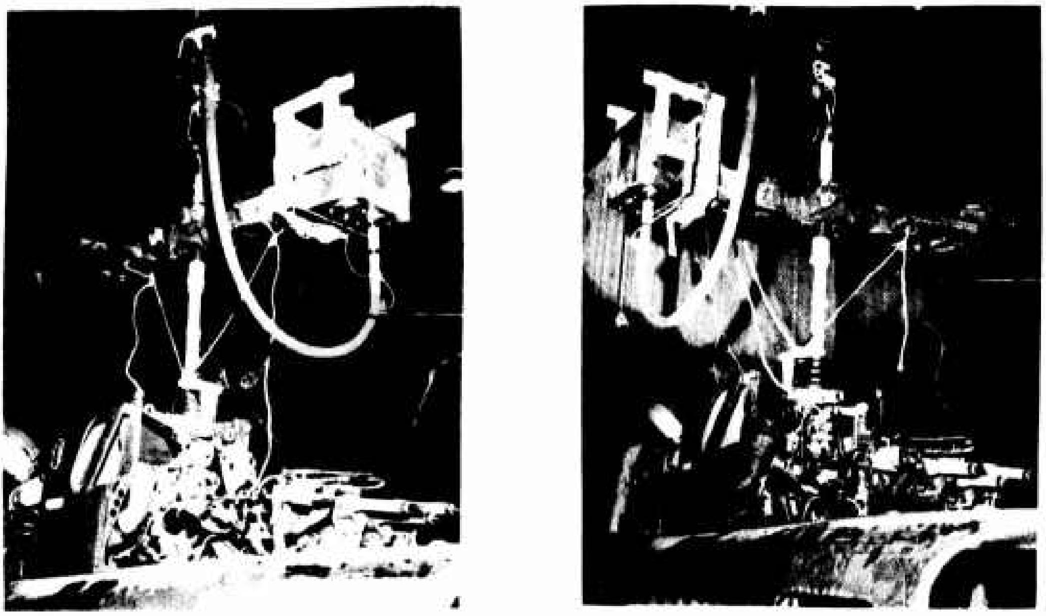

b) Longitudinal Excitation

c) Lateral Excitation

Figure 84. Detailed View of Mechanical Shaker and Hub Installation for Excitation at the Main Rotor.

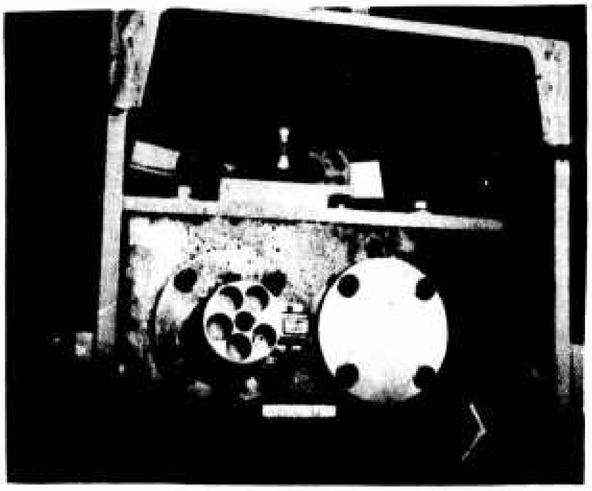

Figure 85. Arrangement of Impedance Head for Force Measurement Using the Lazan Mechanical Shaker for Longitudinal and Lateral Excitation at the Main Rotor Hub.

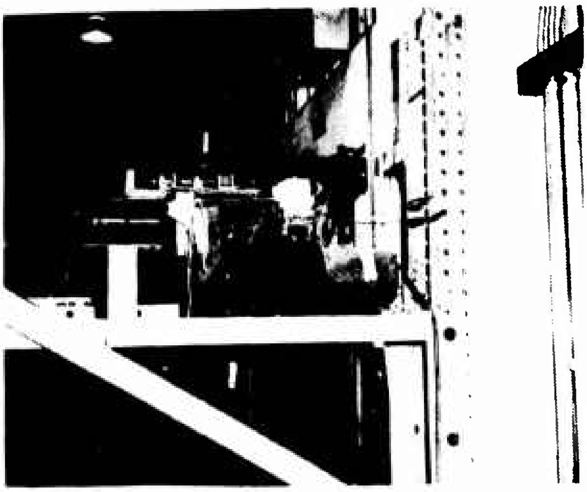

Figure 86. Vari-Drive Assembly.

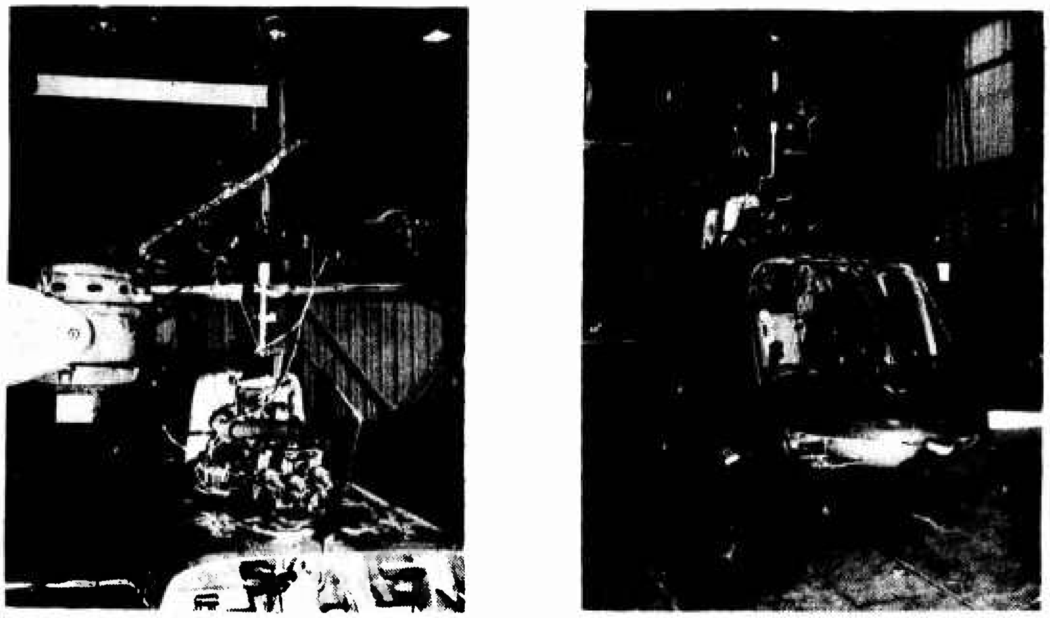

a) Vertical Excitation b) Lateral Excitation

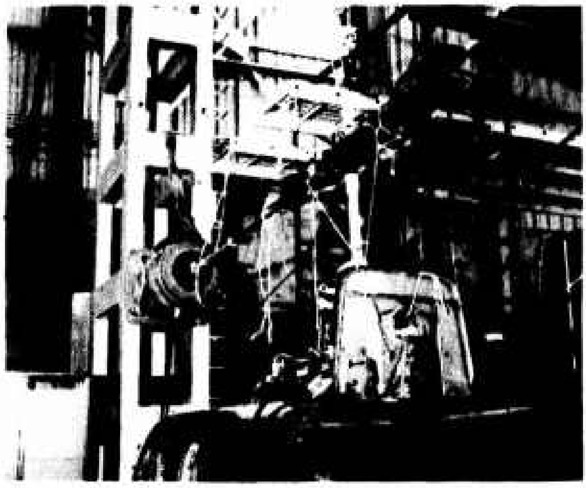

c) Longitudinal Excitation

Figure 87. Arrangement of Electromagnetic Exciter and Hardware for Excitation at the Main Rotor Hub.

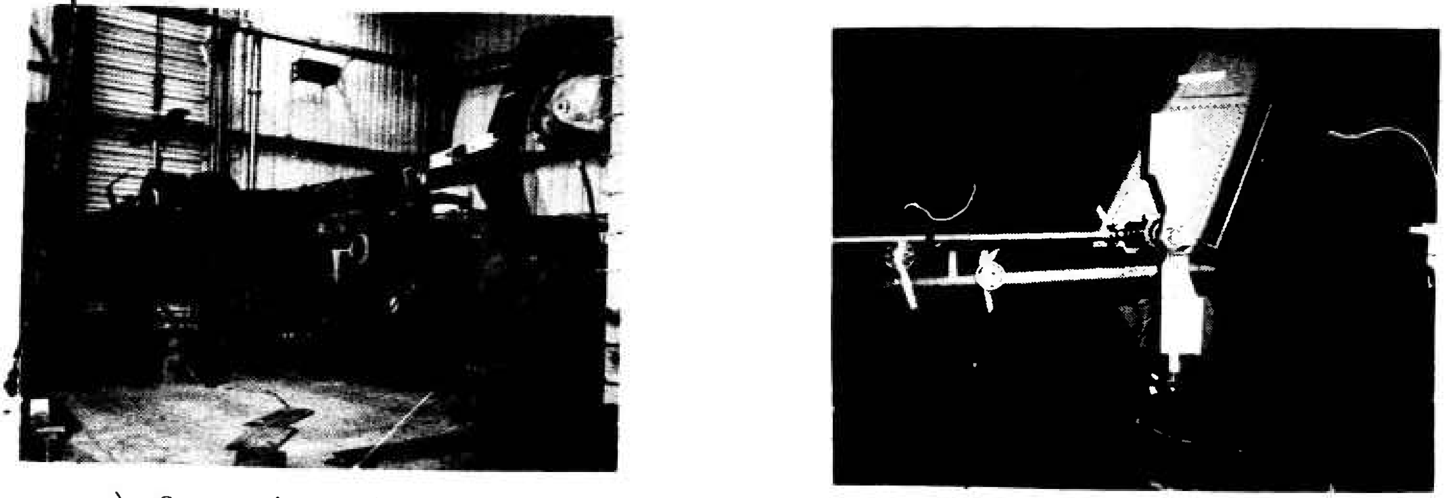

a) Suspension and Installation

b) Vertical Excitation

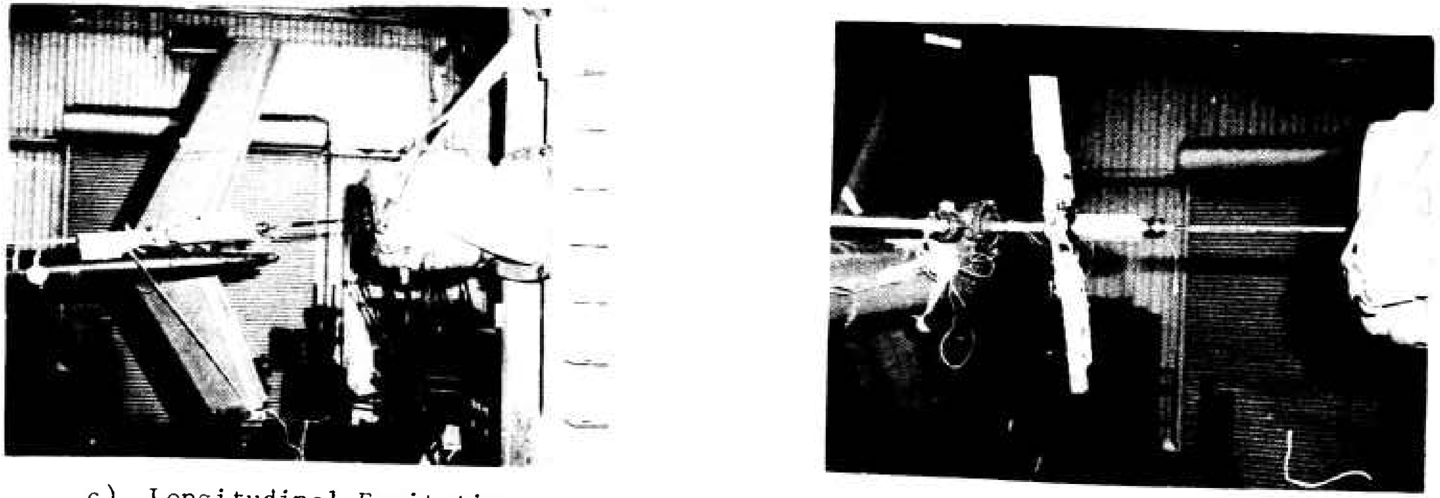

c) Longitudinal Excitation

d) Lateral Excitation

Figure 88. Arrangement of Electromagnetic Exciter and Hardware for Excitation at the Tail Rotor Hub.

Figure 89. Installation of Electromagnetic Exciter and Crank Assembly for Typical Excitation at Engine Mounts.

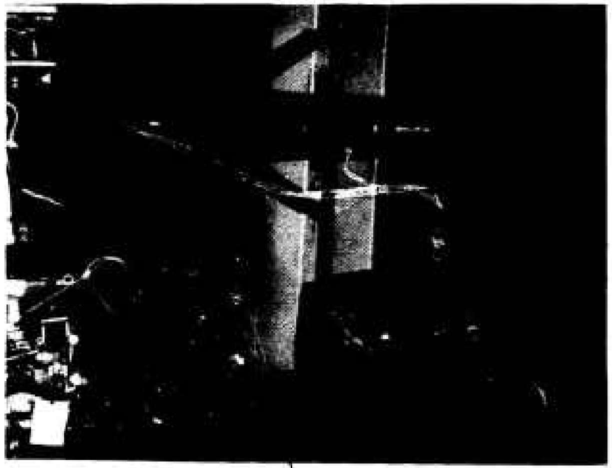

a) Vertical Excitation

b) Longitudinal Excitation

c) Lateral Excitation

Figure 90. Arrangement of Exciter and Crank Assembly for Excitation at Right- or Left-Hand Engine Mount.

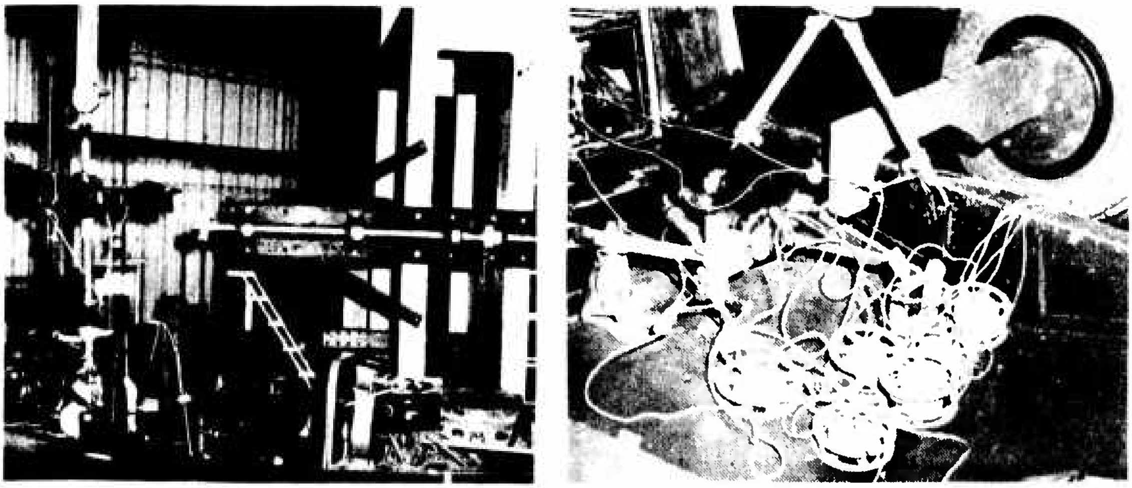

a) View of Crank Assembly

b) Lateral Excitation

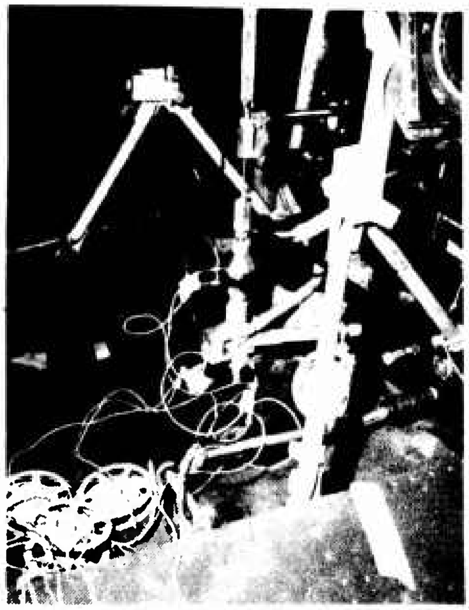

c) Vertical Excitation

Figure 91. Arrangement of Exciter and Crank Assembly for Excitation at Lower Engine Mount.

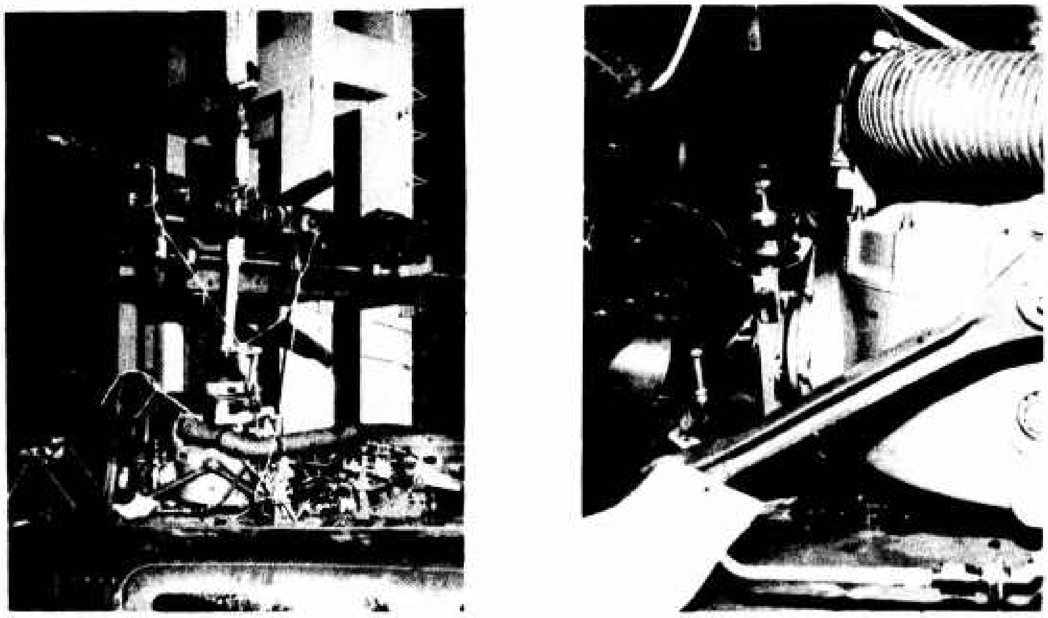

a) View of Crank Assembly b) Vertical Excitation

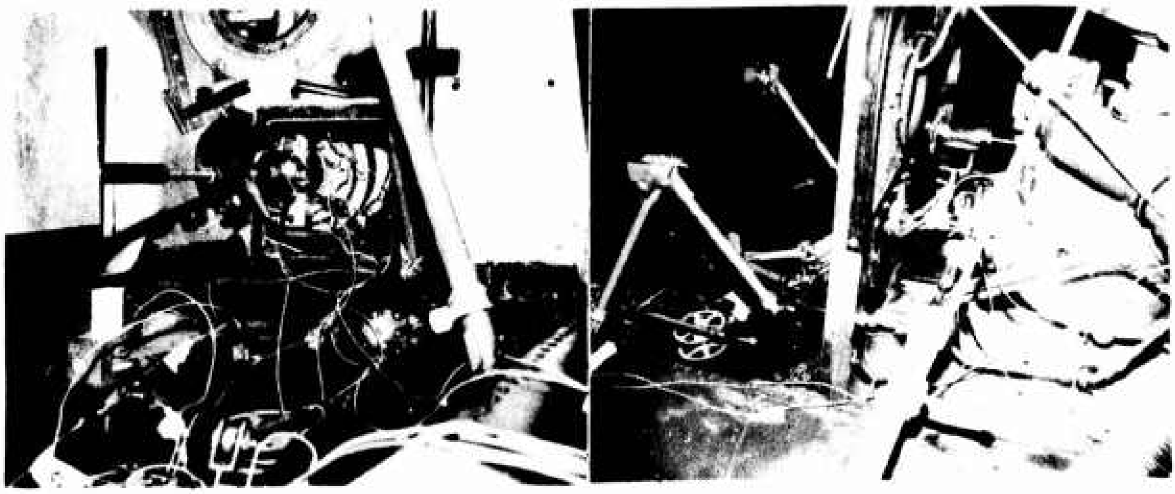

c) Longitudinal Excitation d) Lateral Excitation

Figure 92. Arrangement of Exciter and Crank Assembly for Excitation at Main Transmission Input Shaft.

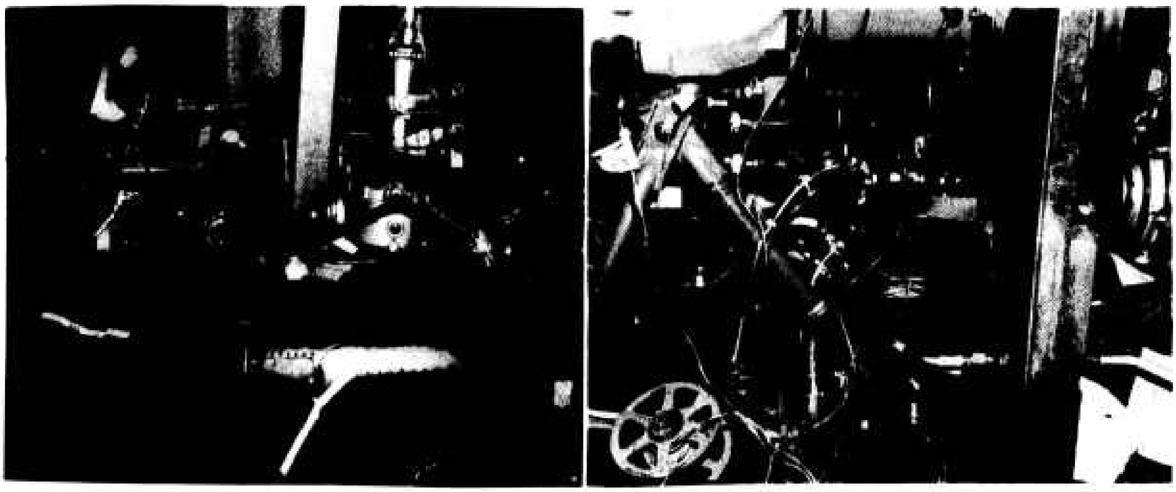

a) Crank Assembly   b) Longitudinal Excitation

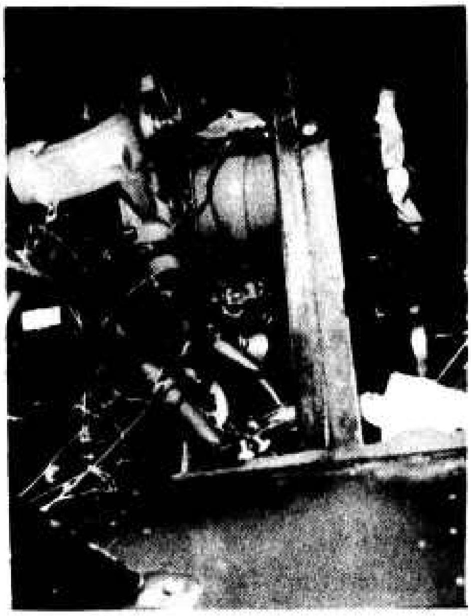

c) Lateral Excitation

Figure 93. Arrangement of Exciter and Crank Assembly for Excitation at Engine Output Shaft.

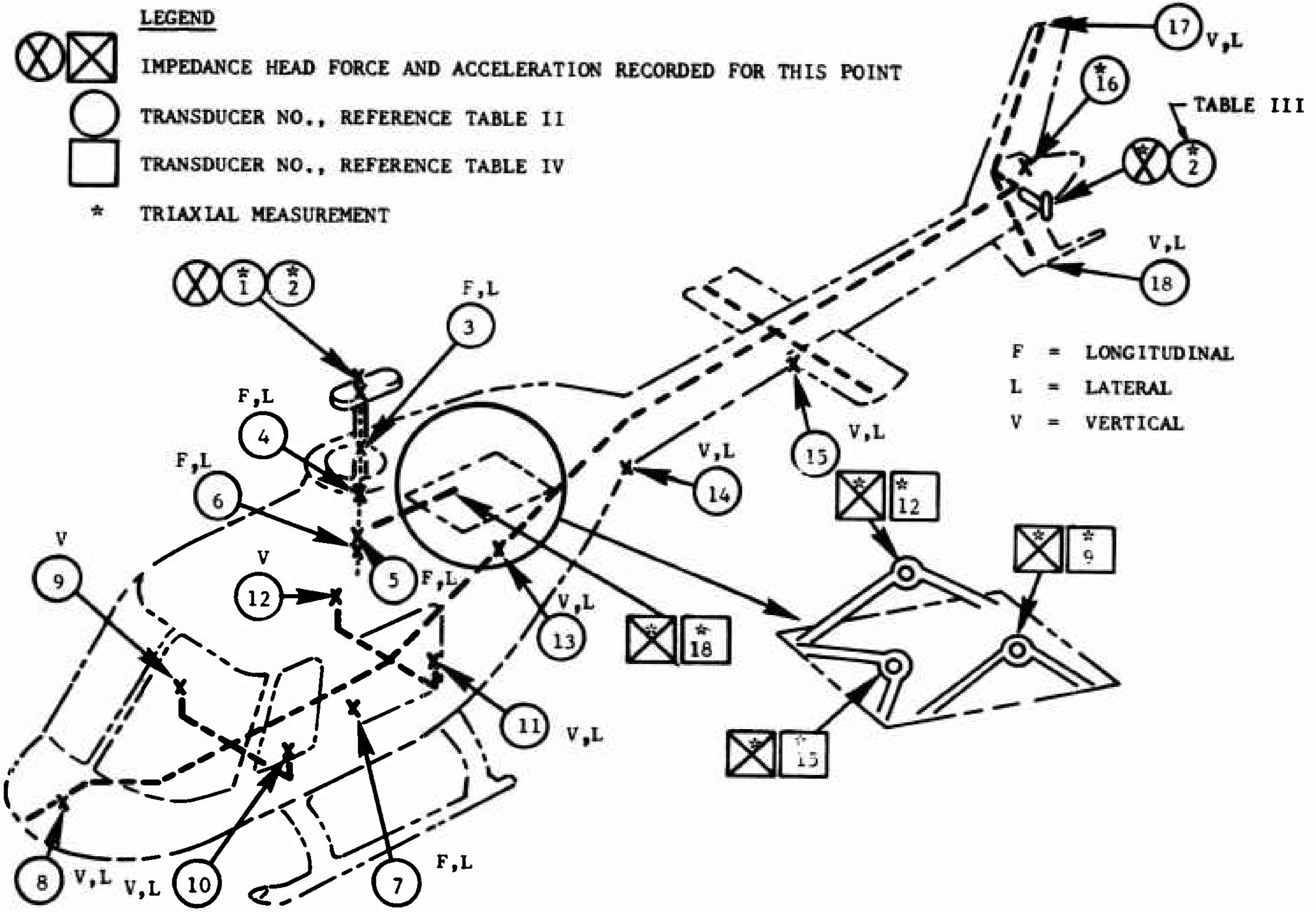

Figure 94. Approximate Location of Fuselage-Mounted Transducers.

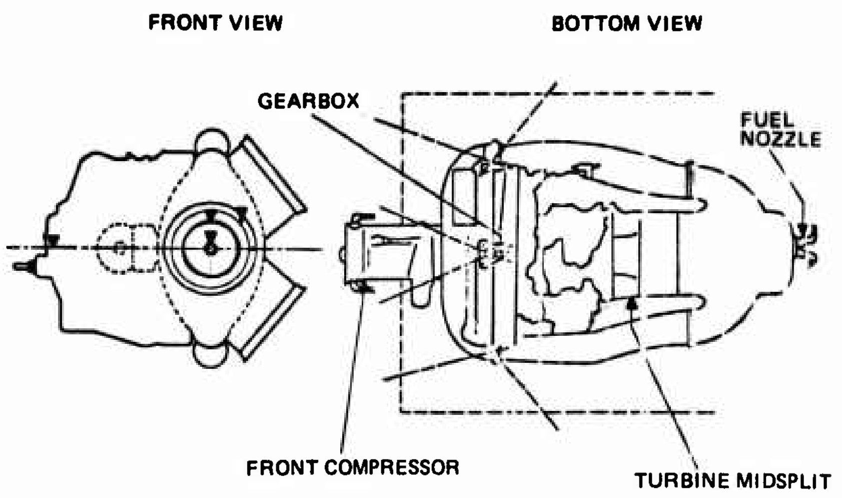

a) Lateral

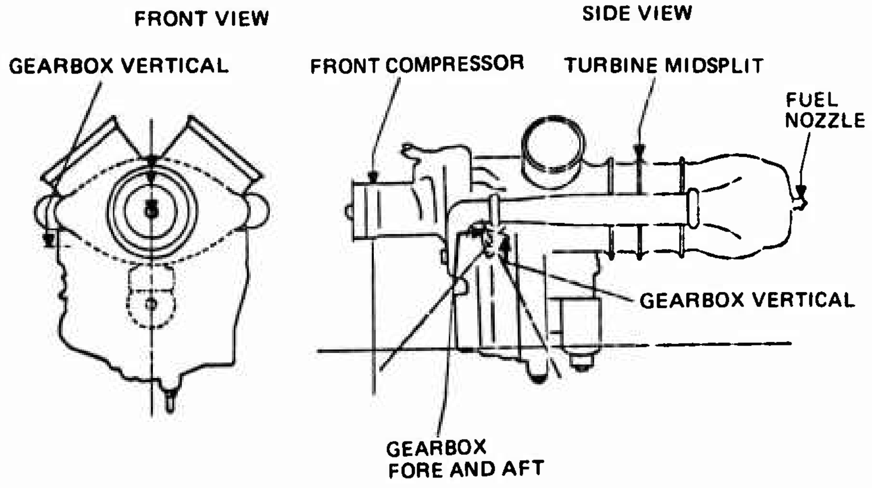

b) Vertical and Longitudinal

Figure 95. Approximate Location of Engine-Mounted Transducers.

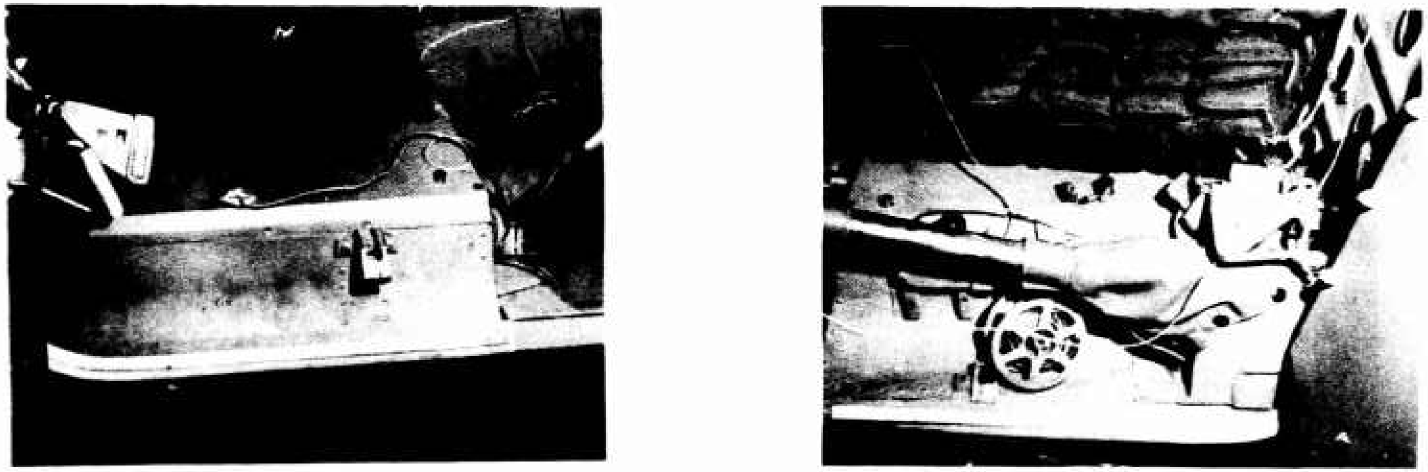

a) Pilot Seat

b) Copilot Seat

c) Fuselage at Elevator

d) Vertical Fin

Figure 96. Typical Installations of Vertically Mounted Airframe Transducers.

a) Fuselage Nose

b) Baggage Compartment

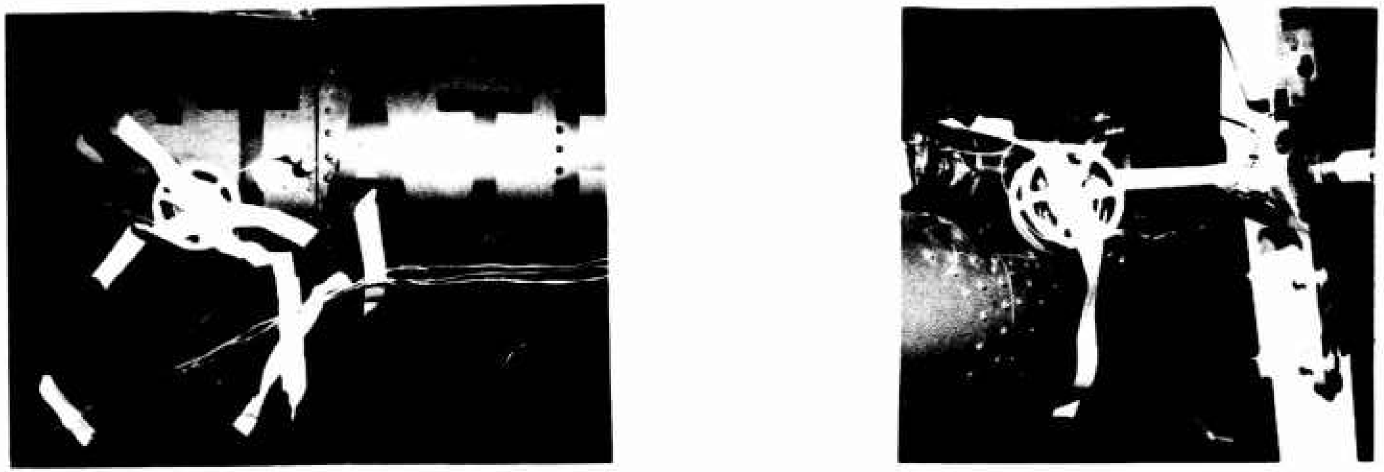

c) Fuselage at Tail Boom Joint

d) Tail Rotor Gearbox

Figure 97. Typical Installations of Laterally Mounted Airframe Transducers.

a) Transmission

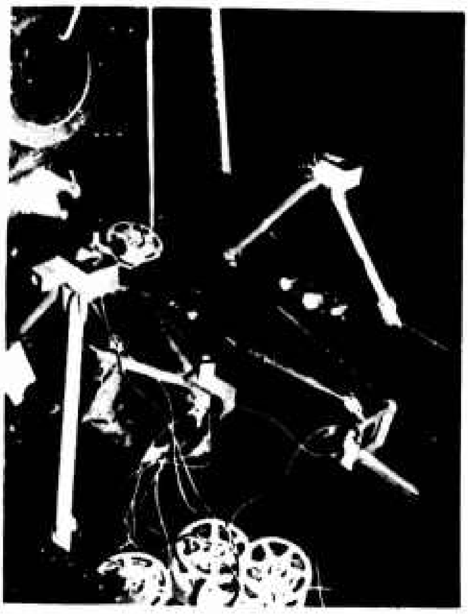

b) Engine Bipods

Figure 98. Typical Installations of Triaxial Transducers on Engine Bipods and Main Transmission.

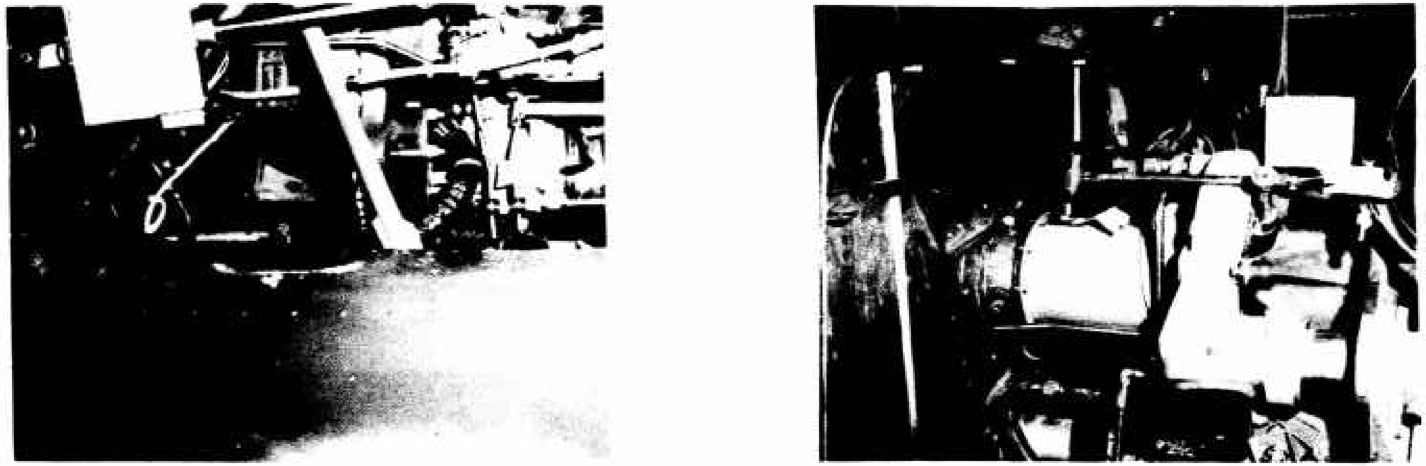

a) Gearbox Lateral

b) Front Compressor Vertical

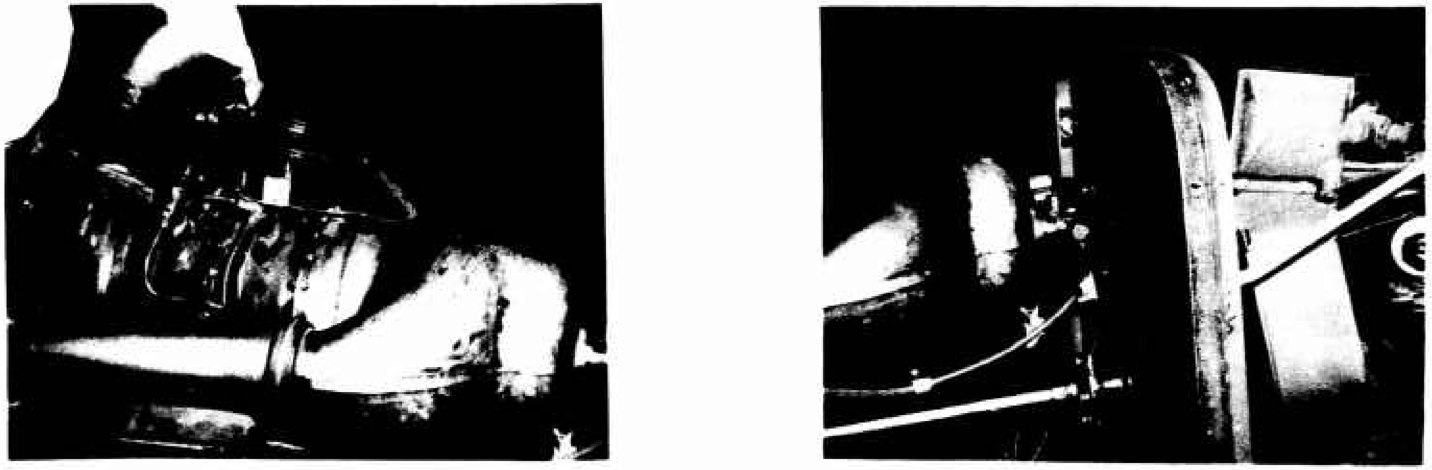

c) Turbine Midsplit Vertical

d) Fuel Nozzle Vertical and Lateral

Figure 99. Typical Installations of Engine-Mounted Transducers.

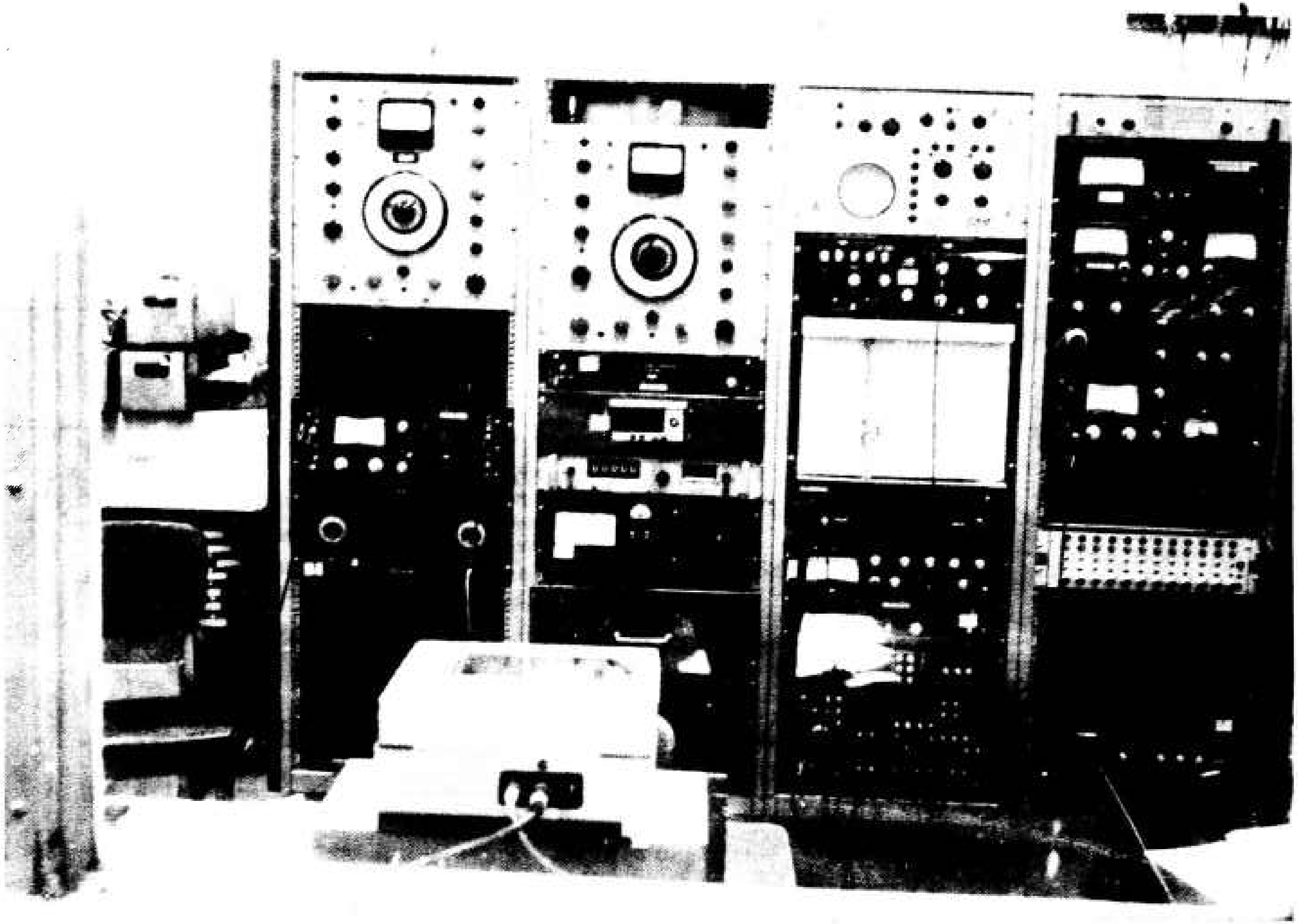

Figure 100. Data Acquisition System.

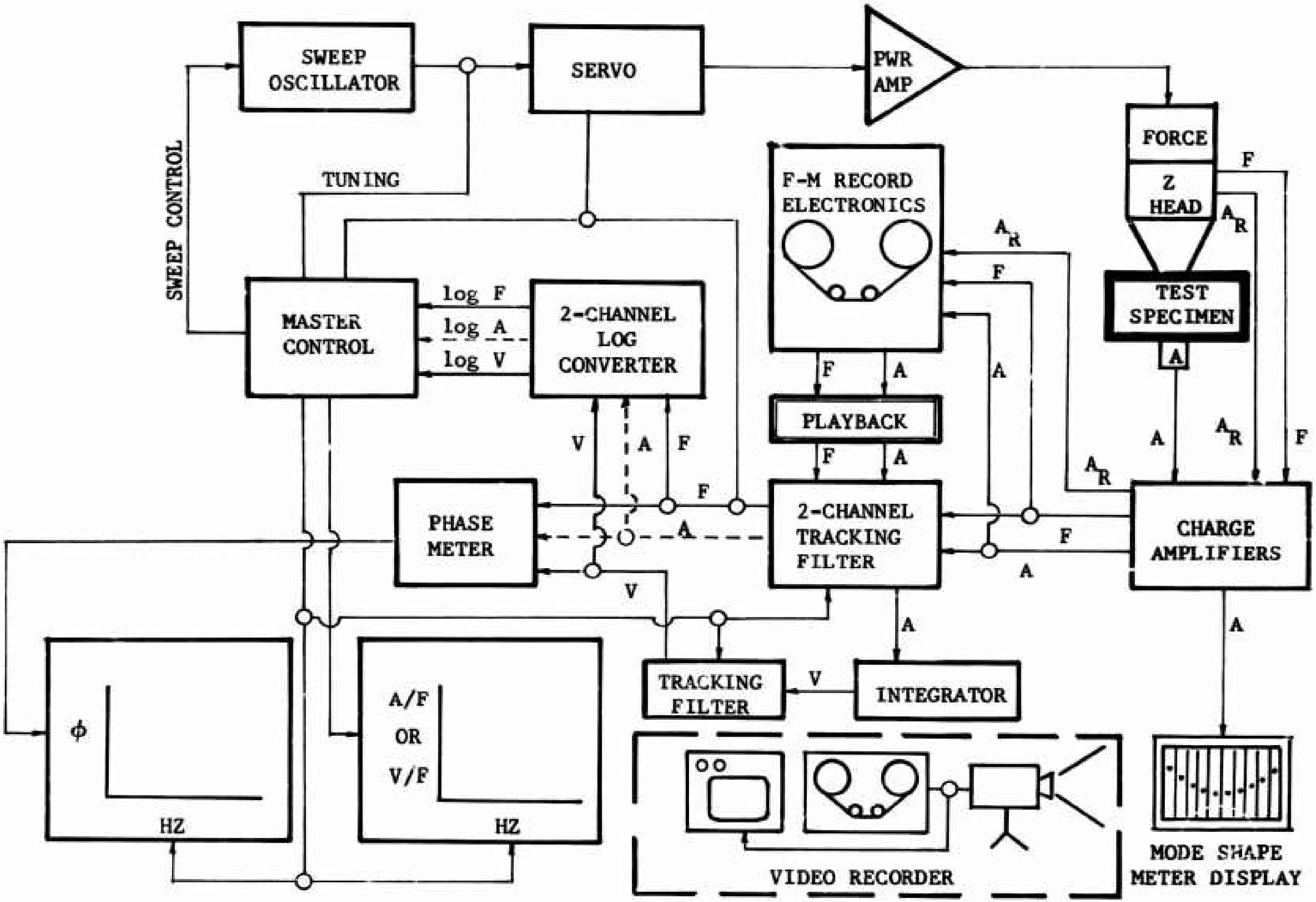

Figure 101. Block Diagram of Ground Vibration Test Data Acquisition System.

FORCED COORDINATES			RESPONSE COORDINATES											
			XMSN INPUT SHAFT			LEFT BIPOD			RIGHT BIPOD			LOWER BIPOD		
			Z	Y	X	Z	Y	X	Z	Y	X	Z	Y	X
			7	8	-9	10	-11	12	13	14	15	-16	17	18
XMSN INPUT SHAFT	Z	-7	70 6	70 5	70 4	71 6	71 5	71 4	71 1	71 2	70 3	70 1	70 2	70 3
XMSN INPUT SHAFT	Y	8	56 6	56 5	56 4	57 1	57 3	57 2	57 6	57 5	57 4	56 1	56 3	56 2
XMSN INPUT SHAFT	X	9	75 6	75 5	75 4	76 3	76 2	76 1	76 6	76 5	76 4	75 3	75 2	75 1
LEFT BIPOD	Z	-10	69 4	69 2	69 3	68 4	68 3	68 2	68 1	68 6	68 5	69 1	69 6	69 5
LEFT BIPOD	Y	-11	62 6	62 5	62 4	63 3	63 1	63 2	63 6	63 5	63 4	62 3	62 1	62 2
LEFT BIPOD	X	12	74 2	74 3	74 4	73 3	73 2	73 1	73 6	73 5	73 4	74 6	74 5	74 1
RIGHT BIPOD	Z	-13	65 6	65 5	65 4	64 4	64 3	64 2	64 1	64 6	64 5	65 1	65 3	65 2
RIGHT BIPOD	Y	14	60 6	60 5	60 4	58 6	58 4	58 5	58 2	58 1	58 3	60 3	60 1	60 2
RIGHT BIPOD	X	15	80 6	80 5	80 4	81 6	81 5	81 1	81 2	81 3	81 4	80 3	80 2	80 1
LOWER BIPOD	Z	-16	66 6	66 5	66 4	67 6	67 5	67 4	67 1	67 2	67 3	66 1	66 3	66 2
LOWER BIPOD	Y	17	83 2	83 3	83 4	82 3	82 1	82 2	82 6	82 5	82 4	83 6	83 1	83 5
LOWER BIPOD	X	18	79 6	79 5	79 4	78 6	78 5	78 1	78 2	78 3	78 4	79 2	79 3	79 1

RESPONSE I. D.

EXCITATION I. D.

TEST RUN NO.

PLOT NO.

ELEMENT DATA

Figure 102. Test Log Matrix for Airframe Mobility Matrix, $[Y_{EE}]$.

			REPONSE COORDINATE											
			XMSN INPUT SHAFT			LEFT BIPOD			RIGHT BIPOD			LOWER BIPOD		
			Z	Y	X	Z	Y	X	Z	Y	X	Z	Y	X
FORCED COORDINATE			7	8	-9	10	-11	12	13	14	15	-16	17	18
MAIN ROTOR	Z	-1	86 6	86 5	86 4	87 4	87 3	87 2	87 1	87 6	87 5	86 1	86 3	86 2
MAIN ROTOR	Y	2	55 6	55 5	55 4	53 1	53 3	53 2	53 6	53 5	53 4	55 1	55 3	55 2
MAIN ROTOR	X	-3	50 6	50 5	50 4	51 1	51 3	51 2	51 6	51 5	51 4	50 1	50 3	50 2
TAIL ROTOR	Z	4	45 6	45 5	45 4	42 2	42 3	42 4	42 7	42 6	42 5	45 1	45 3	45 2
TAIL ROTOR	Y	-5	49 6	49 5	49 4	48 1	48 3	48 2	48 6	48 5	48 4	49 1	49 3	49 2
TAIL ROTOR	X	6	46 6	46 5	46 4	47 1	47 3	47 2	47 6	47 5	47 4	46 1	46 3	46 2

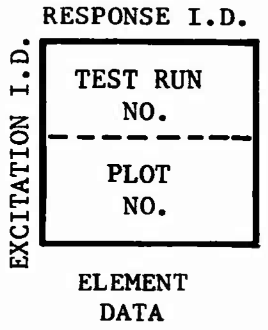

Figure 103. Test Log Matrix for Airframe Mobility Matrix, $\lfloor Y_{EI} \rfloor$.

			RESPONSE COORDINATE								
			TURBINE MIDSPLIT		FORWARD COMPRESS.		IGNITER		ENGINE GEARBOX		
			Z	Y	Z	Y	Z	Y	Z	Y	X
FORCED COORDINATE			19	-20	21	-22	23	24	25	26	27
MAIN ROTOR	Z	-1	89 6	89 3	89 1	89 2	89 5	89 9	89 4	89 8	89 7
MAIN ROTOR	Y	2	90 6	90 3	90 1	90 2	90 5	90 9	90 4	90 8	90 7
MAIN ROTOR	X	-3	92 6	92 3	92 1	92 2	92 5	92 9	92 4	92 8	92 7
TAIL ROTOR	Z	4	95 3	95 8	95 1	95 7	95 10	95 6	95 9	95 5	95 4
TAIL ROTOR	Y	-5	94 3	94 8	94 1	94 7	94 10	94 6	94 9	94 5	94 4
TAIL ROTOR	X	6	93 6	93 3	93 1	93 2	93 5	93 9	93 4	93 8	93 7
ENGINE INPUT SHAFT	Z	-7	99 3	99 8	99 1	99 7	99 10	99 6	99 9	99 5	99 4
ENGINE INPUT SHAFT	Y	8	98 3	98 8	98 1	98 7	98 10	98 6	98 9	98 5	98 4
ENGINE INPUT SHAFT	X	9	100 3	100 8	100 1	100 7	100 10	100 6	100 9	100 5	100 4

RESPONSE I.D.

EXCITATION I.D.

ELEMENT DATA
REST RUN NO.
PLOT NO.

Figure 104. Test Log Matrix for Engine Response Check Matrix $[Y_{CHK}]$.

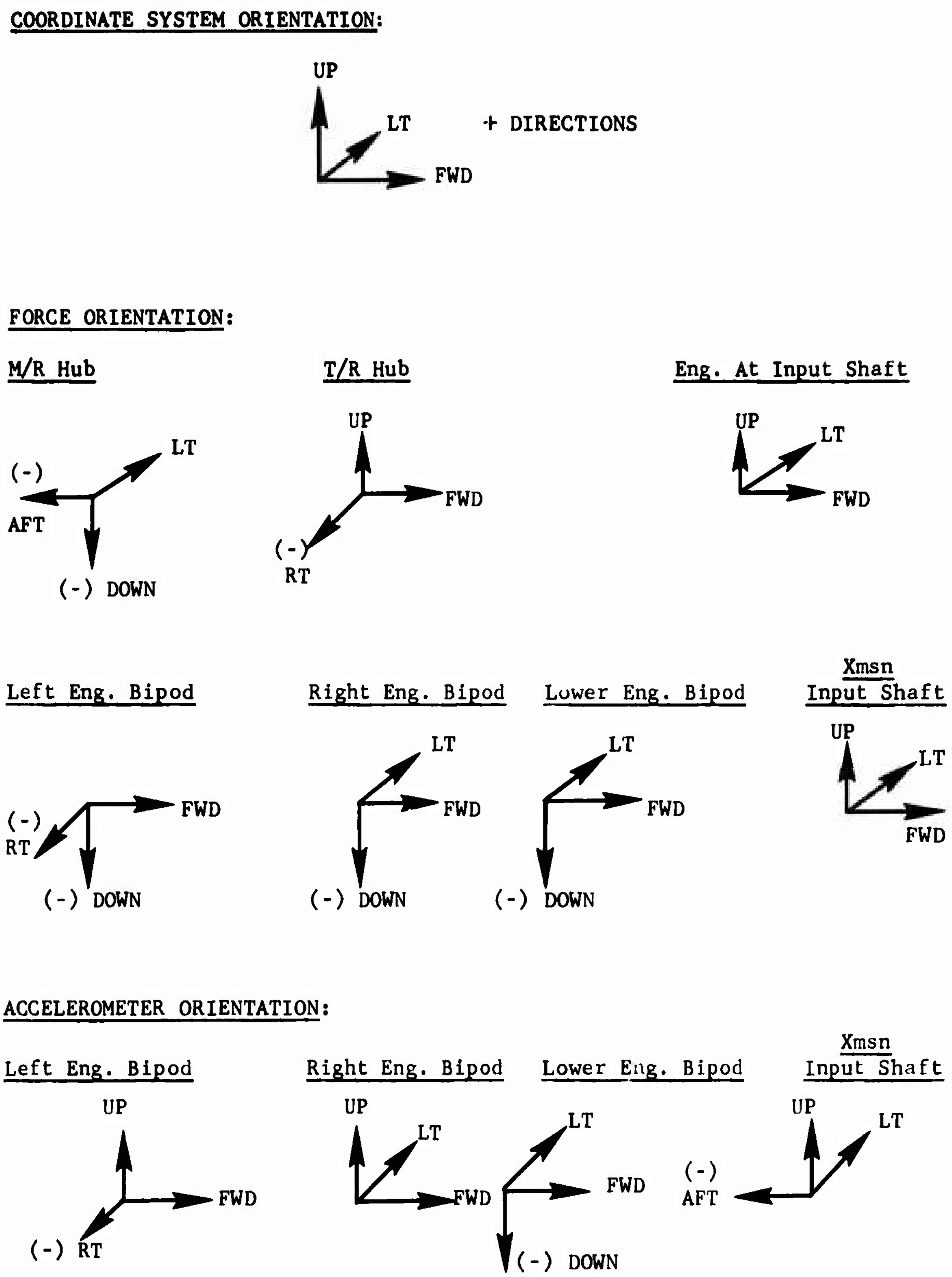

Figure 105. Coordinate System, Force, and Transducer Orientations.

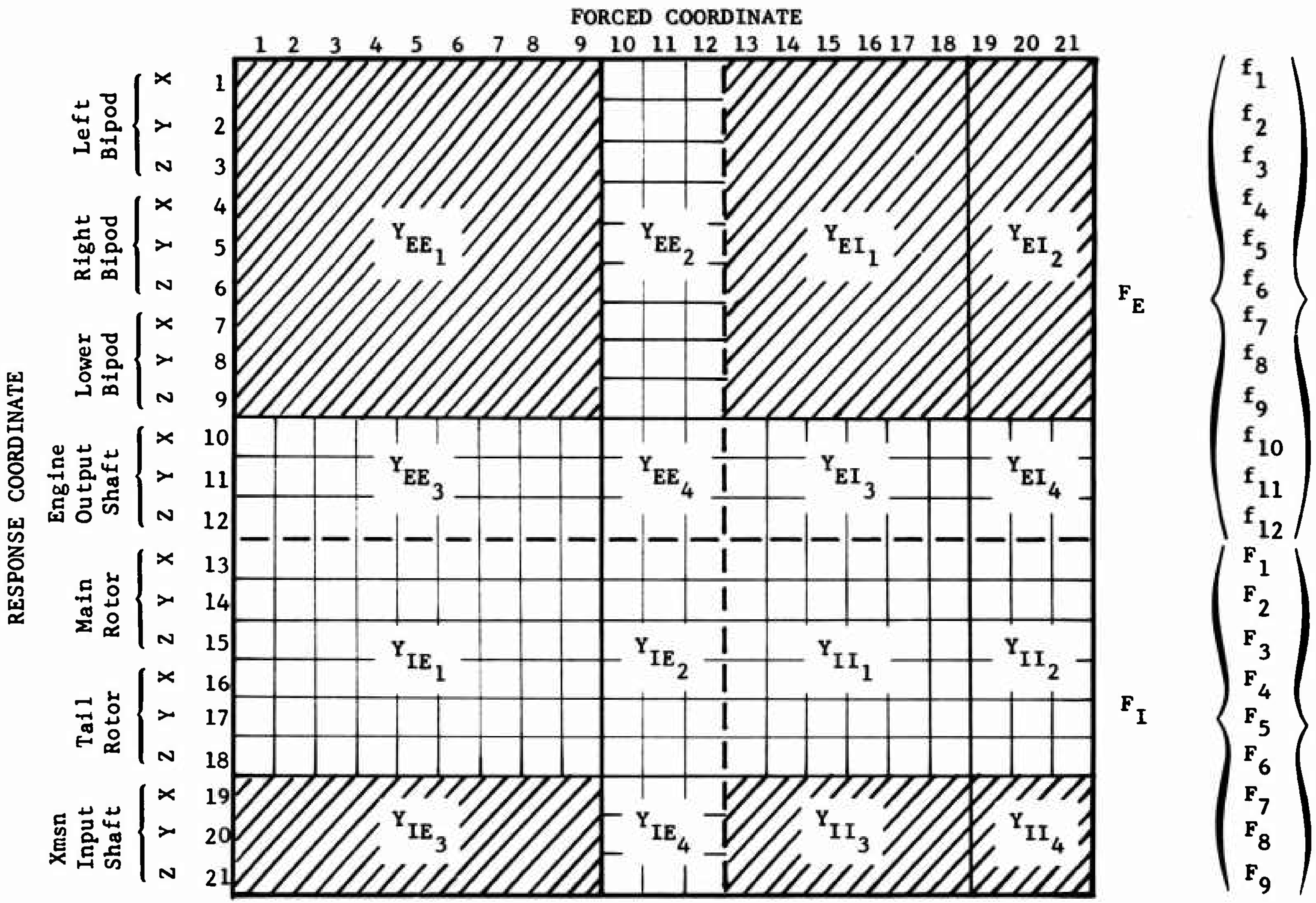

Figure 106. Partitioning for the Airframe Mobility Matrix.

X DATA REQUIRED FOR ANALYSIS

O DATA FURNISHED BUT NOT USED

			RESPONSE COORDINATE																			
			LEFT MOUNT			RIGHT MOUNT			LOWER MOUNT			OUTPUT SHAFT			TURBINE MIDSPLIT		FWD COMPRESS.		IGNITER		TOP GEARBOX	
			X	Y	Z	X	Y	Z	X	Y	Z	X	Y	Z	Y	Z	Y	Z	Y	Z	Y	Z
FORCED COORDINATE			1	2	3	4	5	6	7	8	9	10	11	12	13	14	15	16	17	18	19	20
LEFT ENGINE MOUNT	X	1	X	X	X	X	X	X	X	X	X	X	X	X	X	X	X	X	X	X	X	X
LEFT ENGINE MOUNT	Y	2	X	X	X	X	X	X	X	X	X	X	X	X	X	X	X	X	X	X	X	X
LEFT ENGINE MOUNT	Z	3	X	X	X	X	X	X	X	X	X	X	X	X	X	X	X	X	X	X	X	X
RIGHT ENGINE MOUNT	X	4	X	X	X	X	X	X	X	X	X	X	X	X	X	X	X	X	X	X	X	X
RIGHT ENGINE MOUNT	Y	5	X	X	X	X	X	X	X	X	X	X	X	X	X	X	X	X	X	X	X	X
RIGHT ENGINE MOUNT	Z	6	X	X	X	X	X	X	X	X	X	X	X	X	X	X	X	X	X	X	X	X
LOWER ENGINE MOUNT	X	7	X	X	X	X	X	X	X	X	X	X	X	X	X	X	X	X	X	X	X	X
LOWER ENGINE MOUNT	Y	8	X	X	X	X	X	X	X	X	X	X	X	X	X	X	X	X	X	X	X	X
LOWER ENGINE MOUNT	Z	9	X	X	X	X	X	X	X	X	X	X	X	X	X	X	X	X	X	X	X	X
ENGINE OUTPUT SHAFT	X	10	X	X	X	X	X	X	X	X	X	X	X	X	X	X	X	X	X	X	X	X
ENGINE OUTPUT SHAFT	Y	11	X	X	X	X	X	X	X	X	X	X	X	X	X	X	X	X	X	X	X	X
ENGINE OUTPUT SHAFT	Z	12	X	X	X	X	X	X	X	X	X	X	X	X	X	X	X	X	X	X	X	X
TURBINE MIDSPLIT	Y	13	O	O	O	O	O	O	O	O	O	O	O	O	O	O	O	O	O	O	O	O
TURBINE MIDSPLIT	Z	14	O	O	O	O	O	O	O	O	O	O	O	O	O	O	O	O	O	O	O	O
FORWARD COMPRESSOR	Y	15	O	O	O	O	O	O	O	O	O	O	O	O	O	O	O	O	O	O	O	O
FORWARD COMPRESSOR	Z	16	O	O	O	O	O	O	O	O	O	O	O	O	O	O	O	O	O	O	O	O

Figure 107. Engine Test Mobility Matrix.

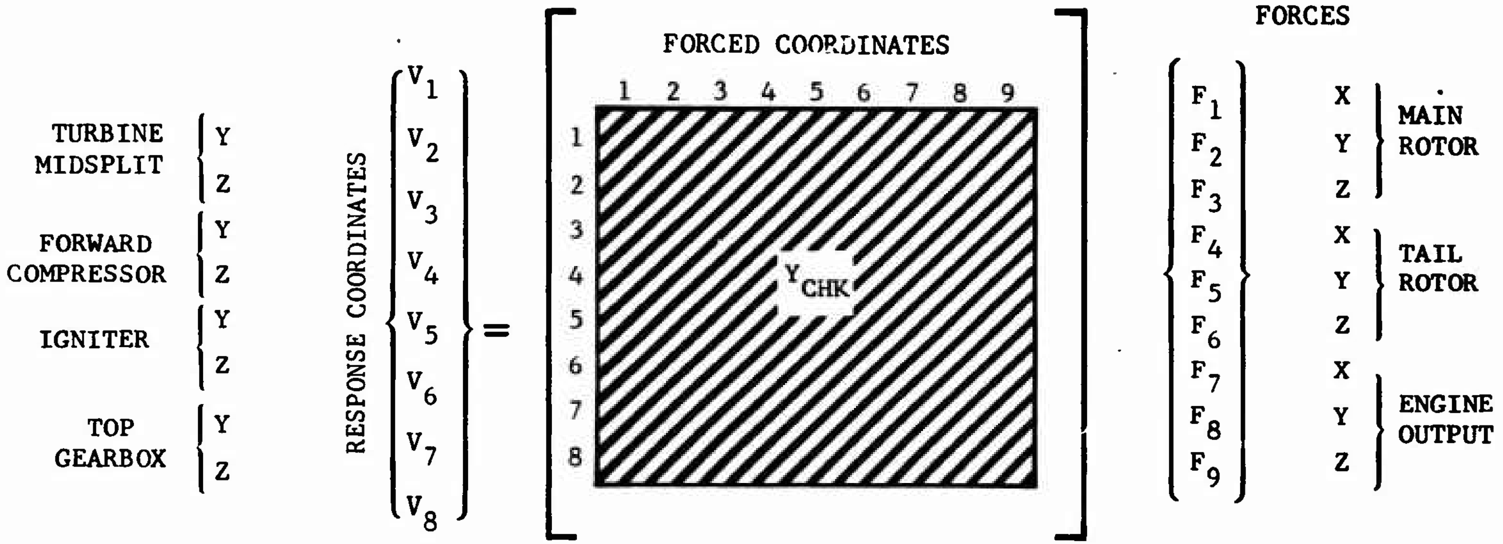

Figure 108. Engine Response Check Matrix.

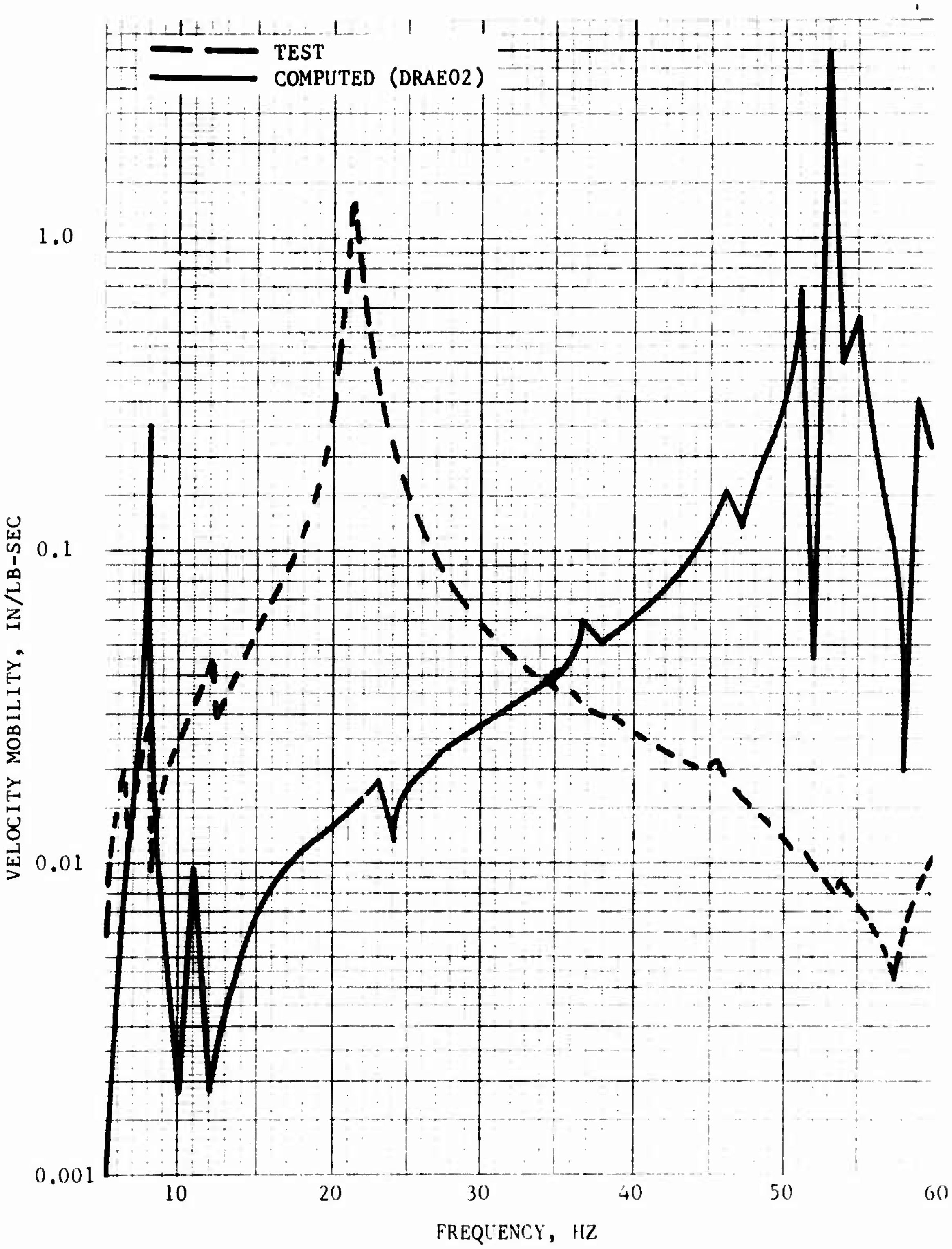

Figure 109. Comparison of Computed and Measured Left-Hand Engine Bipod Vertical Driving Point Mobility.

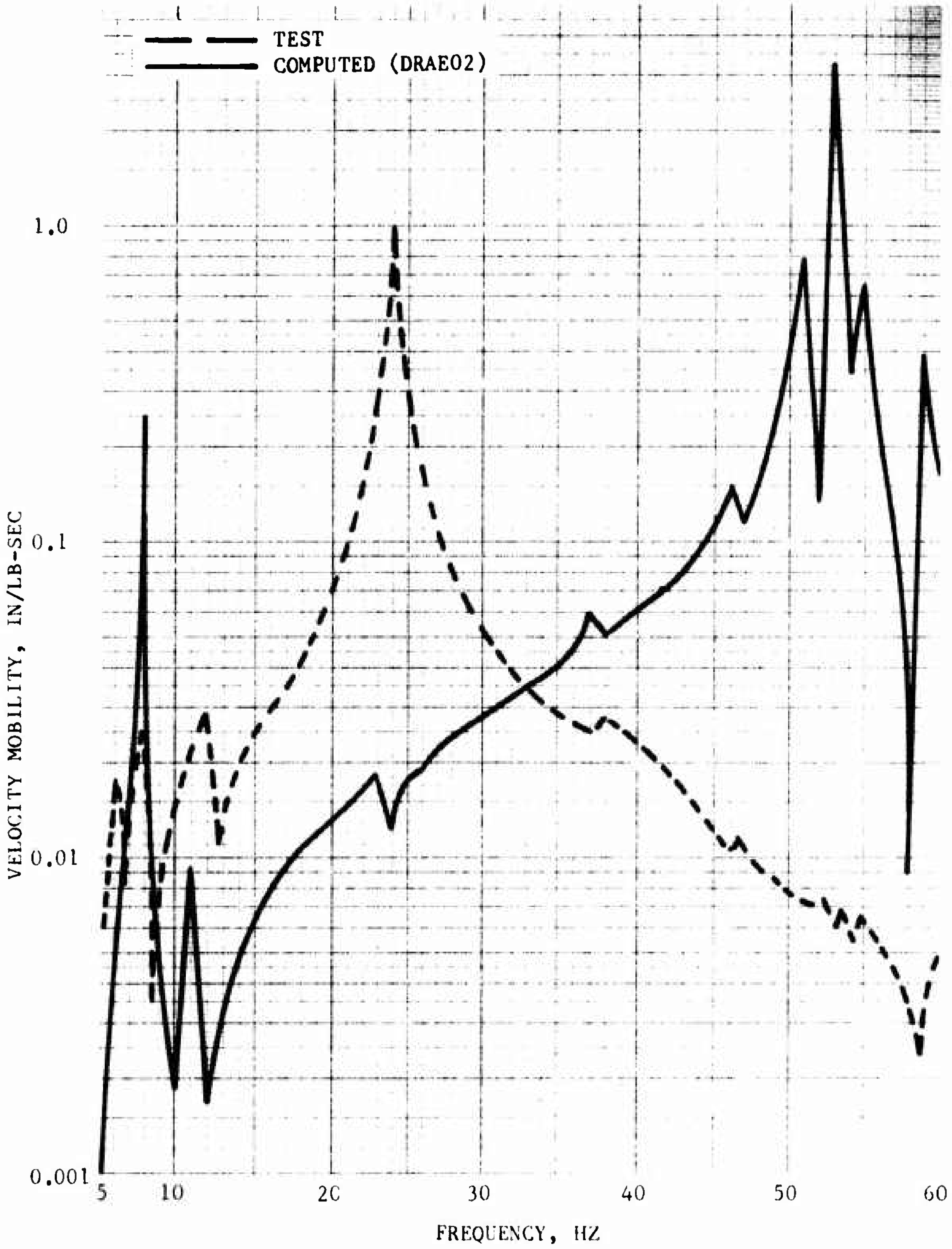

Figure 110. Comparison of Computed and Measured Right-Hand Engine Bipod Vertical Driving Point Mobility.

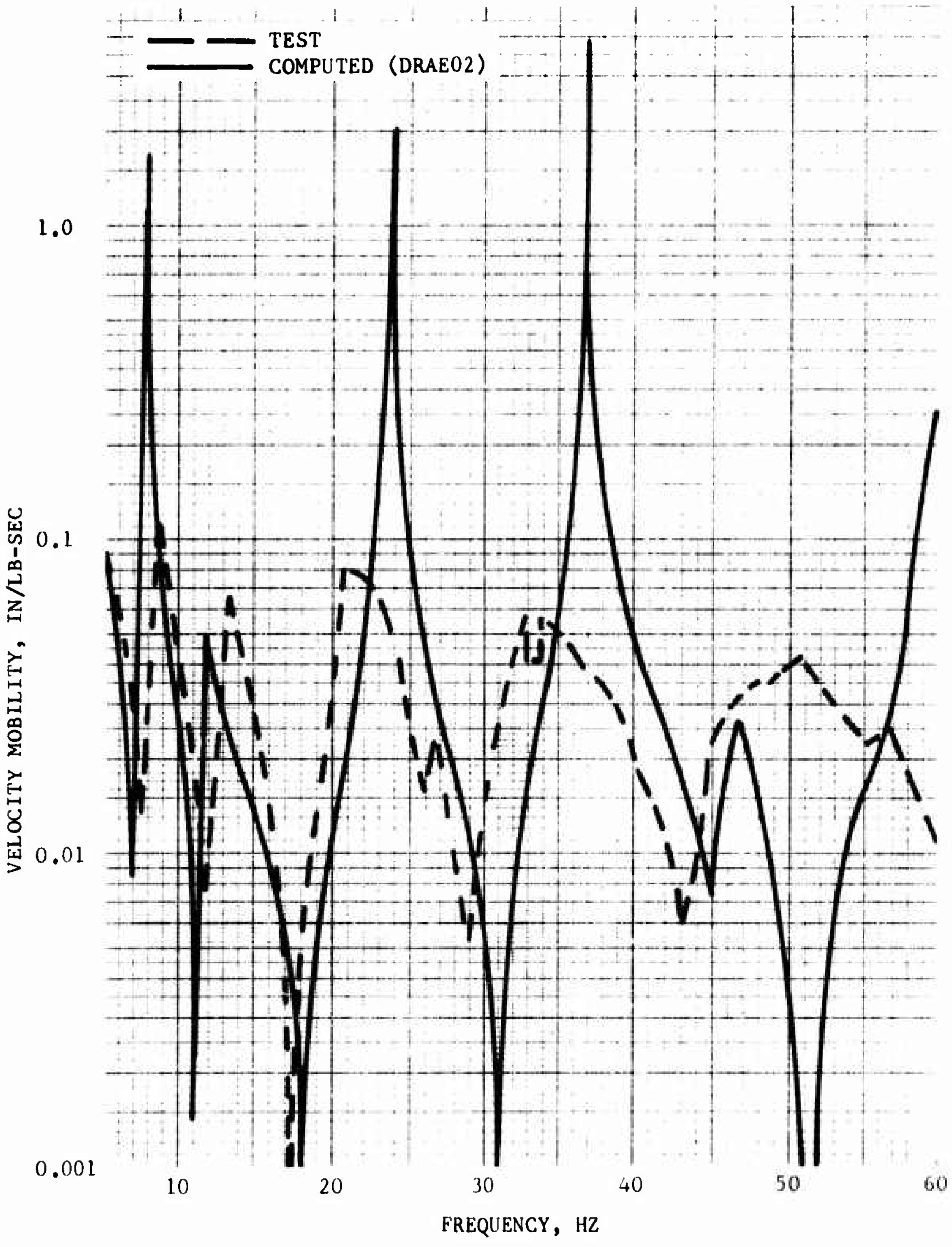

Figure 111. Comparison of Computed and Measured Lower Engine Bipod Longitudinal Driving Point Mobility.

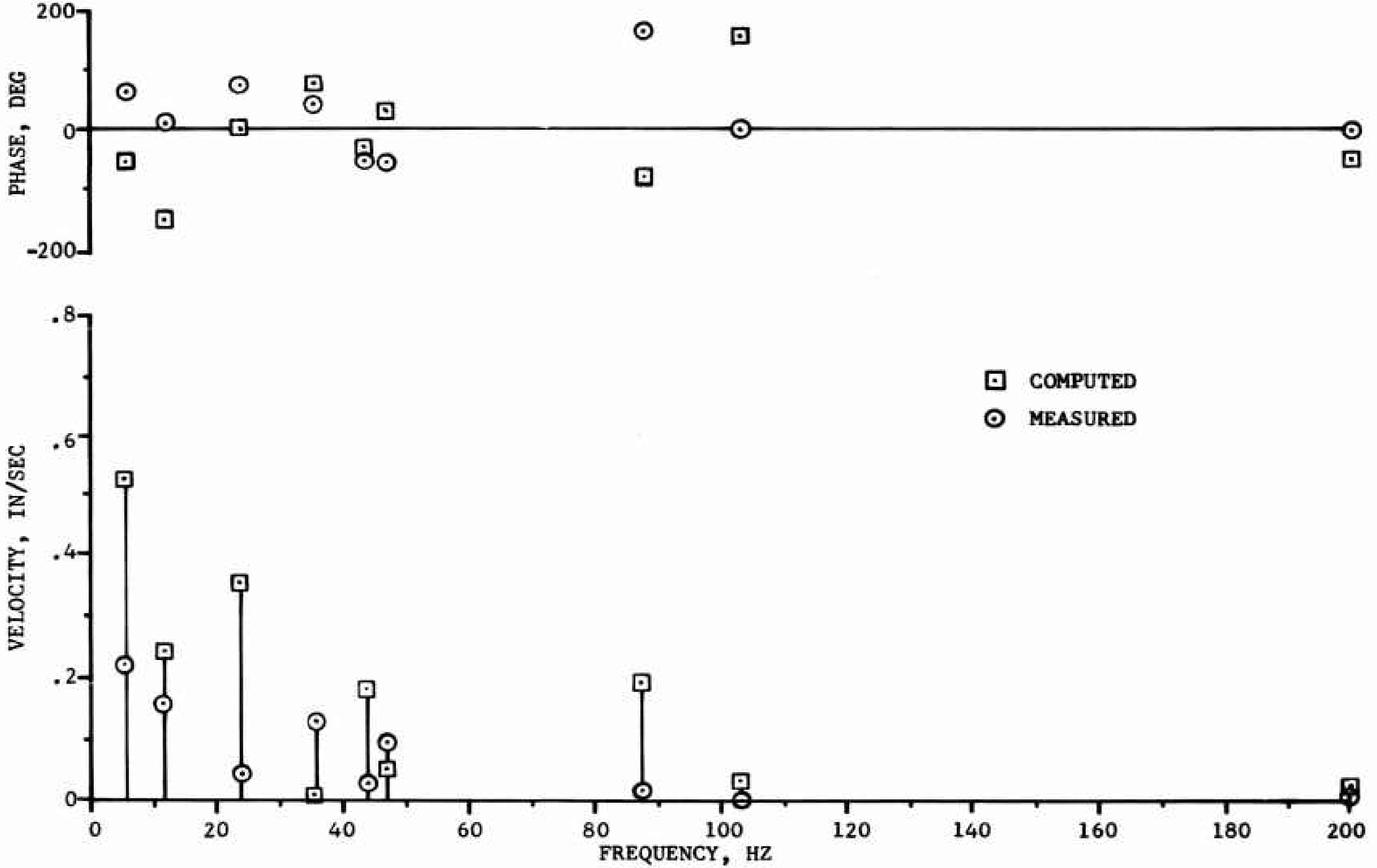

Figure 112. Comparison of Computed (DRAE04) and Measured Shake Test Engine Forward Compressor Vertical Velocity.

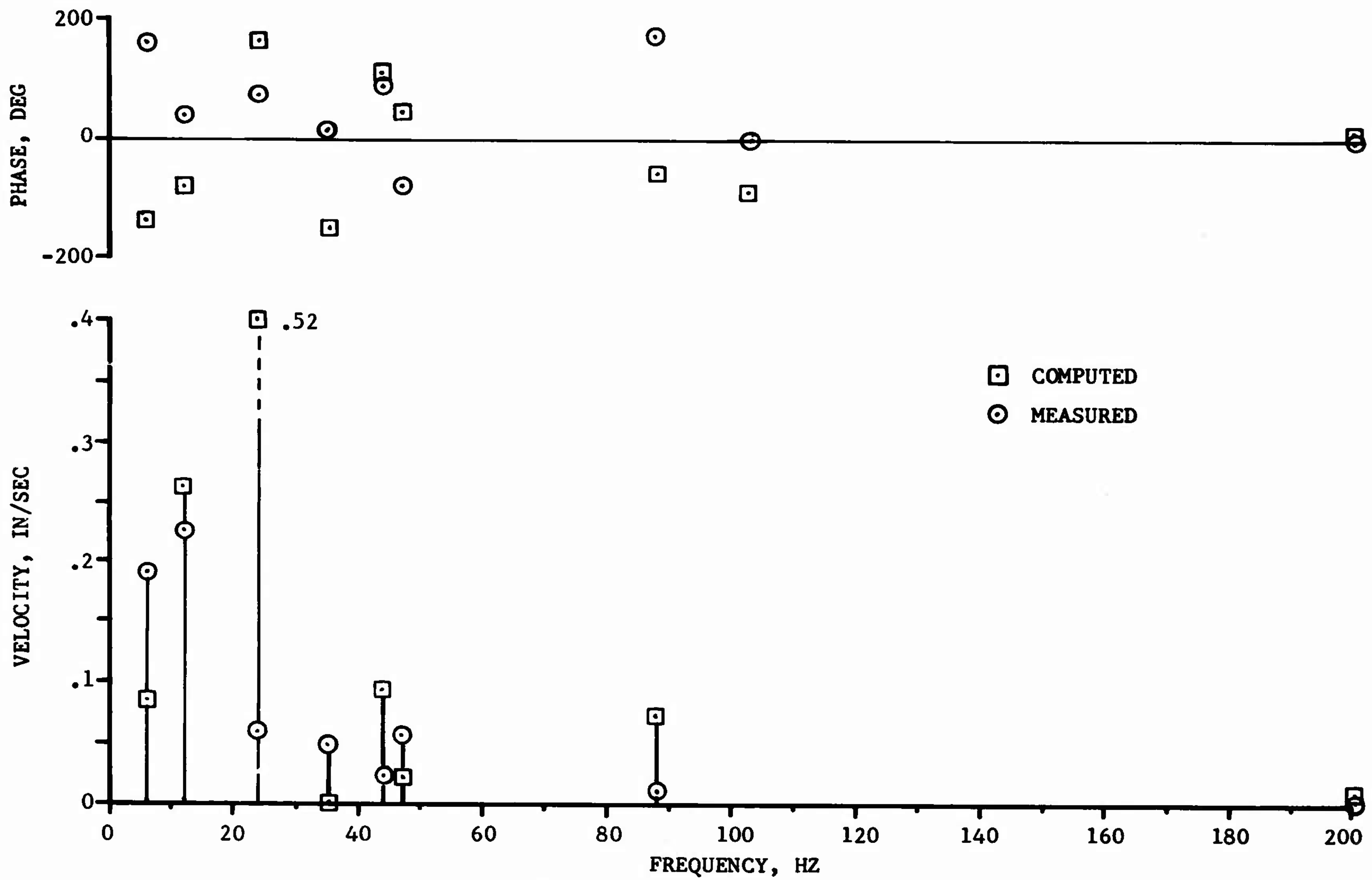

Figure 113. Comparison of Computed (DRAE04) and Measured Shake Test Engine Gearbox Vertical Velocity.

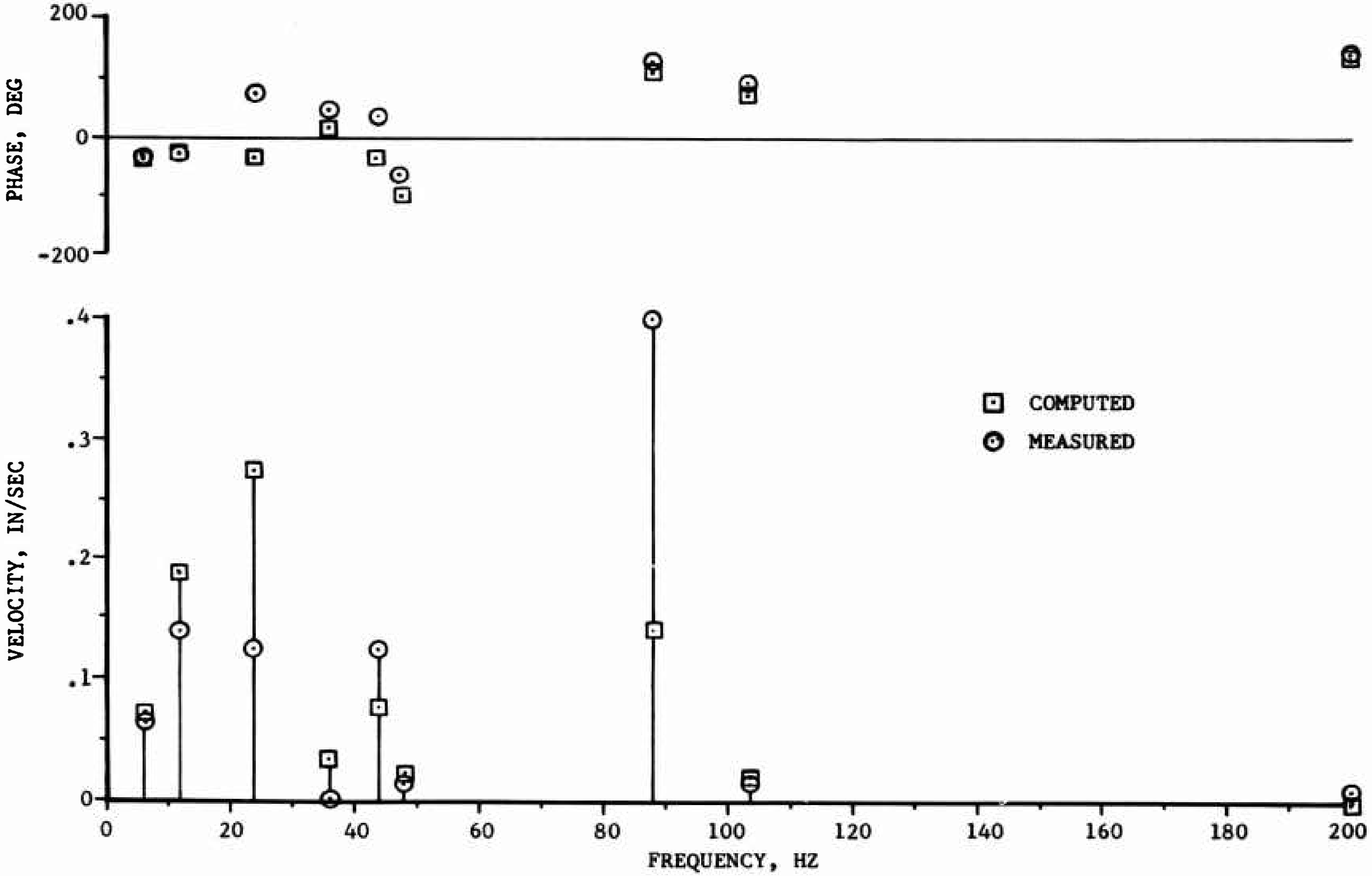

Figure 114. Comparison of Computed (DRAE04) and Measured Shake Test Engine Turbine Midsplit Vertical Velocity.

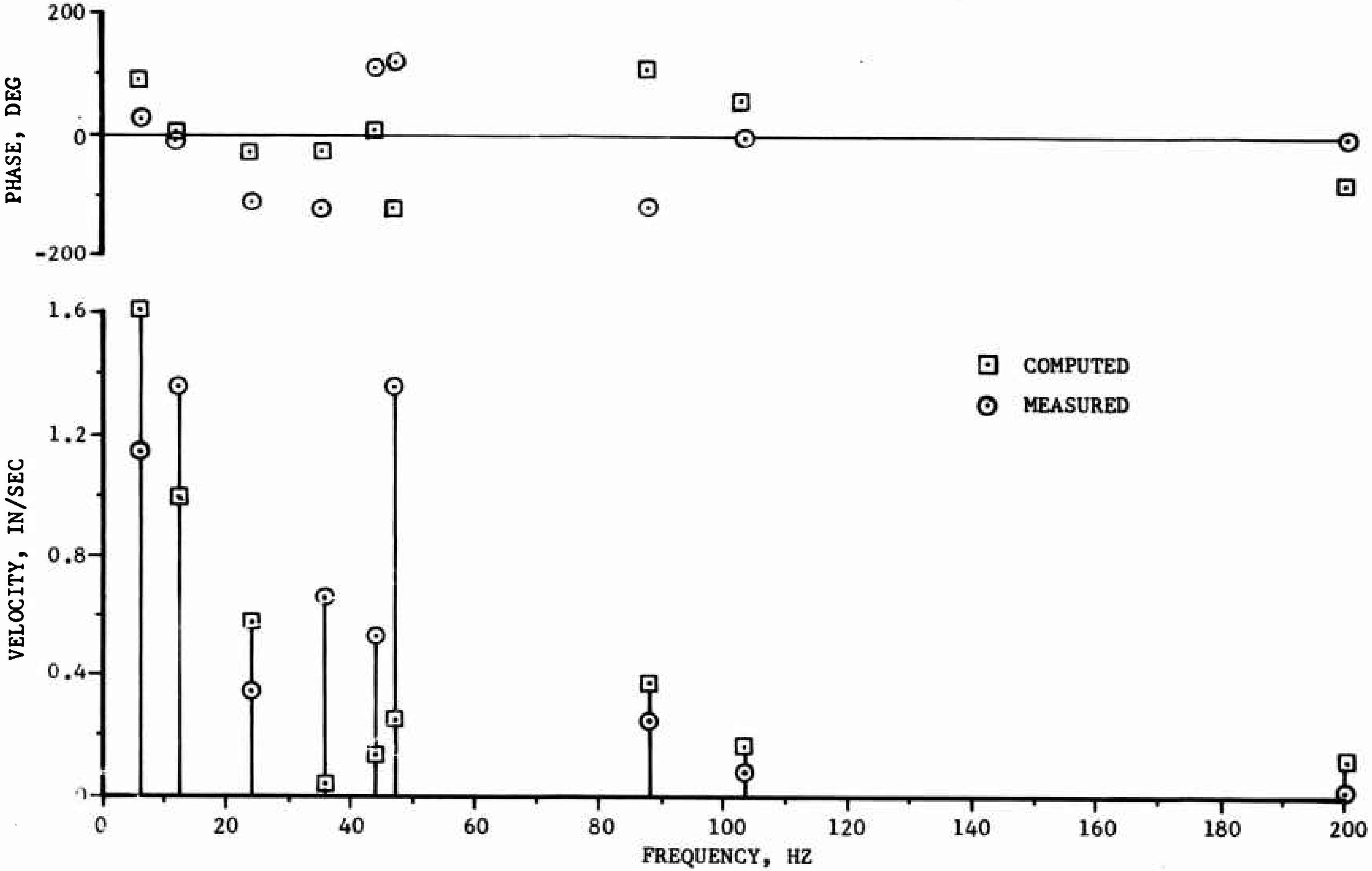

Figure 115. Comparison of Computed (DRAE04) and Measured Shake Test Engine Fuel Nozzle Vertical Velocity.

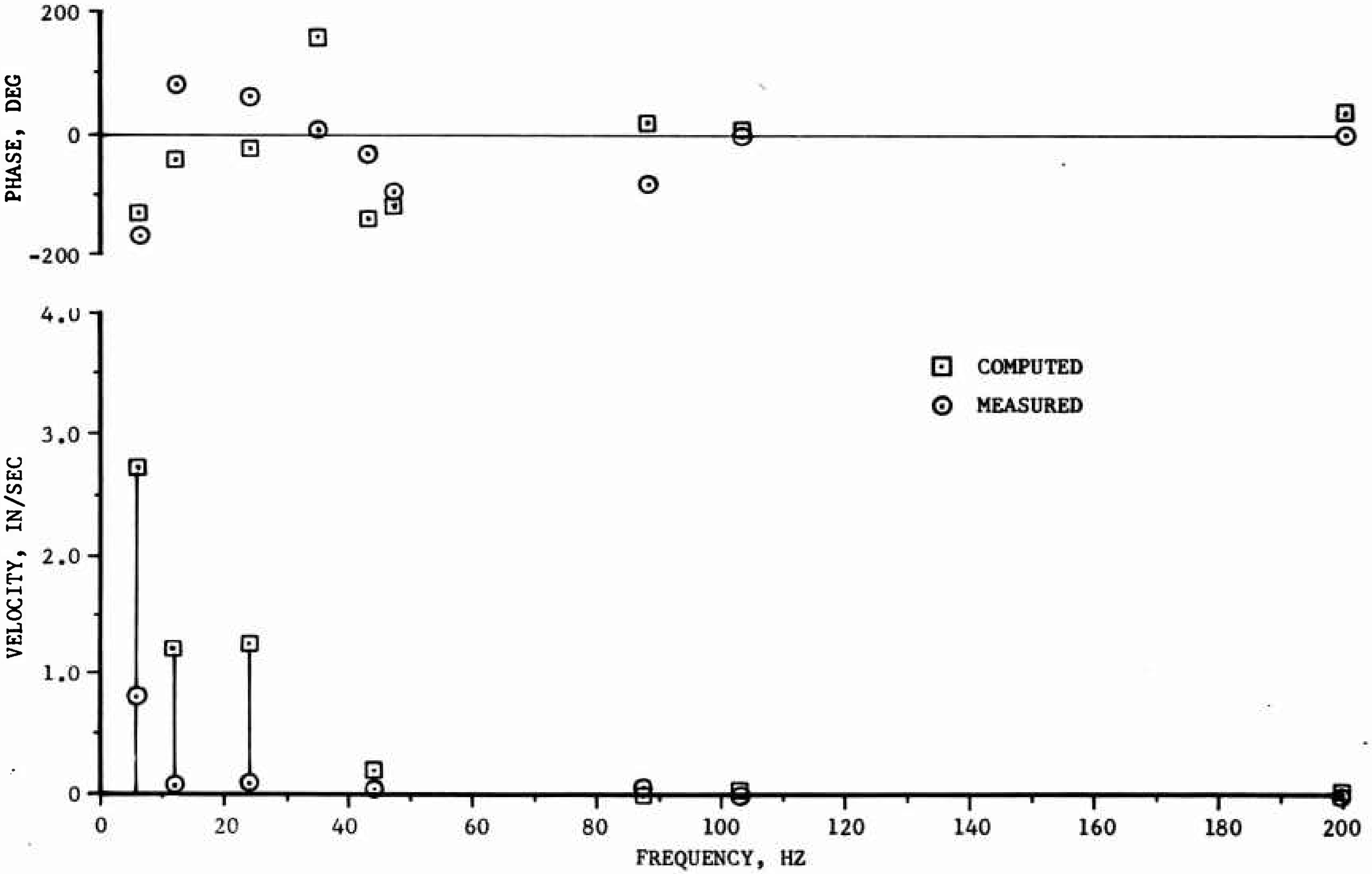

Figure 116. Comparison of Computed (DRAE04) and Measured Shake Test Engine Forward Compressor Lateral Velocity.

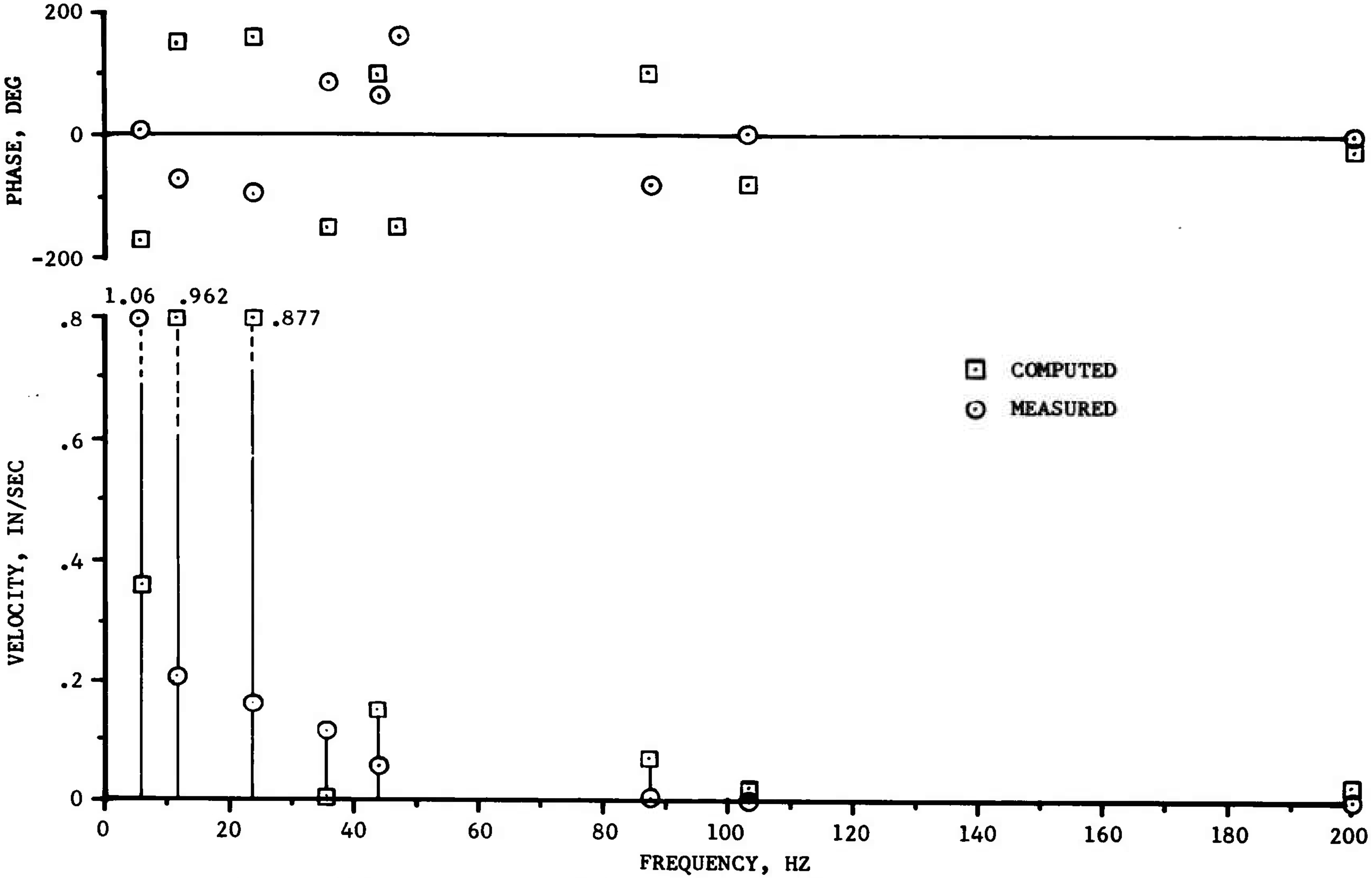

Figure 117. Comparison of Computed (DRAE04) and Measured Shake Test Engine Turbine Midsplit Lateral Velocity.

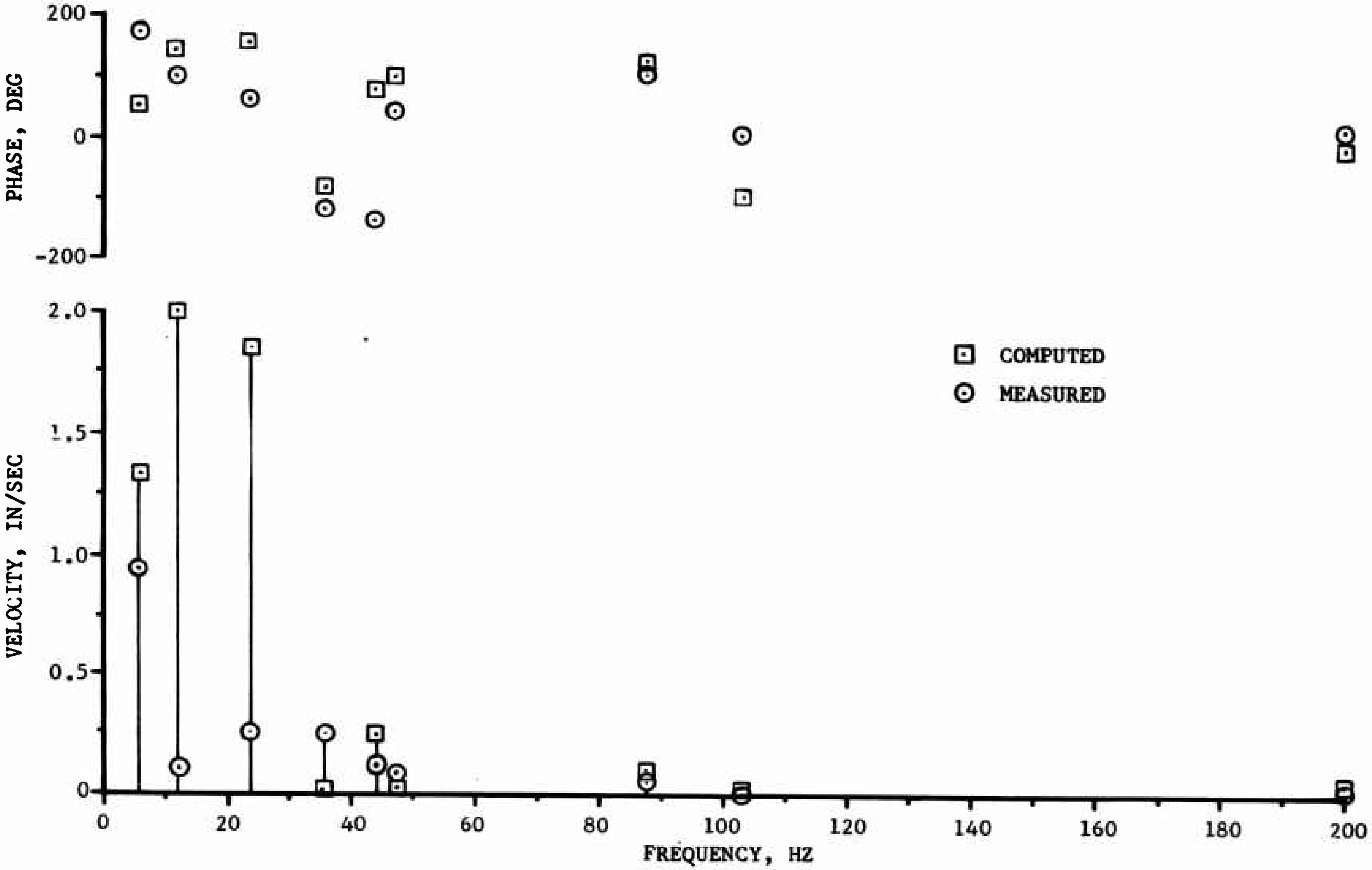

Figure 118. Comparison of Computed (DRAE04) and Measured Shake Text Engine Fuel Nozzle Lateral Velocity.

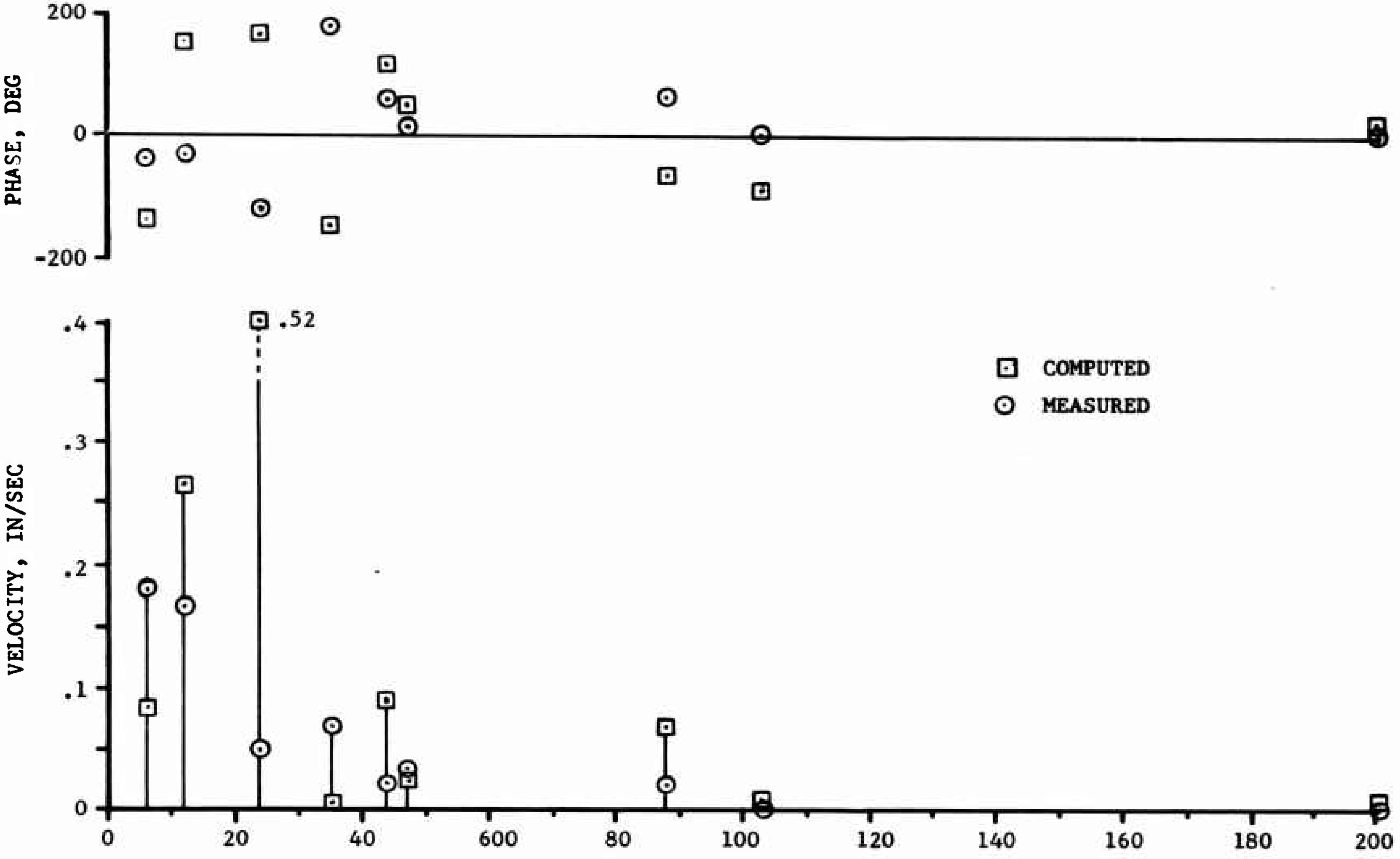

Figure 119. Comparison of Computed (DRAE04) and Measured Shake Test Engine Gearbox Longitudinal Velocity.

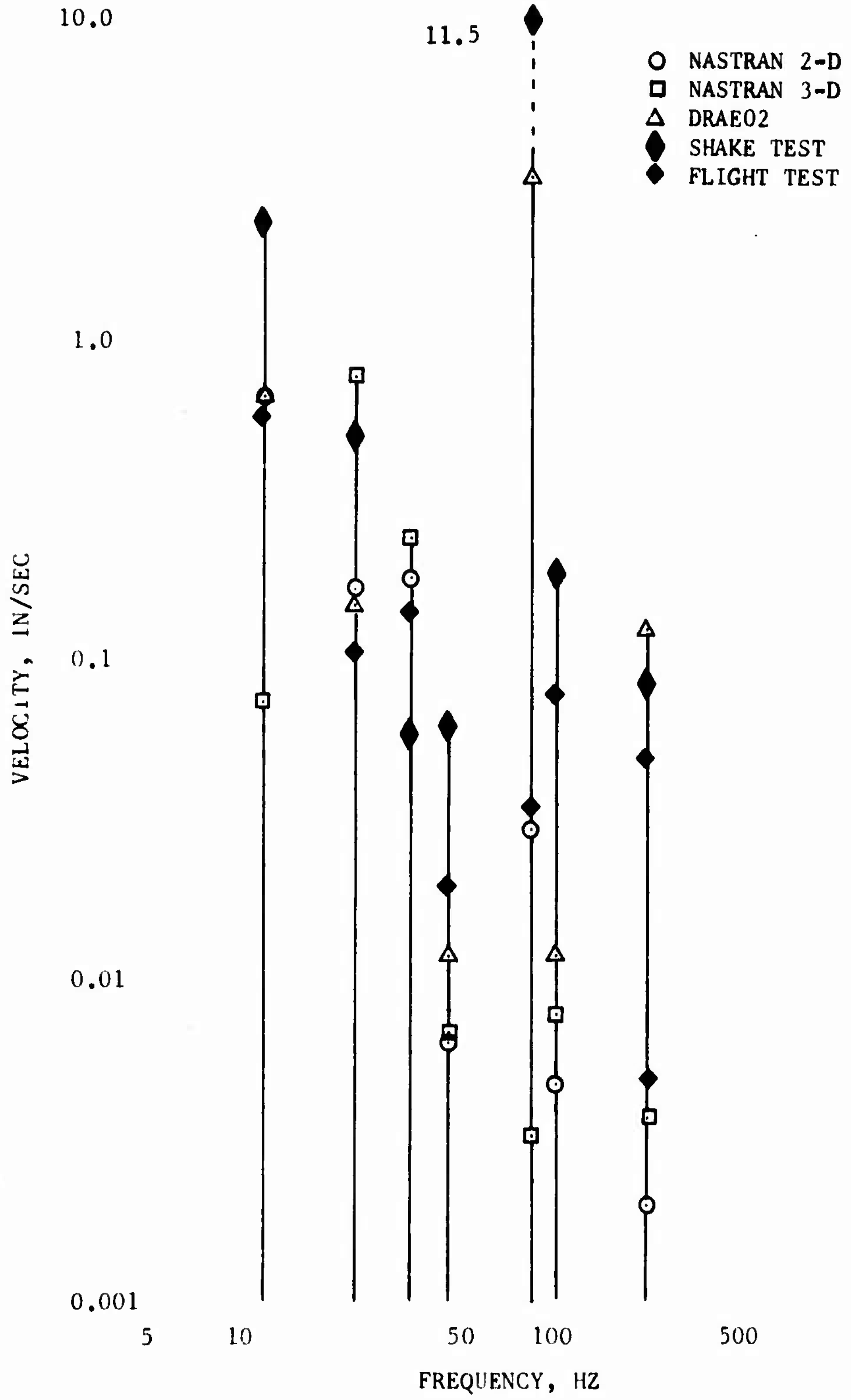

Figure 120. Comparison of Analytical and Test Engine Velocities for Simulated 110-Knot Level Flight Forces; Forward Compressor Vertical Response.

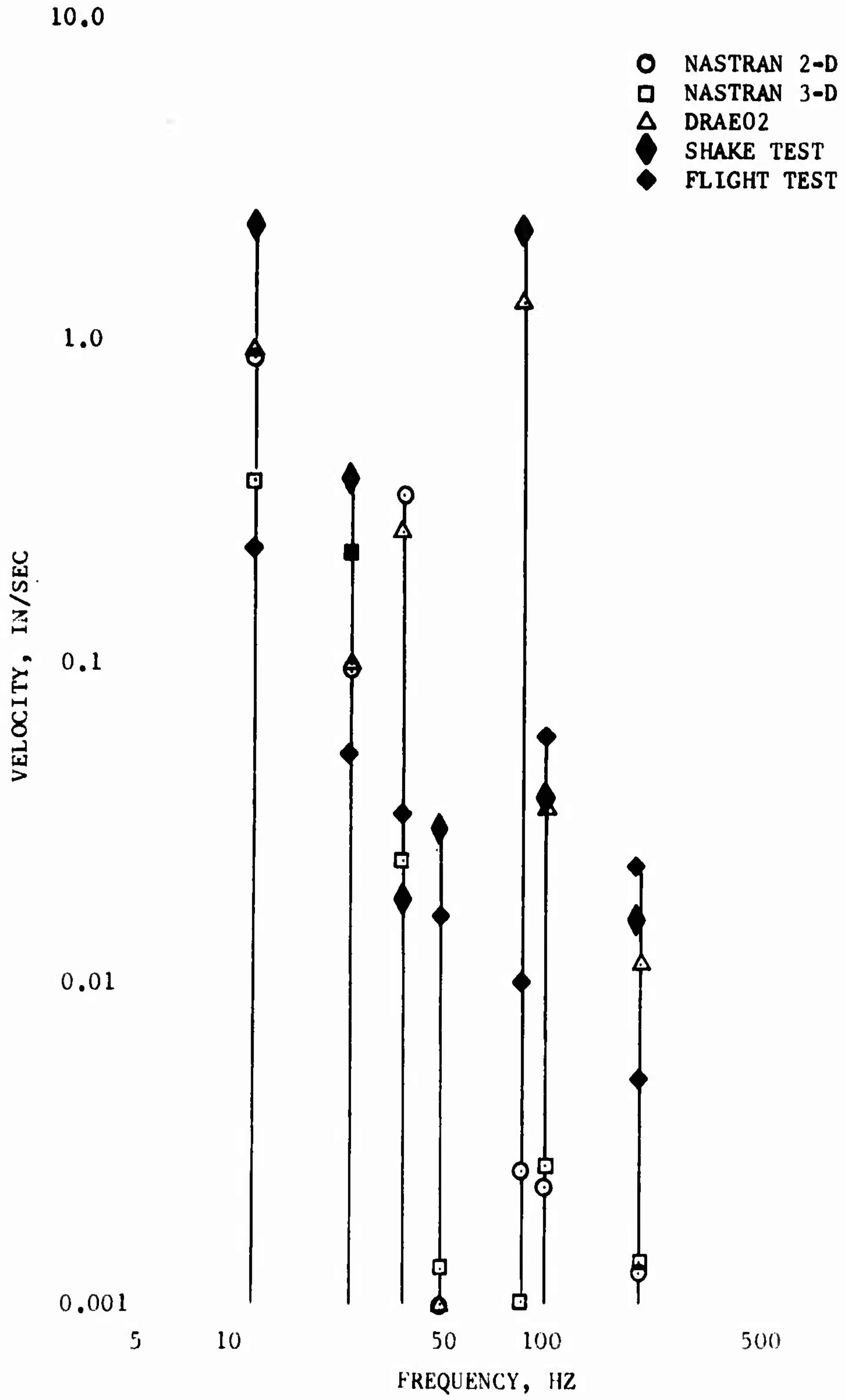

Figure 121. Comparison of Analytical and Test Engine Velocities for Simulated 110-Knot Level Flight Forces; Gearbox Vertical Response.

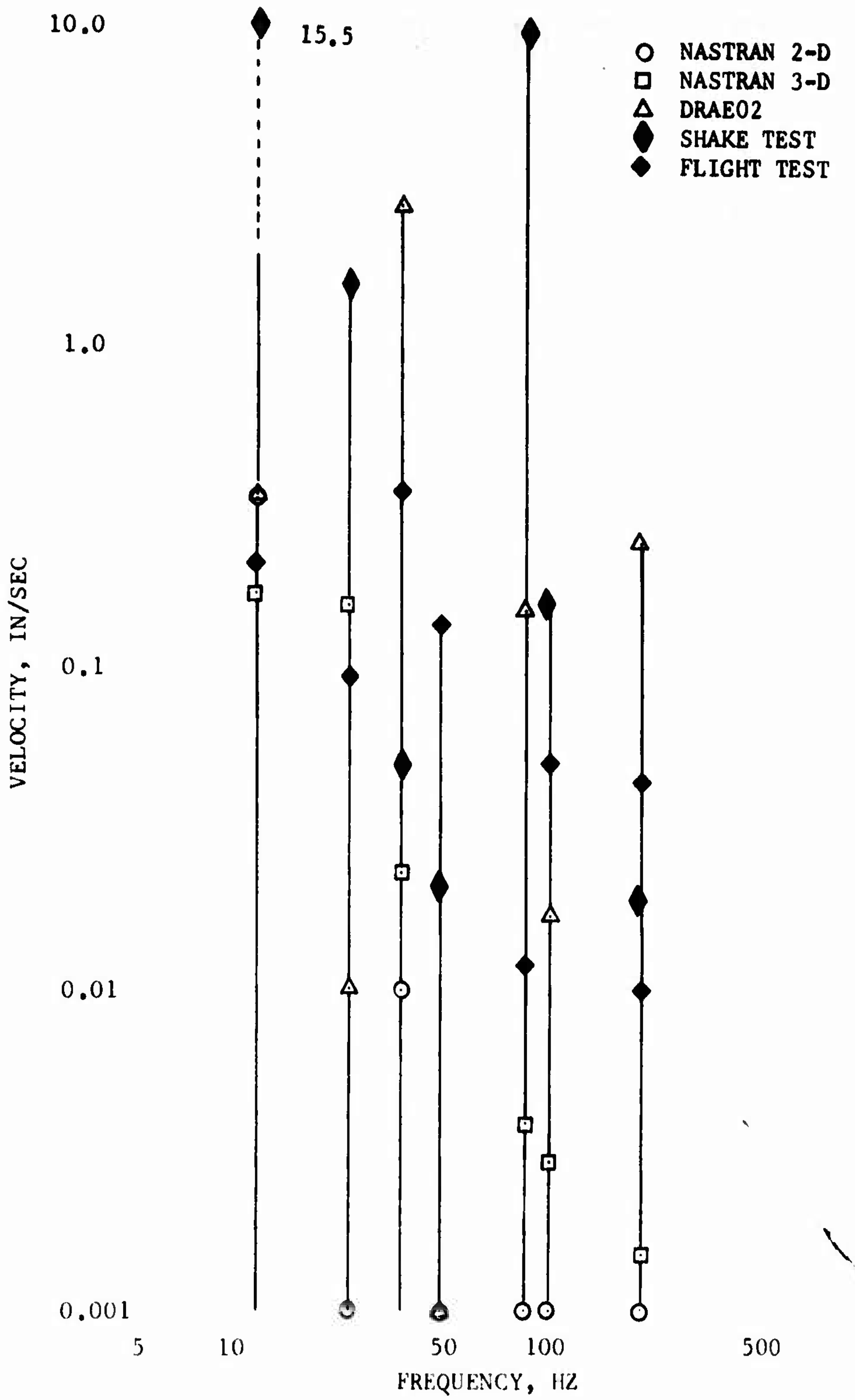

Figure 122. Comparison of Analytical and Test Engine Velocities for Simulated 110-Knot Level Flight Forces; Turbine Midsplit Vertical Response.

LIST OF APPENDIXES

Appendix	
A	SIMPLE MODEL PARAMETERS
B	TWO-DIMENSIONAL OH-58A NASTRAN MODEL PARAMETERS
C	T-63 NASTRAN MODEL PARAMETERS
D	MOBILITY ANALYSIS PROGRAM LISTING
E	THREE-DIMENSIONAL OH-58A NASTRAN MODEL PARAMETERS
F	NASTRAN AND MOBILITY ANALYSIS ENGINE RESPONSE DATA
G	TEST EQUIPMENT AND INSTRUMENTATION CALIBRATION DATA
H	SHAKE TEST RESULTS
J	AIRFRAME AND ENGINE TEST MOBILITIES
K	COMPUTER PROGRAM LISTING
L	MOBILITY ANALYSIS DATA

The above appendixes contain all data generated in the performance of this study. The data is not included in this publication. However, these appendixes are on file at the United States Army Air Mobility Research and Development Laboratory, Fort Eustis, Virginia, and will be furnished on request.

GLOSSARY OF TERMS

A	Acceleration signal
A_R	Impedance head acceleration signal
$[C]$	Matrix of element damping constants
$e^{i\omega t}$	Unit complex vector
$f(t)$	Forcing function, time domain
F	Applied forces
$F(\omega)$	Fourier transform of harmonic forcing function, frequency domain
$[K]$	Matrix of element spring constants (stiffnesses)
$[M]$	Matrix of element masses
V	Coordinate velocity
$V(\omega)$	Fourier transform of harmonic response (velocity), frequency domain
V_o	Free system velocities at external coordinates
V_N	Velocity of coordinate N of a simple system
$x(t)$	Displacement function, time domain
$\dot{x}(t)$	Velocity function, time domain
$\ddot{x}(t)$	Acceleration function, time domain
X	Fuselage station coordinate axis
Y	Element mobility; fuselage buttlines coordinate axis
$[Y(\omega)]$	Matrix of mobilities at frequency ω
$[Y_{CHK}]$	Matrix of engine responses due to airframe excitation sources
Y_N	Transfer mobility of a simple system at coordinate N due to an external force at some other coordinate (specifically an interface coordinate)

GLOSSARY OF TERMS - Continued

Y_{ij}	Mobility element for the response of the i^{th} coordinate due to a force at the j^{th} coordinate
Z	Element impedance; fuselage waterline coordinate axis
$[Z(\omega)]$	Matrix of impedances at frequency ω
ϕ	Mobility phase angle
τ	Period of harmonic function
θ_x	Finite element angular displacement coordinate (torsion)
ω	Excitation frequency
$\{\ \}$	Vector of element forces, velocities, etc.
$[\ ]$	Matrix of element masses, springs, damping, impedances, mobilities, etc.
$\frac{d}{dt}$	Derivative with respect to time
$\int$	Integration

SUBSCRIPTS

1,2,...	Sequential elements
E	External coordinate reference
I	Internal coordinate reference
EE	External coordinate response reference, external coordinate force reference
EI	External coordinate response reference, internal coordinate force reference
II	Internal coordinate response reference, internal coordinate force reference
IE	Internal coordinate response reference, external coordinate force reference

GLOSSARY OF TERMS - Concluded

SUB-SUBSCRIPTS

1,2,3,...	Denotes submatrix of the free system primary mobility matrix partitioning

SUPERSCRIPTS

I	System 1, independent system reference; airframe system parameter
II	System 2, dependent system reference; engine system parameter